In Situ Oxidation Study of Flat and Stepped Binary Alloy Surfaces

Claus S. Ellinger
Stuttgart, 2010

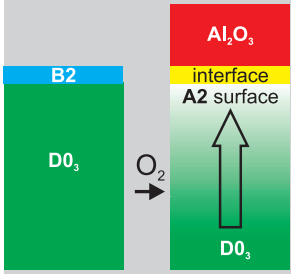

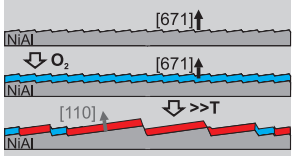

Max-Planck-Institut
für Metallforschung
in Stuttgart

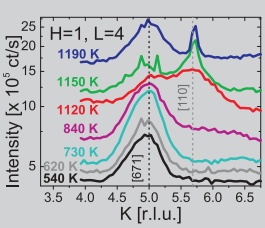

Institut für Theoretische
und Angewandte Physik
der Universität Stuttgart

In situ Oxidation Study of Flat and Stepped Binary Alloy Surfaces

Von der Fakultät Mathematik und Physik der Universität Stuttgart
zur Erlangung der Würde eines Doktors der
Naturwissenschaften (Dr. rer. nat.) genehmigte Abhandlung

Vorgelegt von

CLAUS STEFFEN ELLINGER

aus Stuttgart

Hauptberichter:	Prof. Dr. H. Dosch
Mitberichter:	Prof. Dr. P. Michler

Tag der mündlichen Prüfung: 21. Mai 2010

Institut für Theoretische und Angewandte Physik
der Universität Stuttgart
Max-Planck-Institut für Metallforschung
in Stuttgart

2010

Contents

Chapter 1

Deutsche Zusammenfassung

Motivation

Durch Beimischung von Zinn und Arsen zu Kupfer lassen sich härtere und stabilere Werkzeuge und Waffen produzieren als mit reinem Kupfer. Dies erkannte die Menschheit schon vor über 5000 Jahren. Heute gilt Bronze unter Historikern als die erste, von Menschenhand erzeugte Legierung. Auch Stahl, heutzutage das wohl wichtigste Strukturmaterial für die industrielle Anwendung, ist eine Legierung aus Eisen und geringen Mengen an Kohlenstoff und anderen Additiven wie Chrom oder Titan. Allerdings stößt die hohe mechanische Stabilität von Eisen-basiertem Stahl bei Anwendungen unter sehr hohen Temperaturen und sehr reaktiven Umgebungen an ihre Grenzen. Zu diesen Anwendungen zählen Gasturbinen in Flugzeugen, Kohlevergaser in Kraftwerken und spezielle Druckbehälter für chemischen Reaktionen. Um auch in diesen Prozessen hohe mechanische Stabilität und Oxidationsbeständigkeit gewährleisten zu können, greift man auf so genannte Superlegierungen zurück. Diese basieren auf den geordneten Phasen von intermetallischen Verbindungen wie Fe_3Al und NiAl [1,2]. Die binären Legierungen Fe_3Al und NiAl zeigen sehr gute mechanische Stabilität bis hin zu ihrem Ordnungs-Unordnungsphasenübergang, welcher bei sehr hohen Temperaturen liegt. Als Korrosionsschutz unter zum Teil sehr aggressiven Anwendungsbedingungen dient eine dünne, homogene Oxidschicht auf der Oberfläche der Legierungen. Dabei schützt eine reine Al_2O_3-Schicht die Legierung am besten.

Während der Oxidation bei niedrigen Sauerstoffdrücken (ca. 10^{-6} mbar) bilden sich auf einkristallinen Legierungsoberflächen wie NiAl (1,1,0) oder CoGa (1,0,0) wissenschaftlich interessante Oberflächenoxide aus [3–6]. Als Oberflächenoxid werden langreichweitig geordnete, ultradünne Filme mit einer wohldefinierten Dicke bezeichnet, deren atomare Struktur sich vom Volumenoxid unterscheidet und von der Substratoberfläche stabilisiert wird. Ein Beispiel ist der $Al_{10}O_{13}$-Film auf NiAl(1,1,0), welcher sehr häufig als Templat zur Untersuchung der katalytischen Aktivität von Nanopartikeln verwendet wird. Für die Anwendung als Nanotemplat ist ein Oxidfilm mit einer geringen Anzahl an Defekten wünschenswert.

Wie beschrieben ist es für die technischen und wissenschaftlichen Anwendungen

wichtig, möglichst homogene, geschlossene, eindomänige Oxidfilme herzustellen. Dafür ist ein grundlegendes Verständnis des anfänglichen Oxidationsprozesses auf Legierungsoberflächen erforderlich. In den letzten Jahren wurde daher die Oxidation von flachen Einkristalloberflächen wie NiAl(1,1,0), FeAl(1,1,0) oder CoGa(1,0,0) ausführlich und auf atomarer Ebene untersucht [3–8]. Die vorliegende Arbeit baut auf diesen Ergebnissen auf, erhöht aber die Komplexität der untersuchten Systeme. So wird die Oxidation der Fe_3Al (1,1,0)-Oberfläche bei Sauerstoffdrücken bis 10^{-6} mbar untersucht. Fe_3Al besitzt bis zu einer Temperatur von 820 K eine hoch geordnete $D0_3$-Struktur. An diesem System kann somit erforscht werden, wie die Ausbildung der vor Korrosion schützenden Oxidschicht die intermetallische Ordnung beeinflusst, welche für die mechanische Stabilität des Systems verantwortlich ist. Zudem soll die chemische Zusammensetzung der Oxidlage für verschiedene Oxidationsbedingungen analysiert werden, um möglichst homogene α-Al_2O_3-Schichten zu wachsen. Für das NiAl-System wird die Oxidation der (6,7,1)- und der (4,3,0)-Oberfläche für niedrige Sauerstoffdrücke untersucht. Beide Oberflächennormalen sind vizinal zur $[1,1,0]$-Richtung, das heißt die Oberflächen bestehen aus einer regelmäßigen Anordnung von Stufen und kleinen, (1,1,0) orientierten Terrassen. Zum einen wird anhand dieser Oberflächen überprüft, ob die vizinalen Oberflächen thermodynamisch stabil sind. Zum anderen wird der Einfluss von Stufen auf den anfänglichen Oxidationsprozess untersucht. Ändert sich die Morphologie der Oberfläche durch die Ausbildung einer Oxidschicht? Beeinflussen die Stufen die Struktur des aufwachsenden Oxids? Ist es möglich, mit Hilfe gezielt ausgerichteter Stufen bestimmte Oxidstrukturen zu wachsen? Diese Fragen werden auch für eine gestufte CoGa-Oberfläche beantwortet, welche aus 200 Å großen (1,0,0) Terrassen besteht. Zudem wird für diese Oberfläche der zeitliche Verlauf des Oxidwachstums im Druckbereich bis 10^{-6} mbar analysiert. Zusammenfassend gibt diese Arbeit Einblicke in das Zusammenspiel zwischen intermetallischer Ordnung und Oxidbildung auf Legierungsoberflächen und stellt den Einfluss von Stufen, welche auf jeder Oberfläche vorhanden sind, auf den Oxidationsprozess dar.

Experimentelles

Die hauptsächlich verwendete Untersuchungsmethode dieser Arbeit ist Oberflächenröntgenbeugung (SXRD) [9, 10]. Zusammen mit einer transportablen Kammer für die Experimente mit Röntgenstrahlung, in der sich Temperaturen von 300 K bis 1750 K und Gasdrücke von 10^{-11} bis 10^{-5} mbar einstellen lassen, kann somit die Oxidation von Legierungsoberfächen *in situ* verfolgt werden. Mit Hilfe von so genannten "Crystall Truncation Rod(CTR)"-Messungen können dabei die Struktur der Oberfläche und Strukturänderungen während der Oxidation auf atomarer Skala bestimmt werden [11]. Die SXRD Messungen werden an brillanten Synchrotronstrahlungsquellen wie der Angströmquelle Karlsruhe (ANKA), der Europäischen Synchrotron Strahlungsquelle (ESRF) in Grenoble und der Swiss Light Source (SLS) in Villingen durchgeführt. Zur chemischen Analyse der Oxidschichten und zur Bestimmung der Bindungszustände der Atome in Legierung und Oxid wird hochauflösende Rumpfniveauphotoelektronenspektroskopie

(HRCLS) angewendet. Die Experimente werden am Synchrotron des MAX-Lab in Lund (Schweden) durchgeführt. Für erste Strukturbestimmungen und zur Überprüfung der Reinheit der Proben werden die Proben im Labor mit niederenergetischer Elektronenbeugung (LEED) und Auger Elektronen Spektroskopie (AES) charakterisiert.

Alle, in dieser Arbeit verwendeten Einkristalle wurden am Max-Planck Institut für Metallforschung gewachsen, geschnitten und poliert. Die sauberen Oberflächen wurden im Ultrahochvakuum (UHV) durch mehrere Sputter- und Heizzyklen präpariert. Kontrollierte Oxidation erfolgte bei Probentemperaturen zwischen 300 K und 820 K und Sauerstoffdrücken zwischen 10^{-9} und 10^{-5} mbar. Die CoGa-Probe wurde auch mit Wasserdampf oxidiert.

Ergebnisse

Die Oxidation der Fe_3Al (1,1,0)-Oberfläche

Die Analyse der CTRs der sauberen Fe_3Al (1,1,0)-Oberfläche zeigt, dass die oberste Atomlage eine andere intermetallische Ordnung aufweist als der darunter liegende, $D0_3$-geordnete Volumenkristall. Durch Al Segregation in die oberste Lage liegt dort eine FeAl-Stoichiometrie vor, was zu einer B2-artigen Ordnung führt. Ein einfaches, schematisches Modell der saubere Oberfläche ist in Abbildung 1.1c gezeigt. Nach 30 minütiger Oxidation bei einem Sauerstoffdruck von 10^{-6} mbar und Temperaturen zwischen 400 K und 720 K verschwindet sowohl die $D0_3$- als auch die B2-Ordnung im oberflächennahen Bereich. Im Experiment wird dies durch das Verschwinden des Signal entlang von CTRs sichtbar, welche nur von Streuung an Untergittern der B2- bzw. $D0_3$-artigen Ordnung herrühren. Abbildung 1.1b zeigt dieses Verschwinden exemplarisch für einen Punkt auf einem B2-artigen Rod. Abbildung 1.1a zeigt, dass die CTRs, welche vom fundamentalen, kubisch raum-zentrierten Gitter herrühren, noch messbar sind. Die Oberfläche rauht also während der Oxidation nur geringfügig auf und ist noch kristallin. Gleichzeitig zeigen spekuläre Röntgenreflektivitätsmessungen nach der Oxidation, dass sich ein 8.4 Å dicker Oxidfilm mit einer Grenzflächenrauhigkeit von ca. 2 Å ausbildet. Wir folgern, dass zur Ausbildung von Aluminiumoxid das Aluminium aus dem Oberflächenbereich des Fe_3Al Kristall gezogen wird, was die intermetallische Ordnung in diesem Bereich deutlich verringert. Nach Oxidation ist an der Oxid-Fe_3Al-Grenzschicht nur noch das fundamentale Gitter vorhanden. Die $D0_3$- und B2-Ordnung baut sich zum Volumenkristall hin nur langsam wieder auf. Dies ist schematisch in Abbildung 1.1c dargestellt. Nimmt man an, dass sich das Verschwinden der B2- bzw. $D0_3$-artigen Ordnung vom Volumen bis zur Oberfläche mit einem Gaussschen Profil oder einem Potenzgesetz für die Besetzung (ähnlich dem β-Rauhigkeitsmodell) beschreiben lässt, kann man das beobachtete Verschwinden des CTR-Signals erklären. Der Oberflächenbereich mit gestörter Ordnung kann auf 2 bis 3 nm abgeschätzt werden.

Bei Oxidationstemperaturen von 300 K, 420 K und 650 K und Sauerstoffdrücken von 10^{-8} und 10^{-6} mbar wurde die chemische Zusammensetzung des gewachsenen Oxidfilms

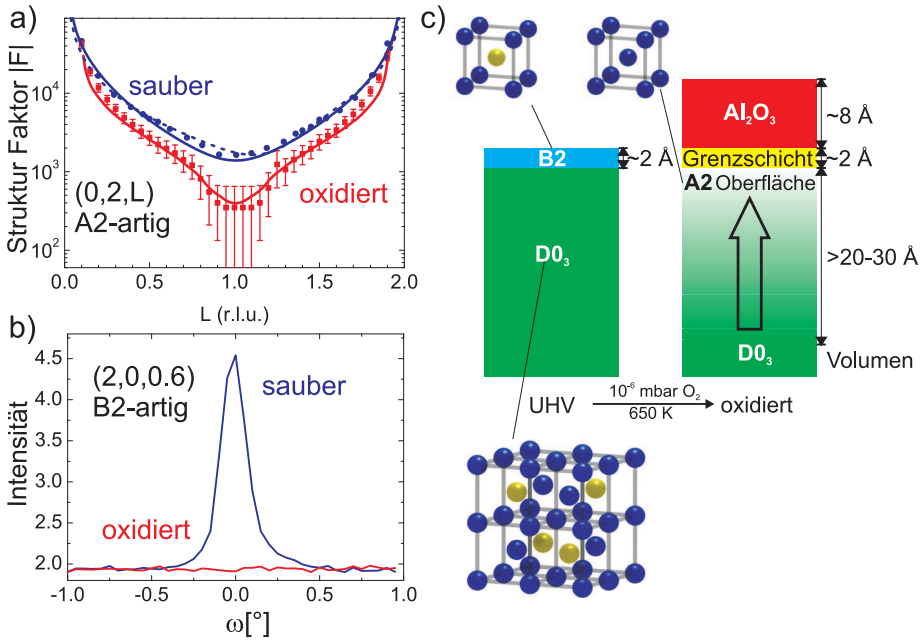

Abbildung 1.1: a) A2-artiger CTR vor (blau) und nach (rot) der Oxidation: Das Signal nach der Oxidation ist noch vorhanden. b) Signal an einer Stelle entlang eines B2-artigen CTRs vor (blau) und nach (rot) der Oxidation. Das Signal der B2-Ordnung verschwindet nach der Oxidation. c) Schematisches Modell der sauberen (links) und oxidierten (rechts) Oberfläche. Die eingefügten Einheitszellen zeigen die A2-, B2- und $D0_3$-Struktur.

mit HRCLS-Messungen analysiert. Abbildung 1.2 zeigt, bei welchen Oxidationsbedingungen oxidiertes Al oder eine Mischung aus oxidiertem Al und oxidiertem Fe an der Legierungsoberfläche gefunden werden. In Kombination mit Röntgenreflektivitätsmessungen zeigt sich, dass sowohl die chemische Zusammensetzung, als auch die Dicke des Oxidfilm stark von der Oxidationsrate und der Al Segregation aus dem Volumen abhängen. Für hohe Oxidationsraten bei einem Sauerstoffdruck von 10^{-6} mbar bilden sich für alle untersuchten Temperaturen Fe- und Al-Oxid aus. Für niedrigere Oxidationsraten bei einem Sauerstoffdruck von 10^{-8} mbar und einer ausreichenden Al Segregation bei erhöhten Temperaturen findet man hingegen eine reine Al-Oxidschicht, die bei 650 K schon gut geordnet ist. Ein nachträgliches Aufheizen der oxidierten Probe auf 770 K führt in allen untersuchten Fällen zu einer reinen Al_2O_3 -Lage, das oxidierte Fe wird wieder metallisch. Für die technische und wissenschaftliche Anwendung ist eine reine, homogene Aluminiumoxidschicht sehr wichtig, um gute Oxidationbeständigkeit zu gewähren. Die Ergebnisse dieser Arbeit zeigen, dass dafür während der anfänglichen Oxidation eine niedrige Oxidationsrate und eine hohe Al Segregation gewährleistet werden müssen. Die Sauerstoff induzierte Unordnung im Oberflächenbereich könnte jedoch die mechanischen Eigenschaften der Oberfläche verändern, so dass das Fe_3Al an der Oberfläche spröder wird.

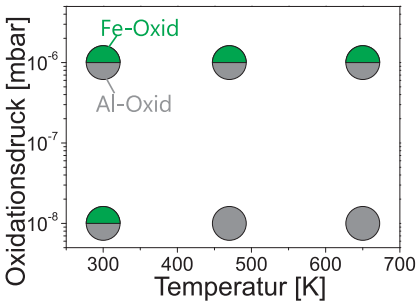

Abbildung 1.2: Das Diagramm zeigt die durch HRCLS bestimmte Komposition des Oxids auf Fe_3Al(1,1,0) in Abhängigkeit von Sauerstoffdruck und Oxidationstemperatur. Grün und grau gefüllte Kreise bedeuten, dass sich Fe- bzw. Al-oxid gebildet hat.

Die Oxidation regelmäßig gestufter NiAl Oberflächen

Die untersuchten vizinalen NiAl-Oberflächen haben die Orientierung (6,7,1) und (4,3,0). Das volumen-terminierte Modell beider Oberflächen besteht aus einer regelmäßigen Anordnung von (1,1,0) Terrassen, welche eine Breite von circa 14 Å haben. Die monoatomaren Stufen laufen auf NiAl(6,7,1) entlang der $[\bar{1}, 1, \bar{1}]$-Richtung und auf NiAl(4,3,0) entlang $[0, 0, 1]$. Mit Hilfe von SXRD und LEED wurde für beide Oberflächen die saubere Oberfläche charakterisiert und die Oxidation bei 550 K und 10^{-6} mbar O_2 untersucht.

Die Oxidation von NiAl(6,7,1)

Die CTR-Messungen zeigen, dass die präparierte, saubere, vizinale (6,7,1) Oberfläche in UHV für Temperaturen zwischen 300 K und mindestens 1190 K thermodynamisch stabil ist. Die Oberfläche besteht aus einer regelmäßigen Anordnung von Terrassen und Stufen und ist nicht facettiert. Eine genauer Analyse der CTRs zeigt, dass die größeren Al-Atome der obersten Terrassen nach außen und die kleineren Ni-Atome nach innen relaxieren. Der vertikale Abstand der beiden Atomsorten beträgt dabei 0.2 Å, wobei dieser Wert sehr gut mit dem für die flache NiAl(1,1,0)-Oberfläche gemessenen Wert übereinstimmt [12]. Für die Atome direkt an der Stufenposition findet sich immer eine Relaxation zum Kristall hin, während die Atome an den Ecken unterhalb der Stufenatome immer nach außen relaxieren. Dieses Relaxationsverhalten führt zu einem Abrunden der Elektronendichte an den Stufen, was von der Theorie für Oberflächenstufen vorhergesagt wird [13]. Zudem induziert dieses Relaxationsprofil an jeder Stufe einen Spannungsdipol. Diese elastischen Dipole der einzelnen Stufen wechselwirken miteinander und führen zu einer gegenseitigen Abstoßung der Stufen, welche die Stabilität der Vizinaloberflächen erklären kann [14].

Nach 15-minütiger Oxidation der Oberfläche bildet sich -analog zur NiAl (1,1,0)-Oberfläche- ein 5 Å dünner, amorpher Al-Oxidfilm aus. Dabei wird die regelmäßige Anordnung von (1,1,0) Terrassen nicht zerstört. Die Analyse der CTRs der oxidierten Oberfläche zeigt jedoch, dass sich das Relaxationsprofil in den ersten Lagen stark ändert.

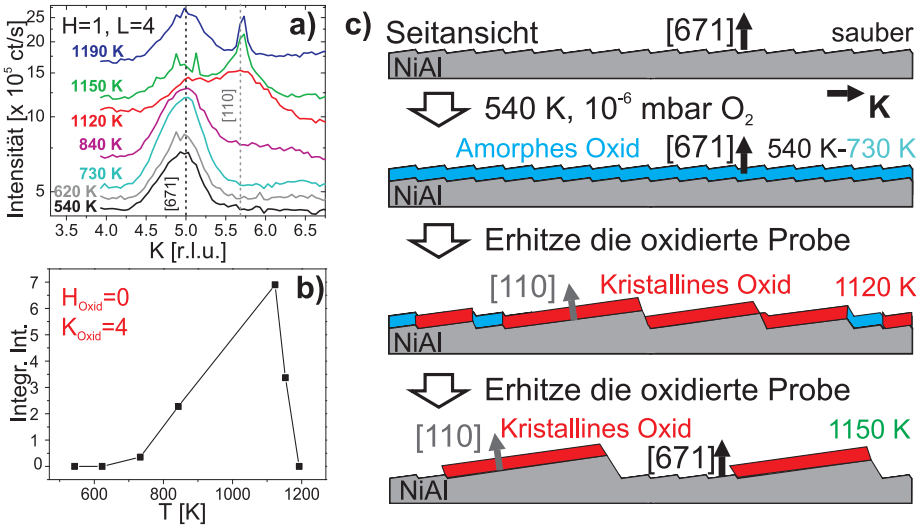

Abbildung 1.3: a) Temperaturabhängige K-Scans quer zur Stufenrichtung, die nach der Oxidation durchgeführt wurden, zeigen das Anwachsen des Signals an der Position für (1,1,0) Facetten (gestrichelte graue Linie) und die Abnahme der Signals des CTRs der (6,7,1)-Oberfläche (schwarze gestrichelte Linie). Dies zeigt die Facettierung der Oxid-Legierungsgrenzfläche. b) Integrierte Intensität eines Oxidreflexes in Abhängigkeit der Glühtemperature der oxdierten Probe: Ab 840 K bildet sich langreichweitig geordnetes Oxid aus. c) Schematische Darstellung des Oxidations- und nachfolgenden Glühprozesses der NiAl(6,7,1)-Probe. Dargestellt ist eine Seitenansicht der sauberen Probenoberfläche mit regelmäßigen Stufen, welche nach Oxidation und Heizvorgang facettiert, während sich das Oxid ordnet.

Al und Ni Atome relaxieren nach innen. Zudem bilden sich in einem 13 Å tiefen Bereich Al- und Ni-Fehlstellen aus. Einige Ni-Atome besetzen Al-Plätze. Dies kann dadurch erklärt werden, dass durch bevorzugte Al-Oxidation Al-Atome in den Oxidfilm und an die Oxid-NiAl-Grenzfläche gezogen werden. Die beschriebenen Defekte im Oberflächenbereich der Legierung bilden sich aus.

Von der NiAl (1,1,0)-Oberfläche ist bekannt, dass sich durch Heizen der Probe auf 1100 K ein langreichweitig geordnetes Oberflächenoxid ausbildet, welches zwei Zwillingsdomänen besitzt [3]. Abbildung 1.3a zeigt Scans durch das CTR-Signal der oxidierten (6,7,1) Oberfläche quer zur Stufenrichtung für verschiedenen Probentemperaturen. Ab 840 K nimmt das CTR-Signal ab und ein neues Signal wird detektiert, welches der Ausbildung von größeren (1,1,0) Facetten zugeordnet werden kann. Somit können ab 840 K kinetische Barrieren für den Materialtransport überwunden werden. Die für die Oxid-NiAl-Grenzfläche stabilen (1,1,0) Facetten bilden sich aus. Die Facetten sind bis zu 50 Mal größer als die Terrassen der sauberen Oberfläche. Ab 1150 K beginnt die Desorption des Oxids, die saubere (6,7,1)-Oberfläche bildet sich aus. Der gesamte Prozess ist schematisch in Abbildung 1.3c dargestellt. Wie Abbildung 1.3b zeigt, bildet sich während

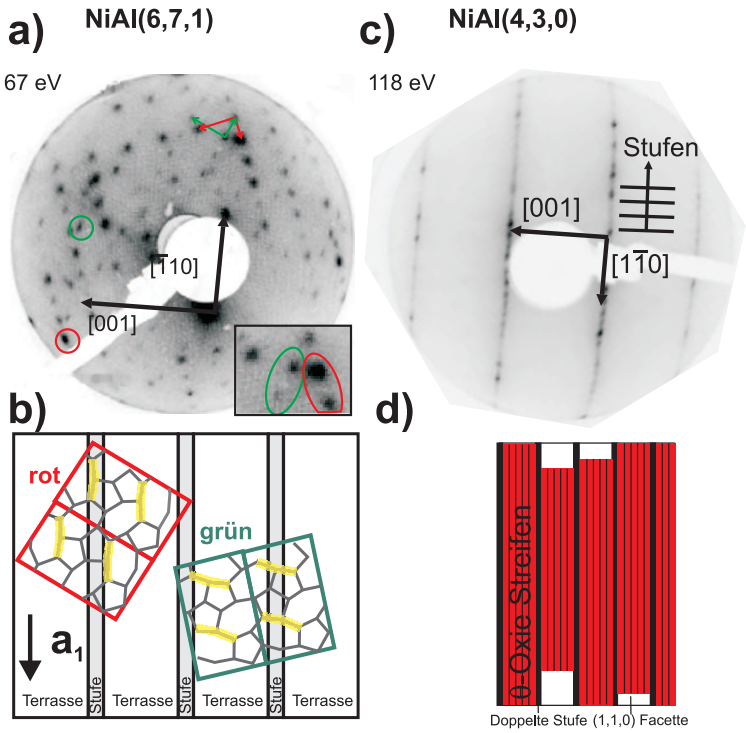

Abbildung 1.4: a)+c) LEED-Bilder der oxidierten und geheizten (6,7,1)- und (4,3,0)-Oberfläche. Auf der (6,7,1)-Oberfläche wächst das von der (1,1,0)-Oberfläche bekannte Oxid auf. Die Reflexe der ”roten” Domäne sind deutlich stärker, da diese bevorzugt aufwächst. b) Schematische Darstellung beider möglichen Domänen auf NiAl(6,7,1): Für die ”rote” Domäne laufen die gelb markierten Al-Reihen in den grauen Pentagon-Heptagon-Paaren der Grenzschicht in Richtung der Stufen, was einen bevorzugten Spannungsabbau und somit eine bevorzugtes Wachstum ermöglicht. c) Das LEED-Bild zeigt eine komplett andere Oxidstruktur als auf der (6,7,1)-Oberfläche. In Bezug auf die $[1, \bar{1}, 0]$- und die $[0, 0, 1]$-Richtung hat das neue Oxid eine (1×7)-Überstruktur, weshalb man entlang $[1, \bar{1}, 0]$ neue Reflexe beobachtet. d) Streifenartiges Wachstum von 5 Einheitszellen breitem θ-Al_2O_3 auf mindestens 27 Å breiten (1,1,0)-Facetten.

des schrittweisen Aufheizens auch ein langreichweitig geordnetes Oxid auf den Facetten aus. LEED (siehe Abbildung 1.4a) und SXRD zeigen, dass das gewachsene Oxid dieselbe Struktur wie das von NiAl(1,1,0) bekannte Oberflächenoxid hat. Dabei bildet sich eine der zwei möglichen Zwillingsdomänen bevorzugt aus. Vom Oberflächenoxid ist bekannt, dass das Al an der Oxid-NiAl-Grenzschicht Pentagon-Heptagon-Paare mit charakteristischen Al-Reihen bildet (siehe Abbildung 1.4b) [5]. Entlang diesen Al-Reihen bauen sich Verspannungen auf. Für die beobachtete Oxiddomäne auf der (6,7,1) Oberfläche laufen diese Reihen genau entlang den Stufenkanten, an welchen bevorzugt Spannungen abgebaut werden können. Dieser Spannungsabbau löst wahrscheinlich das eindomänige Wachstum aus.

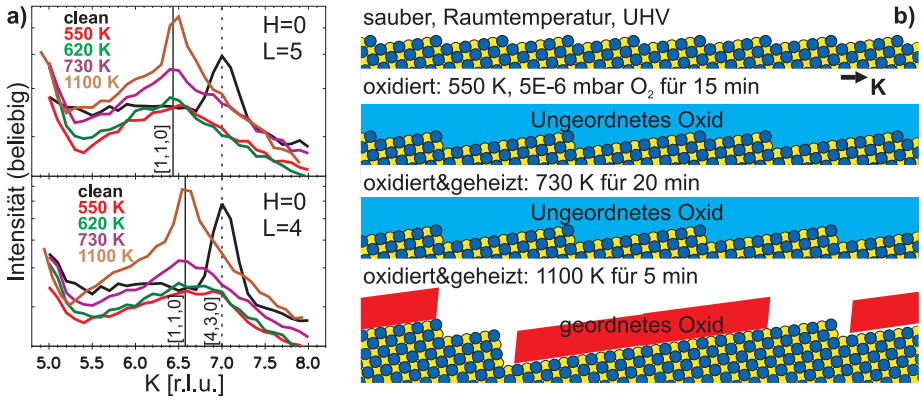

Abbildung 1.5: a) Temperaturabhängige K-Scans quer zur Stufenrichtung, die nach der Oxidation durchgeführt wurden, zeigen das Anwachsen des Signals an der Position für (1,1,0) Facetten (durchgezogene Linie) und die Abnahme des CTR-Signals (gestrichelte Linie). Die Scans zeigen die Facettierung der Oxid-Legierungsgrenzfläche. b) Schematische Darstellung des Oxidations- und nachfolgenden Glühprozesses der NiAl(4,3,0)-Probe. Dargestellt ist eine Seitenansicht der sauberen Probenoberfläche mit regelmäßigen Stufen, welche nach Oxidation facettiert. Bei Erhöhen der Temperatur werden die Facetten größer und das Oxid ordnet sich.

Die Oxidation von NiAl(4,3,0)

Auch von der sauberen (4,3,0)-Oberfläche wurde die Struktur der Oberfläche mit Hilfe von CTR-Messungen bestimmt. Die Ergebnisse der (4,3,0) und (6,7,1)-Oberfläche sind dabei qualitativ und quantitativ sehr ähnlich. Die (4,3,0)-Oberfläche ist bis mindestens 1350 K stabil und facettiert nicht. Al- und Ni-Atome in den obersten Terrassen relaxieren nach außen bzw. innen. An den Stufen zeigt sich wieder eine Abrundung der Elektronendichte, die Stufenatome relaxieren nach innen und die Kantenatome nach außen.

Oxidiert man die (4,3,0) Oberfläche bei gleichen Bedingungen bildet sich auch hier ein 5 Å dicker, amorpher Al-oxidfilm aus. Die durchgeführten CTR-Messungen zeigen, dass auch das durch bevorzugte Al-Oxidation hervorgerufene Segregationsprofil und die Änderungen der Relaxationen sehr ähnlich zur oxidierten NiAl (6,7,1)-Oberfläche sind. So treten bis zu einer Legierungstiefe von 12 Å Al-Fehlstellen auf, während sich die Ni-Fehlstellen auf die ersten 6 Å Tiefe beschränken. Etwas Ni besetzt vor allem in einer Tiefe zwischen 6-8 Å die leeren Al-Plätze. Die vertikalen Segregationsprofile der vizinalen wie auch der flachen (1,1,0)-Oberfläche sind sehr ähnlich, was auf eine geringere Bedeutung der Stufen als Kanäle für die Diffusion zwischen den Lagen schließen lässt.

Analog zur (6,7,1)-Oberfläche zeigen die K-Scans durch einen CTR (Abbildung 1.5a) Morphologieänderungen auf. Abbildung 1.5b stellt den beobachteten Facettierungsprozess schematisch dar. Schon bei der Oxidationstemperatur von 550 K verwindet das CTR-Signal der (4,3,0)-Oberfläche und ein sehr breites Signal an der Position von (1,1,0)-Facetten wird beobachtet. Daraus folgt, dass auch für die oxidierte

(4,3,0)-Probe (1,1,0) Facetten thermodynamisch stabil sind. Die durchschnittliche Facettenbreite bei 550 K beträgt 27 Å, was einer Bündelung von zwei ursprünglichen Terrassen entspricht. Aufgrund kinetischer Barrieren für den weiteren Materialtransport wächst die Facettenbreite erst ab 830 K weiter an und erreicht ein Maximum, welches 5 mal größer als die ursprüngliche Terrasse ist. Die Temperaturabhängigkeit und die maximale Größe der Facetten der beiden untersuchten vizinalen Oberflächen unterscheidet sich deutlich, was auf verschiedene Oberflächenstabilitäten zurückzuführen ist.

Der größte Unterschied der beiden oxidierten vizinalen Oberflächen liegt jedoch in der Struktur des sich ausbildenden Oxids. Obwohl auch die (4,3,0)-Oberfläche (1,1,0)-Terrassen hat und beim Heizen der oxidierten Probe facettiert, bildet sich nicht das von NiAl(1,1,0) bekannte Oberflächenoxid aus. Aus der Analyse des LEED-Bildes in Abbildung 1.4c folgt, dass das Oxid eine zu θ-Al_2O_3 ähnlich Struktur hat. Eine Achse von θ-Al_2O_3 und die $[0,0,1]$-Richtung entlang den Stufen haben nur eine 1-prozentige Diskrepanz der Gitterparameter. Wächst nun θ-Al_2O_3 auf der (4,3,0)-Oberfläche auf, gibt es in diese Richtung kaum Spannungen, was wahrscheinlich das Aufwachsen dieser Oxidstruktur auslöst. In Richtung senkrecht zu den Stufen sind im LEED-Bild auch Reflexe des neuen Oxids zu erkennen. Im Bezug auf die sich bildenden (1,1,0) Facetten hat das Oxid eine (1×7)-Überstruktur. Die im LEED-Bild ebenfalls vorhandene, streifenartige Intensitätsverteilung quer zu den Stufen ist ein Indiz für eine kleine Domänengröße des Oxids in diese Richtung. Ein streifen-artiges Wachstum, wie es schematisch in Abbildung 1.4d dargestellt ist, kann das LEED-Bild vollständig erklären. Es zeigt lang-ausgedehnte Oxiddomänen auf den (1,1,0)-Facetten, welche für das beschriebenen Oxidwachstum mindestens aus zwei ursprünglichen Terrassen bestehen müssen.

Der Vergleich der Oxidation beider vizinaler NiAl-Oberflächen zeigt, dass es die gezielte Ausrichtung von Stufen auf der Oberfläche erlaubt, die aufwachsende Oxidstruktur und sogar das Domänenwachstum zu steuern. Dabei spielt Spannungsabbau an der Oxid-Legierungsgrenzfläche entlang den Stufen die ausschlaggebende Rolle.

Die Oxidation einer regelmäßig gestuften CoGa Oberfläche

Ergänzend wurde in dieser Arbeit die Oxidation einer einkristallinen, gestuften CoGa Oberfläche mit 200 Å breiten (1,0,0)-Terrassen untersucht. Der Kristall ist so geschnitten, dass alle Stufen entlang der $[0,0,1]$-Richtung ausgerichtet sind. Von der Oxidation der einkristallinen, flachen CoGa (1,0,0)-Oberfläche ist bekannt, dass bei Sauerstoffdrücken bis 10^{-6} mbar und Temperaturen ab 550 K ein Oberflächenoxid aufwächst [8,15]. Dieses hat eine (2×1)-Überstruktur in Bezug zum Substrat und wächst entlang den Substratachsen in zwei, um $90°$ gedrehten Domänen auf. STM-Bilder zeigen deutlich, dass das Oxidwachstum an den wenigen Stufenkanten der (1,0,0)-Oberfläche beginnt. Ziel dieser Arbeit ist es, durch die gezielte Vorgabe von Stufen senkrecht zu einer der Oxidachsen nur das Wachstum einer Domäne zu fördern und eine monodomänige Oxidschicht herzustellen. An der gestuften Oberfläche wird das Oxidwachstum bei Temperaturen zwischen 700 K und 820 K, sowie Sauerstoff- und Wasserdampfdrücken zwischen

10^{-9} und 10^{-5} mbar untersucht. In den LEED- und SXRD-Experimenten kann jedoch kein bevorzugtes Domänenwachstum beobachtet werden. Wie auf der flachen (1,0,0)-Oberfläche wachsen immer beide Oxiddomänen auf. Eine mögliche Erklärung hierfür liefert das LEED-Bild, welches von der sauberen Probe bei 820 K aufgenommen wurde. Es zeigt keine Reflexe einer kristallinen geordneten Oberfläche. Aufgrund der Temperatur und der hohen Beweglichkeit der Co- und Ga-Atome ist die Oberfläche ungeordnet. Auch Stufen an der Oberfläche sind dadurch nicht exakt definiert und können kein Oxidwachstum entlang einer bestimmten Richtung auslösen.

Mit Hilfe von SXRD-Messungen kann der genaue zeitliche Verlauf der Oxidbildung auf der gestuften CoGa-Oberfläche bestimmt werden. Abbildung 1.6a zeigt das Oxidsignal, welches proportional zur Bedeckung der Oberfläche ist, als Funktion der Zeit für die Oxidation mit O_2. In Abbildung 1.6a erkennt man deutlich, dass das Wachstum für alle untersuchten Sauerstoffdrücke bei einer Bedeckung von etwa $2/5$ (ca. 1.4×10^5 cts/s) ein erstes Plateau erreicht. In einem weiteren Schritt wächst das Oxid verlangsamt weiter, bis Vollbedeckung der Oberfläche erreicht ist. Wie die durchgezogenen Linie in der Abbildung zeigen, kann das Wachstum durch ein zweifach exponentiell verzögertes Wachstumsmodell beschrieben werden, welches ein epitaktisches Wachstum bei einer 2-dimensionalen Nukleation von Oxidinseln beschreibt. Von STM-Bildern der flachen (1,0,0)-Oberfläche ist bekannt, dass die (2×1) Oxiddomänen streifenartig aufwachsen, da es eine schnelle und eine langsame Wachstumsrichtung der Domänen gibt [16]. Ausgehend von diesen Ergebnissen kann dies für die gestufte Oberfläche folgendes Szenario bedeuten: Im ersten, schnellen Wachstumsschritt entlang der schnellen Wachstumsrichtung bilden beide Oxiddomänen auf jeder Terrasse ein Gitter von Inseln aus, welches nicht oxidbedeckte Lücken enthält. Die Domänen blockieren sich gegenseitig vom schnellen Weiterwachsen. Die Lücken werden im zweiten Wachstumsschritt durch das langsame Wachstum geschlossen. Ein Wachstum der Oxidinseln über die Stufen scheint nicht möglich, was auch die im Vergleich zur flachen Oberfläche kleinen Oxiddomänen von etwa 30×30 Å^2 erklärt [15].

Die Oxidation mit Wasserdampf, welche in Abbildung 1.6b gezeigt ist, verläuft im Vergleich zur O_2-Oxidation stark verzögert und mit kleineren Wachstumsraten ab. Möglicherweise ist die H_2O-Dissoziation und die Diffusion von O-Atomen an der Oberfläche gehemmt und H_2O-Moleküle blockieren die Stufenplätze, welche wichtige Nukleationskeime für Oxidwachstum sind.

Die Untersuchung der CoGa-Oberfläche im Vergleich mit den gestuften NiAl-Oberflächen zeigt deutlich, wie wichtig die Existenz stabiler, geordneter Stufen ist, um Oxidwachstum und Oxidstruktur mittels gezielt gewählter Stufen steuern zu können. Im Vergleich zur flachen CoGa (1,0,0)-Oberfläche, bei welcher das Oxidwachstum mit einem einfachen, exponentiell verzögertem Modell beschrieben werden kann, verändern Stufen das zeitliche Wachstum. Dies sind grundlegende Informationen für zukünftige Anwendungen der Oxidfilme als Nanotemplate oder als isolierende Schicht in elektronischen Bauteilen.

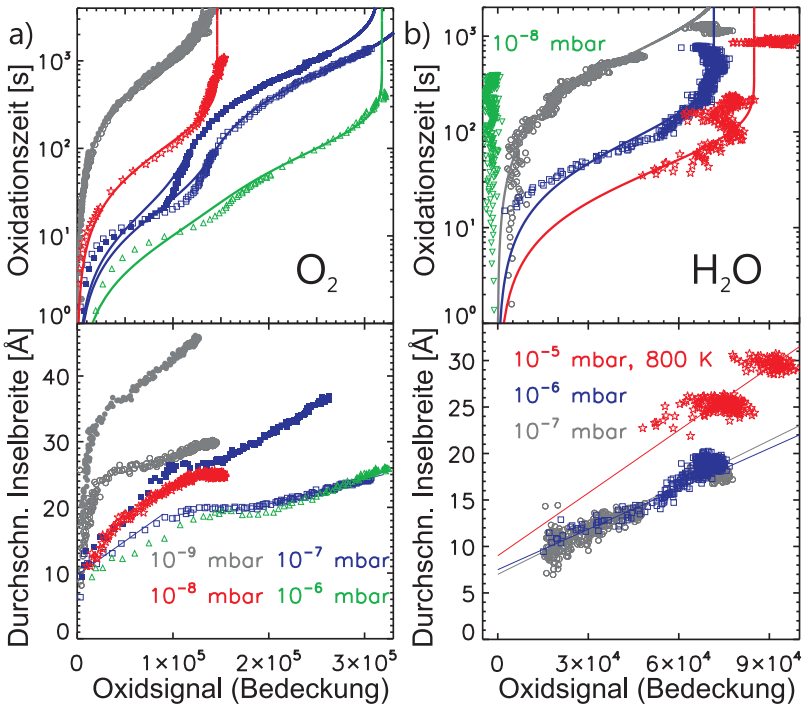

Abbildung 1.6: a)+b) Intergrierte Intensität eines Oxidreflexes (proportional zur Oxidbedeckung bei 2D Wachstum) in Abhängigkeit der Oxidationszeit (oberer Teil) und Oxiddomänenbreite in Richtung des langsamen Wachstums (unterer Teil). Die offenen und gefüllten Datenpunkte wurden für eine (1×2) bzw. eine (2×1)-Domäne aufgenommen. Die durchgezogenen Linien sind Ergebnisse eines Fit, für welchen eine zweifach exponentiell abgebremstes Wachstum verwendet wurde. Die Experimente wurden mit O_2 (a) und H_2O (b) bei 700 K und den angegebenen Drücken durchgeführt.

Chapter 2

Introduction

One main goal of material science is to optimise material properties for any needed application. A method to improve properties of metals like mechanical strength, ductility and corrosion resistance is alloying. The first intentionally produced alloy was Bronze. Already 3300 BC small amounts of tin and often arsenic were added to copper to render the alloy harder than the pure metal. The Bronze age ended around 1000 BC when it became technically possible to melt iron. Steel which consists of Fe with small amounts of C and other metallic additives had become -and probably still is- the favourite structural material. It has a high mechanical stability due to its complex defect structures. However, the properties of steel hit their limits in applications like gas turbine engines, nuclear reactors, chemical processing vessels, coal gasification plants and heat exchangers tubing. In theses processes a high strength, an excellent creep resistance as well as a good corrosion and oxidation resistance are required up to very high temperatures. Thus, so-called (single-crystal) superalloys are used which are based on ordered intermetallic phases of (binary) alloys like Fe_3Al or NiAl [1, 2]. The ordered phases show a very good creep resistance up to their order-disorder phase transition which is found at very high temperatures. The superalloy devices of the mentioned applications are also operated under highly reactive conditions in oxidizing and sulfidizing atmospheres. To prevent the alloy from further oxidation or sulfidation its surface needs to be covered by a thin homogeneous, closed, temperature resistant oxide layer. The oxide layer protects the underlying alloy from corrosion by blocking further charge transfer of ions and electrons necessary for further oxide formation. Improving the quality of the protective oxide layers would contribute to the reduction of the enormous costs which are caused by metal corrosion every year.

On some binary alloy surfaces like NiAl(1,1,0) or CoGa (1,0,0) long-range ordered, ultra-thin oxide films with only little amounts of defects are formed [3–6]. In scientific research these systems are popular nanotemplates to study the catalytic reactivity of nanoparticles. Especially Al_2O_3 is often used as support material for metallic particles in technical catalysis but also for organic molecules to study their electronic and vibrational properties. This makes alumina films on NiAl an ideal model system [17, 18]. Thin semi-conductive oxide films can also be used in gas sensors. Gallium oxide, for example, changes its conductivity depending on the adsorbed gases which makes the thin oxide films on CoGa an

interesting system for research. Furthermore thin oxide films could be used as insulating layers in electrical devices. Thus, low defect concentrations of the oxide films on the alloy surfaces are needed to provide an ideal isolation of the layers. In a magnetic random access memories (MRAM), for example, two magnetized layers have to be separated by a very thin insulating layer.

For all mentioned applications it would be desirable to further improve the homogeneity of the protective oxide films and to tailor the properties of the ultra-thin oxide layers on alloy surfaces. For this a fundamental understanding of the initial oxidation process on an atomic scale is necessary. Thus, the initial oxidation of alloys has been investigated for flat, low-index single crystal surface like FeAl(1,1,0), NiAl(1,1,0) and CoGa(1,0,0) in numerous former studies [3–8]. The studies show the formation of complex, ultra thin surface oxides. The surface oxides consist of one metallic layer surrounded by two oxygen layers. The studies are a first step to understand the initial oxidation process of an alloy and the structural properties of the oxides. However, defects like steps and kinks are present on every surface of polycrystals, nanoparticles but also of single crystals. As the step atoms are the least coordinated of all surface atoms they are preferential adsorption sites and strongly influence surface reactions like the oxidation [19]. This work continues the research on the oxidation of NiAl, FeAl and CoGa by increasing the complexity of the investigated single crystal surfaces. To further understand the influence of surface steps on the oxidation process regularly stepped alloy surfaces are investigated. In case of the Fe_3Al system the low-index (1,1,0) surface is investigated. Here the complexity is increased by the existence of a highly ordered phase of the system at the applied oxidation conditions, as the interplay between ordering and oxide formation is the another main aspect of the thesis. In the following the main questions of this thesis are summarized.

Motivation

The iron aluminide Fe_3Al is a binary alloy which is used as a basis for Fe-Al superalloys which have less weight but a higher mechanical stability then normal steel [1]. Despite its importance for application most of the former studies focus the initial oxidation of FeAl surfaces. In this thesis the oxidation of the Fe_3Al (1,1,0) surface is investigated on an atomic scale. Fe_3Al exhibits the highly ordered $D0_3$ phase up to a temperature of 820 K. This phase is responsible for its high creep resistance. In addition, the Fe_3Al surface is highly oxidation-resistant as an initially formed oxide layer prevents further oxidation. This arises the following questions that are investigated within this work:

- How does the formation of an oxide layer influence the ordering within in surface region of the alloy? How does the protective layer influence the mechanical stability?

- What is the chemical composition of the oxide layer formed at different oxidation conditions? Which kind of oxide (Fe-oxide, Al-oxide,...) is formed on the surface?

- Which conditions are needed to grow very homogeneous, smooth, closed, protective layers?

As described above, the influence of surface steps on the oxidation of alloy surfaces is another main aspect of this work. The NiAl (6,7,1) and (4,3,0) surfaces which are vicinal to the (1,1,0) surface have been chosen for the experiments. NiAl is also a basis for superalloys which makes a detailed knowledge on the initial oxidation valuable [2]. Furthermore comparisons to the low-index (1,1,0) surface can be made as this surface has been investigated intensively in the past. We also studied a stepped CoGa surface with (1,0,0) terraces to detect the influence of steps in comparison with the flat (1,0,0) surface. Following questions are tackled for the regularly stepped surfaces:

- Are the vicinal surfaces stable in UHV?
- How is the surface morphology changed during oxidation? How is the ordering within the surface region affected by the oxidation?
- How do the surface steps influence the oxide structure, compared to the corresponding low-index surfaces?
- Is it possible to tailor the growth of certain oxide structures or of certain oxide domains via the surface steps and a distinctive step orientation?

In addition differences between water and oxygen oxidation are highlighted for the CoGa system.

Within this thesis *in situ* surface x-ray diffraction (SXRD) is applied to determine the surface structure and composition as well as the morphology of the surface region before and after oxidation on an atomic scale. In combination with low energy electron diffraction (LEED) the formed oxide structures are identified. In addition, the ordering of the phases is investigated with glancing angle x-ray diffraction. For an auxiliary chemical analysis of the surface composition high resolution core level spectroscopy is applied.

Outline of the Thesis

In chapter 3 existing theories of oxide film growth on metals and alloys are presented. The results of the most relevant studies, concerning the oxidation of FeAl, NiAl and CoGa surfaces, are summarized. The theoretical background of the experimental techniques, applied in this thesis, is explained in chapter 4. The experimental set-ups of the beamlines and the oxidation chambers are described in chapter 5. Chapter 6 introduces the investigated material systems and corresponding oxides. Chapter 7 deals with the oxidation of the Fe_3Al (1,1,0) surface. Oxygen-induced changes of the ordering in the surface region are highlighted. The oxidation of the vicinal NiAl (6,7,1) and (4,3,0) surfaces is described in chapter 7. Similarities in the relaxation and occupation pattern before and after oxidation are pointed out, differences in the formed oxide structures are explained. In chapter 9 the time-dependency of the surface oxide growth on the stepped CoGa surface is compared for water and oxygen oxidation. Differences with respect to the flat CoGa(1,0,0)

surface are pointed out. Chapter 10 gives a summary of all results. Conclusion, regarding the question formulated above, are drawn and an outlook is given.

Chapter 3

Oxidation of Metal and Alloy Surfaces

Within this chapter the basic principles behind the oxidation of metals and alloys are discussed. In the first section a short introduction into the theory of oxidation is given. It starts from the clean surface exposed to oxygen and then introduces different growth models for oxides scales. The second section presents the most relevant results of former studies on the oxidation of binary alloys like FeAl, NiAl and CoGa. It demonstrates the complexity of the initial oxidation process and of the formation of oxides on single crystal surfaces. By introducing regular patterns of surface steps this complexity is increased further. Thus, relevant studies on the oxidation of stepped metallic surfaces are presented in the third section.

3.1 Theory of Oxidation

The oxide growth on a metal can be divided into two steps. First, oxygen has to adsorb on the metal surface. Then an oxide formations starts, if an oxide covered surface is energetically favoured over the metallic surface and no kinetic barriers exist. Once a first oxide layer has formed it grows further in thickness. Within this second step a charge transfer through the oxide scale is crucial to preserve charge neutrality and therefore further growth.

3.1.1 Initial stages of oxidation

Depending on the partial pressure and on the temperature, oxygen molecules impinge on the metal surface with a certain rate. To finally adsorb to the surface the molecules have to interact with the metal by physisorption or chemisorption [20]. *Physisorption* is based on the weak Van-der-Waals interactions[1] between the oxygen molecules and the metallic substrate. With a maximum of 0.5 eV per molecule in case of O_2 the binding energy is very small why physisorption occurs at high gas pressures and low temperatures only. *Chemisorption* is a chemical interaction where the orbitals of atoms or molecules in the

[1] Van-der-Waals interaction is a polarization induced multipol interaction.

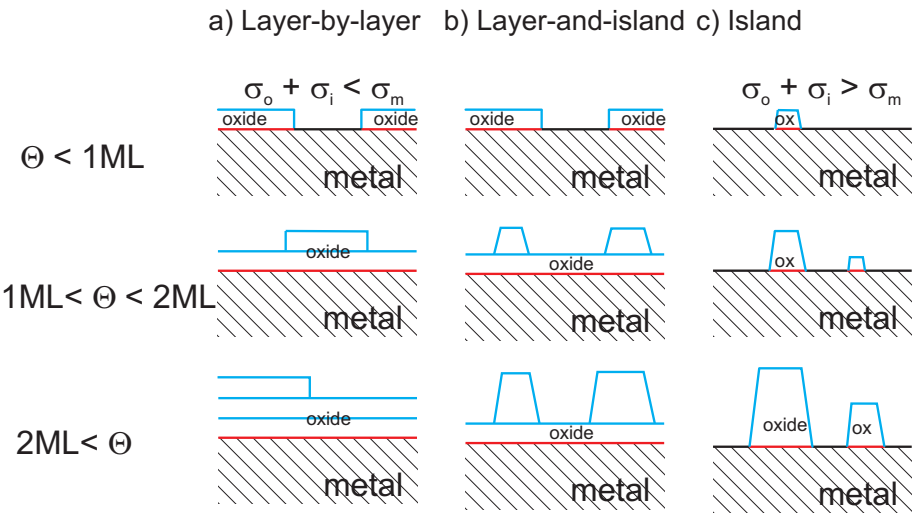

Figure 3.1: 3 different growth modes where θ is the coverage. Black, red and blue lines mark the metal, the interface and the oxide surface areas, relevant for the corresponding surface energies σ_m, σ_i and σ_o, respectively.

gas and the metal overlap and form a new orbital. Bonding energies of more than 1 eV are achieved. The bonding can either be molecular or atomic. A simplified model to determine if a molecule is chemi- or physisorbed is based on the relative position of the anti-binding energy levels of the gas molecule with respect to the energetic position of the metal's Fermi level. If the anti-bonding orbital of the molecule lies above the Fermi level no electrons will be transferred. The molecule is physisorbed. For the opposite case the anti-bonding orbitals are filled with electrons from the metal. An incomplete filling leads to molecular, a complete filling to a dissociative chemisorption.

Depending on the temperature, the partial pressure and the surface energy of the metal an oxide can form when the adsorbates mix with the substrate atoms. Oxide nucleation mainly starts at surface defects like vacancies, kinks and step edges. Afterwards there are three possibilities for further growth like depicted in fig. 3.1 [6]. Layer-by-layer growth occurs if the sum of the surface energies from the oxide film and the interface $\sigma_o + \sigma_i$ is smaller than the surface energy of the substrate σ_m or if high kinetic barriers at step edges (Ehrlich-Schwoebel barriers) are present. If $\sigma_o + \sigma_i$ is larger than σ_m it comes to pure island growth. As the surface energy of the oxide film increases with increasing thickness, the growth mode can change during oxide formation leading to a layer-and-island growth [21].

Important factors during the initial oxide formation which are not included in the growth models are kinetic barriers which prohibit that the system reaches thermal equilibrium. As an example the temperature can be too low for a sufficient mobility of the atoms to form an oxide or to segregate to the surface.

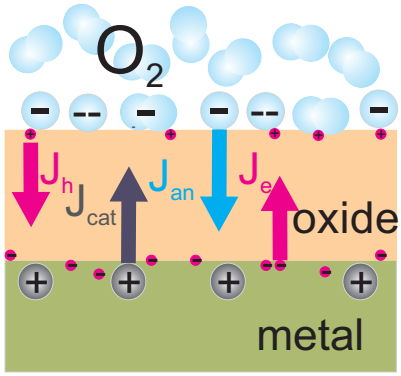

Figure 3.2: For oxide growth either metal cations (J_{cat}) or oxygen anions (J_{an}) or both have to penetrate to the opposite interface of the oxide scale. For charge neutrality electron holes (J_h) or electrons (J_e) have to travel in the opposite direction.

3.1.2 Oxide film growth

Once a closed oxide layer has formed on the metal surface two factors are crucial for a further layer growth. On the one hand oxygen has to be chemisorbed on the oxide surface. On the other hand either metal or oxygen ions have to diffuse through the oxide layer to get to the metal-oxide or oxide-metal interface for further oxide formation. Driving force behind this charge transfer is an oxide thickness dependent surface charge field. During the charge transfer charge neutrality is a necessary condition, like shown in fig. 3.2. It results in the following equation [22–25]:

$$q_i J_i + q_e J_e = 0 \tag{3.1}$$

While the ionic current J_i is caused by an electro-chemical potential gradient between the interfaces, the electron current originates from electron tunnelling or thermal emission. Both currents depend on the temperature, the oxygen pressure, the oxide thickness and the dielectrical properties of the oxide layer. Thereby, the time dependence of the oxide thickness growth is always determined by the slowest of the charge currents J_c. The growth rate is consequently expressed by

$$\frac{d\,L(t)}{d\,t} = R_c J_c \tag{3.2}$$

R_c is the oxide volume formed per particle transported through the oxide scale, L the thickness of the oxide scale. Depending on the conditions the oxide growth can be either limited by the electron-tunnelling-, the thermal-electron-emission- or the ion-diffusion-current.

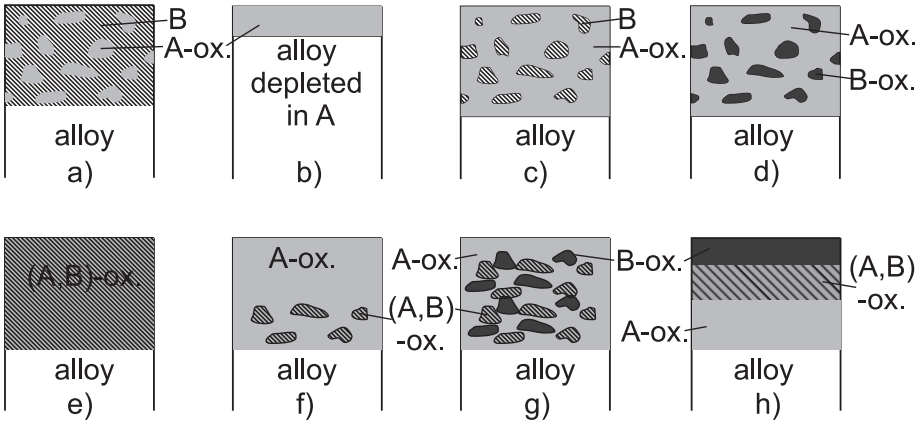

Figure 3.3: Schematic representation of different oxidation modes of the alloy AB with variable compositions where A is the less noble metal: a) A-oxide formed in the matrix of element B. b) Single A-oxide layer formed on the alloy matrix. c) Metal B is dispersed in A-oxide layer. d) B-oxide is dispersed in A-oxide. e) Single solid solution of A- and B-oxide or double oxide (A,B)-oxide are formed on top of the alloy. f) Double-oxide like AB_2O_4 is present in a A-oxide layer g) An oxide layer containing A-oxide, B-oxide and (A,B)-oxide is formed. h) Same as g) but A-oxide, B-oxide and (A,B)-oxide grow layer by layer [26].

3.1.3 Oxidation of Alloys

So far, the models describe the oxide formation for single metals but their validity is restricted to certain conditions. As an example, they neglect the properties of the oxide scale: Is it a smooth homogeneous film or does it exhibit pores, cracks and various domain walls to enhance ion diffusion? Furthermore they do not take into account the increased complexity of alloy oxidation. To describe distinctive features of alloy oxidation a simple binary alloy AB is investigated where A is the less noble metal. Here the formation and composition of the oxide scale depends on factors like the alloy composition or the difference in oxygen affinity of the two constituents. Preferential segregation to the alloy surface will also influence the oxidation behaviour. In addition, oxidation itself can induce compositional changes in the alloy, leading to a depletion of the reactive component and thus to a change of the growth behaviour. Thereby the oxidizing temperature as well as the oxidation rate are important magnitudes as we will also see later in this thesis (chapter 7). A summary of possible scenarios of the binary alloy oxidation is given in fig. 3.3.

3.2 Relevant Studies on the Initial Alloy Oxidation

In the last decades numerous theoretical and experimental studies on the oxidation of binary alloy surfaces have been performed. The studies show that the initial oxidation

process, which is not included in the growth model described above, can be very complex. Thus the most relevant results, which focus on FeAl-, the NiAl- and CoGa-surfaces, are presented in the following sections.

3.2.1 Studies on Fe-Al-surfaces

Phenomena like segregation of one alloy constituent can influence the oxide formation on alloy surfaces. As shown by Monte Carlo simulations the segregation on clean binary alloy surfaces is often favourable. If one constituent segregates to the surface the surface energy is lower compared to a bulk-terminated alloy surface [27]. Many experimental studies, using LEED, AES, STM and XRD, on clean, low index $Fe_{1-x}Al_x$ surfaces show that Al segregates to the surface layers. The higher the Al concentration x, the more Al is found at the surface. Higher temperatures further promote Al segregation [28–32]. LEED studies on the clean FeAl (1,1,0) surface show that the appearance of surface reconstructions depends on the Al content in the surface [30, 31]. For the most thesis-relevant Fe_3Al (1,1,0) surface Al segregation to the surface is shown in a low-energy ion scattering study (LEIS). At room temperature a slightly enhanced Al concentration of 41 at.% is reported while for temperatures close to the $D0_3$-B_2 phase transition (T_C) at 700 K a Al concentration of 94 at.% within the first layer is found [33]. A glancing angle x-ray scattering study (GIXRD) on the same surface finds that close to T_C the top three layers are strongly affected by surface segregation phenomena and display a complicated structure [34]. The critical fluctuations of the order parameter are fundamentally altered and a higher phase-transition temperature is found in the surface region as compared to the bulk values [35].

Studies on the oxidation of $Fe_{1-x}Al_x$ surfaces of polycrystalline and single crystal samples show that the chemical composition of the oxide strongly depends on the oxidation rate and the amount of the constituents at the surface. A transmission electron microscopy study on $Fe_{0.85}Al_{0.15}$ and $Fe_{0.6}Al_{0.4}$ polycrystals, oxidized at temperatures around 1000 K in synthetic air, shows a thin Fe_2O_3-containing outer layer followed by a inner, nearly pure Al_2O_3-layer. The Fe_2O_3-content decreases with time, temperature and Al concentration of the bulk alloy [36]. A XPS study of the oxidation of Fe_3Al polycrystals shows that with 200 mbar of O_2 at 300 K a mixed Fe and Al oxide layer is formed. Oxidation at 770 K produces oxides scales with an outer layer rich in Fe oxides and an inner layer rich in Al oxides [37]. This oxidation-rate dependent oxide formation is also observed for the FeAl (1,1,0), (1,0,0) and (1,1,1) surfaces by LEED, XPS and STM. For a large amount of Al within the surface region and low O_2 pressures pure alumina films are formed [7, 38].

The experiments summarized above clearly show that either mixed Fe-Al-oxides or pure Al oxide can grow on iron-aluminide surfaces during oxidation. However, a detailed understanding on the atomic scale which is essential for the growth of more homogeneous, smooth coating layers is only found for the $Fe_{0.5}Al_{0.5}$ composition. No in situ oxidation study exists on the technologically more relevant Fe_3Al where the oxidation behaviour might change due to the higher iron content. Therefore, the chemical composition of the oxide on Fe_3Al as well as the structural changes within the alloy are investigated in this thesis.

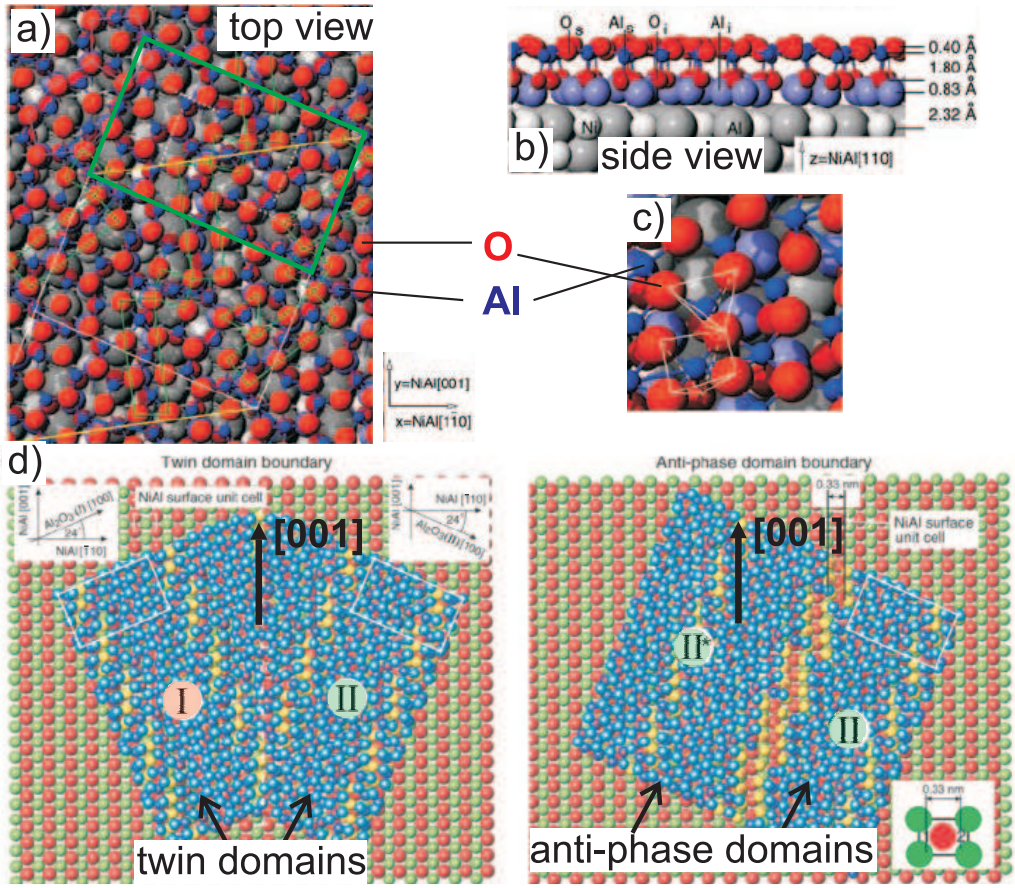

Figure 3.4: a)+ b) Top and side view of the DFT-based model for the ultrathin, aluminium oxide film on NiAl(1,1,0). c) Close up of the complex structure. d) Atomistic models for the twin domain boundaries (left) and the antiphase domain boundaries (right). The oxide unit cells are indicated by white rectangles. The twin domains are labelled red(I) and green(II) (from [4, 5]).

3.2.2 Studies on the Ni-Al-system

The regularly stepped NiAl surfaces, investigated in this thesis, consist of (1,1,0) oriented terraces. For comparison, former results of the clean and oxidized NiAl (1,1,0) single crystal surface are briefly presented in the following.

According to LEED and SXRD studies no segregation occurs on the clean (1,1,0) surface. Within the first two layers relaxations of the Ni and Al atoms are found while the larger Al atoms relax outwards towards the vacuum and the smaller Ni atoms inwards. The buckling between Ni and Al is 0.2 Å for the surface layer and 0.02 Å for the first subsurface layer [4, 39]. During the thermally controlled oxidation of NiAl, structural properties of the formed aluminium oxide film as well as its thickness and morphology strongly depend on the oxidation conditions and the surface orientation. Oxidation of

NiAl(1,1,0) at high temperatures of 1140 K and high O_2 pressures of 1 bar leads to the formation of well-ordered, epitaxial γ-Al_2O_3. A stepwise increase of temperature after the oxidation transforms the γ- into δ- and finally to α- alumina [40, 41]. The oxidation of the (1,1,0) surface at lower oxygen pressures produces an epitaxially grown, long-range ordered, ultra-thin alumina film with a complex structure and a small roughness. An amorphous alumina layer is formed after oxidation at 540 K and 10^{-6} mbar O_2. An annealing step to 1070 K orders the 5.4 Å thin surface oxide. LEED, STM, SXRD and DFT studies resolved the complex structure which is depicted in fig. 3.4 [3–5, 42]. The oxide layer is composed of a double layer of strongly distorted hexagonal oxygen ions that hosts aluminium on both octahedral and tetrahedral sites with equal probability. Al, sitting at the oxide-alloy, prefers Ni neighbours which leads to pentagon-heptagon pairs of Al. The oxide unit cell grows commensurate along the NiAl $[\bar{1}10]_{bulk}$-direction but incommensurate along $[001]_{bulk}$. As shown in fig. 3.4c, twin domains of the oxide are observed. The long, inplane unit cell axis of the surface oxide is rotated by either plus or minus 24° with respect to the NiAl $[\bar{1}10]_{bulk}$-direction. The oxide's inplane axis a = 18.01 Å and b = 10.59 Å are not perpendicular towards each other but have an angle of 91.15°. In the SXRD study Al depletion within the interfacial region is detected after the oxidation which is induced by preferential Al oxidation. Ni and Al vacancies and Ni anti-sites are found with in the first 5 layers [4]. An investigation of the thermodynamic stability shows that the surface oxide is not in thermodynamic equilibrium [43]. However, the ultrathin oxide is stable up to 1×10^{-2} mbar at an oxidation temperature of 620 K and then partially transforms to γ-Al_2O_3 [40].

The initial oxidation of a flat NiAl (1,1,0) surface is understood very well. In this thesis the oxidation of stepped surfaces, vicinal to the $[1, 1, 0]$ direction, is investigated as steps and kinks play important roles in every initial oxidation process. The results will bring us one step further to understand and tailor the initial oxidation process of polycrystals and nanoparticles.

3.2.3 Studies on the Co-Ga-system

Most studies on the Co-Ga system in the regime of low oxidation pressures focus on the CoGa (1,0,0) surface[2]. The clean surface surface shows a $c(4\times2)$ reconstruction, probably terminated by Co atoms [44]. STM, SXRD, DFT, HRCLS, HREELS, AES and LEED studies show the formation of a surface oxide at low partial pressures ($10^{-8} - 10^{-6}$ mbar O_2) and temperatures above 550 K, like depicted in the STM-image of fig. 3.5a [6, 15, 45]. The oxide possesses a (2×1) reconstruction on the CoGa substrate and grows in two-dimensional, anisotropic, stripe-like islands. Two $90°$-rotated domains exist which grow fast in the direction of their longer inplane axis. Island nucleations starts at the steps edges of the surface which are oriented preferentially along the [0,0,1] and [0,1,0] direction. The oxide structure, shown in fig.3.5b, is build up of an oxygen ion double layer which contains the basic building block of bulk β-Ga_2O_3. According to the SXRD measurements

[2]The surface normal of the sample investigated in this work is also vicinal to the [1,0,0] direction.

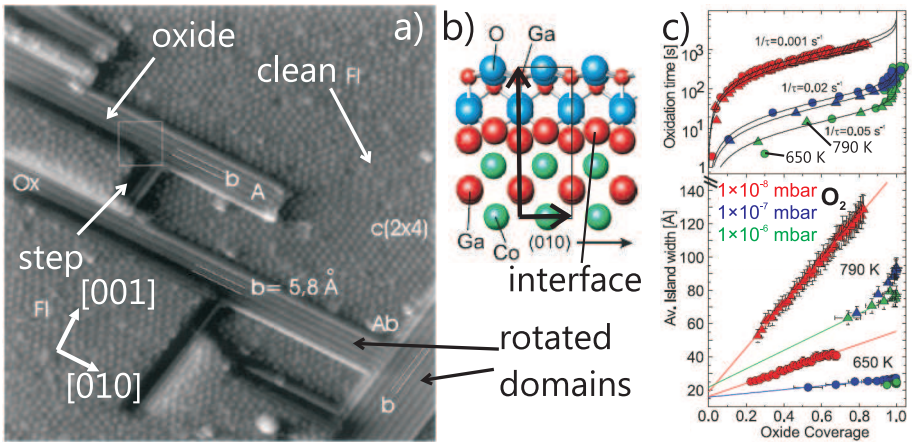

Figure 3.5: a) STM image after oxidation of CoGa(100) with 1 L O_2 at 700 K (320×320 Å^2). Stripe-like, rotated oxide domains are observed (from [6]). b) View of the oxide structure along the $(0, 0, \bar{1})$ axis [15]. c) Oxidation time and island width along the slow growing direction as a function of oxide coverage(from [15]).

in fig. 3.5c, the oxide growth can be described as exponentially slowed down which is characteristic for a hetero-epitaxial growth [15, 40]. The formation of thermodynamically stable $\beta-Ga_2O_3$, which was blocked by kinetic boundaries during the formation of the surface oxide, is observed for higher pressures and higher temperatures [40].

3.3 Relevant Studies on Vicinal Surfaces

Steps and kinks play an essential role in the adsorption process of molecules on a surface due to their low coordination number. Adsorption is necessary for every reaction on a surface for example the oxidation process. However little detailed experimental and theoretical studies on vicinal alloy surfaces are found in literature. The most relevant studies are briefly summarized in the following.

Clean, Vicinal Surfaces

Elasticity theory shows that clean vicinal surfaces are stable against faceting due to a step-step repulsion arising from the interaction of strain fields, present around every step. Capillary forces, acting at the upper and lower side of a step and pointing away from the step, create an elastic force dipole at the step. The atom at the step position is pulled towards the bulk, while the corner atom below the step relaxes outwards. This results in a charge smoothing around the steps. The elastic dipoles, created in this way, are compensated by internal strain which is crucial for the stability of vicinal surfaces on which temperature has only a little effect [14, 46].

These general results for relaxations at surface steps can be transferred to the results

of an embedded atom method study on the $L1_2$ alloy Cu_3Au with a (5,1,1) surface, exemplarily discussed here. The surface is composed of 8 Å wide, (1,0,0) terraces separated by monoatomic steps. The calculations demonstrate that the terraces occupied by Au- and Cu atoms show a buckling of about the same size then the low-index (1,0,0) surface of the system. Around the steps a complex relaxation pattern is observed where the step atoms and the atoms at the corner show the most prominent relaxations. As expected, the step atoms are relaxed inwards, the corner outwards [47]. In a combined SXRD and molecular dynamics calculation study on a clean Pt (9,7,7) surface the found strain field also reveals huge vertical and lateral relaxations of the atoms around the step, similar to the one described by the mentioned theoretical studies [48].

The Oxidation of Vicinal Surfaces

Two former studies on stepped surface, combining STM, SXRD, HRCLS and LEED, show oxygen induced faceting and step bunching which is often observed on metallic vicinal surfaces. A well-ordered Rh (5,5,3) surface, consisting of 5 atoms wide (1,1,1) terraces, facets upon oxidation at 10^{-6} mbar O_2 and 750 K while (3,3,1) facets with one-dimensional oxide chains along the steps and (1,1,1) facets are formed [49]. Further increase of pressure and temperature solely results in (1,1,1) facets, covered by the known O-Rh-O surface oxide. The similar Pd (5,5,3) surface facets upon oxidation with oxygen pressures between 10^{-6} and 1 mbar and sample temperatures between 570 and 670 K. (3,2,2) and (1,1,1) facets coexist mainly covered by PdO-like surface oxide. Higher oxygen pressures promote the exclusive formation of (1,1,1) facets and of bulk oxide [50].

Very little studies on the oxidation of vicinal alloy surfaces exist. In a LEED investigation of a Pt_3Ti (5,1,0) surface, which consists of regularly arranged (1,0,0) terraces, the formation of (1,0,0) and (2,1,0) facets is observed upon oxidation at 10^{-7} mbar O_2 and 800 K [51]. The faceting goes along with the formation of titanium oxide islands on the surface. A recent STM-study on a regularly stepped NiAl (16,14,1) surface also shows morphology changes upon oxidation [52]. The clean (16,14,1) surface is stable in UHV. It is characterized by 2.5 nm wide (1,1,0) terraces while the step edges appear ragged-shaped with short sections running along the $[001]_{bulk}$ and $[111]_{bulk}$ directions. As shown in fig. 3.6 a small O_2 dose and a following annealing process lift the original terraces of identical width. Larger, triangular-shaped (1,1,0) facets are formed. The formed oxide islands exclusively nucleate at the topside of step edges and cover small sections of the (1,1,0) terraces. Preferential single domain formation of the complex surface oxide, described in section 3.2.2, is observed. This is assigned to strain release along the steps in the direction of the short axis of the oxide's unit cell.

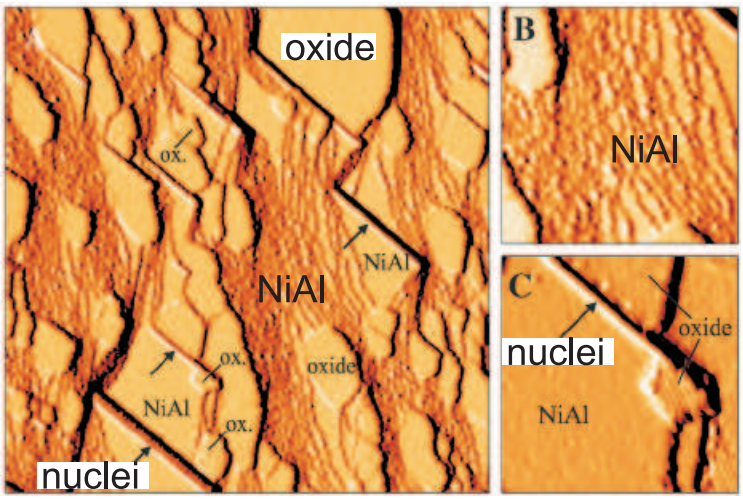

Figure 3.6: STM study on the oxidation of the NiAl (16,14,1) surface where the images are recorded after 60 L oxygen at 550 K and annealing to 1000 K. A) 200×200 nm^2 overview with parts of the clean stepped surface, larger metallic NiAl(1,1,0) terraces and oxide covered (110) terraces. B) 45×45 nm^2 close up of the original well-ordered steps covered with small oxide nuclei (brighter spots) C) Close up of the NiAl(1,1,0) terrace with oxide formation on the rim and small oxide covered parts. Arrows mark protruding stripes with $[001]_{bulk}$ orientation that often boarder (1,1,0) terraces (from [52]).

Chapter 4

Theoretical Background of Experimental Methods

It was in 1895 when Wilhelm Conrad Röntgen (1845 - 1923) discovered a new kind of radiation, the “X-rays”. His discovery of electromagnetic waves with wavelengths around 10^{-10} m had a huge impact on the scientific community. In the following decades various new techniques and applications came up, using either the scattering of the x-rays by electrons or the absorption process of the photons in a material. Nowadays these techniques are well established, giving detailed information on material properties. Glancing angle x-ray scattering (section 4.1.2), surface x-ray diffraction (SXRD, Section 4.1.1) and X-ray photoelectron spectroscopy (XPS, section 4.2) are just three of many examples and also the underlying experimental methods of this work.

4.1 X-Ray Scattering

4.1.1 Diffraction

Until today X-ray diffraction (XRD) is one of the most powerful tools for non-destructive, structure determination, e. g. for complex molecules or viruses [53, 54]. The underlying theory of the interference of x-rays in a crystal lattice was predicted by Max von Laue and proven experimentally by his colleagues P. Knipping and W. Friedrich in 1912 [55]. Laue applied the concepts of optical interference from gratings to x-rays scattered from crystals, as the lattice parameters and the x-ray wavelength are of the same size. In the following a brief introduction to x-ray diffraction is given. For a detailed introduction the references [9, 56, 57] are recommended.

The fundamental process of XRD is the elastic scattering of x-rays by an electron which ability to scatter is expressed in terms of the Thomson scattering length r_0. Thus, to derive the total scattering length of an atom one has to sum over all atomic electrons or, in other words, integrate over the atoms’ electron distribution. In both cases one has to account for the correct phases the electrons have relative towards each other. This cor-

responds to a Fourier transformation of the atomic electron density distribution from the real to the space of momentum transfer (reciprocal space). As atomic electrons occupy certain shells and are differently bound, one has to correct the atomic scattering length for dispersion (dispersion corrections $f^{'}(\hbar\omega)$ and $if^{''}(\hbar\omega)$), depending on the energy $\hbar\omega$ of the x-rays[1].

A phase sensitive superposition of all atoms within a crystals unit cell results in the structure factor $\mathrm{F}_{hkl}^{u.c.}$, proportional to the scattered amplitude of one unit cell. A superposition of all unit cells in the crystal (the so called lattice sum) leads to the scattering factor of the whole crystal, again proportional to the scattered amplitude:

$$F^{\mathrm{crystal}}(\mathbf{q}) = \overbrace{\sum_{\mathbf{r_j}} f_j(\mathbf{q},\omega)\, e^{i\mathbf{q}\cdot\mathbf{r_j}}}^{\text{Unit cell structure factor } \mathrm{F}_{hkl}^{u.c.}} \overbrace{\sum_{\mathbf{R_n}} e^{i\mathbf{q}\cdot\mathbf{R_n}}}^{\text{Lattice sum}} \tag{4.1}$$

$\mathbf{q} = \mathbf{k}_f - \mathbf{k}_i$ is the wave vector transfer from the incoming ($\mathbf{k}_i$) and the scattered ($\mathbf{k}_f$) wave, $\mathbf{r_j}$ is position of atom j within one unit cell and $\mathbf{R_n}$ is the lattice vector that describes the position of unit cell n in the crystal. $\mathbf{q}\cdot\mathbf{r_j}$ is the phase difference between an atom j and the origin of the unit cell, projected onto the the wave vector transfer, while $\mathbf{q}\cdot\mathbf{R_n}$ is the equivalent phase difference for unit cell n. As mentioned before, $f_j(\mathbf{q},\omega)$ is the atomic form factor corrected for dispersion due to resonant behaviour at atomic absorption edges and dissipation in the crystal. Again the two terms in equation 4.1 can be interpreted as Fourier transformation from real to wave vector transfer space. The first sum is the transformation of electron density distribution within one unit cell, the second one of the periodic distribution over the whole crystal lattice.

In crystals, the number n of unit cells is very large (10^{12} or more). Therefore the sum of all phase factors in the lattice sum is 0, except if all scattered x-rays interfere constructively, that means all phases fulfil the condition $\mathbf{q}\cdot\mathbf{R_n} = 2\pi\times\mathrm{integer}$. In terms of the crystal lattice this condition can be expressed via the Laue condition

$$\mathbf{q} = \mathbf{G}. \tag{4.2}$$

$\mathbf{G} = h\mathbf{a_1^*} + k\mathbf{a_2^*} + l\mathbf{a_3^*}$ is the reciprocal lattice vector of the crystal, defined by the unit cell basis vectors $\mathbf{a_i}$ via the relationship $\mathbf{a_i}\cdot\mathbf{a_j^*} = 2\pi\delta_{i,j}$. h,k and l are the Miller indices. The Laue conditions give the possible positions for sharp intensity peaks of the scattered x-rays, the so-called Bragg-Peaks.

So far, the scattered amplitude of the x-rays A(**q**) was derived which is proportional to $r_0\times F^{\mathrm{crystal}}$. However the main goal of diffraction theory is to describe the measurable scattered intensity I(**q**). Thereby I(**q**) is equal to $|A(\mathbf{q})|^2$. Using the geometrical series [2] in

[1] ω is the angular frequency of the x-rays.

[2] $S_N = \sum_{n=0}^{N-1}(e^{i\boldsymbol{qa}})^n = \frac{1-(e^{i\boldsymbol{qa}})^N}{1-e^{i\boldsymbol{qa}}}$

equation 4.1 one finally gets

$$I(\mathbf{q}) \propto |F^{u.c.}(\mathbf{q})|^2 \left| \underbrace{\frac{\sin(\mathrm{N}_1 \mathbf{q}\cdot\mathbf{a_1}/2)}{\sin(\mathbf{q}\cdot\mathbf{a_1}/2)}}_{\mathrm{S}_{\mathrm{N}_1}} \right|^2 \left| \underbrace{\frac{\sin(\mathrm{N}_2 \mathbf{q}\cdot\mathbf{a_2}/2)}{\sin(\mathbf{q}\cdot\mathbf{a_2}/2)}}_{\mathrm{S}_{\mathrm{N}_2}} \right|^2 \left| \underbrace{\frac{\sin(\mathrm{N}_3 \mathbf{q}\cdot\mathbf{a_3}/2)}{\sin(\mathbf{q}\cdot\mathbf{a_3}/2)}}_{\mathrm{S}_{\mathrm{N}_3}} \right|^2 \tag{4.3}$$

where $\mathrm{S}_{\mathrm{N_i}}$ are N-slit-interference functions which result in the Laue-equations for a infinite number of unit cells. As seen in equation 4.3 the absolute square of the amplitude leads to a loss of the absolute phase information. It is not possible to determine the structural information directly from the measured intensity and a trial and error procedure is requisite for structure determinations.

In summary, scattering from a crystal is confined in distinct reciprocal lattice points, resulting from the lattice sum and containing information of the crystal lattice. The intensity in each point is modulated by the absolute square of the unit cell structure factor, containing information of the unit cell structure. Consequently, the intensity in a distinct reciprocal lattice point is only unequal from zero if the unit cell structure factor does not vanish at this point. This leads to distinctive exception rules for different types of crystal structures which are especially interesting for chemically ordered systems, like shown for binary alloys in chapter 6.

In the whole theory described above the Compton and Photo effect are neglected. Furthermore it is based on the *kinematical approximation*: due to the fact that the interaction between the x-rays and the crystal is weak (small cross-section) and most crystals are imperfect[3], the effect of multi-scattering from the beam before leaving the crystal can be neglected. For x-ray diffraction from perfect crystals where the photons are re-scattered the references [9, 56, 57] are recommended. The technique of XRD is not restricted for structural investigations of the bulk. Crystal truncation rod (CTR) measurements and x-ray diffraction under gracing incidence are two methods how structural information of surfaces can be exploited. These techniques are described in the following sections.

Crystal Truncation Rods

For an infinite three-dimensional crystal scattering events are restricted by the Laue conditions (see equation 4.2) to certain wave vector transfers, resulting in a delta-function distribution of the scattered intensity (Bragg peaks). Truncating an infinite crystal along a crystalline direction produces a sharp surface. This relaxes the Laue conditions in the direction of the surface normal while they are still fulfilled parallel to the surface plane. Additional to the Bragg peaks scattered intensity can be measured along wave vector transfer perpendicular to the surface. The intensity distribution is called crystal truncation rod (CTR) [11] and is shown in fig. 4.1. To describe the truncated crystal mathematically, one has to consider that the lattice sum $\mathrm{S}_{\mathrm{N}_3}$ along the surface normal[4] (see equation 4.3) is

[3] Most crystals are formed from microscopic mosaic blocks which are so small that the magnitude of the wave field does not change over the depths of one block.

[4] By definition the a_3-direction was set to be parallel to the surface normal.

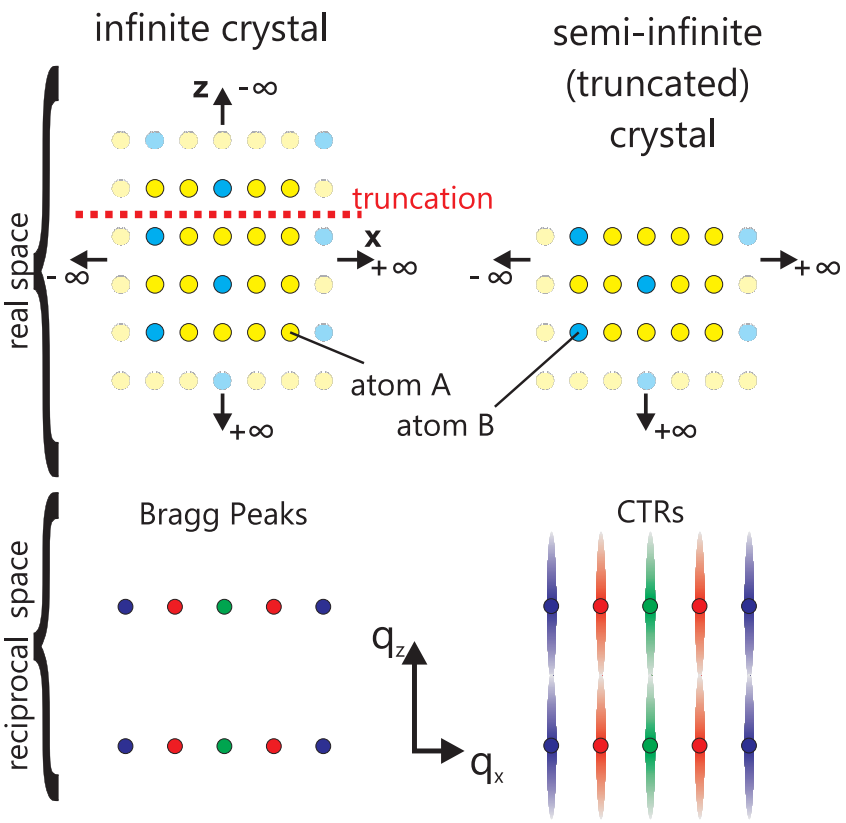

Figure 4.1: Comparison of an infinite (left) and a truncated (right) binary alloy crystal. For the infinite crystal all scattered intensity between the Bragg peaks vanishes. For the truncated crystal it is distributed along rods perpendicular to the surface. The blue and yellow circles (upper part) are the two constituents of alloy. The different colours in the reciprocal space map (lower part) symbolize scattering from different sub lattices in the crystal (see section 4.1.1).

only semi-infinite while the sums $\mathrm{S_{N_1}}$ and $\mathrm{S_{N_2}}$within the surface remain infinite and give delta-functions . The structure factor results in:

$$F^{\mathrm{CTR}}(\mathbf{q}) = \overbrace{\sum_{\mathbf{r_j}}^{u.c.} f_j(\mathbf{q},\omega)\, e^{i\mathbf{q}\cdot\mathbf{r_j}}}^{\text{Unit cell structure factor}} \overbrace{\delta(\mathrm{q_x} - \mathrm{ha_1^*}) \times \delta(\mathrm{q_y} - \mathrm{ka_2^*}) \times \sum_{j=0}^{\infty} e^{i\mathbf{q_z}\mathbf{a_3}j}}^{\text{Lattice sum of Truncated crystal}} \tag{4.4}$$

When the in-plane Laue conditions $\mathbf{q}_{\parallel} = \mathbf{G}_{\parallel}$ are fulfilled equation 4.4 can be rewritten to

$$F^{\mathrm{CTR}}(\mathbf{q}) = \sum_{\mathbf{r_j}}^{u.c.} f_j(\mathbf{q},\omega)\, e^{i\mathbf{q}\cdot\mathbf{r_j}} \times \frac{1}{1 - e^{i\mathbf{q_z}\mathbf{a_3}}} \tag{4.5}$$

where $\mathrm{q_z} = 2\pi l/\mathrm{a_3}$. $\mathrm{a_3}$ is the lattice constant normal to the surface, $\mathrm{a_1}$ and $\mathrm{a_2}$ lie in the surface plane. The absolute structure factor $|\mathrm{F}_{CTR}|$ of an ideal bulk terminated crystal is

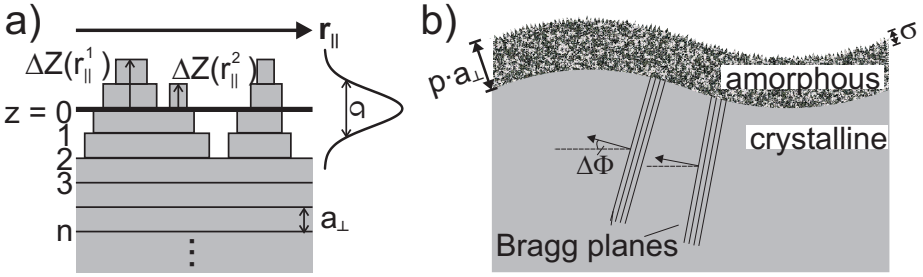

Figure 4.2: a) Schematic view of roughness on a microscopic scale. The height of the sample deviates from the average surface at z = 0 by deviations ΔZ depending on the lateral position $r_\parallel$. Here a Gaussian distribution of the height deviation is shown. b) Schematic view of a wavy surface with a "dead", amorphous layer of thickness $p \cdot a_\perp$ on top which is not contributing to the diffraction signal. Waviness leads to small deviations $\Delta\Phi$ of the Bragg planes with respect to the surface normal.

proportional to $1/q_z$ as shown by the black line in fig. 4.3. The semi-kinematic sum for Bragg scattering, which is proportional to measurable intensity, is the absolute square of this structure factor.

The intensity distribution of a CTR is very sensitive to the structural composition of the surface region and therefore to surface phenomena like relaxation, segregation or ordering. Surface phenomena are described by a surface unit cell where for example the inplane (reconstruction) or the out-of-plane (relaxation) periodicity or the site occupancies (segregation) are different from the bulk. The structure factor of this surface unit cell is then coherently added to the bulk contribution:

$$F^{\text{total}} = F^{\text{CTR}} + F^{\text{Surface Unit Cell}} \tag{4.6}$$

The example of the $Fe_3Al(110)$ surface, given later in section 4.1.1, demonstrates this surface sensitivity of the CTRs.

Crystal Truncation Rods from "Real" Surfaces

To get from an ideal crystal surface towards a more realistic system, effects like photon absorption or surface phenomena like microscopic roughness, amorphous oxide layers and macroscopic waviness have to be included to the kinematic sum of Bragg scattering.

Firstly, when the incoming and scattered x-rays travel through the material they get absorbed. The absorption depends on the linear photoabsorption coefficient μ and the angle of the beam direction with respect to the surface. An absorption parameter $\beta = a_3\mu/\sin\theta$ [5] can be introduced leading to an exponential decay of the diffracted amplitude perpendicular to the surface. Therefore the structure factor for the ideal surfaces in equation 4.5

[5] θ is the Bragg angle.

changes to:

$$F^{\mathrm{CTR}}(\mathbf{q}) = \sum_{\mathbf{r_j}} f_j(\mathbf{q},\omega)\, e^{i\mathbf{q}\cdot\mathbf{r_j}} \times \frac{1}{1 - e^{i\mathbf{q_z}\mathbf{a_3}} e^{-\beta}} \tag{4.7}$$

The corresponding semi-infinite kinematic sum for Bragg scattering for fulfilled in-plane Laue conditions is the evaluated to

$$S_B(\mathbf{q}) = \left|F^{\mathrm{CTR}}(\mathbf{q})\right|^2 = \left|F^{\mathrm{u.c.}}_{hkl}(\mathbf{q})\right|^2 \times \frac{1}{\left|1 - e^{i\mathbf{q_z}\mathbf{a_3}} e^{-\beta}\right|^2} \tag{4.8}$$

Secondly, microscopic roughness of the surface as depicted in fig. 4.2a decreases the signal along the CTR. To account for roughness the lateral average of the lattice sum in equation 4.8 has to be taken. By assuming a Gaussian distribution for the height deviation $\Delta \mathrm{Z}(\boldsymbol{r}_{\parallel})$ this can be solved analytically, leading to a reduction of the Bragg scattered intensity:

$$\mathrm{S}^{\sigma}_{B}(\mathrm{q}_z) = \mathrm{e}^{-2M_\sigma}\mathrm{S}_B(\mathrm{q}_z) \tag{4.9}$$

with

$$2M_\sigma = \left(\kappa_z'^2 - \frac{1}{\Lambda^2}\right)\sigma^2 \tag{4.10}$$

where σ is the roughness parameter and $\kappa_z' = \mathrm{Re}\{\mathrm{q}_z\}$. The "missing" Bragg scattered intensity is scattered diffusely along the wave vector transfer parallel to the surface. Another mathematical concept to treat roughness is the so called β-model. The occupancy at the first not fully occupied layer is defined by the parameter β and decreases to vacuum layer by layer with the power law β^j [11].

Phenomena, like amorphous oxide layers or surface melting are described by "dead layers" of the thickness $p \cdot a_3$ (fig. 4.2b), which lead to a reduction of the lattice sum from ∞ to p instead of 0, as the "dead layers" do not contribute to the Bragg scattering. The kinematic sum is re-written to:

$$\mathrm{S}^{p}_{B}(\mathrm{q}_z) \propto \sum_{m,n=p}^{\infty}\sum^{\infty} \mathrm{e}^{-i\mathrm{q}_z a_3 n}\mathrm{e}^{-i\mathrm{q}_z^* a_3 m} = \mathrm{e}^{-2M_p}\mathrm{S}_B(\mathrm{q}_z) \tag{4.11}$$

with

$$2M_p = 2pa_3/\Lambda \tag{4.12}$$

Additional to a microscopic roughness, a surface or an interface can be wavy as shown in fig. 4.2b. When the height deviations of the interface are within the length scales of the longitudinal and transversal coherent length, x-rays scattered from different height interfere coherently. These deviations are considered as roughness. Deviation on larger length scale are called waviness and are expressed by little variations of the surface normal making an averaging of the scattered intensity over the incident and exit angles necessary.

Example 1: CTRs of Fe_3Al(1,1,0)

This example demonstrates the high surface sensitivity of CTR measurements on the surface structure. The orthogonal surface unit cell of Fe_3Al (1,1,0) is shown in fig. 6.1b. $a_{sur} = 5.79$ Å and $b_{sur} = 4.09$ Å are the lattice constants within the surface plane running along the $[1, \overline{1}, 0]$ and $[0, 0, 1]$ direction. $c_{sur} = 4.09$ Å is parallel to the surface normal $[1, 1, 0]$. The coordinates of the lattice sites are as follows: α-sites: (0,0,0), (0.5,0,0), (0,0.5,0.5) and (0.5,0.5,0.5); β-sites[6] (0.75,0.5,0) and (0.25,0,0.5); γ-sites: (0.25,0.5,0) and (0.75,0,0.5). The unit cell structure factor, defined in equation 4.1, is therefore calculated to:

$$\begin{aligned} F_{h+2k=4n} &= (2f_\alpha + f_\beta + f_\gamma)(e^{i\pi k} + e^{i\pi l}) \quad \text{fundamental} \\ F_{h+2k=4n+2} &= (2f_\alpha - f_\beta - f_\gamma)(e^{i\pi k} + e^{i\pi l}) \quad \text{B2-type} \\ F_{h=2n+1} &= (f_\beta - f_\gamma)e^{i\frac{\pi}{2}h}(e^{i\pi k} - e^{i\pi l}) \quad \text{D0}_3\text{-type}\,, \end{aligned} \tag{4.13}$$

where h, k, l are the Miller indices of the surface unit cell. The scattering contribution of each site is given by:

$$f_j = \theta_j^{Fe} f_{Fe} + \theta_j^{Al} f_{Al} \qquad \text{, for } j = \alpha, \beta, \gamma \tag{4.14}$$

where f_{Fe} and f_{Al} are the atomic scattering factors of Fe and Al atoms, respectively. The occupancy of site j is given by θ_j^p, with $p = Fe$ or Al. The three different types of structure factors in equation 4.13 can be assigned to scattering from three different lattices which are explained in detail in section 6.1. The first term depends on the sum of all lattice site structure factors and therefore on the average electron density of the crystal. It is assigned to the fundamental bcc lattice (A2-type). The second term results from a B2-type superlattice which builds up when site β and γ are differently occupied than α. If additionally the γ-site is occupied with another probability than the β site, the $D0_3$-type superlattice is formed. For the (1,1,0) surface the fundamental lattice and the ordered sub-lattices are easy to distinguish in CTR measurements, as every CTR originates from scattering of one certain type of lattice only like shown in fig.6.1b.

The samples, used in the present work, are slightly rich in aluminium compared to perfectly $D0_3$- ordered Fe_3Al. This assures that upon heating one stays away from the phase separation region, explained later in section 6.1. It also induces a slight disorder compared to the ideal case. From the bulk it is known that higher amount of aluminium leads to Al-anti sites on the γ-positions as it cost almost no energy for the Aluminium to move there . From an energetical point of view, Al-anti sites on α-positions are very unlikely [58,59]. This leads to the following assumptions describing the off-stoichiometry: $f_\alpha = f_{Fe}$, $f_\beta = f_{Al}$,and $f_\gamma = (1-\epsilon)f_{Fe} + \epsilon f_{Al}$, with the $\epsilon < 1$ an arbitrary number. Using these scattering contributions to compare structure factors of samples rich in Al (F_{hkl}^{ϵ}) and

[6] Do note confuse with the occupancy parameter of the β-model describing roughness!

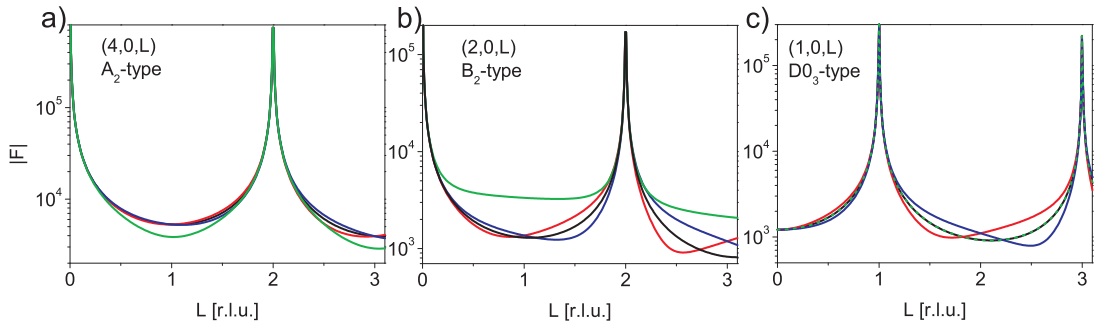

Figure 4.3: Fundamental(a)-, B2(b)- and $D0_3$(c)-type CTRs of the $Fe_{.72}Al_{.28}$(110) surface simulated for a bulk-terminated crystal (black curve), for relaxation (blue and red curve) and for Al segregation to γ-sites (green curve). In part c the black and green curve overlap.

of ideal $D0_3$ case (F^0_{hkl}), one obtains:

$$\begin{aligned} F^{\epsilon}_{h+2k=4n} &= \epsilon(f_{Fe} - f_{Al})(e^{i\pi k} + e^{i\pi l}) + F^0_{h+2k=4n} \quad \text{fundamental} \\ F^{\epsilon}_{h+2k=4n+2} &= (1+\epsilon)F^0_{h+2k=4n+2} \quad \text{B2-type} \\ F^{\epsilon}_{h=2n+1} &= (1-\epsilon)F^0_{h=2n+1} \quad \text{D0}_3\text{-type} \end{aligned} \tag{4.15}$$

One can now introduce order parameters $m_{D0_3} = (1-\epsilon)$ and $m_{B2} = \frac{1}{2}(1+\epsilon)$, such that the different kinds of Bragg peaks scale quadratically with them [7]. The different kinds of CTRs behave differently upon the Al-enrichment. Whereas the $D0_3$-type CTR decreases, the B2-type CTR increases due to the fact that one is closer to the ideal B2 composition FeAl and away from the ideal $D0_3$ one. The CTR probing the A2-type order is merely changed by the difference in total composition and will therefore never vanish, irrespective of the composition.

Fig. 4.3 demonstrates the influence of two typical phenomena at alloy surfaces on the intensity distribution along the three types of CTRs . First buckling of the different type of atoms is simulated. The red line shows the behaviour when Al in the first layer is moved inward by 2 % of the lattice distance d_{110} while Fe is moved outward by the same amount. The blue line shows the reverted situation. A clear shift of the structure factor minimum is observed on the superstructure CTRs, while the shift points in the opposite direction for inverted relaxations. The effect of surface segregation is demonstrated by the green line. The first layer has an ideal B2-like ordering with 50 % of Aluminum in the surface layer. This decreases the electron density of the surface layer and increases the B2-type ordering in the surface region. Consequently, the intensity of the fundamental CTRs decreases, while it increases on the B2-type CTRs. As the first layer has no $D0_3$-type ordering anymore, it does not contribute to the scattering along the corresponding CTR and no signal change is observed.

[7] The order parameters $m = m(\epsilon, T)$ are a function of the composition (described by ϵ) and temperature (T). Here the temperature-independent part is described.

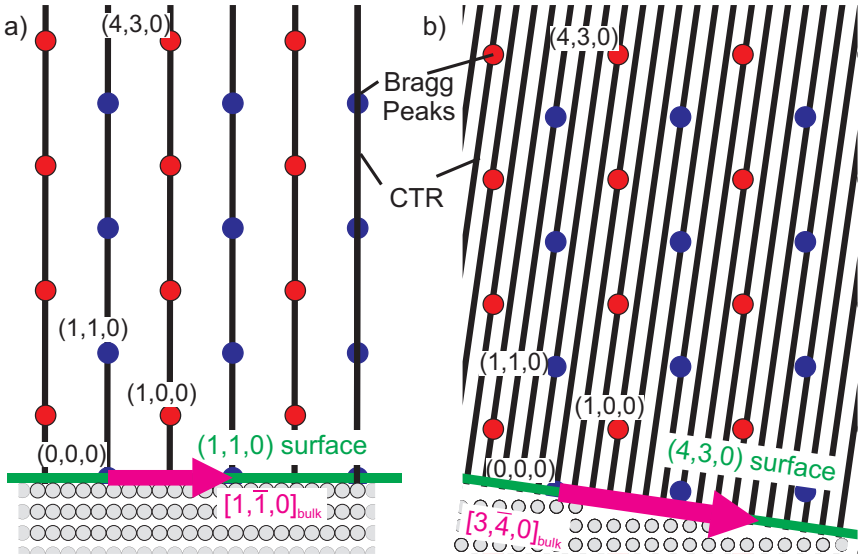

Figure 4.4: K-L map of the reciprocal space of a low-index (1,1,0) surface (a) and a vicinal (4,3,0) surface (b) of crystal with CsCl structure: CTRs (black lines) run through the Bragg Peaks, perpendicular to the surface (green line). The magenta arrows mark the direction within the surface plane, running across the steps in case of the vicinal surface. The grey atoms show the corresponding real space models.

Example 2: CTRs of a Vicinal Surface

In the theory of CTRs no restriction is made on the crystalline direction along which the crystal is truncated but it has to be a crystalline direction defined by the Miller indices (h,k,l). The CTRs are always perpendicular to the surface, no matter how the surface is oriented. Therefore the theory can be applied to any surface with Miller indices (h,k,l) [60]. However, the CTR pattern of a vicinal surface is more complex compared to a low index surface as shown in fig. 4.4. The smaller in-plane distance between 2 CTRs in the direction across the steps resembles the width of the terraces of the vicinal surface. The larger distance of two Bragg peaks on a CTR resembles the smaller planar distance perpendicular to the surface. From an experimental point of view, the intensity along the CTRs of a vicinal surface is lower and more difficult to measure, compared to a low index surface. This is due to a much lower electron density in the planes perpendicular to the surface normal. The minimum intensity along a CTR of a bulk-terminated NiAl (4,3,0) surface is by a factor of 100 smaller than the minimum intensity of a bulk-terminated (1,1,0) surface. Therefore, very smooth surfaces and high brilliances of the x-ray beam are needed in the experiments.

Surface Rods

On many crystal surfaces two dimensional structures like oxide films or reconstructions form which are extended within the surface plane but limited to one or two layers perpendicular to the surface. Such 2-D layers produce rod-like scattering known as surface rods. The intensity modulation along such a surface rod depends on the number of layers in the surface film. Mathematically the layers can be treated like a surface unit cell as described in equation 4.6.

Surface rods, which appear at different inplane positions than the CTRs of the substrate, provide information of the surface oxide structure only . At some position the diffracted intensity of the surface oxide and the truncated substrate are superimposed coherently according to equation 4.6. Then the CTRs also contain information about the interface between surface structure and underlying substrate. Ga oxide on CoGa, like investigated in section 9.1, demonstrates these effects.

Debye Waller Parameter

So far, the lattices have been assumed to be perfectly rigid. Due to thermally activated phonons the atoms within a lattice vibrate with an temperature depending amplitude. Thus, a temporal displacement $\mathrm{u_{q}}_j$ is added to every mean position of the atoms and the time average of the measured intensity is evaluated. This introduces an exponential term to the unit cell structure factor in equation 4.1. This term is called Debye-Waller factor.

$$F^{\text{unit cell}}(\mathbf{q}) = \sum_{\mathbf{r_j}} f_j(\mathbf{q},\omega)\, e^{-M_j} e^{i\mathbf{q}\cdot\mathbf{r_j}} \tag{4.16}$$

where $M_j = \frac{1}{16\pi^2} B_T^j \mathrm{q}^2$ with $B_T^j = 8\pi^2 \left\langle \mathrm{u}_{\mathrm{q}j}^2 \right\rangle$. The Debye-Waller term only reduces the elastic scattered intensity by atomic vibrations but does not increase the width. It contains the self-correlation $\left\langle \mathrm{u}_{\mathrm{q}j}^2 \right\rangle$ of the displacement from every atom j. The DW-factor does not need to be isotropic as the bonding within a crystal can restrict vibrations in a certain direction.

Structure Factor Determination

Within this work the integrated diffracted intensity at a point along the CTR is measured by two standard methods. When a point detector is used, so-called rocking scans are performed. At a constant perpendicular wave vector transfer the azimuth angle θ is varied through the rod position to record all the intensity from this point. When a 2D detector is used, the complete signal of a certain rod position is measured at once. No rocking scans need to be performed in this stationary geometry. For every reflection (H,K,L), recorded in these ways, the background intensity is subtracted and the signal is normalized by the incoming flux. Standard corrections, like the Lorentz-, the active area-, the polarization- and the rod interception term, are applied according to the measuring geometry and the used diffractometer [61]. Finally, the square root of the corrected integrated intensity is

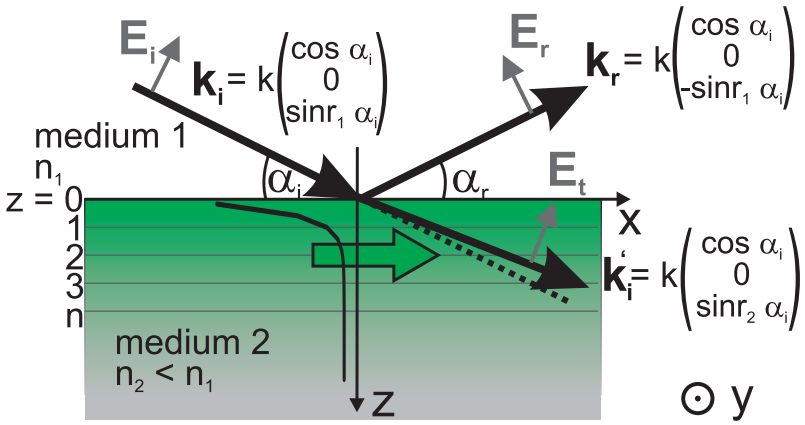

Figure 4.5: Side view (the x-z plane is the plane of incidence) of the interface between medium 1 and medium 2: The incoming wave with wave vector $\boldsymbol{k}_i$ hits the interface. One part gets reflected into medium 1 with an angle of $\alpha_r = \alpha_i$ and the wave vector $\boldsymbol{k}_r$. Another part of the wave is transmitted into medium 2 with a wave vector $\boldsymbol{k}'_r$. The direction of $\boldsymbol{k}'_r$ can be calculated by Snell's law. For angles smaller than the critical angle no wave is transmitted into the crystal but an evanescent wave travels parallel to the surface. The wave field of the evanescent is exponentially damped into the medium. The green arrow shows the direction of this evanescent wave. The prime $'$ signalizes a quantity to be within medium 2.

proportional to the structure factor at the corresponding position.

The measured structure factors can be compared to the ones, calculated for a structural model with equation 4.6. In a structural model atomic positions can be relaxed or site occupations varied by introducing the corresponding parameters. For comparison a normalized residuum $\chi^2_{norm.}$, defined by difference of calculated and measured structure factor, is introduced by the following equation:

$$\chi^2_{norm} = \frac{1}{N-P-1} \sum_i \frac{(|F_{exp,i}| - |F_{cal,i}|)^2}{\sigma^2_{exp,i}}. \tag{4.17}$$

N is the number of data points, P the number of fitting parameters, F_{exp} the experimental structure factor (with error bar σ_{exp}) and F_{cal} the calculated structure factor. In a fit the program ROD minimizes this residuum with respect to the free parameters of the applied structural model. The number of fit parameters, the number of data point and the error bars are thereby taken into account. For normalized residua lower than 1, all calculated structure factors lie within the error bars.

4.1.2 Refraction and Reflection from interfaces

This section gives a brief introduction into the basic principles of grazing incidence diffraction (GID) and reflectivity measurements. For a detailed description of the phenomena,

the references [10] and [62] are recommended for GID and reflectivity, respectively. Short summaries for GID are also given in [34, 63, 64].

Refraction at an interface

The Helmholtz equation,

$$\text{rot rot } \mathbf{E}(\mathbf{r}) + \mathrm{k}^2\mathrm{n}^2\mathbf{E}(\mathbf{r}) = 0, \tag{4.18}$$

describes the propagation of an electromagnetic plane wave $\mathbf{E}(\mathbf{r}) = \mathbf{E_0}\ \exp(i(\mathbf{k}\cdot\mathbf{r} - \omega\mathrm{t}))$ in a medium with an index of refraction n. The electromagnetic wave is characterised by its amplitude $\mathbf{E_0}$, its wave vector $\mathbf{k}$ and its frequency ω. For x-rays, where the photon energy is larger than the energy of the electronic resonances in the material's atoms, the refractive index, as important material property for the propagation, is defined as

$$\mathrm{n}\,(\mathbf{r}) = \overbrace{1\ -\ \delta\ +\ i\beta}^{\text{average value n}}\ \ \overbrace{+\ \Delta\mathrm{n}(\mathbf{r})}^{\text{local deviation from n}} \tag{4.19}$$

with

$$\delta = \lambda^2\frac{\mathrm{N}r_0\mathrm{Z_{eff}}}{2\pi} \quad \text{and} \tag{4.20}$$

$$\beta = \lambda\frac{\mathrm{N}\sigma_a}{4\pi} = \frac{\lambda\mu}{4\pi}. \tag{4.21}$$

n is the average refraction index resulting from the average electron density of the material. Local deviations from this average represent the atomic-scale structure and are taken into account by $\Delta\mathrm{n}(\mathbf{r})$[8]. λ is the wavelength, N is the average number density of the material, r_0 is the classical electron radius and Z_{eff} the charge number of the atoms corrected for dispersion. σ_a is the absorption cross section and μ the linear photo absorption coefficient. Calculating δ and β for Fe_3Al and a wave length of 1.239 Å results in 1.30×10^{-5} and 9.15×10^{-7}, respectively. These are typical numbers for the quantities and lead to a refraction index slightly smaller than 1. Thus, total external reflection occurs when the x-rays impinge on the vacuum-Fe_3Al interface with an angle smaller then the critical, defined as $\alpha_c = \sqrt{2\delta}$.

A typical situation for evanescent x-ray diffraction is shown in fig. 4.5. An incoming plane x-ray wave, characterized by its amplitude $\mathbf{E}_i(\mathbf{r})$ and its wave vector $\mathbf{k}_i$, hits the interface between two materials with different index of refraction[9]. It will be reflected and for angles larger than α_c transmitted into the material. The field, $\mathbf{E}_t(\mathbf{r}')= \mathcal{T}_i\mathbf{E}_i\mathrm{e}^{\mathrm{i}\mathrm{k}_i'\cdot\mathrm{r}'}$, of the wave transmitted in medium 2 and the field, $\mathbf{E}_r(\mathbf{r})=\mathcal{R}_i\mathbf{E}_i\mathrm{e}^{\mathrm{i}\mathrm{k}_r\cdot\mathrm{k}}$, of the wave reflected into medium 1 are calculated by solving the Helmholtz equation, taking the boundary conditions of continuous, tangential E-field components across the surface into account.

[8] The deviation is important for the distorted Born approximation later in this section but can be neglected when the basic principles of optics are applied.

[9] In many cases material 1 is vacuum or air with n_1=1.

k_i' and k_r are the wave vectors of the transmitted and reflected waves, respectively, and defined in fig. 4.5. $\mathcal{T}_i$ and $\mathcal{R}_i$ are the diagonal transmission and reflection tensors. Their diagonal components are the Fresnel coefficients for transmission and reflection, defined from the principle of optics. Here only the Fresnel coefficients for a wave polarisation perpendicular to the plane of incidence are given [10, 65]:

$$T_{iy} = \frac{2sinr_1\ \alpha_i}{sinr_1\ \alpha_i + sinr_2\ \alpha_i}, \quad R_{iy} = -\frac{sinr_1\ \alpha_i - sinr_2\ \alpha_i}{sinr_1\ \alpha_i + sinr_2\ \alpha_i} \tag{4.22}$$

$sinr_{1,2}\ \alpha_i = (\sin^2\ \alpha_i - 2\delta_{1,2} + i2\beta_{1,2})^{1/2}$ where the indices 1 and 2 indicate medium 1 and medium 2, respectively.

Fig. 4.6 shows the results for the reflectivity $|R_i|^2 \equiv (E_r/E_i)^2$ and transmissivity $|T_i|^2 \equiv (E_t/E_i)^2$ for a vacuum-Fe_3Al interface. E_i, E_r and E_t are the amplitudes of the incoming, reflected and transmitted waves, respectively. As $n_{Fe_3Al} < n_{vac.}$ the reflectivity shows total reflection below the critical angle. For angles greater than the critical the reflectivity decreases by $1/q^4$ with increasing angles. For the description of GID the transmissivity is the important property. At larger angles the incoming wave is mainly transmitted and $|T_i|^2$ approaches 1. As striking feature $|T_i|^2$ exhibits an enhancement at the critical angle up to a value of 4. This is due to a coherent coupling between the incident, reflected and transmitted wave field. Calculating the transmitted wave field $E_t(\mathbf{r}')$ results in a exponentially damped wave within the less dense material:

$$E_t(\mathbf{r}') \propto e^{i\mathrm{Re}\left\{\mathbf{k}_i'\cdot\mathbf{r}'\right\}} e^{-z/\mathcal{L}_i} \tag{4.23a}$$

$$\mathcal{L}_i \equiv \left|\mathrm{Im}\left\{\mathbf{k_{iz}'}\right\}\right|^{-1} = \frac{\lambda}{2\pi l_i} \text{ with} \tag{4.23b}$$

$$l_i = 2^{-1/2}\left\{\left(2\delta - \sin^2\alpha_i\right) + \left[\left(\sin^2\alpha_i - 2\delta\right)^2 + 4\beta^2\right]^{1/2}\right\}^{1/2} \tag{4.23c}$$

$\mathcal{L}_i$ is the penetration depth of the transmitted beam, as shown in 4.6c. For an incoming angle close to 0 it has an asymptotic behaviour towards $\mathcal{L}_{i0} = \lambda/2\pi\alpha_c \approx 40$ Å. For angles smaller than the critical angle $\mathcal{L}_i$ gets a purely real value. According to equation 4.23a this leads to an evanescent wave field which travels parallel to the surface like shown in fig. 4.5. A purely evanescent wave exists only for ideal systems without absorption ($\beta = 0$). For real systems with absorption a small perpendicular component of the wave field remains, as $\mathcal{L}_i$ always has an imaginary part.

Furthermore a real surface is never completely flat but has an unavoidable microscopic roughness which is described by local deviations $\Delta z(\mathbf{r}_\parallel)$ from the average position $z = 0$ at the surface, as demonstrated by fig. 4.2. The reflectivity and transmissivity of a rough interface result in [66–69]

$$R_\sigma = R\, e^{-2i\mathbf{k_{iz}}\mathbf{k_{iz}'}\sigma^2} \tag{4.24a}$$

$$T_\sigma = T\, e^{\frac{1}{2}(\mathbf{k_{iz}'}-\mathbf{k}_{iz})^2\sigma^2} \tag{4.24b}$$

R and T are the reflectivity and transmissivity corresponding to a ideal, flat surface. $\mathbf{k_{iz}}$ and $\mathbf{k_{iz}'}$ are the wave vectors perpendicular to the surface of the incoming and transmitted

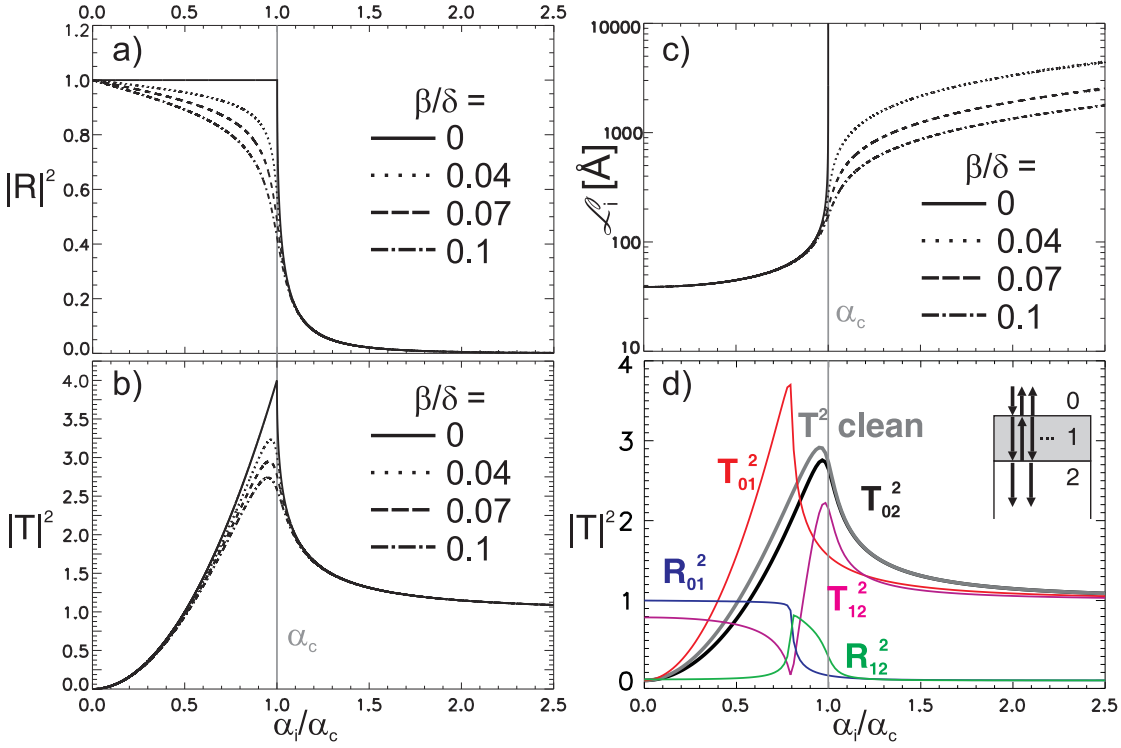

Figure 4.6: The reflectivity $|\mathrm{R}_i|^2$ (a), the transmissivity $|\mathrm{T}_i|^2$ (b) and the penetration depth $\mathcal{L}_i$ (c) are shown as a function of the incoming angle. The curves are calculated for a vacuum-Fe_3Al interface and a photon energy of 10 keV. δ is always kept at the constant value, while β is varied. A β/δ-ratio of 0.07 (dashed line) corresponds to the situation of Fe_3Al at 10 keV. Part d) shows the total transmissivity of the sketched vacuum-alumina-alloy system (thick black line) in comparison with a clean vacuum-alloy system (thick grey line). The single components of equation 4.25 are shown by thin, coloured lines.

beam, respectively. T_σ is enhanced for rough surfaces as less x-rays get reflected.

So far the transmissivity of a single interface has been discussed. Now the situation of a truncated crystal, covered by a dielectric layer with a different refractive n_1 and of thickness Y, is investigated. It reflects the case of an oxide film on a binary alloy surface. Like shown in fig. 4.8b the x-rays impinge on the vacuum-dielectric interface and get transmitted and reflected. The transmitted wave impinges on the dielectric-substrate interface. It is again transmitted but also reflected back on the first interface. This process continues. Solving the Helmholtz equation with continuity requirements for two interfaces finally results in the following expression for the transmissivity T_{02} of the described vacuum-dielectric-substrate system [10, 65]:

$$T_{02} = \frac{\mathrm{E}_2}{\mathrm{E}_0} = \frac{T_{01}T_{12}\mathrm{e}^{ik'_{1,z}Y}}{1 + \mathrm{e}^{2ik'_{1,z}Y}R_{01}R_{12}} \tag{4.25}$$

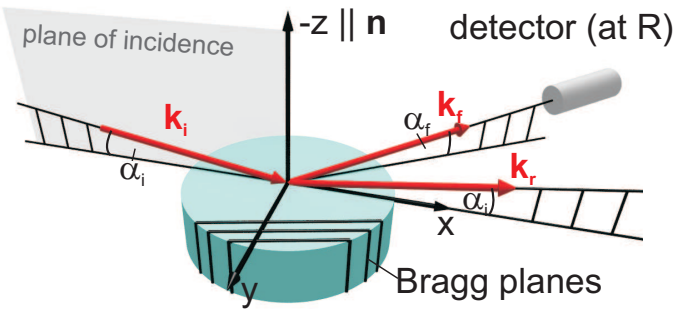

Figure 4.7: Schematic description of GID. The incoming beam with the wave vector $\boldsymbol{k}_i$ hits the surface with an angle α_i below the critical angle. The resulting evanescent wave in the surface region of the medium travels parallel to the surface and is scattered from the Bragg planes perpendicular to the surface. The scattered beam $\boldsymbol{k}_f$ is measured as a function of the outgoing angle α_f.

T_{ab} and R_{ab} are the Fresnel coefficients of the single interfaces, defined by equation 4.22. $k'_{1,z}$ is the wave vector perpendicular to the interface within the dielectric layer. Fig. 4.6d shows the transmissivity T_{02} for a vacuum-Al_2O_3-Fe_3Al system where the oxide layer is 8 Å thick. T_{01} and R_{01} at the vacuum-oxide interface and T_{12} and R_{12} at the oxide-alloy interface are also depicted. The oxidized surface is compared to a clean vacuum-Fe_3Al system. The oxide layer clearly decreases the transmissivity in the region close to the critical angle.

Grazing Angle Diffraction

X-ray diffraction at glancing angles is depicted schematically in fig. 4.7. An incident beam, described by the amplitude of the electric field $\mathbf{E}_i(\mathbf{r})$ and the wave vector $\mathbf{k}_i$, impinges on the surface under an angle smaller than the critical. It gets reflected ($\mathbf{E}_r$,$\mathbf{k}_r$) and additionally creates an distorted evanescent wave $\mathbf{E}_t(\mathbf{r}')$ parallel to the surface within the medium. This distorted wave $\mathbf{E}_t(\mathbf{r}')$ acts as the "new" incident wave in the surface region which is scattered by the atomic scale structure represented by $\Delta\mathrm{n}(\mathbf{r})$ in equation 4.19. This Distorted Wave Born Approximation (DWBA) was first applied by Vineyard and completed by Dietrich and Wagner [70, 71]. Again, the solution of the Helmholtz equation results in the scattered wave $\mathbf{E}_f(\mathbf{r})$. All refraction effects are taken into account as the previously described concept for the transmissivity is applied when the scattered wave travels through the medium-vacuum interfacial region. According to the Helmholtz reciprocity principle in optics[10] $\mathbf{E}_f(\mathbf{r})$ is symmetric with respect to the interchange of the indices i and f [72]. The intensity I_{GID}, resulting from the scattered wave's amplitude, is given by:

$$\mathrm{I}_{GID}(\mathbf{q}') = \mathrm{I}_0 r_0^2 \left|\mathrm{T}_i\right|^2 \mathrm{S}(\mathbf{q}') \left|\mathrm{T}_f\right|^2 P \tag{4.26}$$

[10] "If the source and the point of observation are interchanged, the same amplitude would result"

$I_0 = E_i^2$ is the incoming flux. P is a polarization factor which is 1 if the incoming x-rays are polarized parallel to the plane of incidence and $\cos^2(2\theta)$ for perpendicular polarization. $\mathbf{q}'$ is the wave vector transfer inside the medium. $S(\mathbf{q}') = \langle F^* F \rangle$ is the kinematic sum of Bragg scattering, defined as thermal average of the structure factor F calculated in section 4.1.1.

If the structure factor is known, one can calculate the intensity diffracted from the sample, depending on the incoming and outgoing angle and compare it to the measurements. The structure factor F_{CTR} for a semi-infinite crystal, corresponding to the situation shown in fig. 4.7, was derived in the previous section and is given in equation 4.4 and 4.5. It is pointed out here that the part of the wave vector parallel to the interface ($\mathbf{q}_{\parallel} = \mathbf{q}_x + \mathbf{q}_y$) is not affected by the presence of an interface, or expressed mathematically $\mathbf{q}_{\parallel} = \mathbf{q}'_{\parallel}$. However, the part of the wave vector perpendicular to the surface $\mathbf{q}'_3$ inside the medium has a depth dependence due to the depth-dependence of the distorted wave. Consequently the scattering originates only from a region up to the scattering depth Λ [64]:

$$\Lambda \equiv \left| \mathrm{Im} \left\{ q'_3 \right\} \right|^{-1} = \frac{\lambda}{2\pi(l_i + l_f)} \tag{4.27}$$

l_i and l_f are both defined by equation 4.23c. To account for this effect within the calculation of F_{CTR} the perpendicular wave vector transfer $\mathbf{q}_3$ outside the medium has to be replace by $\mathbf{q}'_3$ inside the medium.

So far it was tacitly assumed that the Bragg conditions parallel to the surface are fulfilled when moving along q_3. Therefore $\alpha_i = \alpha_f$ has to be valid, resulting in equal projections of $\mathbf{k}_i$ and $\mathbf{k}_f$. For $\alpha_i \neq \alpha_f$ it can be shown that the deviation $\Delta\theta$ of the exact Bragg angle θ is in the order of μrad which is much smaller than the mosaicity of the imperfect crystals investigated in this work [73]. Therefore the Bragg conditions are regarded as fulfilled. Fully incoherent diffuse scattering like Compton scattering or fluorescence are treated as background within this thesis, which is subtracted from the signal.

To get from the ideal truncated crystal to a more realistic situation, the phenomena described in section 4.1.1 have to be included into the coherent Bragg scattering sum. Refraction effects play an important role for small outgoing angles and the wave vector transfer $\mathbf{q}$ has to be exchanged by $\mathbf{q}'$ in the corresponding equations.

Theory of Reflectivity

The specular[11] reflected intensity contains information on the electron density distribution perpendicular to the sample surface. Having a stratified material, important details like layer thickness, interfacial roughness or the refracted index can be obtained for every single layer.

The ability of an ideal flat surface to reflect an incoming electromagnetic wave was described above using the principles of optics [65, 74, 75]. The normalized reflected intensity of a single interface is shown in fig.4.6a and is called Fresnel reflectivity. With the same

[11] The wave vector transfer is perpendicular to the sample surface

principle as for a single interface - using the continuity of the tangential components of the electric field at the interface- the reflectivity of a stratified medium can be calculated. The concept was introduced by Parratt [76] and is demonstrated in fig. 4.8. One starts with the Fresnel coefficient for reflectivity for one interface [12] assuming the absence of multiple reflections (marked by a prime'):

$$r'_{j,j+1} = \frac{\mathrm{E}_{r,j}}{\mathrm{E}_{t,j}} = \frac{k_{z,j} - k_{z,j+1}}{k_{z,j} + k_{z,j+1}} \tag{4.28}$$

$k_{z,j}$ is the wave vector component perpendicular to the surface within the jth layer. The inplane component is not affected by refraction effects. Due to the infinity no multiple scattering can occur at the "last" interface N and equation 4.28 becomes correct for $\mathrm{r}'_{N,\infty}$. Calculating the ratio $\mathrm{r}_{N-1,N} = \mathrm{E}_{r,N-1}/\mathrm{E}_{t,N-1}$ multiple refractions have to be taken into account like demonstrated in fig. 4.8b [13]. The reflectivity from the next interface can be calculated in the same way, leading to a recursive formula for the intensity reflected from the surface at j = 0 where $\mathrm{E}_{t,0}$ is 1 by definition. For an arbitrary interface j the reflectivity, including multi-reflections, is calculated to

$$r_{j,j+1} = \frac{\mathrm{E}_{r,j}}{\mathrm{E}_{t,j}} = \exp(-2ik_{z,j}z_j) \cdot \frac{r'_{j,j+1} + r_{j+1,j+2}\exp(-2ik_{z,j+1}z_j)}{1 + r'_{j,j+1}r_{j+1,j+2}\exp(-2ik_{z,j+1}z_j)}. \tag{4.29}$$

Roughness is included in the same way as shown in the equations 4.24 for a single interface.

Example: Reflectivity curves of oxidized Fe_3Al surfaces

Fig. 4.9 shows the reflectivity curves and the corresponding δ-profiles of Fe_3Al, covered by different kind of oxide layers. The curves of oxide covered surfaces show distinctive oscillations depending on the thickness of the oxide film. The thicker the oxide layer the smaller the distance between two minima in the curve, like demonstrated for a 8 Å and 16 Å thick alumina film on the alloy.

Different type of oxides have different electron densities and therefore different $\delta-$values. While the curve of Fe_2O_3 on Fe_3Al is still distinguishable from Al_2O_3 on Fe_3Al, the density difference between alumina and the spinel $FeAl_2O_4$ is to small to detect it in the reflectivity curve.

[12] The interface from layer j to $j+1$

[13] $\mathrm{r}_{N-1,N} = \mathrm{r}'_{N-1,N} + \mathrm{t}'_{N-1,N}\mathrm{t}'_{N,N-1}\mathrm{r}'_{N,\infty}\exp(2\mathrm{id}_N\mathrm{k}_{z,N})^2 + \ldots$ is a geometric series which can be solved [9]

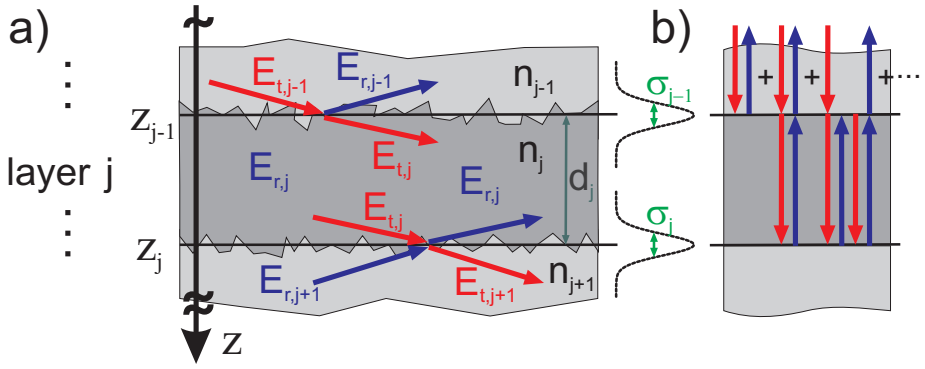

Figure 4.8: a) Side view of a rough stratified homogeneous media consisting of layers with different refractive indices n_j and thickness $d_j = z_j - z_{j-1}$. The flat interfaces are show by thin, horizontal black lines. Transmitted wave vectors are depicted by red arrows and their layer-dependent, wave field amplitudes are $\mathbf{E}_t$. Reflected waves vectors are coloured blue and have amplitudes $\mathbf{E}_r$. A wave field transmitted into layer j-1 ($\mathbf{E}_{t,j-1}$) impinges on the interface z_{j-1} and gets transmitted ($\mathbf{E}_{t,j}$) and reflected ($\mathbf{E}_{r,j-1}$). In the same way, a wave field reflected into layer j ($\mathbf{E}_{r,j}$) gets transmitted ($\mathbf{E}_{r,j-1}$) and reflected ($\mathbf{E}_{t,j}$) at the interface j-1. These processes happen at every interface of the layered system, leading to series of reflections as demonstrated in part b). To calculate the total reflected amplitude at the surface (z=0) one has to add up the reflected wave field from all interfaces and take the layer thickness dependent phases between them into account.

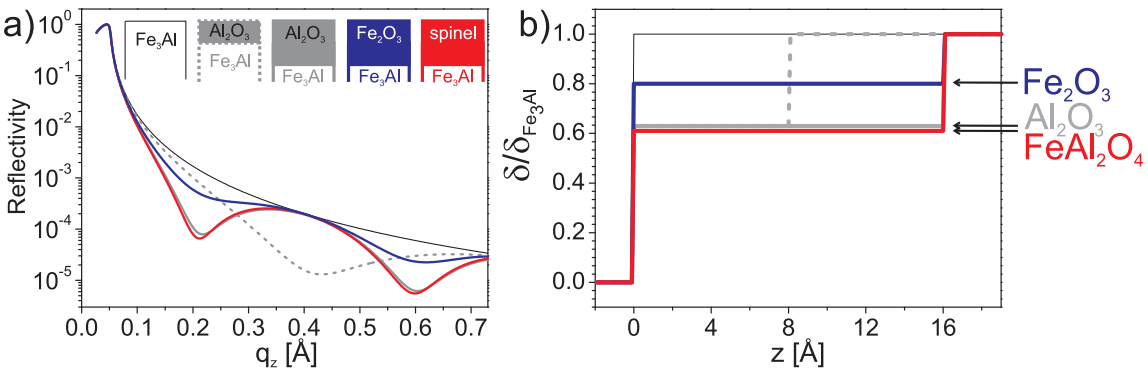

Figure 4.9: a) Specular reflectivity curves for a clean Fe_3Al sample (thin black line) and its surface covered with 8 Å thick alumina (dashed grey line), 16 Å thick alumina (solid grey line), 16 Å thick Fe_2O_3 (solid blue line) and 16 Å thick spinel $FeAl_2O_4$ (solid red line), respectively. b) The corresponding delta-profiles which are proportional to the electron density profiles. No roughness is assumed.

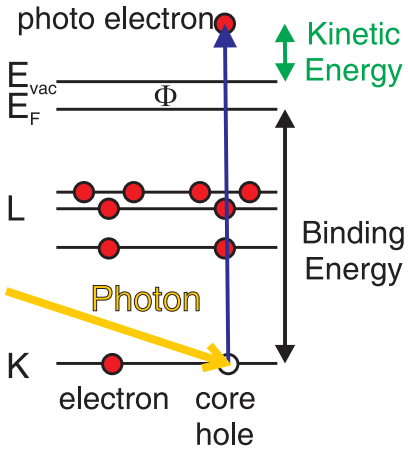

Figure 4.10: Schematic view of the energy levels in a system: A photo electron is emitted from a core hole created by an incoming photon.

4.2 High Resolution Core Level Spectroscopy

The basic process of high resolution core level spectroscopy (HRCLS), also known as X-Ray Photo electron Spectroscopy (XPS) is the photoelectric effect which was discovered in 1887 by H.R. Hertz and fully explained by A. Einstein in 1905 [77, 78]. A schematic view is shown in fig. 4.10. A core hole in an inner electronic shell of the atom is created by an incident photon and a photo electron with a kinetic energy E_{kin} is emitted, if the energy of the incoming photon $h\nu$ is big enough to overcome the binding energy E_{bind} of the core electron as well as the work function Φ of the material. The material dependent binding energy can be calculated to [79, 80]:

$$E_{bind} = h\nu - E_{kin} - \Phi \quad . \tag{4.30}$$

Thereby, the binding energy is defined as the difference between the neutral, *initial* state before the creation of an core level hole and the ionized, *final* state after the photoelectric process. The binding energies of the core level electrons are element specific and standard tables exist [81]. The technique can be applied to all elements with at least one electron in the L shell which excludes only hydrogen and helium. Due to the low inelastic mean free path of the photo electrons XPS is a highly surface sensitive technique[14]. This main free path mainly depends on the energy of the electron and less on the material as shown in fig. 4.11.

4.2.1 The XPS Spectrum

The use of synchrotron radiation for HRCLS measurements allows to tune the energy of the incoming photons, making depth dependent measurements possible. Due to the

[14]The photo electron looses energy within the material e.g. by phonon excitation or exciton creation.

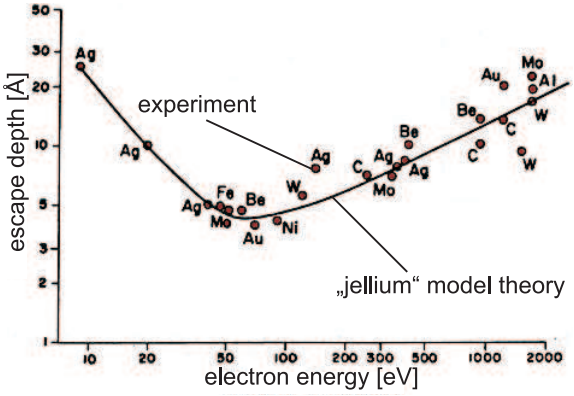

Figure 4.11: Escape depth (proportional to the mean free path) of the electrons depending on the kinetic energy.

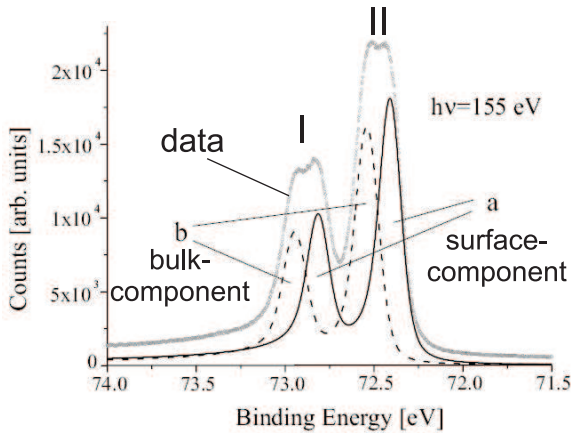

Figure 4.12: This normal emission Al 2p core level spectrum consists of two components a and b and the spin-orbit split components. Component b is assigned to photo electrons out of the bulk and a of the surface (from [82]).

high brilliance of synchrotron radiation, a very high energy resolution is achieved. As an example a HRCLS- spectra from the Al 2p electrons of an NiAl(1,1,0) surface is shown in fig. 4.12 [82]. It demonstrates how different *initial* and *final* state effects appear in the spectra.

A typical *initial* state effect, observed by the two main peaks I and II in fig. 4.12, is the spin-orbit splitting for orbitals with non-zero angular momentum (quantum number $l \neq 0$). The orbital angular momentum (l) and the electron spin ($s = \pm 1/2$) can align parallel and anti-parallel leading to a splitting of the atoms energy level and therefore to two lines in the HRCLS spectra. Another *initial* state effect (not shown here) is a chemical shift of the binding energy depending on the chemical surrounding of the corresponding atoms. Different oxidation states of an atom or the chemisorption of oxygen lead to different

chemical shifts, making XPS a suitable method to determine different chemical states on a surface.

The two components assigned a and b in the spectrum of fig. 4.12 show a typical *final* state effect [15]. The appearance of two doublets is a effect due to a different binding situation at the surface. The surface leads to a lower binding energy compared to the bulk. For vicinal surfaces it is even possible to detect atoms at the step edge of stepped surfaces where the binding of the atoms is different from terrace atoms [49, 50]. A chemical shift towards smaller binding energies can also occur due to relaxations. In the described final state effects the created, localized hole is often screened by electrons from the exited or surrounding atoms and becomes delocalized, letting the photo electron escape with more kinetic energy and leading to a lower binding energy.

During the photoelectric effect the atom is put from a neutral to an excited state. This exited state can return to the ground state by an electronic rearrangement and thereby adopt several intermediate states. The outgoing photo electron can appear to have left from these intermediate states. This leads to satellite peaks with higher binding energy, as the energy which is needed for the excited state, is taken from the kinetic energy of the photo electron. The excited electron can either stay in the atom (shake-up process) or leave it (shake-off). Other final state effects are the creation of plasmons, or in case of an insulator a charging of the system.

4.2.2 The peak shape

A first complete analysis of the line shape of a XPS-spectra was performed by Doniach and Šunjić [83]. As described above, the atoms can be excited by the creation of the core holes while the needed energy for the excitation process is taken from the photo electron. Therefore the photo emission cross section and the x-ray line spectra is changed from a delta function to a curve tailing of on the low photon energy side as shown by curve A in fig. 4.13. Due to the finite life time of the the core hole, the curve A has to be convoluted with a Lorentzian which gives the final curve B in the figure 4.13. Line B is analytically described by the photo electron yield function line shape

$$Y(\epsilon) = \frac{\Gamma(1-\alpha)}{(\epsilon^2+\gamma^2)^{(1-\alpha)/2}}\, cos\left\{\frac{\pi\alpha}{2} + \theta(\epsilon)\right\} \tag{4.31}$$

with

$$\theta(\epsilon) = (1-\alpha)/\tan^{-1}(\epsilon/\gamma) \qquad . \tag{4.32}$$

$\epsilon = E_{kin} - E_{kin,max}$ and Γ is the gamma function. α is a singularity index which influences the asymmetry of the spectrum and γ is the full width half maximum value of the Lorentzian. To account for broadening due to instrumental resolution and thermal vibrations of the atoms the curve has to be convoluted by a Gaussian.

[15] Final state effects are caused by changes in the charge after the impact of the photon or while the photo electron is leaving the material.

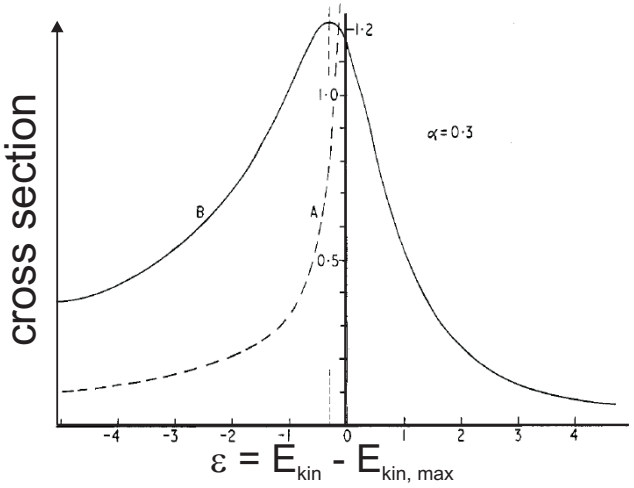

Figure 4.13: XPS spectra in the absence of life time broadening (dashed curve A) and with finite hole life time (full curve B). The spectra is shown as a function of the kinetic energy relative to the maximum energy which corresponds to the case when the photo electron leaves from ground state (from [83]).

4.3 Low Energy Electron Diffraction

The wave length of electrons is related to their momentum q and consequently their energy E according to the $deBroglie$ relation [79, 80]:

$$\lambda = \frac{h}{p} = \frac{h}{\sqrt{2m_e E}} \tag{4.33}$$

h is the Planck constant, m_e the electron mass.

Thus, electrons with energies in the range between 20 eV and 250 eV have wave lengths between 2.7 Å and 0.8 Å. This is of the same order than the lattice constants of metal and oxide crystals. Therefore low energy electrons will be diffracted from a crystal structure which was fist observed for Ni single crystals in 1923 [84]. Thereby the diffraction signal comes from the surface region only. Due to the strong interaction of electrons with matter, the escape depth of the elastically scattered electrons is small (see fig. 4.11).

Typically, low energy electron diffraction (LEED) is performed in back scattering geometry. Incoming electrons impinge perpendicular to the sample surface while the back scattered electrons are detected by a fluorescence screen. The principle is schematically depicted in fig. 4.14. Similar to SXRD, the scattered intensity is distributed along rods in the reciprocal space of the truncated crystal. Due to small scattering depth, the intensity is distributed more homogeneously along the rods, as compared to SXRD. For a detailed structure determination of the surface region the intensities of the diffraction spots are recorded as a function of the energy of the incoming electrons. To analyse these I-V-curves the complex theory of dynamical scattering has to be applied as the electrons

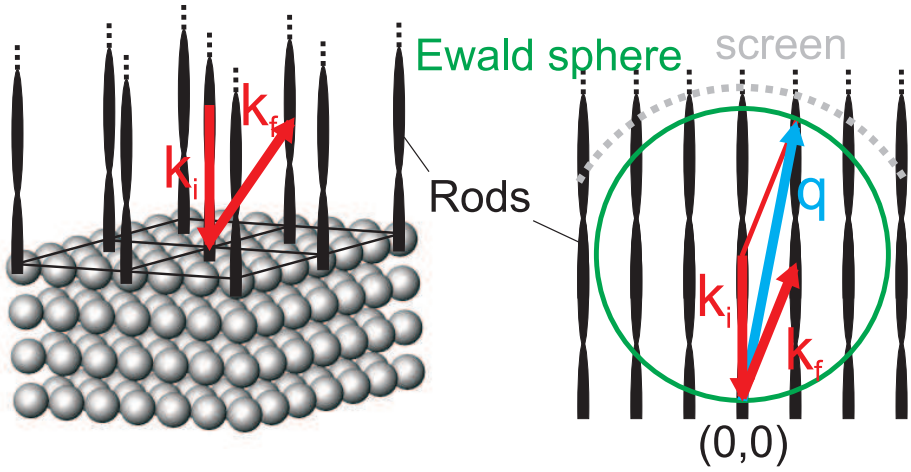

Figure 4.14: *left:*Truncated crystal and the corresponding intensity along the rods in reciprocal space. k_i is the wave vector of the incoming, k_f of the back scattered electrons. *right*: 2D-view of the reciprocal space with Ewald sphere and fluorescent screen. The higher the energy, the larger the radius of the Ewald sphere, the higher-order reflexion spots are detectable.

undergo multiple scattering due to the strong interaction.

Within this thesis, LEED is used qualitatively to monitor the quality of the single crystal samples during the preparation process. The formation of ordered surface oxides or of surface reconstructions is followed by LEED.

4.4 Auger Electron Spectroscopy

The Auger process is named after his discoverer P. Auger and is schematically shown in fig. 4.15 [79, 80, 85]. A core hole is created in an inner shell by electron bombardment or photo emission. This hole is re-occupied by an electron of a higher shell in an energetically favourable transfer. Instead of fluorescence the gained energy is transferred to a third electron in the atom located in the same or an higher energy level than the second one. With the transferred energy the third electron can overcome the work function and is emitted with the remaining characteristic kinetic energy. The whole process is independent of the energy of the incoming radiation. Measuring a spectrum of the kinetic energy of the Auger electrons only depends on the energy levels participating in the process, making Auger electron spectroscopy (AES) an element specific technique. Due to the low energy of the Auger electrons the signal depth is small, leading to a high surface sensitivity. AES spectra for all elements[16] are tabulated. AES is commonly used to monitor the cleanness of samples during preparation and to detect contaminations on the surface [86]. Typically,

[16] All elements besides H, He and Li where the Auger process is not possible

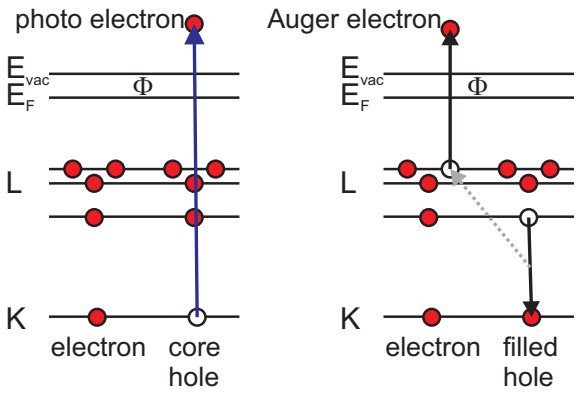

Figure 4.15: The KL_1L_3 Auger transition.

the spectra show the derivative of the counted electrons to emphasis the respective AES peaks.

Furthermore, the energy levels of an atom are influenced by the chemical environment. A shift of the energy levels leads to a change in the AES spectrum especially for electrons with small kinetic energies. As an example it is possible to determine if Al (or Fe) is metallic or oxidized by measuring the AES spectrum [87, 88].

Chapter 5

Experimental Details

5.1 X-Ray Diffraction Set-up

This section is devoted to the experimental set-up used for the x-ray diffraction studies. Firstly, the need of synchrotron radiation as source for x-rays is discussed, followed by a description of the beamline optics and the end stations where the experiments are performed. Last but not least the special requirements of the experimental chamber are introduced.

5.1.1 Synchrotron Radiation

A synchrotron is a specific particle accelerator where highly relativistic electrons are kept on a closed orbit with a constant energy in a so-called storage ring. The electrons in the ring are accelerated by high frequency generators. At the synchrotron Angströmquelle Karlsruhe (ANKA) the electrons have an energy of 2.5 GeV , at the Swiss light source (SLS) in Villingen an energy of 2.4 GeV and at the European Synchrotron Radiation Facility (ESRF) in Grenoble an energy of 6.03 GeV. The storage rings of ANKA and the ESRF are operated with a maximum ring current of 200 mA, while the current is 400 mA at the SLS.
The storage ring consists of straight sections and deflection magnets which magnetic fields keep the electrons on an orbit. Like shown in fig. 5.1 or 5.2, radiation is produced by accelerated charge and therefore by the circular motion of the electrons either in bending magnets or in insertion devices like undulators or wigglers situated in the straight sections. A bending magnet has a constant magnetic field where -according to the Lorentz force- the electrons are deflected perpendicular to the magnetic field and direction of travel. In an undulator an alternating magnetic field forces the electrons away from the straight on an oscillating path. As the amplitude of these oscillations is small, radiation from the oscillations adds coherently. In the case of highly relativistic electrons the radiation is focused strongly in the direction of travel and therefore emitted tangentially with very small angles of aperture in the order of 0.1 mrad. It is polarized within the plane where the electrons oscillate.

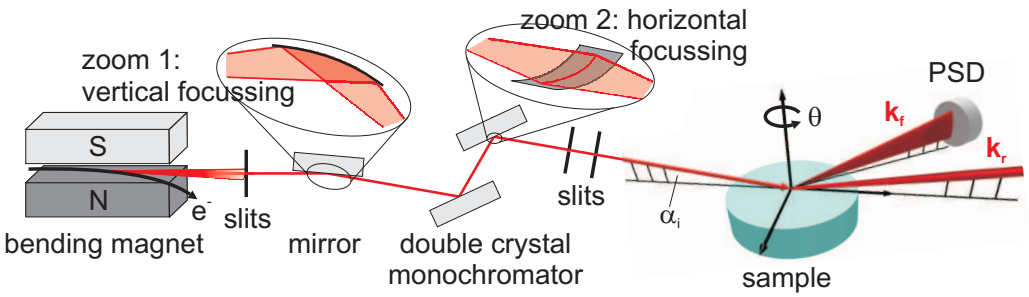

Figure 5.1: Schematic set-up of the MPI-MF-Beamline at ANKA. A GID-set-up with a position sensitive detector is shown.

The synchrotron spectrum of the produced radiation ranges from infra-red up to hard x-rays while the quality of the x-ray radiation is defined by the brilliance after the monochromator [9]:

$$\text{Brilliance} = \frac{\text{Photons/second}}{(\text{mrad})^2(\text{mm}^2\ \text{source area})(0.001 \cdot \text{bandwidth})} \tag{5.1}$$

The brilliance depends on the photon flux after the monochromator, the angular divergence (in mrad), the source area (in mm^2) and the relative bandwidth of the monochromator. Here the advantages of synchrotron radiation become obvious as synchrotrons produce a high photon flux and have an intrinsic small angular divergence and source area. Furthermore, the energy of the radiation is tunable and the radiation is polarized within the plane of the ring.

5.1.2 The Beamline Set-up

After the synchrotron radiation leaves the storage ring a certain wavelength, appropriate for the experiments, is cut out of the broad synchrotron spectrum. Furthermore the photon beam is guided and focused onto the investigated sample. This is done by several optical instruments within a beamline. The SXRD experiments within this thesis are carried out at three beamlines: the undulator beamline ID3 at the ESRF, the wiggler beamline MS at the SLS and the bending magnet MPI-MF beamline at ANKA. As the MS and the MPI-MF beamline are similar in their optical components, only the ID3 and MPI-MF set-up are briefly described in the following.

The MPI-MF beamline is depicted in fig. 5.1 [89]. The white beam with a source size of 190 μm$\times$90 μm (fwhm, HxV) impinges on a water cooled Si mirror coated by Rh. By bending the mirror the beam is focused vertically (fig. 5.1, zoom 1). Making use of the total reflection of x-rays below an energy-dependent critical angle the mirror cuts off higher photon energies. After the mirror the beam is reflected on a double-crystal monochromator consisting of a first flat, water-cooled Si(111) crystal and a second, bendable Si(111) crystal which is used for horizontal focusing (fig. 5.1, zoom 2). The desired energy of

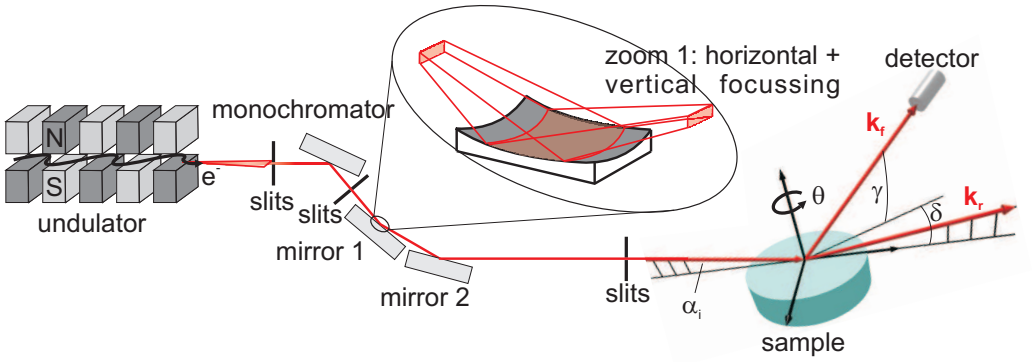

Figure 5.2: Schematic set-up of the ID03-Beamline at the ESRF. A SXRD set-up is shown.

the x-rays is selected by a rotation of the monochromator so that the crystal's (111) planes have the corresponding Bragg angle with respect to the incoming beam. Doing so photon energies between 6 to 25 keV can be achieved. The measurements at ANKA presented in this thesis are performed at 10 keV photon energy while a resolution of $\Delta E/E = 3 \times 10^{-4}$ is obtained. The beam is focused on the sample position having a size there of 500 μm horizontally and 300 μm vertically. The incoming photon flux is measured by an ionization chamber serving as monitor to correct for variations of the flux.

The ID03 beamline is illuminated by three undulators resulting in a source size of 140 μm $\times 50$ μm (fwhm, H$\times$V). As shown in fig. 5.2 the set-up of the optical components is similar to the MPI-MF beamline [90]. It consists of a liquid nitrogen cooled, monolithic channel cut Si (111) crystal as monochromator which is optimized for a 5-24 keV energy range and does not allow any focalisation. Two Pd coated focusing mirrors are mounted after the monochromator. The first mirror is a cylindrical Si piece (sagittal radius of 3.2 cm) which is bendable for a controllable vertical focusing while the horizontal focusing is fixed (fig. 5.2, zoom 1). The second, flat mirror is necessary to put back the X-ray beam in a horizontal direction. The beam is focused on the sample position having a size there of 50 μm horizontally and 30 μm vertically.

5.1.3 The Diffractometer

The end-stations at the described beamlines are equipped with multicircle (2+3 or 6) surface x-ray diffractometers. This makes it possible to measure in a wide range of in-plane and out-of-plane momentum transfer as enough degrees of freedom are available for sample and detector movements [61]. As an example the diffractometer at the MPI-MF beamline is described in fig. 5.3.

For the SXRD and GID measurements the sample is mounted horizontally. Furthermore all shown XRD experiments are performed in the z-axis mode of the diffractometer. The

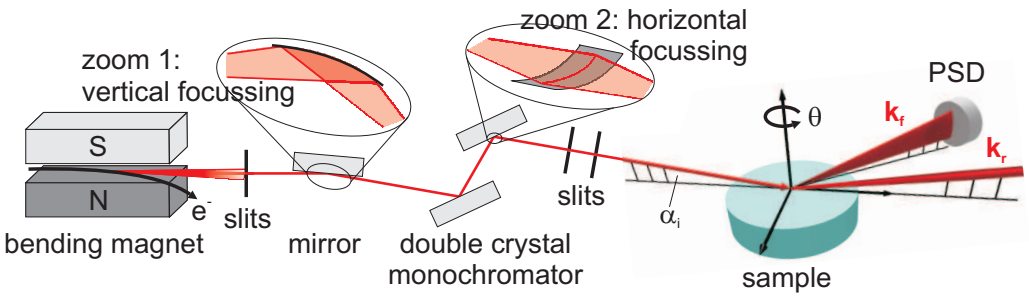

Figure 5.3: a) Photo of the 2+3 diffractometer at the MPI-MF beamline. b) Schematical drawing of the different circles for detector, sample and incident angle movements [89].

incident angle set by the μ-circle is fixed at a value close to the critical angle[1]. The χ- and ϕ-circles are fixed after the sample alignment as well. Within the z-axis mode the sample can only be rotated around its surface normal with the θ-circle, while the detector moves on the circles γ and δ. To find a Bragg peak for example, the detector has to be moved around δ and γ until the conditions for the corresponding momentum transfer are achieved. Then the sample is rotated around θ until the Bragg planes have the corresponding angle with respect to the incident beam. To transform between the real space of the detector- and sample-movements to the reciprocal space of the investigated samples a orientation matrix is defined by an alignment of at least two Bragg peaks. All motors are controlled by the SPEC-software [91].

To detect the x-rays different detectors are used during the various experiments. For the SXRD-measurements at the MPI-MF beamline and for two experiments at the ID03-beamline, namely the experiments on the Fe_3Al(1,1,0) and NiAl(6,7,1) surface, a scintillation point detector is used which is equipped with 2 pairs of slits in front of it to define its angular acceptance. The experiments on the NiAl(4,3,0) surface at the ID03-beamline are carried out with the 2D-detector MAXIPIX with a pixel size of 55×55 μm^2 and a count rate of 100000 photons per second and pixel. For the GID-measurements at the MPI-MF beamline a CCD-camera from MAR with a round, 165 mm wide x-ray sensitive surface, a pixel size of 80×80 μm^2 and a count rate of 65000 photons per second and pixel is utilized [92]. For the SXRD measurements at the SLS-MS beamline a all silicon, 2D PILATUS detector is used with a pixel size of 172×172 μm^2 and a maximum count rate per pixel of 10^6 cts/s [93].

5.1.4 The Experimental Chambers

To study the oxidation of the binary alloys *in situ* as well as to prepare a clean sample a portable oxidation chamber for x-ray diffraction as shown in fig. 5.4 is essential. The investigated binary alloy sample is mounted horizontally in the chamber which is then fixed

[1]This results in a optimal signal-to-noise-ratio as the scattering depth is restricted to the surface region and the transmissivity is enhanced

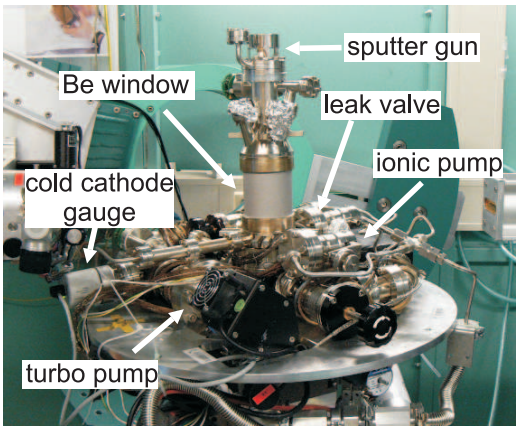

Figure 5.4: Photo of the portable UHV, *in situ* oxidation chamber used for the experiments. The sample is fixed on a heating station behind the Be window.

on the diffractometer at the beamline. With the shown chamber it is possible to apply temperatures ranging from room temperature up to 1700 K as the used heating station has the option of electron bombardment of the samples' backside. Thereby the temperature is either measured by a thermocouple attached to the side of the sample with a precision of ± 5 K or determined by a calibration curve with a precision of ± 20 K. Gas pressures up to 10^{-5} mbar can be applied while the base pressure after the bake out is around 3×10^{-10} mbar. The pressure is measured by a cold cathode ionization gauge. Furthermore, one of the used leak valves for gas dosing can be remote controlled allowing *in situ* measurements from the start of the reaction with oxygen or other gases.

The x-rays enter and leave the chamber through a 2 mm thick, freestanding beryllium window[2]. Thus no restrictions for in-plane scattering measurements exist due to the chambers construction. Out of plane scattered signal can be detected up to an angle γ of 54 °. Additionally, it is possible to connect a sputter gun to the top of the chamber, making a cleaning of the sample by sputter-anneal cycles possible.

5.2 High Resolution Core Level Spectroscopy Set-up

The HRCLS experiments are performed at beamline I311 of the synchrotron MAX II at MAX-Lab, Lund, Sweden. The storage ring is operated with an electron energy of 1.5 GeV, the photons for the end station of the beamline are produced by an undulator. The optical instruments to focus the photon beam and to select the needed energy are similar to the two set-ups described in the previous section. The white beam first hits a spherical mirror for horizontal pre-focusing. Then it is guided through a system of two mirrors with the monochromator in between. The system is moved in such a combined way that the

[2]Be is used due to its low density and its resulting low attenuation factor for x-rays.

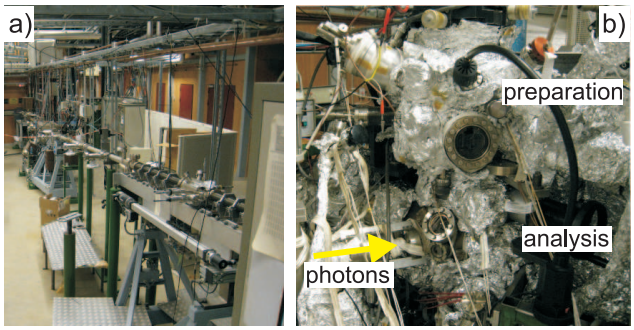

Figure 5.5: a) Beamline I311 at MAX-II b) Experimental end station with the two connected chambers.

focused beam spot is at a fixed position. It allows a high flexibility concerning the interplay between photon flux, resolving power and higher order suppression. The modified SX-700 monochromator with a plane grating of 1220 l/mm allows a photon energy range from 30 eV to 1500 eV with an resolution E/dE ranging from 5×10^3 to 2×10^4, respectively. The monochromator system is followed by a re-focusing system which consists of two spherical mirrors mounted in a Kirkpatrick-Baez arrangement [94]. A photo of the beamline is shown in fig. 5.5a.

The experimental end station can be used for high resolution XPS and XAS. As shown in fig. 5.5b it consists of individual but connected analyser and preparation chambers. The preparation chamber includes the standard equipment for preparation and characterization of surfaces like an ion sputtering gun, LEED optics and a mass spectrometer and is connected to a gas-inlet system . In the analysing chamber a hemispherical electron energy analyser (SCIENTA SES200) is used for photoelectron spectroscopy usually set-up for normal photoemission spectra measurements [95].

The analysis chamber has a base pressure of the order of 10^{-11} mbar and gas reactions can be studied *in situ* up to 10^{-5} mbar. For higher pressures the oxidation has to be conducted in the preparation chamber *ex situ*, with the HRCLS measurements performed afterwards. The sample itself is fixed between a tungsten wire which is simultaneously used as heating filament. Temperature is measured via a thermocouple at the back of the sample. Due to a very thin heating wire, necessary for fixing the samples, temperatures up to only 870 K and 1050 K could be achieved in the experiments on Fe_3Al and NiAl, respectively. The samples can also be cooled down to liquid nitrogen temperature to minimize contributions to the line width due to phonons. However, for the measurements on Fe_3Al cooling was not used as the quality of ordering within the iron-aluminide sample depends strongly on the cooling rate and low cooling rates are desired.

Chapter 6

The Material Systems

6.1 The Fe-Al System

The Fe-Al-System features some interesting intermetallic phases to be used as functional material in technological applications especially at the Fe-rich side. Alloying Fe with Al leads to a decrease of the density, as well as an enormous increase of the mixed crystal solidification, the elasticity modulus and the tensile strength. All these properties arise from an ordering of the system. The different disordered and ordered structures are shown in the phase diagram in fig. 6.1 [96].

The fundamental, A2-type lattice of the Fe-Al-system has a bcc structure like shown in fig. 6.1b. For low concentrations of Al up to about 20 atomic percent all sites in this bcc lattice are occupied randomly by either Al or Fe according to the corresponding composition of the system. By increasing the concentration of Al the system starts to order. Depending on the temperature and the composition the system can adopt two type of superstructures. Due to preferential site occupation a "new" lattice is formed within the fundamental one. In the B2-type structure shown in fig. 6.1b, Al preferentially sits on the β-site which is the centre atom of the bcc-unit cell. Perfect B2-type order like depicted in the figure is only possible for a 50/50-stoichiometry. The B2-type unit cell can be constructed by two single cubic lattice shifted along the [1,1,1]-direction. The second superstructure, the so called the $D0_3$-type phase, is demonstrated in fig. 6.1b for the ideally ordered case of Fe_3Al. To describe its lattice a larger unit cell is needed, made up of 8 bcc-unit cells. Additional to the B2-type order between α- and β-sites some of the centre atoms of the single bcc-unit cell are now preferentially occupied by Fe (γ-sites) and some by Al (β-sites). The $D0_3$-type of order describes an ordering between the centre atoms in the bcc unit cells(γ-and β-sites). Apart from the A2-,B2- and $D0_3$-type phases there are K-regions where only a short-range order exist. The shaded parts of the phase diagram mark regions of phase separation where A2- and $D0_3$- type ordering (light grey area) or A2- and B2- type ordering (dark grey area) coexist.

The lattice parameter a_0 of the bcc unit cell depends on the type of ordering as well as the composition of the Fe-Al system [97–99]. For the A2-type structure it increases with the Al content as well as for the $D0_3$ type structure but to a much smaller extent. The

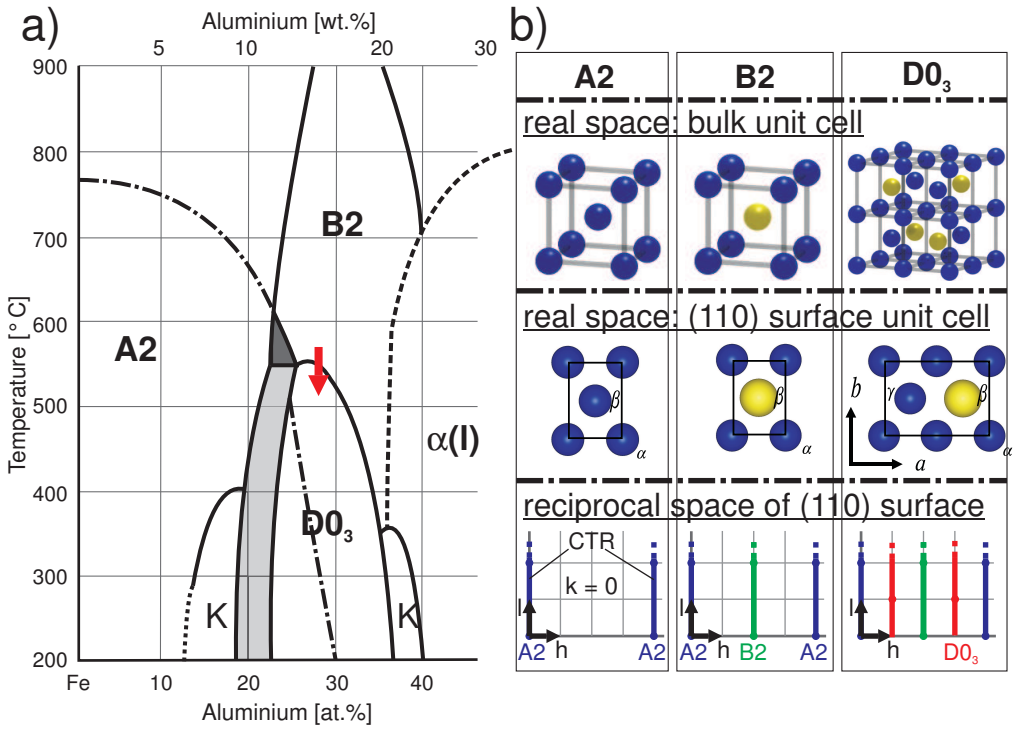

Figure 6.1: a) Phase diagram of the Fe-Al-system. b) Description of the A2-, B2- and $D0_3$-type phase. Shown are a bulk unit cell (top), a in-plane unit cell of the (1,1,0) surface with the different atomic sites (middle) and a corresponding h-l-map of the reciprocal space from a truncated crystal with a (1,1,0) surface(bottom).

lattice parameter of the B2-type phase decreases with higher Al content. For the stoichiometric Fe_3Al with a $D0_3$-type structure $a_0 = 2.896$ Å. Its density is 6.5 g/cm^3 at room temperature. Going from a B2- to a $D0_3$-type phase, e.g. by decreasing the temperature (red arrow in fig. 6.1a), leads to a considerable increase in the tensile strength, accompanied with a decrease in the elasticity modulus [1, 100].

Fig. 6.1b shows the three mentioned structures for perfect stoichiometry and perfect order, leading to a order parameter of 1[1]. Off-stoichiometry intrinsically reduces this order parameter but for a fixed composition order can only be changed if the two type of atoms change sites. For $D0_3$-type bulk-Fe_3Al, like investigated in this thesis, the energies for Al and Fe to change sites from β to γ and vice versa are almost zero. It costs 1.82 eV for Al to sit on an α-site. Vacancies on α-, $\beta-$ and γ-sites cost 1.25 eV, 1.39 eV and 2.27 eV, respectively [101, 102]. By increasing the temperature atoms get more mobile and have enough energy to change sites. Getting towards the $D0_3$-B2 or the B2-A2 phase transition leads to a decrease of the ordering and an increase of ordering fluctuations. Both mentioned phase transitions are continuous [98]. The Fe-Al-system has also a magnetic and

[1]The definition of the order parameter is in appendix A

an non-magnetic phase transition. The Currie temperature T_C is shown in the phase diagram (fig. 6.1a) by the dash-dotted line. $D0_3$-type Fe_3Al is magnetic at room temperature and has a T_C of 510 °C.

Due to the mentioned properties alloys based on Fe_3Al are candidates for light weight steel as their density is 20 % lower and their high-temperature strength is up to 60 % higher compared to stainless steel. Furthermore a thermally stable oxide layer is formed on the alloy surface leading to a high corrosion resistance under highly reactive oxidizing and sulfidising conditions [100, 103]. As the initial growth of this oxide layer is also investigated in this work, possible Fe- and Al-oxides are discussed briefly in the following section.

6.1.1 The Oxides of Fe and Al

In principle, it is possible to form iron-, aluminium- and mixed FeAl-oxides during the oxidation of an Fe-Al alloy. Fe- and Al-oxide are one of the most abundant oxides on earth and a whole zoo of different structures exists. In this section the most prominent ones are described.

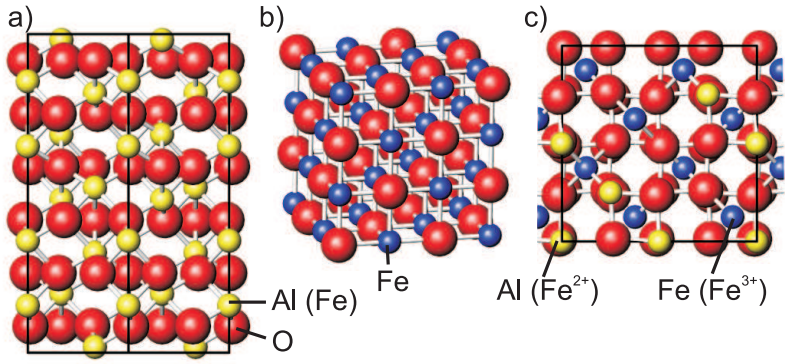

Figure 6.2: a) α-Al_2O_3 with its hexagonal unit cell: The view is perpendicular to the [11$\bar{2}$0]-[0001]-plane. Haematite has the same structure. b) 3D-view of the sodium-chloride structure of FeO. c) Side view along the [$\bar{1}$,0,0]-direction of the spinel-structure of $FeAl_2O_4$ or $Fe^{3+}Fe^{2+}_2O_4$ with its cubic unit cell.

Aluminium oxide phases

The most common Al oxide is Al_2O_3. It is used in ceramics, as grinding material or, due to its melting point of 2050 °C, as fire resistant material in ovens. For this use it is produced industrially out of aluminium hydroxides which are extracted from the ore bauxite. Many different phases of Al_2O_3 exist, like α-, γ-, δ- or κ-Al_2O_3 just to name a view [104, 105].

The thermodynamically most stable phase is α-Al_2O_3, also know as corundum. Its structure was already resolved by XRD-measurements in 1925 and is shown in fig. 6.2a

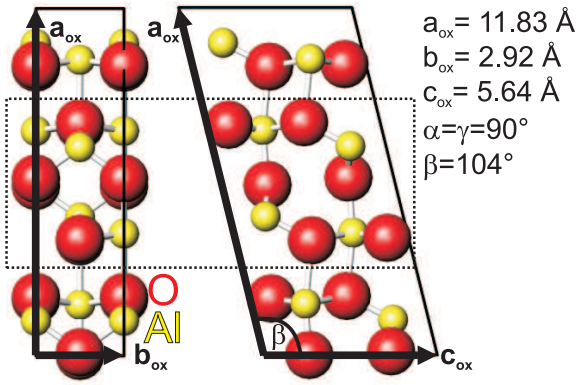

Figure 6.3: The structure of θ-Al_2O_3

[106]. The hexagonal unit cell with $a_0 = b_0 = 4.7589$ Å, $c_0 = 12.991$ Å, $\alpha = \beta = 90°$ and $\gamma = 120°$ contains 6 units Al_2O_3 and has a room temperature density of 4.00 g/cm^3 [107]. In the α-phase the oxygen ions sit on a hexagonal close packed lattice forming layers along the $[0, 0, 0, 1]$-direction. While the oxygen ions form a ABAB-hcp stacking sequence, the Al ions have a ABCABC stacking. The Al-ions occupy 2/3 of the octahedral and no tetrahedral sites, while the remaining octahedral vacancies are shifted laterally by one site going from one layer to the other.

All the metastable alumina structures have either a face-centred cubic or a hexagonal closed-packed oxygen sublattice, like γ-, δ-, η- and θ-Al_2O_3 or κ- and χ-Al_2O_3, respectively. The Al ions sit on octahedral and tetrahedral interstices sites [104, 105]. As an example, θ-Al_2O_3 is shown in fig. 6.3. Due to their high transition temperatures the metastable oxides received a lot interest from industry as a use as adsorbent, coatings and catalyst support. To shed light into the atomistic understanding of the formation process of alumina on alloys, the model system NiAl was intensively investigated for the low index (1,1,0) surface. Results of these studies are sketched in chapter 3 and in literature [40].

Iron oxide phases

There are three iron-oxides: Wuestite (FeO), Haematite (α-Fe_2O_3) and Magnetite (Fe_3O_4) as shown in the Fe-O phase diagram in fig.6.4. The latter two are abundant in the earth's crust. The stoichiometric compound FeO is not stable. Wuestite is formed for O/Fe ratios slightly greater than one with oxygen contents between 51.3 and 54.6 at.%. Below 570 °C Wuestite dissociates to a mixture of Fe_3O_4 and metallic iron. At 1371 °C a eutectic mixture[2] with iron is formed [109, 110]. Wuestite has a sodium chloride structure, like shown in fig. 6.2b, with a_0 between 4.282 and 4.301 Å and densities between 5.61 and 5.73 g/cm^3 for oxygen contents between 51.3 and 54.6 at.% [105, 111]. It is strongly ferro-magnetic.

[2] A eutectic mixture has such proportions that the melting point is as low as possible, and that all the constituents crystallize simultaneously at the eutectic temperature.

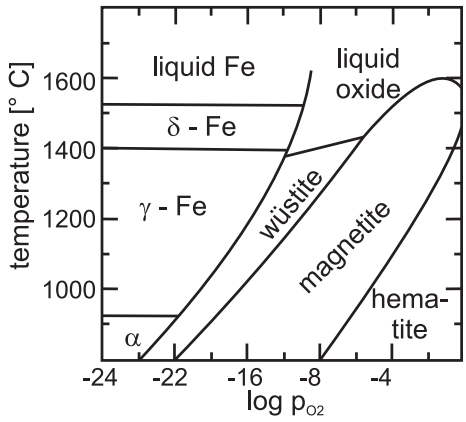

Figure 6.4: The Fe-O phase diagram as function of the oxygen partial pressure [108].

Magnetite (Fe_3O_4) is the most stable iron oxide and one of the strongest ferri-magnetic minerals with a Curie temperature of 580 °C. Due to this property and its appearance in the earth's crust, it conserves the earth's magnetic field. It is technologically used as magneto pigment in data storage devices. The oxygen content of magnetite can vary between 51.4 and 57.1 at.%. The melting point of Fe_3O_4 lies at 1596 °C and its room-temperature density is 5.20 g/cm^3. Like depicted in fig. 6.2c, it has a cubic unit cell with $a_0 = 8.394$ Å and a spinel like structure ($Fe^{3+}[Fe^{2+}Fe^{2+}]O_4$) where 1/3 of the Fe ions are coordinated tetrahedrally and 2/3 octahedrally [112].

Haematite (α-Fe_2O_3) has a corundum structure like α-Al_2O_3 (fig. 6.2a) with the following unit cell parameter: $a_0 = b_0 = 5.025$ Å, $c_0 = 13.735$ Å, $\alpha = \beta = 90°$, $\gamma = 120°$ [106]. Its density at 25 °C is 5.25 g/cm^3 for ideal stoichiometry while the oxygen concentration can lie between 57.1 and 59.8 at.%. α-Fe_2O_3 dissociates at 1457 °C. It is a weak ferro-magnet between -11 °C and 677 °C and an anti-ferro-magnet below -11 °C [105].

Fe-Al-oxide phases

In the Fe-Al system Al and Fe can form a common oxide like the ferrimagnetic $AlFeO_3$ [113] or $FeAl_2O_4$ (=$FeO{\cdot}Al_2O_3$) which has the mineral name hercynite. Like magnetite and haematite, hercynite is an ubiquitous mineral in the earth's mantle and crust. It is a spinel of AB_2O_4 type where A and B are divalent and trivalent cations, respectively. It has a cubic structure ($a_0 = 8.150$ at 25 °C [105]), where the oxygen ions occupy 32 general positions. Among the 64 tetrahedral and 32 octahedral interstices available in this arrangement, at low temperatures the divalent Fe cations occupy 8 tetrahedral sites while the trivalent Al cations occupy 16 octahedral sites. Its structure is shown in fig. 6.2c. However the deviation from stoichiometry in this compound is large. 16.3% of the Fe-sites are occupied by Al and 8.1 % of the Al-sites by Fe [114, 115]. It density is 4.265 g/cm^3.

At last, the Fe-Al-O phase diagram is briefly discussed due to its relevance for the oxidation of Fe_3Al in chapter 7. In a temperature range between 1280 °C and 1500 °C the phase equilibria of the Fe-Al-O system show some characteristic features as a function of the Fe-ion/Al-ion ratio ξ_{Fe} [114]. For a very low ratio ξ_{Fe} or oxygen pressures below 10^{-10} mbar only corundum (α-Al_2O_3) is present. Increasing ξ_{Fe} to values between roughly 0.05 and 0.35 leads to a coexistence between spinel ($FeAl_2O_4$ and Fe_3O_4) and corundum. For higher ξ_{Fe} it is strongly oxygen pressure dependent if spinel and iron ($10^{-9.5}$ - 10^{-8} mbar), spinel and Wuestite (10^{-8} - 10^{-6} mbar), just spinel (10^{-6} - 10^{1} mbar) or just haematite (10^{1} - 10^{3} mbar) exist. For high Fe-ion concentrations the spinel phase consists of mainly magnetite, for lower concentration of hercynite.

6.2 The Ni-Al System

The phase diagram of the Ni-Al-system is shown in fig. 6.5. Five stable intermetallic phases exist: Al_3Ni with a orthorhombic Cementite (CFe_3) structure, Al_3Ni_2 with its own trigonal structure, NiAl with the cubic CsCl structure, Al_3Ni_5 with a orthorhombic Ga_3Pt_5-structure and $AlNi_3$ with a cubic Cu_3Au-structure. The solid solutions of Ni and Al are both based on a fcc unit cell.

In this thesis NiAl-samples with a 50/50-stoichiometry are investigated which have the B2-type structure. This ordered structure, consisting of two interpenetrating single cubic lattices, was already described in section 6.1 and is depicted once more in the inset of fig. 6.5. In case of $Ni_{0.5}Al_{0.5}$ the B2-type phase is stable up to a high melting point of 1638 °C. Therefore NiAl possesses a high structural stability over a big temperature range. Compared to stainless steel NiAl has a larger thermal conductivity, a higher melting point, a lower density and a better oxidation resistance.

The B2-type NiAl structure has a density of 5.85 g/cm^3 and a bulk lattice parameter of $a_0 = 2.887$ Å at room temperature and ideal stoichiometry [116]. Perfect 100 percent ordering with Al only in the center, Ni only on the corners of the bcc unit cell and no vacancies can only be achieved for 50/50 composition and at T$= 0$ K. Increasing the amount of Ni in the composition leads to a replacement of the Al atoms by Ni atoms, i.e. Ni atoms sit on Al-sites (Ni anti-sites). As Ni atoms are smaller but heavier than Al, the lattice parameter decreases while the density of the alloy increases. Increasing the Al content does not create Al anti-sites but Ni vacancies in the Ni lattice which leads to an decrease of the lattice parameter and the density [98, 117–119]. DFT calculations of the bulk confirm these findings as Al anti-sites (E = -0.89 eV) and Al vacancies (E = 1.03 eV) are energetically unfavourable compared to Ni anti-sites (E = 1.94 eV) and Ni vacancies (E = 1.36 eV) [120].
Similar to the Fe-Al-system a stable oxide film forms on NiAl surfaces protecting the alloy underneath under highly reactive conditions. It consists of Al oxides which are introduced in section 6.1.1.

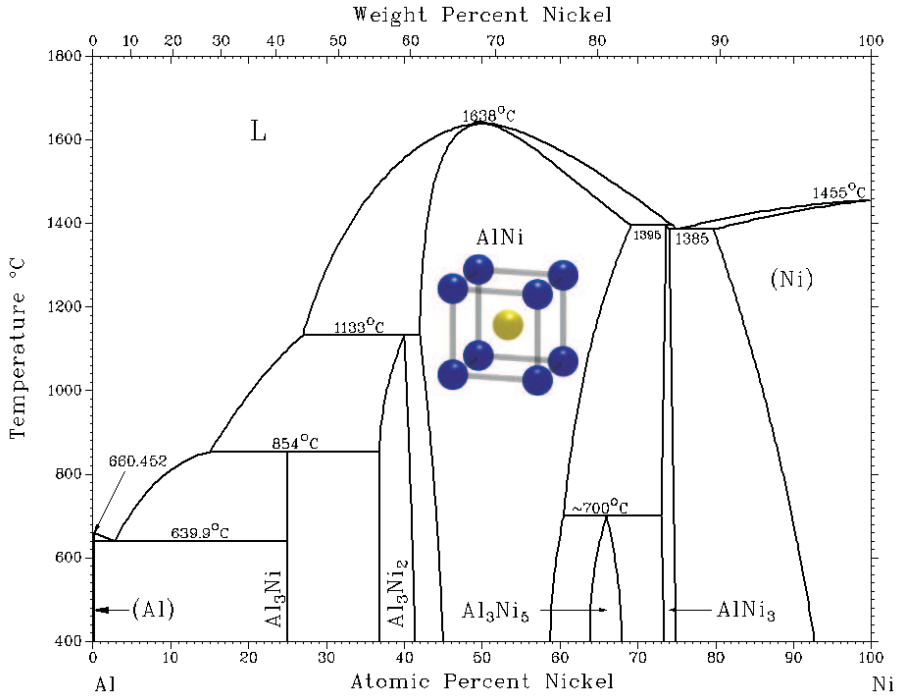

Figure 6.5: Phase diagram of the Ni-Al-system. The inset shows the B2-structure of NiAl (from [110]).

6.3 The Co-Ga System

The binary phase diagram of the Co-Ga system is shown in fig. 6.6. Two stable intermetallic compounds exist: β-CoGa and $CoGa_3$. The terminal phases of $\alpha-$cobalt, $\epsilon-$cobalt and $\alpha-$gallium are based on a fcc, hcp and orthorhombic unit cell, respectively.
The CoGa sample with 50-50-stoichiometry, investigated in this work, possesses the CsCl (B2-type) structure up to the melting point at 1483 K. At room temperature CoGa has a lattice constant of 2.878 Å. Its defect structure is very similar to the one of NiAl described in section 6.2. Vacancies on the Co sublattice and Co atoms on the Ga sublattice are the main point defects.
Similar to Al_2O_3, different Ga_2O_3 phases exist, based on a closed packed oxygen sublattice. α-Ga_2O_3 has a corundum structure with an hcp sublattice of O atoms. The Ga^{3+} ions occupy octahedral sites, only. δ-Ga_2O_3, γ-Ga_2O_3 and β-Ga_2O_3 have a fcc oxygen sublattice and Ga^{3+} ions sit on octahedral and tetrahedral sites. β-Ga_2O_3 is the only thermodynamically stable gallium oxide phase. Its structure is isomorph with θ-Al_2O_3, as shown in fig. 6.3.

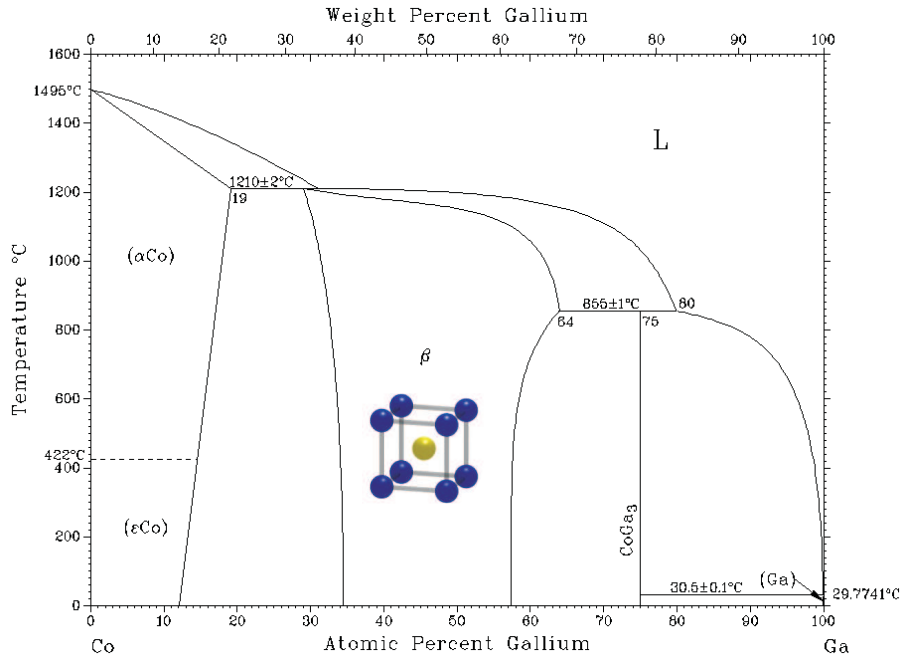

Figure 6.6: Phase diagram of the Co-Ga system (from [110]).

Chapter 7

The Oxidation of $Fe_3Al(110)$

Iron-aluminides are promising materials as future light-weight replacements of steel, because of their potentially favourable density-strength ratio, their use in deep draw processes, and their high-temperature stability [1]. Their stability arises from the ordering of the constituents, like shown in chapter 6.1. In order to be used in high-temperature applications it is necessary that a protective oxide scale is formed on the surfaces of these materials to prevent them from further corrosion. Unlike in other binary alloys, both elements in the iron-aluminides have a high affinity for oxygen, which further complicates the understanding of the oxidation process as a function of the thermodynamic parameters. It is a challenge to contemporary surface science to understand and control on a microscopic scale such an oxidation process.

It may be expected that the formation of the oxide layer has a large effect on the surface segregation of the constituents and the ordering of the system. The experimental work in this chapter is intended to obtain a better understanding of the segregation and subsequent ordering processes in the subsurface region of Fe_3Al under oxidizing conditions. Application-oriented properties of the oxide film, like chemical composition, thickness or homogeneity, are also investigated for different growth conditions. To tackle this difficult problem we use the method of SXRD in combination with x-ray reflectivity, AES and HRCLS. As the former technique is ideally suited to follow the order in the (sub)surface region, the latter allow to determine the thickness and chemical composition of the oxide layers. Oxygen pressures range from 10^{-8} to 10^{-5} mbar, the oxidation temperature reaches from 300 K up to 720 K.

The results for the clean surface demonstrate that the topmost atomic layer exhibits in-plane B2 order, with a $D0_3$ bulk beneath it. Upon oxidation at 10^{-6} mbar of molecular oxygen at temperatures between 400 K and 720 K, long-range superlattice order disappears in an extended subsurface region, without affecting the surface roughness nor the crystallinity. At the same time, a smooth 8 Å thin oxide layer is formed on the surface. These results can be understood by preferential Al surface segregation in combination with a high affinity of Al for oxygen. The chemical composition of the oxide film is shown to depend strongly on the amount of Al present at the surface during the oxidation process. For low Al segregation rates (low temperatures) or high oxidation rates (high O_2 pres-

sures), Fe and Al are oxidized. Pure Al oxide layers are found when fast Al segregation is possible or the oxidation rates are small.

In section 7.1 the experimental set-up, the system of $Fe_3Al(1,1,0)$ and the sample preparation are described. The results of the clean and the oxidized system are presented in section 7.2 and are discussed in section 7.3. Conclusions are drawn in section 7.4.

7.1 Experimental Details and Sample Preparation

Dependent on the temperature, Fe_3Al has a A2-type, B2-type or $D0_3$-type structure. These structures are presented in the Fe-Al phase diagram in section 6.1. The Fe_3Al (1,1,0) surface was chosen with regard to the SXRD experiments. It distinguishes between CTRs probing the order of the underlying A2-type fundamental bcc lattice and the B2-type and the $D0_3$-type decoration of atoms over the bcc lattice points. This is described in detail in section 4.1.1.

The two single-crystals used in the experiments have a nominal composition of 72 at.-% Fe and 28 at.-% Al and are shown in fig. 7.1. According to the Fe-Al phase diagram of fig. 6.1, the samples exhibit a $D0_3$-type ordered structure at room temperature. The slightly higher Al concentration away from the ideal 3:1 stoichiometry was chosen in order to stay away from the A2-B2 phase separation area. The samples were grown from the melt at the Max Planck Institute for Metals Research (MPI-MF) in Stuttgart. They are cut out of a $Fe_{.72}Al_{.28}$-Rod perpendicular to the $[1,1,0]$-direction which has been determined by Laue x-ray diffraction. After a refined x-ray alignment with an 0.1 $^\circ$ accuracy, the samples are lapped with Al_2O_3 and diamond suspensions, starting with a grain size of 20 μm, then successively going down to 0.05 μm. High energy x-ray diffraction of the final plate-like samples showed excellent crystallinity in the bulk, with typical Bragg reflection rocking curve widths better than 0.01 degrees.

In situ SXRD experiments are carried out in the portable UHV oxidation chamber, described in section 5.1.4. Sample 1 was measured at beamline ID03 of the ESRF, sample 2 was measured at the MPI-MF beamline at the ANKA (see section 5.1.2). A monochromatic x-ray beam ($\Delta E/E \simeq 10^{-4}$) with a photon energy E of 12 keV was used at beamline ID03 and with a photon energy E of 10 keV at the MPI-MF beamline.

The HRCLS experiments were performed at the beamline I311 at Max Laboratory,

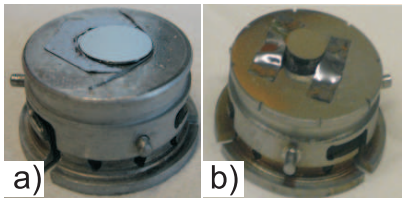

Figure 7.1: The two $Fe_{.72}Al_{.28}$ (110) samples, labelled sample 1 (a) and 2 (b) in the following, are spot welded on Molybdenum sample holders with Tantalum foils.

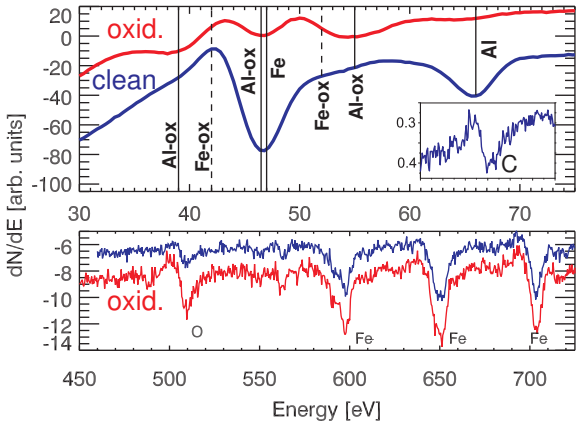

Figure 7.2: AES spectra of the $Fe_3Al(110)$ surface. The top graph shows the low energy part of the clean (blue) and oxidized (red) surface; the curves are displaced for clarity. The vertical lines indicate the following elements: metallic Al (66 eV), metallic Fe (47 eV), oxidized Al (39, 46.5 and 55 eV) and oxidized Fe (42 and 52 eV). The inset shows the small amount of carbon present on the clean surface, probably resulting from CO adsorption. The bottom part shows the spectra in the energy range where the oxygen (510 eV) and Fe (598, 651 and 703 eV) signals are visible.

described in section 5.2. The photoemission measurements were performed at room temperature, at a fixed incident angle of about $55°$ and at normal emission. For all measured spectra a scan of the Fermi level region was recorded immediately afterwards and used as binding energy reference.

For quantitative measurements a chemically clean and well-defined crystal surface is essential. Clean and well-ordered surfaces were obtained by repeated cycles of annealing and sputtering with Ar^+ ions (argon pressure $p_{Ar} = 6 \times 10^{-6}$ mbar, energy E=1.5 keV, sputter current density 10 μAcm^{-2}). After a final high-temperature anneal step at 1173 K, special care was taken to not cool the samples too quickly through the B2-$D0_3$ phase transition at 800 K. This would cause many $D0_3$ anti-phase domains and therefore broadened superstructure CTRs, resulting in poor signal-to-noise ratios [121]. AES was used to check for surface contaminations. In fig. 7.2 the spectra of the prepared surface clearly show the signal of metallic Fe and Al. However, even after many cycles of prolonged sputtering and annealing (up to two hours and 1500 K per cycle), still a small oxygen signal remains present. Although some remains of oxide patches cannot be excluded, most likely the remaining oxygen signal is due to the adsorption of CO, which at the UHV base pressure of approximately 5×10^{-10} mbar is still present in small amounts. This also correlates with a tiny carbon signal in the AES spectrum that is present after cleaning the surface. It is known that CO adsorbs molecularly at room temperature on $Fe_{0.6}Al_{0.4}$(1,1,0) at exposures below 1 L [122]. Nevertheless, all the results presented here are not very sensitive to such a minor contamination, in particular since the coverage is expected to be very small. During all the XRD experiments oxide films formed under controlled conditions could be

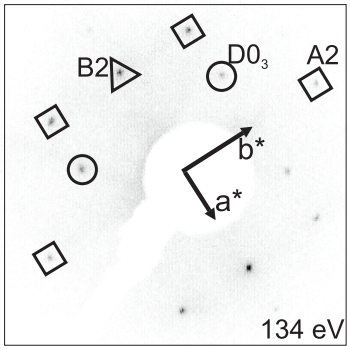

Figure 7.3: LEED-image of the clean $Fe_{.72}Al_{.28}$(1,1,0) surface of sample 1: reflexions arising from A2-type, B2-type and $D0_3$-type lattices are marked by open squares,triangles and circles, respectively. The arrows indicate the inplane (1,1,0) unit cell.

removed by annealing the sample up to 1270 K for 600 s. Due to the experimental set-up at the HRCLS measurements it is not possible to achieve temperatures higher then 873 K. By prolonged sputtering not all the alumina could be removed as seen in the Al2p spectra of the clean sample in fig. 7.10. Nevertheless, a LEED image of a well ordered clean surface, like described in section 7.2.1, is observed. Accordingly, only a tiny amount of oxide patches is still present on the prepared surface.

7.2 Results

7.2.1 The clean $Fe_3Al(1,1,0)$ surface

After the cleaning procedure a LEED image of the surface has been recorded and is depicted in fig. 7.3. Diffraction spots arising from the fundamental lattice as well as the ordered B2-type and the $D0_3$-type superlattices are observed. This shows that the surface region is crystalline and chemically well ordered with no larger oxide patches present.

A typical x-ray reflectivity curve of the clean sample is shown in fig. 7.4. It exhibits a Fresnel-like shape which indicates that there is a near-perfect vacuum-crystal interface. The results of fitting a density profile to the reflectivity data render a smooth Fe_3Al surface.

The crystallographic SXRD data, obtained by taking rocking scans at each point along the CTRs, were integrated and corrected in a standard way [61]. The program ROD was used to fit different structure models to the experimental structure factors, which are shown in fig. 7.5 [123]. The scattering from the bulk is calculated by using equations 4.13 and 4.15 with $\epsilon = 0.12$, which follows from the Al-enriched nominal composition $Fe_{3-\epsilon}Al_{1+\epsilon}$. The Debye-Waller parameters of all atoms are kept at bulk values, with $B_{Fe} = 0.345$ Å^2,and $B_{Al} = 0.45$ Å^2 [124]. When comparing the experimental data with the CTRs calculated for a bulk terminated crystal, the (1,1), (1,2) and (0,2) rods are fairly well re-

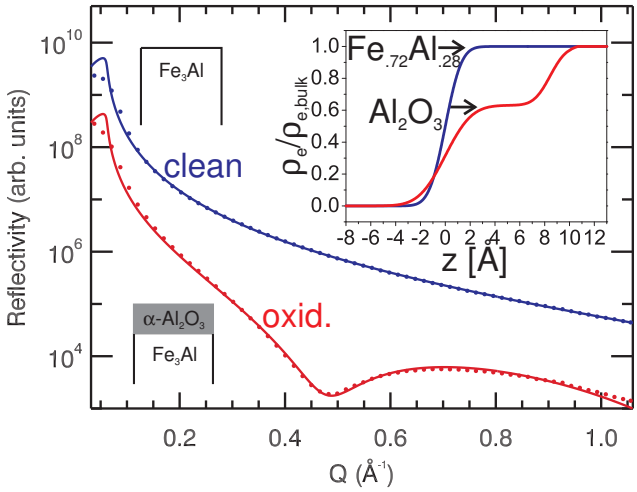

Figure 7.4: X-ray reflectivity curves obtained from the clean surface(blue) and after oxidation at 650 K and 6×10^{-6} mbar O_2 for 30 min (red). The curves are displaced for clarity. The experimental data (points) and fits (solid lines) using the Parratt formalism [76] are shown, the results of which are given in table 7.1. The inset shows the resulting electron density (ρ_e) profiles for the clean (blue) and oxidized (red) surfaces as a function of the z-direction along the surface normal. The sketches of the samples indicate the applied fitting models.

produced. However, the (2,0) rod is much higher in intensity than the simulation for bulk termination. This rules out that roughness alone can explain the observed rod profiles, since surface roughness would lower all rods in between the Bragg peaks. Qualitatively, from the differences between the bulk termination simulation and the experimental data one can directly conclude that the surface orders in a different symmetry compared to the underlying bulk. Since the (2,0) rod probes the B2-type order in the surface region, the β and γ sites in the surface are crystallographically equivalent (see fig. 6.1). This leads to additional scattering from this layer contributing to the (2,0) rod, without affecting the (1,1) and (1,2) rods.

Having identified that the largest discrepancy between bulk termination and a B2-like overlayer appears on the (2,0) rod, one sees that there is a lot of extra intensity between the Bragg peaks along the (2,0) rod. The parameters that are responsible for this feature are the rumpling of the atoms in the topmost layer and their occupancies. Fitting these, together with structural relaxations and minor disorder in the second and third layer leads to the best fit results presented in table 7.2 and schematically depicted in fig. 7.6.

In the refinement procedure for sample 2 fewer parameters are used, because the total data set is smaller than for sample 1 as the photon flux at ANKA was too small to measure the weak signal of the $D0_3$-type CTRs. Nevertheless, the results for both samples 1 and 2 agree very well. This is because the relaxations in deeper layers, which exhibit $D0_3$ symmetry, are negligibly small. The most important features in the data arise from the

topmost layer, which shows in-plane B2-type order.

T_{ox}	t_{ox}	parameter	clean	oxidized	oxid. & annealed
300 K	60 min	σ_{Fe_3Al} (Å)	1.1(8)	1.0(5)	1.0(5)
		σ_{ox} (Å)	-	1.5(6)	-
		d_{ox} (Å)	-	5.1(4)	-
		$\rho_{e,ox}/\rho_{e,Al_2O_3}$	-	0.5	1.0
		$\sigma_{Al_2O_3}$ (Å)	-	2.3(6)	2.7(6)
		$d_{Al_2O_3}$ (Å)	-	12.2(4)	17.3(4)
300 K	90 min	σ_{Fe_3Al} (Å)	1.1(8)	-	2.1(7)
		$\sigma_{Al_2O_3}$ (Å)	-	-	2.9(6)
		$d_{Al_2O_3}$ (Å)	-	-	15.5(6)
650 K	30 min	σ_{Fe_3Al} (Å)	1.0(8)	1.0(5)	-
		$\sigma_{Al_2O_3}$ (Å)	-	1.7(6)	-
		$d_{Al_2O_3}$ (Å)	-	8.4(3)	-
650 K	60 min	σ_{Fe_3Al} (Å)	1.0(8)	1.4(5)	-
		$\sigma_{Al_2O_3}$ (Å)	-	1.7(6)	-
		$d_{Al_2O_3}$ (Å)	-	8.6(3)	-
730 K	35 min	σ_{Fe_3Al} (Å)	1.4(8)	1.0(6)	-
		$\sigma_{Al_2O_3}$ (Å)	-	4.2(8)	-
		$d_{Al_2O_3}$ (Å)	-	8.8(4)	-
790 K	35 min	σ_{Fe_3Al} (Å)	1.0(7)	1.0(7)	-
		$\sigma_{Al_2O_3}$ (Å)	-	4.8(9)	-
		$d_{Al_2O_3}$ (Å)	-	9.0(3)	-

Table 7.1: Results of the x-ray reflectivity measurements of the clean, the oxidized and the annealed surfaces. The oxidation temperature T_{ox} and the oxidation time t_{ox} are given in the table, the oxidation pressure is 10^{-6} mbar of oxygen in all cases. The root-mean-square roughness (σ) for the interfaces as well as the the oxide thickness (d) are shown.

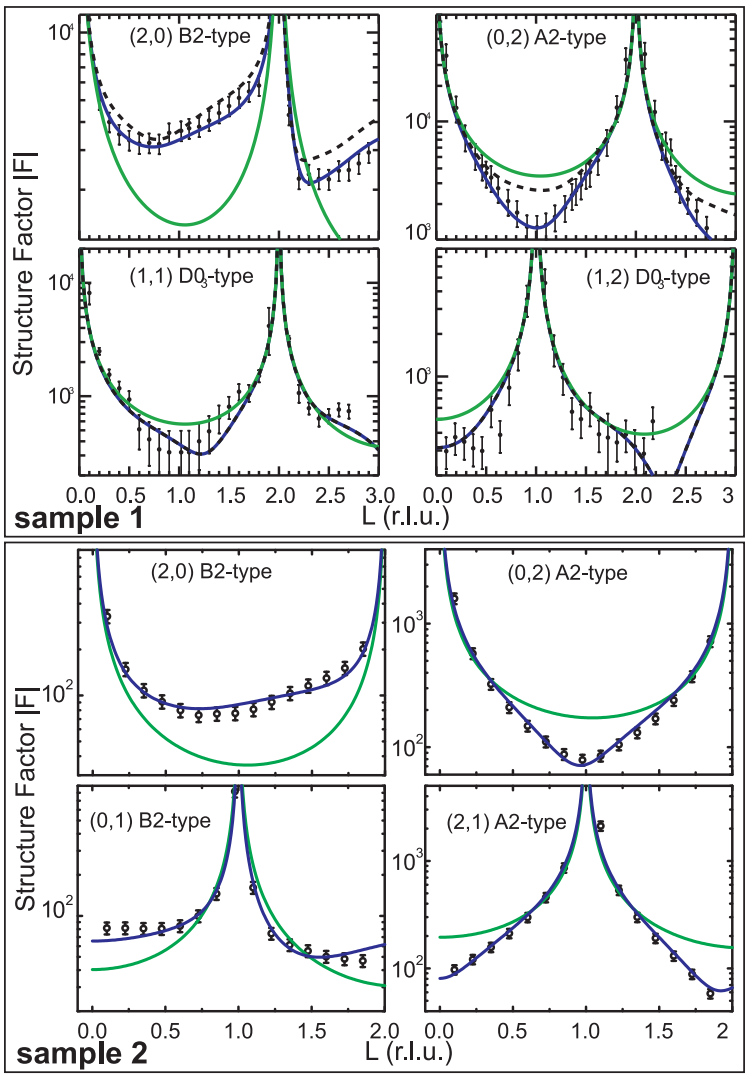

Figure 7.5: CTR data (points) of the clean surface and the results of different structural models (lines) for the two investigated samples. The best fit (blue solid line) and a bulk terminated model (green solid line) are shown together with a calculation for a structure as in the best fit, only without vacancies (black dashed line, only sample 1). For the $D0_3$-type CTRs the best fit model with and without vacancies give the same curve. This is because most of the vacancies appear in the topmost layer, which has a B2-inplane symmetry thereby not contributing to the $D0_3$-type CTRs.

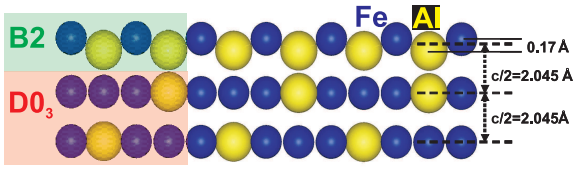

Figure 7.6: Schematic side view of the best fit result which consists of a B2-type top-layer on a $D0_3$ bulk crystal.

	sample 1		sample 2	
Atom	θ_1 (-)	Δz_1 (-)	θ_2 (-)	Δz_2 (-)
$Fe1^{\alpha}$	0.79(3)	0.025(3)	0.81(2)	0.010(5)
$\square 1^{\alpha}$	0.21(3)	-	0.19(2)	-
$Al1^{\beta,\gamma}$	0.65(4)	-0.017(6)	0.77(3)	-0.02(1)
$\square 1^{\beta,\gamma}$	0.35(4)	-	0.23(3)	-
$Fe2^{\alpha}$	0.96(2)	0.003(2)	1.00(1)	-0.004(3)
$\square 2^{\alpha}$	0.04(2)	-	0.00	-
$Al2^{\beta}$	1.00	0.011(5)	1.00	-0.010(5)
$Fe2^{\gamma}$	0.71(2)	0.003(3)	0.88	0.00
$Al2^{\gamma}$	0.30	0.003(3)	0.12	0.00
$Fe3^{\alpha}$	1.00	0.00	1.00	0.00
$Al3^{\beta}$	1.00	-0.006(3)	1.00	0.00
$Fe3^{\gamma}$	0.88	0.002(2)	0.88	0.00
$Al3^{\gamma}$	0.12	0.002(2)	0.12	0.00

Table 7.2: Results of the structural refinement procedures listing displacements Δz_p and occupancies θ_p with $p = 1, 2$ for samples 1 and 2. The best fits of the CTRs are shown in fig. 7.5. The atoms are labelled as Elno.^{j}, where the element El = Fe,Al (or vacancy $\square$), then the number (no.) of the layer, where 1 is the surface and $j = \alpha, \beta, \gamma$ indicates the particular lattice site.

7.2.2 The oxidized Fe_3Al (1,1,0) surface

Oxidation studies of the (1,1,0) surface at temperatures between 300 K and 790 K and O_2 pressures from 10^{-8} mbar up to 10^{-6} mbar are performed. In a first step the thickness of the oxide layer and its chemical composition are investigated for the different growth conditions. Then the ordering of the alloy at the oxide-alloy interface is illuminated on an atomic scale.

The thickness of the oxide films

Specular x-ray reflectivity curves are recorded before and after the oxidation of the $Fe_{.72}Al_{.28}$ (1,1,0) surface and after a 1240 K annealing procedure of the sample. The Parratt formalism described in section 4.1.2 is used to analyse the measured curves and to determine oxygen induced changes in the electron density profile along the surface normal. Fig. 7.7 shows the reflectivity curves obtained of sample 2 before and after oxidation at room temperature with 3×10^{-6} mbar of O_2 and after annealing the oxidized sample in UHV. Fig. 7.8 depicts the curves obtained after oxidation at the higher temperatures of 650 K, 730 K and 790 K and with 3×10^{-6} mbar of O_2. Except for the Fresnel-like curve of the clean crystal all curves show well-defined modulations. They result from the presence of an oxide layer while the layer thickness can be calculated from the position of the minima. The layer models used for the best fits are schematically shown in the figures, together with the resulting electron profiles. The fit results are listed in table 7.1. Thereby a strong temperature-dependence of the oxide layer thickness is observed, which is pointed out by the temperature-thickness diagram in fig. 7.9. At room temperature the oxide thickness of approximately 16 Å is twice as thick compared to the 8 Å thick layer grown at oxidation temperatures between 650 K and 790 K. Furthermore, all curves recorded after oxidation at elevated temperatures or after 1240 K annealing can be fitted well, assuming a single α-Al_2O_3 layer on the alloy substrate[1]. For all curves recorded after 300 K oxidation an additional oxide layer of unknown electron density is needed for a good fit result. This indicates a changed chemical composition or density inhomogeneities of the oxide films grown at room temperature. The formation of pure alumina layers is indicated for elevated oxidation temperatures or after the sample annealing. The chemical composition will be investigated in detail in the next section.

For oxidation temperatures of 300 K and 650 K reflectivity curves are measured for two different oxidation times, respectively (see fig. 7.7 and 7.8). Comparing the curves of different oxidation times shows only minor changes in the oxide film thickness for prolonged oxidation. This indicates that a critical maximum oxide thickness is reached at 300 K and 650 K and 10^{-6} mbar of oxygen. At the oxidation temperatures of 730 K and 790 K an increase of the roughness of the vacuum-oxide interface is observed. Higher oxidation temperatures render the oxide film less smooth than temperatures around 650 K.

[1]Note, that the spinel $FeAl_2O_4$ has nearly the same electron density as α-Al_2O and cannot be distinguished by reflectivity measurements.

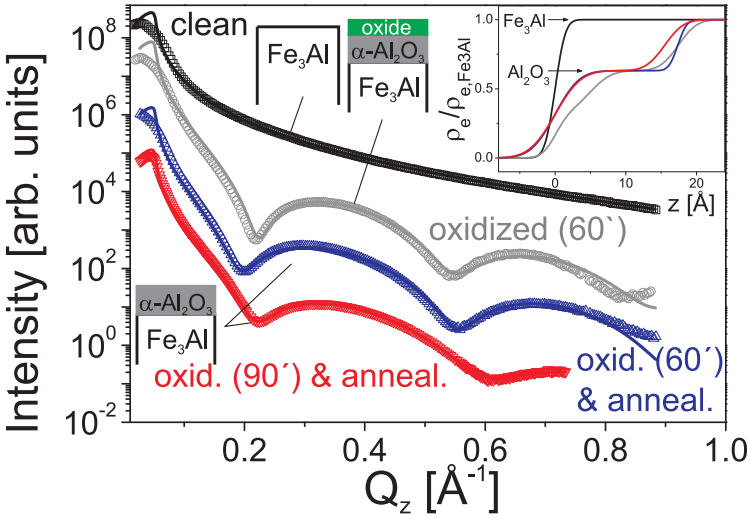

Figure 7.7: X-ray reflectivity curves obtained from the clean surface(black), after oxidation at 300 K and 3×10^{-6} mbar O_2 for 60 min (grey) and after annealing the oxidized surface to 1240 K (blue and red) to order the oxide. The curves are displaced for clarity. Shown are the experimental data (points) and fits (solid lines), using the Parratt formalism [76]. The fit results are given in table 7.1. The sketches of the samples indicate the applied fitting models. The inset shows the resulting electron density (ρ_e) profiles as a function of the z-direction along the surface normal.

The chemical composition of the oxide layer

The chemical composition of the oxide films is monitored with HRCLS measurements. This technique is very sensitive to the coordination number of the atoms and to their chemical environment. It can detect already tiny amounts of oxide on the surface. To follow the likely oxidation of Fe and Al at the surface the spectra of the Al2p, Fe2p and O1s photo electrons are recorded. At the three temperatures of 300 K, 470 K and 650 K the clean Fe_3Al (1,1,0) surface of sample 2 is oxidized with two oxidation pressures of 1×10^{-6} mbar and 1×10^{-8} mbar O_2[2]. Spectra are recorded of the clean and the oxidized surface. Another series of spectra is measured after annealing the sample to 770 K for 5 min, except for the 650 K oxidation experiment. Fig. 7.10, 7.11 and 7.12 show the spectra measured of the oxidation cycles at 300 K, 470 K and 650 K,respectively.

All Al2p spectra, recorded of the clean Fe_3Al surface, show the spin-orbit split doublet of Al2p$\frac{3}{2}$ and Al2p$\frac{1}{2}$ photo electrons at binding energies E_{BE} of 72.0 eV and 72.4 eV, respectively. The splittings are known from metallic Al or polycrystalline Fe_3Al [37, 125]. A very small signal at E_{BE} ≈75 eV is assigned to Al atoms bound to oxygen which is consistent with the small signal observed in the O1s spectra of the prepared surface. All

[2]The oxidation times are different for all recorded spectra, which does not restrict the conclusion in this section. Oxidation times at 10^{-8} mbar O_2: 17 min at 300 K, 55 min at 470 K, 41 min at 650 K; Oxidation times at 10^{-6} mbar O_2: 60 min at 300 K, 30 min at 470 K, 35 min at 650 K;

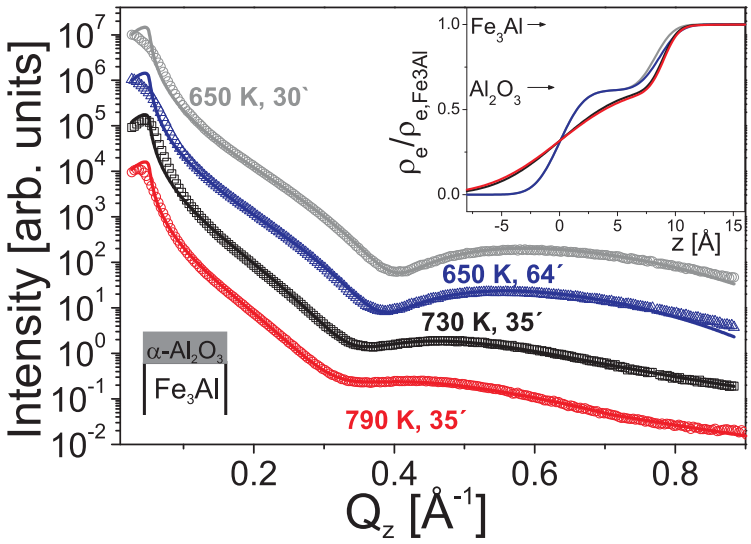

Figure 7.8: X-ray reflectivity curves obtained after oxidation at 650 K, 730 K and 790 K with 10^{-6} mbar O_2 and the indicated oxidation times. The curves are displaced for clarity. Shown are the experimental data (points) and fits (solid lines) using the Parratt formalism [76]. The fit results are given in table 7.1. The sketch of the sample indicates the applied fitting model. The inset shows the resulting electron density (ρ_e) profiles.

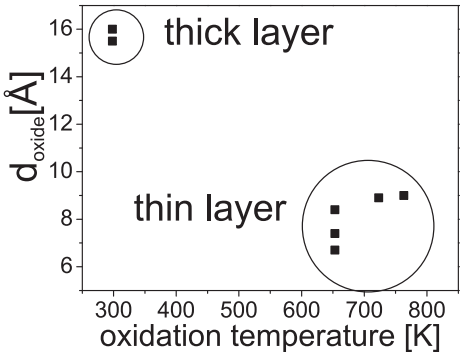

Figure 7.9: Dependence of the oxide layer thickness on the oxidation temperature: at room temperature the film is thicker than at elevated oxidation temperatures.

Fe2p spectra of the clean sample show the spin-orbit split doublet of Fe2p$\frac{3}{2}$ and Fe2p$\frac{1}{2}$ photo electrons at binding energies of 707 eV and 720 eV, respectively [37]. No signal of oxidized Fe is observed. Consequently, large parts of the surface are chemically clean, while tiny parts are covered with Al oxide patches and chemisorbed CO like described in section 7.1. A LEED image recorded after the sample preparation shows the same characteristics like the image shown in fig. 7.3. This further shows that the sample surface can be regarded as clean.

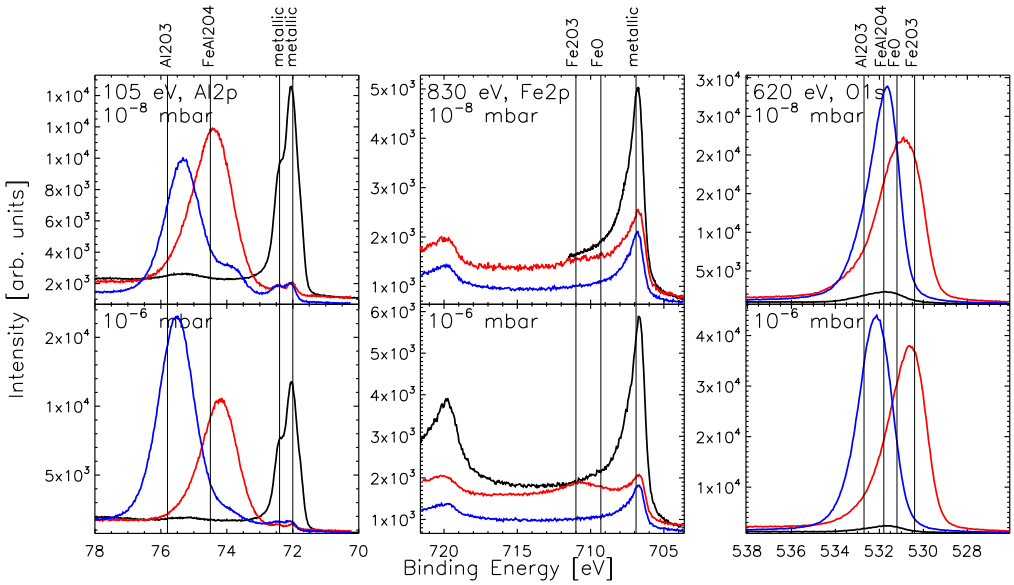

Figure 7.10: Photoemission spectra of the Al2p (left), the Fe2p (middle) and the O1s (right) electrons, recorded at the indicated incoming photon energies and normal emission. Oxidations are performed at 300 K and 10^{-8} mbar (top row) or 10^{-6} mbar (bottom row) of O_2. The spectra of the clean, oxidized and oxidized and annealed (770 K for 5 min) sample are depicted by black, red and blue lines, respectively. The binding energies of the photo electrons in Fe_3Al (metallic), Al_2O_3, $FeAl_2O_4$, FeO and Fe_2O_3 are marked by vertical lines, according to literature values [37].

Oxidized Al can be detected in the Al2p spectra by an arising signal in the binding energy range between 74.5 and 75.5 eV. Oxidised Fe is observed in the Fe2p spectra by a signal around $E_{BE} \approx 711$ eV. Analysing the spectra after oxidation (red lines in fig. 7.10, 7.11 and 7.12) shows that the oxide composition depends on the oxidation pressure and temperature. This is summarized in the pressure-temperature diagram in fig. 7.13. For an oxygen pressure of 1×10^{-6} mbar both alloy constituents, Al and Fe, become oxidized for all investigated temperatures. For the low oxygen pressure of 1×10^{-8} mbar Fe oxide formation is only observed at room temperatures while for higher oxidation temperatures pure Al oxide is formed. The area of Fe oxide signal is proportional to amount of formed oxide. At room temperature and 1×10^{-8} mbar O_2 less oxide is formed than at 1×10^{-6} mbar. This indicates that the oxidation pressure has a stronger influence on the Fe oxide formation than the oxidation temperature. At oxygen pressures of 1×10^{-6} mbar the most amount of oxidized Fe is found at 300 K and 470 K while it decreases strongly for the oxidation temperature of 650 K.

After a 770 K annealing in UHV the peak position of the component, assigned to oxidized Al, clearly shifts from $E_{BE} = 74.5$ to 75.5 eV in the Al2p spectra, recorded after 300 K and 450 K oxidation (see fig. 7.10 and 7.11). Similar shifts from $E_{BE} \approx 531$ to 532

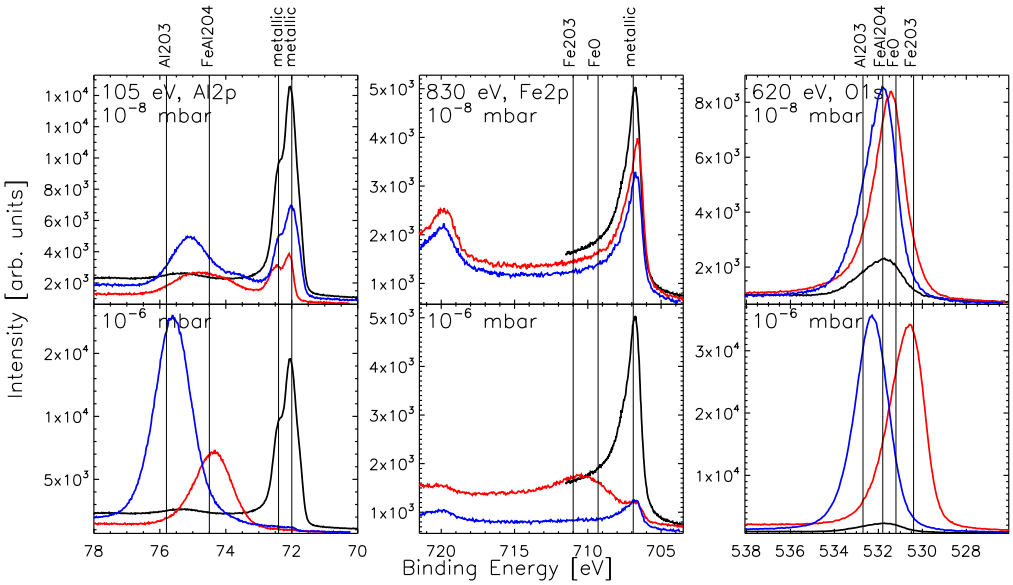

Figure 7.11: Photoemission spectra like described in the caption of fig. 7.10 but the experiments are carried out at an oxidation temperature of 470 K for both oxygen pressures.

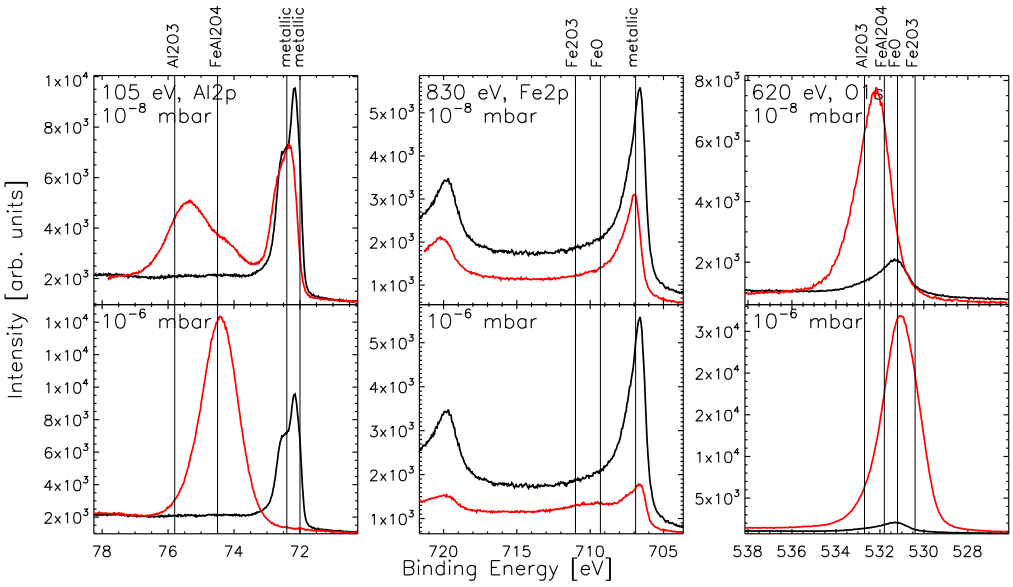

Figure 7.12: Photoemission spectra like described in the caption of fig. 7.10 but the experiments are carried out at an oxidation temperature of 650 K for both oxygen pressures.

eV are observed for the signal in the O1s spectra. Shifts towards higher binding energies indicate a higher number of Al-O bonds which corresponds to a better short-range order.

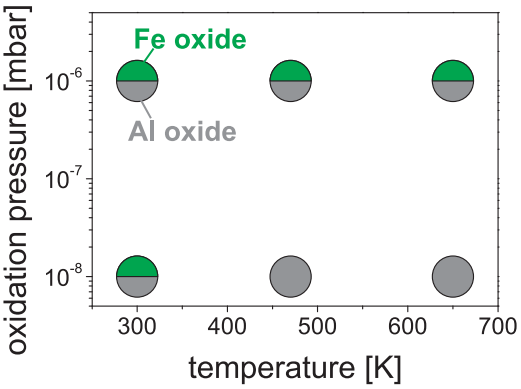

Figure 7.13: The diagram shows the oxide composition dependent on the oxidation pressure and the oxidation temperature. Green and grey (half-)circles mark the formation of Fe- and Al-oxide, respectively

In the Fe2p spectra no signal of Fe oxide is observed any more after the annealing. Thus, annealing leads to a pure alumina layer with less defects and a better ordering. In case of the oxidation cycle at 650 K (fig. 7.12) where no additional annealing has been performed a pure, ordered alumina layer is found only at 1×10^{-8} mbar O_2. The corresponding signals in the Al2p and O1s spectra are found at the same position like after annealing the sample oxidized at lower temperatures. At 1×10^{-6} mbar O_2 and 650 K also oxidized Fe is detected at the surface which seems to block the ordering of Al oxide and to enlarge the number of defects.

For further details on the Fe oxide formation during the oxidation process, the clean sample is first oxidized at 650 K and 1×10^{-8} mbar. As shown in fig. 7.12, a pure ordered alumina film and no Fe oxide is formed under these conditions. Now, after this first low pressure oxidation the pressure is increased to 1×10^{-6} mbar at the same temperature. The Fe2p spectra is measured before and after the increase like depicted in fig. 7.14. Unlike the direct oxidation with 1×10^{-6} mbar O_2 at 650 K (see fig. 7.12) no Fe oxide formation is observed after the stepwise pressure increase. The initial alumina layer formation blocks the formation of Fe oxide. Consequently, the oxidized Fe has to be formed during the initial oxidation process while in the prolonged oxidation Al is preferentially oxidised. The iron oxide is probably found very close to the vacuum-oxide interface of the grown oxide film.

In addition to the HRCLS experiments, the chemical composition of the surface region before and after oxidation at 10^{-6} mbar O_2 and 650 K is also studied with AES. Fig. 7.2 shows the AES spectra of sample 1 after oxidation. The low-energy part of the AES spectrum lends itself for the identification of oxides on the surface. Bonding of Fe or Al with oxygen leads to a chemically shifted AES transition [126–129], which has shown to be an adequate tool for the identification of oxide formation on Fe(110) and NiAl(110) [126–129]. Fig. 7.2 clearly shows that the oxidized surface shows mostly aluminium oxide. The sensitivity of AES is smaller compared to HRCLS. This could explain

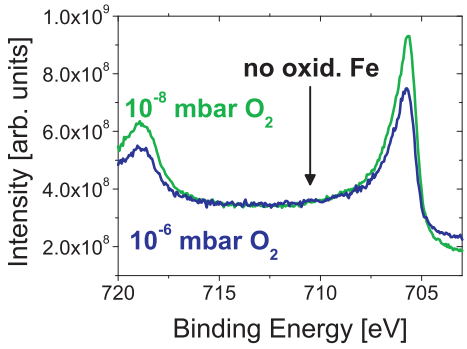

Figure 7.14: Photoemission spectra of the Fe2p photo electrons, recorded at 800 eV photon energy during the oxidation at 650 K. The initial oxidation pressure of 10^{-8} mbar O_2 (green curve) is increased to 10^{-6} mbar O_2 (blue curve) after 55 min. The blue curve is measured 25 min after the increase. Unlike the oxidation with an initial oxygen pressure of 10^{-6} mbar (see fig. 7.12) no signal of oxidized Fe is detected.

why the small iron oxide signal, observed with HRCLS, is not detected by AES.

The atomic structure and order of the oxidized surface region

To probe the influence of the oxidation on the ordering of the $D0_3$ phase in the surface region of the alloy, CTR and GID measurements are conducted. During the formation of the oxide films structural and occupational changes at the oxide-alloy interface are followed *in situ*. Thereby the oxidation at 3×10^{-6} mbar of molecular oxygen at 650 K is followed in great detail by CTR measurements and presented in the first part of this section. In a second part the results of a GID study during the oxidation at 650 K, 680 K and 720 K with 3×10^{-6} mbar O_2 are discussed.

As described above reflectivity measurements show the formation of a 8.4 Å thick, disordered oxide layer after exposing the clean sample to 3×10^{-6} mbar O_2 for 30 minutes at 650 K (see fig. 7.4). After the oxidation CTR measurements are performed on the sample. However, the intensity along the (2,0), (1,1) and (1,2) rods has almost completely vanished. Typical rocking scans at points along the (2,0) and the (1,2) rod before and after oxidation are shown in fig. 7.15b and c. The (0,2) rod, shown in fig. 7.15a, became most significantly weaker halfway the Bragg peaks. None of the Bragg peaks' intensity changed, which means that only in the near-surface region drastic structural changes have occurred. The significant decrease of the intensity is also observed at a lower oxidation temperature of 400 K, like shown for the (2,0) rod in fig. 7.15d.

The different experimental observations after oxidation are summarized as follows: a thin smooth aluminium-oxide layer is formed on top of the alloy which has a strongly decreased B2 and $D0_3$ order in the near-surface region. The lattice itself, as defined

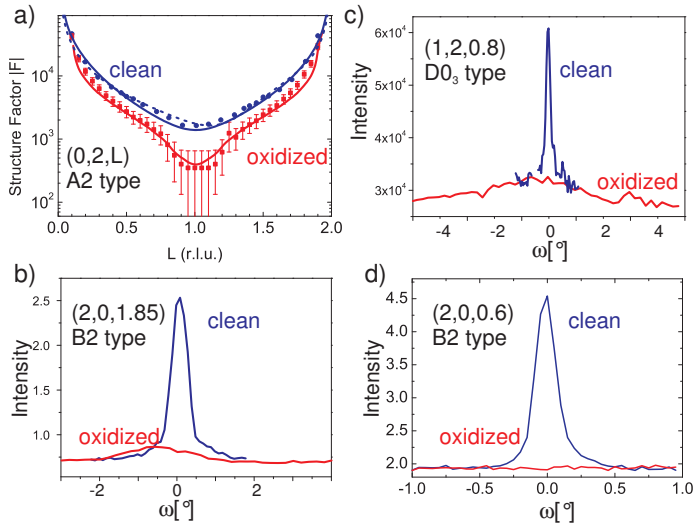

Figure 7.15: a) Experimental (0,2) CTR before (blue) and after (red) the oxidation procedure (650 K, 10^{-6} mbar O_2). The simulation (red solid line) is performed for a $D0_3$ bulk crystal of which the topmost layers gradually change their composition as described in the text and as schematically shown in fig. 7.16. Also shown is the simulation (dashed blue) for the case that the interface between the oxide and the substrate would be perfectly sharp. b)-d) The rocking scan at the points (2,0,1.85), (1,2,0.8) and (2,0,0.6) of the clean (blue) and oxidized (red) surface. b) and c) are recorded after oxidation at 650 K, d) after oxidation at 400 K. The intensity disappears completely upon oxidation.

by the bcc structure is not destroyed, neither has the interface become (much) rougher. These findings raise the following questions: $i)$ Up to which depth is the superlattice in the subsurface region disordered? $ii)$ Is the disorder due to a change in the composition? These questions will be addressed hereafter by further data analysis and simulation.

A rough estimate of the thickness, over which the structure is disordered, can be obtained by calculating from how many substrate layers Al is needed to form the 8.4 Å thin oxide. Taking the electron density of bulk α-Al_2O_3 results in 4 unit cell layers of $Fe_{0.72}Al_{0.28}$ to be completely Al-depleted. This is reduced by half a unit cell layer when the composition of the topmost atomic layer of the surface is FeAl, which follows from the results for the clean surface presented in section 7.2.1.

In general, diminishing CTR signals are caused by either compositional changes or an increase in roughness in the surface region. A drastic increase in surface roughness can be ruled out on the basis of the results of the x-ray reflectivity measurements shown in fig. 7.4. The oxide layer has a well-defined thickness and shows smooth interfaces to the underlying substrate and to the vacuum. Therefore, another explanation is needed in which the CTRs originating from the B2 and $D0_3$ superlattices are suppressed, but not the CTR probing the fundamental bcc lattice. A solution can be given by the $D0_3$ and B2 order parameters decreasing gradually from the bulk towards the surface. The exact

profile of such a transition cannot be determined from the present data, simply because the signals vanished. Nevertheless, and without losing generality, one can investigate the influence of such a disordering process on the CTR signals. The average scattering of each unit cell layer in the subsurface region can be viewed upon as a weighted average of two contributions consisting of a $D0_3$ (and with that also B2) and an A2 part. Here, the weighting is performed by using the so-called β-roughness model, since it gives a simple and exact solution by [11]:

$$F = \underbrace{F_{CTR} + \sum_{j=1}^{n} \beta^j F_{bulk} e^{i2\pi lj}}_{D0_3,B2} + \underbrace{\sum_{j=1}^{n} (1-\beta^j) F_{surf} e^{i2\pi lj} + \theta F_{interface}}_{A2} \qquad (7.1)$$

with F_{CTR} the CTR scattering, F_{bulk} the scattering from a $D0_3$ bulk unit cell, F_{surf} the scattering from an A2 surface unit cell, and β^j the occupation in the j-th layer above the bulk (see fig. 7.16 for a schematic view). The A2 structure is calculated by assuming completely Al-depleted unit cells, resulting in the α, β, and γ sites being occupied by 0.72 Fe atoms. The oxide film has a very poor crystallinity and does therefore not contribute to CTR scattering with in-plane momentum transfer. The interface between the oxide and the subsurface region is not uniform, but shows atomic disorder or roughness. This is modelled by assuming an interface layer of reduced density, having a coverage θ and scattering contribution $F_{interface}$ with A2 symmetry. This describes the scattering for a layer which consists either of a mix of A2 and oxide material or an A2 layer containing many vacancies. The first two terms on the right-hand side of equation 7.1 involve bulk scattering and therefore have a $D0_3$ (and also B2) symmetry. These two terms together render CTRs of which the intensity is reduced between the Bragg peaks as in the case of roughness. The next two terms in equation 7.1 involve scattering by material having A2 symmetry. They do not contribute to the B2 and $D0_3$ rods, thereby not changing the shape as established by the first two terms. However, the contribution to the A2 rods is such that their shape does not change too much from having a well-defined smooth surface region. The characteristic shape of the (0,2) rod shows a strong dip halfway the Bragg peaks, which is well reproduced by the interface layer of reduced density. Fig. 7.15a shows a simulation of the previously described model as parametrized by equation 7.1 [3]. With a gradually changing order parameter not each unit cell layer is completely Al-depleted. The previously estimated depth up to which the disorder takes place ($N_{tot} = 3.5 - 4$) will therefore be enlarged depending on the disordering profile that is used. For the β-roughness model that is used here, the depth up to which the disorder takes place (n) is closely related to the parameter β by: $\frac{\beta - \beta^{n+1}}{1-\beta} = N_{tot}$. The simulations shown in fig. 7.15a are performed with

[3] Equation 7.1 contains a sharp transition between the bulk and the distorted surface region and a finite sum over distorted layers. These two features lead to finite thickness oscillations in the rod profiles, which are experimentally not observed. Most likely, the interface between the bulk and the distorted region is not atomically sharp. Consequently, for the rod calculation the ensemble average over many different thicknesses should be taken. To account for this effect, the simulation includes a convolution with a top-hat function of width $\Delta l = 0.1$.

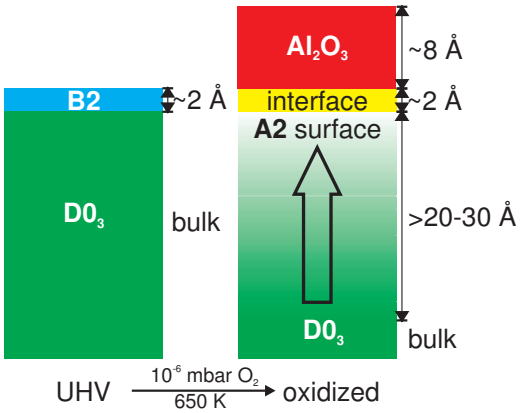

Figure 7.16: Schematic representation of the clean (left) and oxidized (right) surface. The clean surface, which was investigated in UHV shows a topmost atomic layer having B2 symmetry on a $D0_3$ bulk crystal. The oxidized surface shows a gradually changing superlattice order in the subsurface region. The order starts with $D0_3$ in the bulk and changes to A2 at the interface with the oxide. The interface layer has A2 symmetry but a reduced average density which is the result of complete Al-depletion in the topmost atomic layer which before oxidation consisted of $Fe_{.5}Al_{.5}$.

$\beta = 0.85$ and n=8. These values lead to a decrease of at least one order of magnitude on F of the B2 and $D0_3$ rods (two orders of magnitude in intensity), which complies with the detection limit in the experiments. To show the effect of the interface structure between the oxide and the substrate, the (0,2) rod is simulated as well when assuming that an interface with reduced density is absent ($\theta = 0$). In that case the characteristic dip is not present and the intensity is close to the CTR of the clean surface.

The glancing angle Bragg scattering measurements are carried out for the three oxidation temperatures at 650 K, 680 K and 720 K with 10^{-6} mbar O_2. They are performed at the inplane (1,1,0) $D0_3$-type reflection to determine oxygen induced changes of the superstructure lattice in the surface region of the alloy. The profiles of the outgoing angle α_f are shown in fig. 7.17 for the three oxidation cycles, in comparison with the profiles of the clean sample (sample 2). The oxidation of the prepared,clean sample leads to a signal decrease for all three conditions. To analyse the spectra in detail equation 4.26 has to be applied. Therefore, the transmissivity of the vacuum-alloy system and the vacuum-oxide-alloy system have to be calculated according to the equations 4.22 and 4.25, respectively. The needed interfacial roughnesses and the oxide layer thicknesses are taken from the reflectivity measurements of section 7.2.2. For the vacuum-oxide-alloy system Al_2O_3 formation is assumed, while assuming a mixed Fe and Al oxide layer produces very similar results. Note, that the calculations show that the interfacial roughnesses have only minor influences on the transmissivities of the clean and oxidized systems.

In addition to the transmissivities the kinematic sum of Bragg scattering is needed

to calculate the scattered intensity of the (1,1,0) reflection according to equation 4.26. Thereby three models are applied which are schematically depicted in fig. 7.18, together with a model (number 0) to analyse the clean surface. According to equation 4.8, model I assumes perfect $D0_3$-type order within the complete surface region of the alloy. Model II takes a Gaussian-like decay of the $D0_3$-type order towards the oxide-alloy-interface into account, like described by eqn. 4.9 and shown in fig. 7.18 by the grey line. In model III, a completely disordered layer of Fe_3Al is simulated by a "dead", A2-type layer, which is described by eqn. 4.11. Within all simulations a sample curvature of $0.06°$ is taken into account, while a misorientation of the Bragg planes is neglected[4]. An intensity scaling factor is determined from the data set of the clean sample.

To simulate the data of the clean surfaces, model 0 is applied. The resulting calculated intensity is shown in fig. 7.17a-c by the grey solid line and agrees well with the data. For the simulations of the curves of the oxidized surfaces model I, II and III are compared to each other, which is shown in fig. 7.17 by black dotted, solid and dashed lines, respectively. For model II, a FWHM-value of 25 Å is assumed for the Gaussian order-disorder profile, which is consistent with the 20 to 30 Å thick, disordered region, resulting from the CTR measurements in section 7.2.2. The simulated profiles of model I and II are nearly on top of each other and are in good agreement with the data of the experiments performed at 650 K and 680 K. Assuming a disordered, "dead" layer of 20 Å in model III leads to a strong intensity decrease which is not observed experimentally, as shown in fig. 7.17 a and b by the dashed lines. For an oxidation temperature of 720 K, model I and II do not described the data well. An additional disordered layer of 8 Å, like in model III, is needed in model II to reproduce the data well.

In summary, the glancing angle scattering measurements show, that upon oxidation the chemical order in the surface region is not destroyed completely but decreases smoothly (Gaussian-like) towards the oxide-alloy interface. For oxidation temperatures of 650 K and 680 K the disordered region in the alloy is roughly 25 Å thick. At a higher oxidation temperature of 720 K the oxygen induced disorder, especially very close to the interface, is higher compared to lower oxidation temperatures. A completely disordered, 8 Å thick layer is present at the oxide-alloy interface, in addition to the Gaussian disorder profile. Finally, the GID measurements confirm the model resulting from the CTR measurements and presented in fig.7.16.

7.3 Discussion

7.3.1 The clean surface

The results of the SXRD measurements on the clean surface clearly demonstrate that the topmost atomic layer has an in-plane B2 symmetry. This implies preferential surface segregation of Al, thereby destroying the $D0_3$ order in this layer. A related mechanism has been found for similar systems, such as $Ni_{0.9}Al_{0.1}$(110). In this fcc compound the topmost

[4]The curvature has been estimated from the reflectivity measurements.

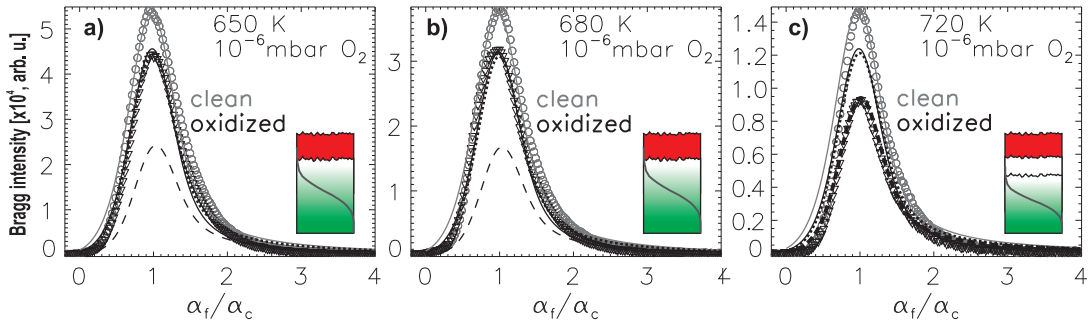

Figure 7.17: α_f-profiles of the evanescent Bragg scattering of the inplane (1,1,0) $D0_3$ superstructure reflection: The profiles are recorded at the indicated temperatures before (grey open circles) and after oxidation (black open triangles) at 3×10^{-6} mbar O_2. The lines are theoretical simulations as described in the text. The profiles were measured for $\alpha_i = 0.24°$. The sketches indicate the best-simulation model for the oxidized data.

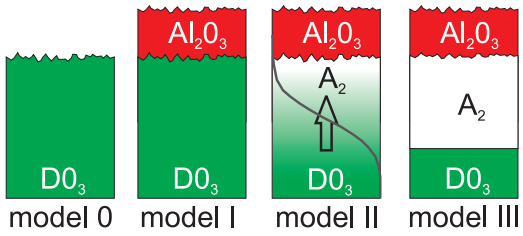

Figure 7.18: Four fitting models to analyse the α_f-profiles of the evanescent Bragg scattering in fig. 7.17. Model 0 describes the clean Fe_3Al surface, model I to III are applied for the oxidized system as described in the text.

layer exhibits the ordered $L1_2$ structure on top of an A1 bulk due to Al segregation, resulting in a composition of $Ni_{.75}Al_{.25}$ [130]. A Low Energy Ion Scattering (LEIS) study of the $Fe_3Al(110)$ surface showed that at room temperature the topmost layer has the composition FeAl [33]. The present results corroborate the idea of Al-enrichment at the surface. However, where the Fe concentration for samples 1 and 2 are similar, the Al content seems not to be unambiguously determined. This could be for the following reasons. First, due to a difference in surface preparation, where preferential sputtering of Al takes place. During the subsequent annealing procedure Al may segregate again, but at temperatures higher than approximately 1150 K, Al starts to evaporate from the surface [30]. Second, the scattering contribution of Al being relatively low makes it difficult to unequivocally obtain unrestrained fit parameters. Last, there is a large correlation between the fit parameters, especially between the occupation and displacements of the topmost β and γ sites, the scale factor, and the surface roughness. In order to keep the number of parameters as low as possible, surface roughness was not explicitly put in the models. Therefore, the occupancies of the atoms should not be taken as a measure for the vacancies, but more as the

total influence of several factors playing a role at different length scales. These include vacancies and atomic roughness, all of which for sample 1 and 2 could have been different. However, since the presently used diffraction method is an excellent probe for the atomic order and symmetry, the model in which a B2-type surface layer terminates a $D0_3$ crystal describes all the features of the data obtained for both samples very well.

For FeAl, which in the bulk already adopts the B2 structure, it is reported that the segregation of Al leads to a composition $FeAl_y$ (with $y > 1$) of the clean (110) surface [30,38]. The LEED patterns for this surface never show a (1×1) structure. For the composition $FeAl_2$ of the topmost layer there is the formation of an incommensurate (2×1) reconstruction, whereas for other compositions the surface layers are disordered in at least one direction [32]. Apparently, the bulk stoichiometry close to Fe_3Al leads after segregation to exactly the right amount of Al to form a well-ordered surface structure which is commensurate with the underlying $D0_3$ bulk.

The results from the surface structure refinement indicate that for both samples the topmost layer shows a corrugation where the Fe atoms are pulled out of the surface. Within two times the estimated standard deviation (e.s.d.) the values obtained for both samples are identical. In general one would expect the larger of the two atoms, in this case Al, being pulled out of the surface, as observed for NiAl(110), Ni_3Al(110), and CoAl(110) [12,131–133]. Although these examples show the expected general behaviour, the presence of magnetism might result in reverted relaxations [134]. A surface leads to a narrowing of the d-band, which in turn enlarges the surface density of states [135]. Hereby the magnetic moment at the surface is expected to be enhanced. The system can reduce the gain in magnetic energy by a structural relaxation whereby the magnetic element is pulled out of the surface. Since iron has a substantial magnetic moment (2.2 μ_B for pure Fe), the previously described effect could be responsible for the observed surface corrugation in Fe_3Al.

7.3.2 The oxidized surface

The atomic structure of oxidized Fe_3Al(1,1,0)

For the surface region of the sample, oxidized between 400 K and 720 K with 10^{-6} mbar O_2, a structural model could be derived from the SXRD and GID measurements, presented in section 7.2.2. This simple structural model that complies with all the experimental observations is shown in fig. 7.16. The main feature consists of a gradually changing order, going from $D0_3$ (and B2) in the bulk towards A2 at the interface between the crystal and the oxide layer. Furthermore, the interface layer between substrate and oxide shows a largely reduced density which can be interpreted as atomic roughness. Since this interface emerges from the B2 layer that is observed for the clean surface, it is expected that after all the Al has been taken out the average density corresponds to half a monolayer of iron. Reverting to the two questions raised in section 7.2.2:i) The GID measurements show that a smooth depletion profile (Gaussian or beta model) has to be assumed and no completely disordered layer of Fe_3Al is present at the oxide-alloy interface. The thickness of the sub-

surface region which is Al depleted is estimated to 25 Å($\pm$5Å) for oxidation temperatures between 400 K and 680 K. The interfacial depletion is slightly increased at 720 K. $ii)$ Pinpointing the exact composition is difficult, since the difference in x-ray scattering power between bulk and Al-depleted Fe_3Al is only 15 %. This is illustrated by the simulations in fig. 7.15a, which show that the calculated, fundamental CTRs for the clean surface (close to bulk termination) and for the Al-depleted subsurface region are almost identical.

It is known that the mechanical properties of alloys of Fe and Al depend strongly on the stoichiometry. With increasing Al content, room-temperature ductility and high-temperature strength become worse [1]. Therefore, it is expected that the mechanical properties in the subsurface region change after oxidation. In the case that the subsurface region would consist of pure iron, it would be expected to be more ductile [136]. However, it is not expected that the subsurface region has a structure similar to bulk iron, since after oxidation either Al segregates into this region or many vacancies remain present. In the latter case, it would be expected that an extremely brittle structure would arise, since many bonds are absent. Even if clustering of Fe would occur, the grain structure would be such that individual grains could move easily since they have a lot of free space around them. Unfortunately, there is not much known about the ternary phase diagram of Fe, Al, and vacancies. Depletion zones can cause severe local chemical changes which can be detrimental to structural materials. For stainless steel, where chromium-oxide forms the protective layer, it is known that chromium-depletion plays an important role for the corrosion properties. Local chemical changes around MnS inclusions caused by chromium-depletion result in an extremely aggressive solution which accelerates pitting corrosion [137]. Chromium-depletion, triggered by chromium carbide precipitation, at grain boundaries in stainless steel is one of the major reasons for intergranular corrosion and is a precursor to crack development [138,139]. It is to be expected that also in the case of the iron-aluminides these processes play an important role. In comparison to the oxidation of related compounds, there are significant differences. In the case of NiAl(110), the near-surface region does not lose its B2 structure upon oxidation at the same conditions [12]. This can be understood by NiAl being strongly ordering, in contrast to Fe_3Al.

Furthermore the x-ray reflectivity measurements show that upon oxidation at 10^{-6} mbar O_2 a thicker oxide film is grown at room temperature than at 650 K. This phenomena is also found for the (1,0,0), the (1,1,0) and the (1,1,1) surface of FeAl, oxidized at similar conditions [7]. A model explaining this contra intuitive behaviour is obtained from the results in the following paragraph.

The chemical composition of the oxide layer

The results of the HRCLS study clearly show that the oxide layer composition as well as the coordination of the oxidized atoms strongly depend on the oxidation rate, the Al supply at the surface and the present kinetic barriers. Thereby, higher (lower) oxidation rates correspond to higher (lower) oxygen pressures of 10^{-6} mbar (10^{-8} mbar). A fast Al supply corresponds to a fast Al segregation from the bulk and therefore high temperatures (470 K and 650 K). To identify the oxide species within the oxide film the chemical shift of

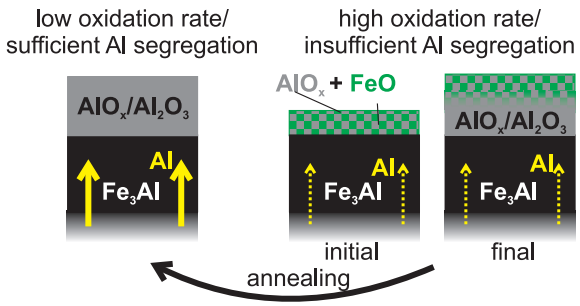

Figure 7.19: Schematic model of the two possible oxidation scenarios.

the Al2p and Fe2p line away from the metallic Al and Fe photoelectrons lines is compared to reference values known from literature [37]. In general, the size of the chemical shift is known to scale with the number of chemical bonds between atoms different in kind. The different binding energies resulting for the Al2p, the Fe2p and the O1s photo electrons in Fe_3Al, in Al_2O_3, in the spinel $FeAl_2O_4$, in FeO and in Fe_2O_3 are shown by vertical lines in fig. 7.10-7.12. However,the position of Al2p electrons in spinel also agrees with Al atoms which have a lower coordination number with O atoms due to chemical or structural disorder. Therefore, spinel formation cannot be distinguished from disordered Al oxide distinctively. Nevertheless, four main conclusions can be drawn from the core level study which are depicted schematically in fig 7.19.

i) Pure Al oxide and no Fe oxide is formed at a fast Al segregation from the bulk and at low oxidation rates. This is due to the higher oxygen affinity of Al compared to Fe. The standard enthalpy of formation for α-Al_2O_3 is over 6 times higher than for FeO. It explains why no oxidized Fe is found during the oxidation at 470 K and 650 K with 10^{-8} mbar of O_2. After oxidation at 650 K the chemical shift of the Al2p line is 3.3 eV and larger than the chemical shift of 2.7 eV after oxidation at 470 K. The former value agrees well with the shifts of ordered Al_2O_3,the shifts found for thin ordered γ-Al_2O_3 films grown on Al foils (3.6 eV) or the well-ordered surface oxide formed on the FeAl(1,1,0) surface (3.4 eV) at similar conditions [7,37,140]. This indicates highly coordinated Al atoms present in the oxide layer. In addition to the strong photo emission line at E_{BE}=75.5 eV the Al2p spectra shows a second component at E_{BE}=74.0 eV. For the ordered surface oxide on NiAl(1,1,0) this component is also observed and assigned to Al at the oxide-alloy interface, bonded only to two oxygen atoms [42]. We conclude that the interfacial Al is also detected here for the thin alumina film formed at 650 K and 10^{-8} mbar of O_2. Oxidation of FeAl(1,1,0) and Al(1,1,1) surfaces at room temperature results in chemical shifts of 2.5 eV and 2.6 eV, respectively [7,125]. This shift is consistent with the shift after oxidation at 470 K. In both studies the smaller shifts are assigned to a disordered, glassy network of Al bulk oxide. As expected, a shift towards higher binding energies is also observed in the O1s spectra when going from 470 K to 650 K in oxidation temperature. Conclusively, the alumina layer formed during oxidation at 650 K has a higher degree of chemical order and less defects compared to the oxide layers grown at 300 K and 470 K.

ii) A mixture of Fe and Al oxide at the initial oxidation is formed for high oxidation rates or slow Al segregation as Al cannot segregate fast enough to maintain a sufficient supply for pure Al oxidation. For the bulk diffusion in $D0_3$ structures with approximate A_3B compositions theory predicts an increased diffusion rate for constituent A in comparison with constituent B. A atoms can diffuse in their own sublattices with nearest-neighbour jumps while B atoms need third-nearest neighbour jumps or anti-site defects to migrate in their sublattice. Both options for B atoms require a higher activation enthalpy for diffusion [141]. Thus, in case of the $D0_3$-type ordered Fe_3Al Fe atoms have a larger diffusion rate than Al atoms[5]. Al supply to the surface is slower than Fe supply. This could induce the formation of Fe oxide along with Al oxide at all investigated temperatures during oxidation with 10^{-6} mbar of O_2 and at room temperature with 10^{-8} mbar O_2. After oxidation with 10^{-6} mbar O_2 at 300 K and 470 K the O1s and Fe2p peak positions agree very well with the values found for haematite (Fe_2O_3) in a XPS-study (marked by vertical lines in fig. 7.10 and 7.11) [37]. Haematite formation was also observed for polycrystalline Fe_3Al after 300 K and 570 K oxidation in air, which is consistent with our results at lower pressures [115]. The analysis of the Fe2p and O1s spectra show that different coordinations of Fe with O atoms, like in FeO, are present in the oxide film. Interestingly, the highest amount of oxidized Fe is found at 470 K despite the higher Al segregation compared to 300 K. An optimization of the interplay between the temperature dependent Al supply and the thermal energy needed to overcome kinetic barriers for Fe oxide formation could explain this result. After oxidation with 10^{-8} mbar O_2 at 300 K and with 10^{-6} mbar O_2 at 650 K less oxidized Fe is detected. This is in line with a oxidation rate- and Al supply-induced growth control. The corresponding photo emission line of oxidized Al is found at a chemical shift of 2.5 eV for all growth condition where Fe oxide is formed. As mentioned above this shift can be assigned to chemically disordered Al_2O_3 or the spinel $FeAl_2O_4$. However, as most Fe atoms are coordinated to O atoms like in Fe_2O_3 a pure spinel-like oxide can be excluded. While during oxidation at 10^{-8} mbar O_2 a chemically ordered alumina layer is formed at 650 K, oxidation at 10^{-6} mbar O_2 lead to Al2p lines consistent with chemically disordered alumina. This indicates an ordering of the thin film at low pressures induced by the oxide-alloy interface.

iii) The stepwise increase of the oxidation pressure during HRCLS measurements of the Fe oxide signal shows that the oxidation of Fe atoms happens primarily during the very initial oxidation process. It is assumed that for prolonged oxidation only Al gets oxidized. After the film of mixed Fe and Al oxides builds a homogeneous layer the supply of oxygen to the metal-oxide interface allows selective oxidation of Al and thereby the development of a continuous film of alumina. Once a homogeneous Al_2O_3 layer is formed the oxide growth slows down drastically as electron tunnelling remains the only possibility for charge equalisation. The Fe oxide formation is blocked. This model can also explain the different maximum oxide film thickness's of 16 Å and 8 Å observed at 300 K and 650 K oxidation, respectively. Fast Al segregation enables a formation of the homogeneous

[5]The diffusion process is different for B2-type alloys with AB composition where the diffusion constants are equal for both constituents. Therefore alloys like NiAl and CoGa show preferentially oxidation of the elements with the higher standard enthalpy of formation.

alumina layer, while a insufficient Al segregation promotes the formation of Fe and Al oxide which leads to more growth channels in form of grain boundaries.

iv) Annealing the sample up to 770 K after oxidation breaks up bonds between Fe and O and leads to the formation of pure Al oxide. The chemical shift of 3.4 eV in the Al2p is consistent with the formation of ordered, bulk-like Al_2O_3 and is also reported for FeAl(1,1,0), FeAl(1,0,0), FeAl(1,1,1) or NiAl(1,1,0) [7, 42]. This transformation is confirmed by the shift of the O1s photo emission line towards higher binding energies (see vertical line in fig. 7.11). Due to its higher formation energy the formation of pure alumina is obvious once kinetic barriers are removed. The standard Gibbs energy of formation of α-Al_2O_3 is -1582260 J/mol which is 6.5-times higher compared to FeO. It is not possible to determine if the "de-oxidized" Fe atoms diffuse into the bulk or remain in the oxide film as metallic clusters.

7.4 Conclusions

The clean Fe_3Al(110) surface comprises a topmost atomic layer with in-plane B2-type order on a $D0_3$ ordered bulk crystal at room temperature after UHV preparation. Upon oxidation for 30 minutes at 10^{-6} mbar of molecular oxygen at temperatures from at least 400 K up to 720 K, the $D0_3$ and B2 order disappears in the subsurface region while an oxide layer is formed. Assuming a β-roughness- or Gaussian-like profile for the disorder, whereby the $D0_3$ and B2 order parameters diminish smoothly from the bulk to the surface, results in a depth of 2-3 nm for the disordered region. At the same time an 8.4 Å thin smooth oxide layer is formed on the surface (see fig. 7.16). This means that the oxidation-induced disorder in the subsurface region affects only the decoration of Fe, Al ,and vacancies over the underlying bcc lattice, and not its crystallinity. The analysis of HRCLS spectra, recorded for oxygen pressures between 10^{-8} and 10^{-6} mbar and oxidation temperatures between 300 and 650 K, show that the chemical composition, thickness and homogeneity of the oxide film strongly depends on the interplay between oxidation rate and Al segregation to the oxide-alloy interface. For high oxidation rates or slow Al segregation Fe oxide and Al oxide are formed in the very initial oxidation process, followed by pure alumina formation in the prolonged oxidation process. For low oxidation rates and fast Al segregation preferential Al oxidation and the formation of a homogeneous Al_2O_3 layer are observed on Fe_3Al. The oxide layer can be ordered by annealing up to 770 K.

The results of the present study are of importance for the application of iron-aluminides under realistic conditions. It is indispensable that a protective oxide scale is formed on the surfaces of such materials to protect them from aggressive environments. This work shows that low oxidation rates and fast Al supply to the surface have to be provided in the initial oxidation process to form this homogeneous, ordered alumina scale. The fact that there are drastic compositional changes upon oxidation in an extended subsurface region, indicates that the oxidation process is not only limited to the very surface. This can have consequence for the processing and integration of iron-aluminides in devices, since the physical

properties, such as ductility and strength, depend on the composition. However, at the time there is little known about the mechanical properties of these alloys in the case that they contain many vacancies. Nevertheless, it may be expected that the oxidation process renders these materials more brittle and vulnerable to aggressive environments.

Chapter 8

The Oxidation of Vicinal NiAl Surfaces

Binary alloys such as NiAl are very stable structural materials which can be used in high-temperature applications. However, a thorough understanding of their oxidation on the atomic scale, which starts at the surface, is missing. Until now, perfect NiAl(1,1,0) surfaces of single crystals are routinely investigated. At low oxidation pressures a ultrathin, twin-domain alumina film is formed. This film has been introduced in more detail in section 3.2.2. As one step towards a better understanding of non-ideal surfaces as encountered in nanoparticles and polycrystalline materials, we investigate vicinal NiAl surfaces to analyse the influences of steps on the oxidation process. The chosen NiAl(6,7,1) and NiAl(4,3,0) surfaces consist of (1,1,0) terraces of very similar widths while the steps run along different directions.

Due to their lower coordination number compared to bulk and on terrace surface atoms, step atoms play an important role in surface processes like oxidation, catalysis and epitaxial growth. They act as preferential adsorption sites and nuclei in the initial formation of oxides, are favourable pathways in inter- and intralayer diffusion processes and have an important role in the release of interfacial strain, set up during oxide formation (see also section 3.3) [15, 16, 50, 142]. To gain detailed understanding of the structural changes at steps during oxidation, we study the two mentioned regularly stepped NiAl surfaces as model systems. The surfaces are oxidized at a low pressure ($\approx 10^{-6}$ mbar O_2) to be able to follow changes during the initial oxidation processes. The focus of interest of the experiments is on the following questions:

1. Are the clean vicinal surfaces stable? What is the atomic structure of the surfaces?

2. Are the vicinal surfaces stable after oxidation? How is the structure of the surface region changed after oxidation?

3. How is the chemical order, present in bulk NiAl, affected in the interfacial region by the formation of an oxide film?

4. Is the morphology of the surface affected by the formation of long-range ordered oxides?

5. Do the surface steps influence the structure of the oxide? Is it possible to tailor the oxide growth by the presence of dedicated surface steps?

In section 8.1 these question will be answered for the NiAl(6,7,1) surface using SXRD and LEED. It is shown that the clean, ordered, nearly bulk-like surface is characterized by a regular pattern of 14 Å wide (1,1,0) terraces and monoatomic (0,1,1) steps. Al and Ni atoms in topmost terraces exhibit a rippled relaxation. The terrace-step structure of the clean surface persists at the oxide-alloy interface after oxidation at 540 K and 6×10^{-6} mbar O_2 while the atoms of the interfacial region are relaxed inwards. A 5.1 Å thick, disordered alumina film is formed. Oxidation induced formation of Al and Ni vacancies as well as Ni anti-sites is observed up to a depth of 1 nm within the alloy. We demonstrate that high temperature annealing enables long-range ordering of the oxide, inducing (1,1,0) facets up to 50 times larger than the original terraces. The formed surface oxide with its complex structure is known from the oxidation of the NiAl(1,1,0) surface but due to the surface steps a suppression of twin domain formation is observed on NiAl(6,7,1).

In section 8.2 the NiAl(4,3,0) surface is investigated with respect to the same questions. The experimental techniques of LEED, SXRD and HRCLS are used. Again, the clean surface is stable. It consists of a pattern of 14 Å wide (1,1,0) terraces and monoatomic $(1,\bar{1},0)$ steps. A buckling of Ni and Al atoms at the surface is detected. Oxidation at 550 K and 6×10^{-6} mbar O_2 lifts the initial terrace-step structure in favour of small (1,1,0) facets. A 5.5 Å thick, disordered Al oxide layer is formed. Preferential Al oxidation induces defects like Al and Ni vacancies as well as Ni anti-sites up to a depth of 1 nm. High temperature annealing increases the average width of the (1,1,0) facets but the maximum width is much smaller compared to NiAl(6,7,1). The results clearly show that a θ-Al_2O_3-like oxide is formed on the (4,3,0) surface instead of the complex surface oxide known from the oxidation of the NiAl(1,1,0) and the (6,7,1) surface.

Conclusions from the results of both surfaces are drawn in section 8.3. Similarities and differences of the vicinal NiAl surfaces are highlighted and compared to the flat (1,1,0) surface. The strong influences of the step edge orientation on the oxide structure are pointed out.

8.1 The NiAl(6,7,1) Surface

8.1.1 Sample Preparation and Experimental Details

A single crystal of nominal composition $Ni_{50}Al_{50}$ was grown, cut and polished in-house in the same way as described for the Fe_3Al(1,1,0) sample in section 7.1 . The (6,7,1) surface orientation was confirmed by LEED and XRD measurements. For the experiments the sample was mounted in a portable or stationary UHV chamber for *in situ* preparation and oxidation. More details of the chambers are given in section 5.1.4. Following the standard procedure for obtaining a clean NiAl(1,1,0) surface, the sample was prepared by several cycles of Ar^+ ion sputtering (E_{kin} = 1 keV, p_{Ar} = 8×10^{-6} mbar, I_{sp} = 10 μA) and annealing to 1300 K, including annealing in a 10^{-6} mbar oxygen atmosphere to remove

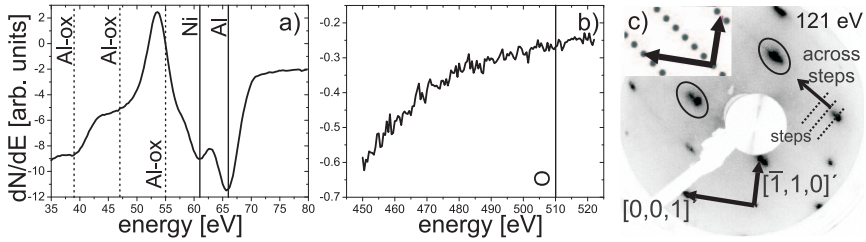

Figure 8.1: AES spectra and LEED image of the clean NiAl(6,7,1) surface. a) Spectra of the low-energy part: The vertical lines indicate the following elements: metallic Al (LVV, 65 eV), metallic Ni (MVV, 60 and 100 eV) and oxidized Al (39, 47 and 55 eV). b) Spectra in the energy range of oxygen (KVV, 510 eV) where no O signal is detected for the clean surface [129]. c) LEED image: The projection of the $[\overline{1}, 1, 0]$- and $[0, 0, 1]$-direction are shown in the image and in the inset. The orientation of the surface steps is indicated by the dashed lines and by the direction across the steps. The ellipses mark splitting of reflexions characteristic for vicinal surfaces. The inset shows the consistent simulated LEED pattern.

.

carbon [42]. Like shown in fig. 8.1 AES was used to check for surface contaminations. The contamination free sample surface was oxidized at 540 K and 6×10^{-6} mbar O_2 for 900 s. To obtain a long-range ordered surface oxide the sample was annealed at several temperatures between 620 K and 1190 K.

The SXRD experiments were carried out with a photon energy of 15 keV at beamline ID03 of the ESRF which is described in section 5.1.2 or elsewhere [143]. Our portable UHV chamber was mounted on a six-circle diffractometer (see section 5.1.3). The incidence angle during the CTR measurements was fixed close to the critical angle of NiAl ($\alpha_c = 0.19°$ at 15 keV). The CTR data were obtained by taking rocking scans at each point along the CTR, followed by an integration and applying standard corrections [61]. Two fundamental and two superstructure CTRs were measured, resulting in 197 independent structure factors. In absence of redundancy of the data, the average error was set to 10 %, which is a typical value using this setup. To analyse the data, the program ROD was used to compare different structure models to the experimental structure factors [123].

The structure of the bulk terminated NiAl(6,7,1) surface is depicted in fig. 8.2, together with an out-of-plane side view of its corresponding reciprocal space. The [6,7,1] direction makes an angle of 7.6° with respect to the $[1, 1, 0]$-direction. The surface consists of 7 atomic rows wide (1,1,0) terraces (14 Å) with mono-atomic (0,1,1) steps. The real space surface unit cell is defined by the orthogonal vectors ($\mathbf{a}_1$,$\mathbf{a}_2$,$\mathbf{a}_3$), where $\mathbf{a}_1$ runs along the steps in the $[\overline{1}, 1, \overline{1}]$-direction of bulk bcc NiAl, $\mathbf{a}_2$ across the steps in the $[\overline{8}, 5, 13]$ direction and $\mathbf{a}_3$ defines the $[6, 7, 1]$ surface normal. No ragged shape of the step edges is expected as the $\mathbf{a}_1$ direction points along a low-energy step orientation on the (1,1,0) surface [52]. The corresponding reciprocal lattice is also orthogonal, with the reciprocal coordinates (H,K,L) running in the directions described above.

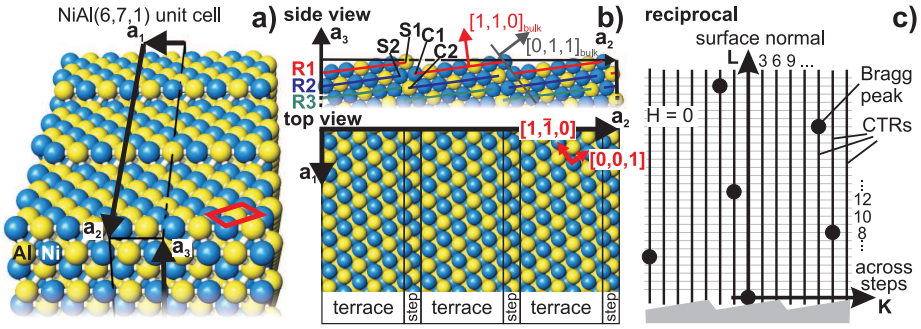

Figure 8.2: a) 3D view of the bulk-terminated NiAl(6,7,1) surface: Thin black lines mark the orthorhombic unit cell ($a_1 = 5.00$ Å, $a_2 = 46.37$ Å, $a_3 = 26.77$ Å), containing 258 Ni (blue) and 258 Al (yellow) atoms. The red rectangle marks the surface unit cell of the (1,1,0) surface. b) Side and top view of the system: one quasi row R consists of 7 layers perpendicular to the surface normal. c) (K,L) reciprocal space plane of the (6,7,1) surface for H=0, together with a sketch of the steps for better orientation. Thick black lines show the CTRs running through the Bragg peaks (black circles) perpendicular to the surface. For even H coordinates the CTRs arise from the fundamental bcc lattice, for odd ones from the CsCl superlattice.

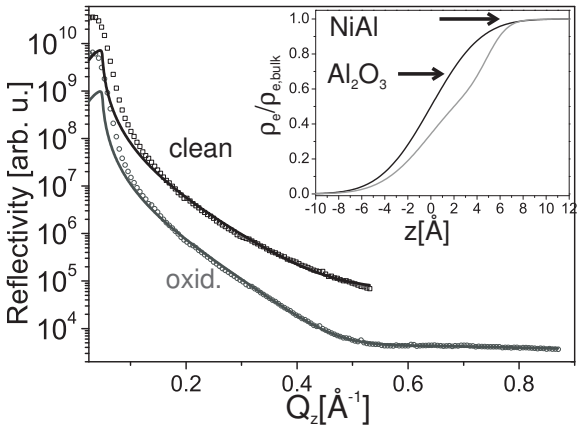

Figure 8.3: X-ray reflectivity curves obtained from the clean (squares) and the oxidized (circles) surface; the curves are shifted for clarity. The fits (solids lines) were obtained using the Parrat formalism, the results are given in table 8.1. In the region of the critical angle a discrepancy between data and fit is observed. A curvature of the sample leads to higher intensities for small angles as well as a rounding of the edge of total reflection and could explain the discrepancy. The inset shows the resulting electron density (ρ_e) profiles as a function of the z direction along the surface normal.

parameter	clean	oxidized
σ_{NiAl} (Å)	3.5	1.3
σ_{ox} (Å)	-	3.4
t_{ox} (Å)	-	5.1
$\rho_{ox}/\rho_{Al_2O_3}$	-	1

Table 8.1: Best-fit results of the x-ray reflectivity measurements of the clean and oxidized NiAl(6,7,1) surface. The root-mean-square roughness (σ) for the interfaces, the oxide thickness (t) and the oxide density ρ_{ox} (compared to α-Al_2O_3) are shown.

8.1.2 Experimental Results

Atomic Structure of the Clean Surface

A LEED image and its simulation of the prepared NiAl(6,7,1) surface are shown in fig. 8.1c. The short periodicity between two spots along one dedicated direction indicates the direction across the surface steps, also marked by the white arrow. The specular x-ray reflectivity of the clean sample is depicted in fig. 8.3. The best fit result is achieved with bulk-like model, including a roughness of 3.5 Å at the vacuum-alloy interface. According to the reflectivity curve and the LEED image the clean surface is relatively smooth and well ordered.

To obtain a more detailed picture of the terrace and step structure on the atomic scale, CTR-measurements of the clean sample were performed. The experimental structure factors are shown in fig. 8.4. As described in the section 4.1.1, the signal on the CTRs is very low for vicinal surfaces. Therefore only parts of the CTRs in the vicinity of Bragg peaks were measurable in the experiment. Another factor hampering the quantitative description of a vicinal surface is the large number of parameters needed to describe the structural relaxations. In principle, every layer within the surface region relaxes in a different way. As the out-of-plane layer spacing of 0.31 Å of the (6,7,1) planes is very small, many layers will be affected by the presence of the surface. For NiAl(1,1,0) it is known that within the first two layers up to a depth of about 4 Å Al and Ni are relaxed out- and inwards, respectively [12, 39]. Assuming relaxations up to a similar depth for the (6,7,1) surface, relaxations of the first 14 layers are expected. In addition, the atoms may relax not only along the surface normal a_3, but also along the a_2-direction due to the existence of the undercoordinated step atoms. As the experimental data set is not large enough to include all relaxations described above, we used a simplified model to analyse the data.

The parameters of this structural model are depicted in the side view of fig. 8.2b. The red lines, labelled R1, mark all atoms sitting in the top most (1,1,0) terraces of the (6,7,1) surface. All these atoms are allowed to relax along the [1,1,0]-directions element specifically. The blue and red lines (R2, R3) mark the atoms within the buried second and third topmost "quasi" rows of (1,1,0) terraces, respectively. According to DFT and MD calculations of other vicinal surfaces [47, 48, 144–147], the step and corner atoms are relaxed

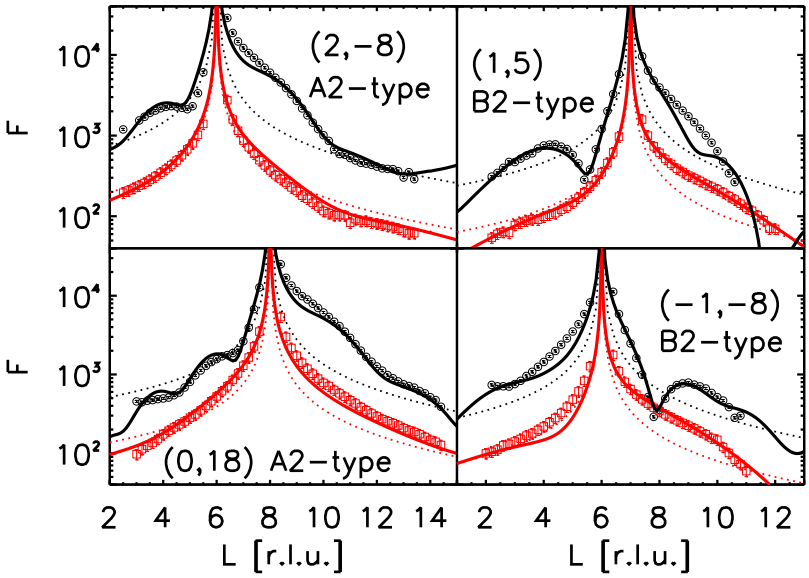

Figure 8.4: Two fundamental (A2-type) and two superstructure (B2-type) CTRs were measured for the clean (red squares) and oxidized, but not annealed surface (black circles), respectively. The results of the best fitting, structural models are shown by solid lines, the dashed lines show the fitting result from bulk-terminated models. The two data sets are shifted for clarity.

in a more pronounced way compared to the terrace atoms. They exhibit strong relaxations not only along the surface normal but also across the steps. Therefore the atoms, labelled S1,C1, S2 and C2 in fig. 8.2b, are allowed to relax in the $\mathbf{a}_2$- and $\mathbf{a}_3$-directions. Ni and Al atoms are allowed to relax independently for all positions. In addition a terrace width distribution is included into the fitting model by applying the so called beta model [60]. It models the surface coverage β per layer n by a power law (β^n, with $0 < \beta < 1$) and is usually used to describe surface roughness. In total 21 structural parameters and one scaling parameter are needed for the simplified model.

The best fit using the above model is shown by the red line in fig. 8.4. The corresponding real space model and the fitting values are presented in fig. 8.5b and table 8.2. The normalized residue of the best fit is χ^2_{norm} = 1.4. The result shows a 0.23 Å and 0.12 Å rumpling of Ni and Al within the first and second row (R1 and R2 in fig. 8.2b), respectively. Al atoms relax outwards, Ni inwards. Relaxations within the third row R3 were not observed. The Al and Ni atoms at the step (S1) are relaxed toward the step edge, while the corner atoms (C1) are both relaxed outwards. The step atoms of the second row (S2) exhibit a more pronounced rumpling compared to the corresponding terrace atoms of row R2. The corner atoms of the second row (C2) are slightly relaxed toward the corner of the kink. As seen in table 8.2 the error bars for the relaxations of the individual step and corner atoms are very high, especially for Al with its lower electron number as compared to Ni. The errors were determined by allowing a χ^2 increase of 10 % while fits were

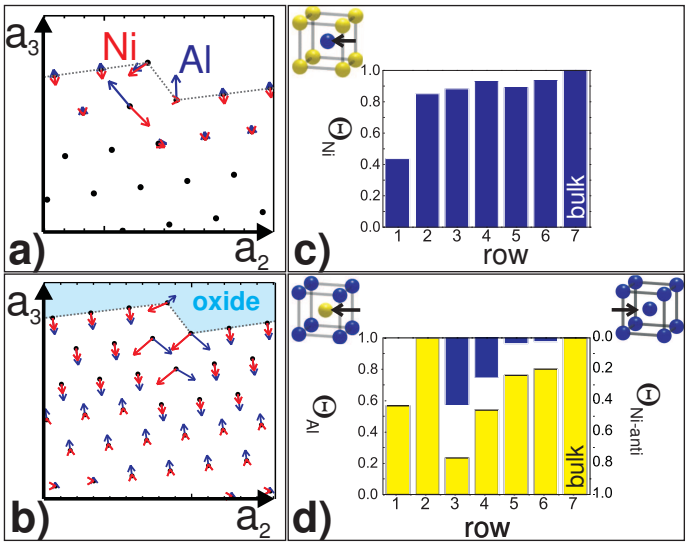

Figure 8.5: The figures show schematic side views of the relaxation profiles of the clean (a) and oxidized (b) sample, resulting from the CTR fits. The relaxations of the Al and Ni atoms are presented by blue and red arrows, respectively. The arrows are magnified by a factor of 5. Black dots show the bulk positions, the grey dotted lines represent the bulk-terminated step. Part c and d depict the row-dependent (R1, R2, ...) occupancy profile for Ni, Al and Ni anti-sites for the oxidized surface region. "Quasi"-row 1 is at the oxide-alloy interface. The sketched bcc bulk unit cells illustrate the ordering and defects in the bcc lattice.

performed with all parameters free, except the one chosen for error estimation [123]. The large errors for the step and corner atom relaxations result from lack of data toward the CTR's anti-Bragg positions, which are most sensitive for these relaxations.

In addition to the best-fitting structural model described above, the influence of several other parameters was investigated systematically to further confirm the findings. The investigation showed the need of the distinctive relaxations of the step and corner atoms (S1,S2,C1,C2) for a good agreement of fit and data. Fitting of the static Debye-Waller factor of the undercoordinated surface atoms did not improve the residue.

Atomic Structure after Oxidation

X-ray reflectivity measurements (see fig. 8.3) after the oxidation at 540 K and 6×10^{-6} mbar O_2 show the presence of a 5.1 Å thick oxide layer which is in good agreement with the oxide thickness found on NiAl(1,1,0) oxidized under the same conditions [4]. To analyse the reflectivity, a homogeneous α-oxide layer on NiAl was assumed. LEED and SXRD could not detect a new diffraction pattern which shows that the formed oxide layer possesses no long-range order. The CTRs arising from the (6,7,1) surface are still present. Thus the regularly stepped pattern of terraces and steps, observed for the clean surface, is

Table 8.2: Results of the structural refinement of the clean and oxidized surface. Listed are the displacements Δz along the surface normal and Δy in the direction across the steps for each atom in the rows R1 to R6 as well as at the steps and corners (S1, C1, S2 and C2). All displacements from the bulk positions are given in Å. The roughness parameter β is (1.1 $\pm$ 0.8) Å and (0.7 $\pm$ 0.7) Å for the clean and oxidized surface, respectively.

	clean		oxidized	
El./Pos.	Δz (-)	Δy (-)	Δz (-)	Δy (-)
Al/R1	0.08(9)	0.01(2)	-0.4(2)	-0.05(3)
Ni/R1	-0.15(2)	-0.018(5)	-0.29(6)	-0.04(1)
Al/R2	0.08(9)	0.01(2)	-0.40(7)	-0.05(1)
Ni/R2	-0.04(2)	-0.005(5)	-0.29(3)	-0.036(6)
Al/R3	-	-	-0.4(2)	-0.05(4)
Ni/R3	-	-	-0.22(2)	-0.027(5)
Al/R4	-	-	0.3(1)	0.03(2)
Ni/R4	-	-	0.03(2)	0.004(5)
Al/R5	-	-	0.25(7)	0.03(2)
Ni/R5	-	-	0.03(2)	0.004(5)
Al/R6	-	-	0.09(6)	0.01(1)
Ni/R6	-	-	0.00(2)	0.000(5)
Al/S1	-0.1(7)	-0.2(9)	0.2(7)	0.2(9)
Ni/S1	-0.2(1)	-0.3(3)	-0.2(1)	-0.5(3)
Al/C1	0.4(4)	0.0(6)	-0.4(4)	0.5(6)
Ni/C1	-0.0(2)	0.0(3)	-0.4(2)	-0.5(3)
Al/S2	0.4(2)	-0.3(7)	-0.4(2)	0.5(7)
Ni/S2	-0.3(2)	0.3(3)	-0.4(2)	-0.5(3)
Al/C2	0.0(4)	0.1 (8)	-0.3(4)	0.5(8)
Ni/C2	-0.1(1)	0.1(2)	-0.4(1)	-0.5(2)

surprisingly conserved at the oxide-alloy interface. To characterize the morphology and oxidation induced segregation profile of the interfacial region, four CTRs of the oxidized, but not yet annealed surface were measured, as shown as in fig. 8.4. Compared to the CTRs of the clean sample, clear oscillations are visible inline with a disturbed chemical composition in the near surface region [12]. The defects and distortions occur up to a well defined depth, which results in characteristic oscillations on the CTRs. Therefore the structural model described in the previous section was extended for the analysis of the oxidized NiAl(6,7,1) surface. Atomic relaxations as well as Ni and Al vacancies and Ni anti-sites were allowed within the first 6 rows (R1 to R6, see fig. 8.2b).

The best fit result ($\chi^2_{norm} = 3.9$, 48 parameters) is shown in fig. 8.4. The corresponding relaxations are given in table 8.2 and are schematically depicted in fig. 8.5b. A

strong inward relaxation of Ni and Al atoms is found in the first three rows (R1 to R3, see fig. 8.5b), with minor relaxations in the following three rows. Comparing the two superstructure CTRs an asymmetry is visible. For the (1,5) rod the oscillation minimum is observed for lower L values compared to the Bragg peak position, for the $(\overline{1}, \overline{8})$ rod for higher L values. To reproduce this asymmetry, relaxations in the $\mathbf{a}_2$-direction have to be allowed within the structure model for the step and corner atoms (S1,S2,C1,C2). Atoms on these positions are strongly relaxed toward the bulk similar to the corresponding terrace atoms, while the inplane relaxation is different for the two constituents. Step rippling occurs where Ni atoms are shifted inplane toward the upper terrace, Al atoms toward the lower terrace.

The occupation profiles for the Ni and Al sites resulting from the best fit are shown in fig. 8.5c and d, respectively. As seen within fig. 8.5c , only 44$\pm$6 % of Ni-sites are occupied by Ni within the first row at the oxide-alloy interface. Within the second row already 85$\pm$5 % of the Ni-sites are occupied while this value smoothly increases towards the bulk value within the following rows. The occupancy profile of the Al sites, depicted in fig. 8.5d, shows the oxidation induced decrease of Al concentration within the first 6 rows of the alloy(1.3 nm). In the first and second row towards the oxide-alloy interface Al-sites are occupied with Al by 57$\pm$14 % and 99$\pm$12 %,respectively, while the Al occupancy drops down to 23$\pm$10 % in the third row . This is accompanied by the formation of Ni anti-site atoms (Ni on Al sites). From the fourth row onwards the amount of Al on Al-sites start to increase towards the bulk value while the Ni anti-sites are disappearing again.

As for the clean surface, the influence of the several parameters on the quality of the fit was examined by applying different structure models. In all tested models the occupancy profile was allowed to vary, but all resulting profiles were similar to the presented one. Again, the agreement factor could be strongly improved by allowing the step and corner atoms to relax independently of the terrace atoms. Introducing static Debye-Waller factors for the interfacial Ni and Al atoms did not improve the fitting results.

Finally we note that the modulation of the structure factor of the B2 type (1,5) CTR disappeared during annealing at a temperature of around 730 K, like depicted in fig. 8.6d. This indicates that the interfacial defects annihilate during annealing.

Structural changes during annealing

It is known from NiAl(1,1,0) that a long-range ordered surface oxide is formed by annealing the oxidized surface [42]. In order to follow a possible ordering of the oxide on the (6,7,1) surface, the sample is annealed stepwise after its oxidation. Morphology changes at the oxide-alloy interface are followed by SXRD measurements. To detect a faceting of the surface, scans across the (1,5)-CTR were performed in the $\mathbf{a}_2$-direction across the steps, as shown in fig. 8.7 and 8.6a. The CTR signal at K=5 starts to decrease at temperatures of 840 K while simultaneously a broad signal arises at K=5.70 for L=4, at K=5.45 for L=5 and at K=5.20 for L=6. The position of the new signal can be ascribed to the formation of

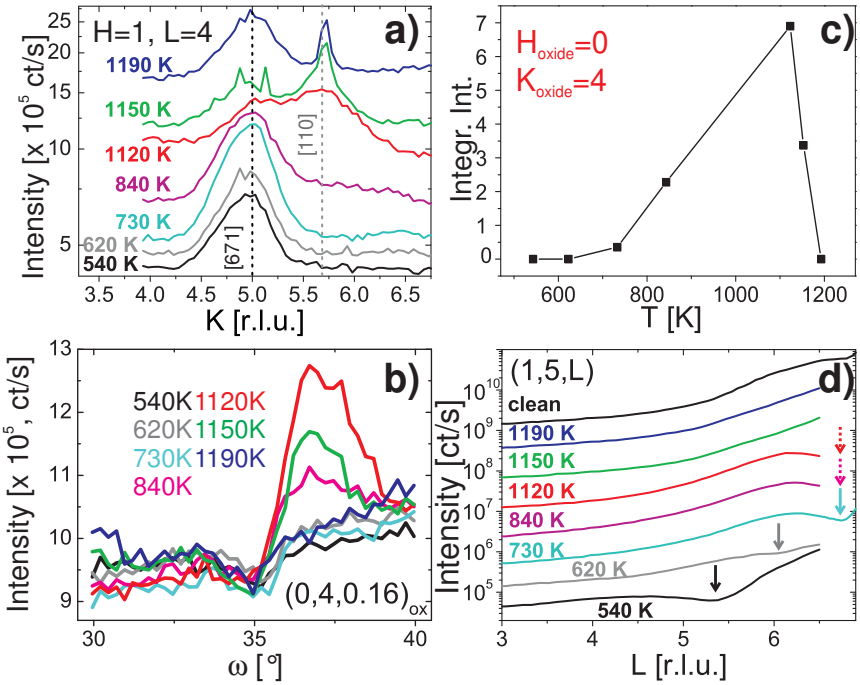

Figure 8.6: a) Temperature dependent K-scans along the $\mathbf{a}_2$-direction recorded after the oxidation. A new peak arises at the (1,1,0) facet position (dashed grey line) while the CTR signal at K=5 (dashed black line) decreases at the same time. The scans are shifted for clarity. b) Rocking scans at a surface oxide peak position of one twin domain ("red" domain) recorded for different annealing temperatures. c) The integrated intensity of the rocking scans, shown in b, shows the formation of long-range ordered oxide during annealing, followed by oxide desorption at higher temperatures. d) L-scans at (1,5,L) during the annealing procedure: The modulation,marked by the arrow, moves towards the Bragg peak and disappears for higher temperatures. This indicates a disappearance of the defects in the interfacial region due to Al segregation.

(1,1,0) facets with nominal position of K = 5.69 for L=4, K=5.46 for L=5 and K=5.23 for L=6. The full width half maximum (FWHM) value of the arising peak is decreasing with increasing temperatures. This corresponds to an increase of the average facet width from 9 nm to 17 nm to 71 nm at 1120 K, 1150 K and 1190 K, respectively(see fig. 8.23).

Fig. 8.6c shows the integrated intensity of the rocking scans of fig. 8.6b. The rocking scan are performed at the (0,4) inplane position of one surface oxide domain for different temperatures (see also fig. 8.8a)[1]. At 730 K a signal is detected, corresponding to the beginning of the transformation from a short-range ordered to a long-range ordered oxide. Increasing the temperature to 840 K and 1120K leads to a further increase of the signal as more long-range ordered oxide is formed. The oxide starts to desorb at 1150 K, as

[1]lattice parameters of the surface oxide: a=18.01 Å, b= 10.59 Å, γ=91.15° and $\angle(\mathbf{a},[\bar{1},1,0])$= 24.01°

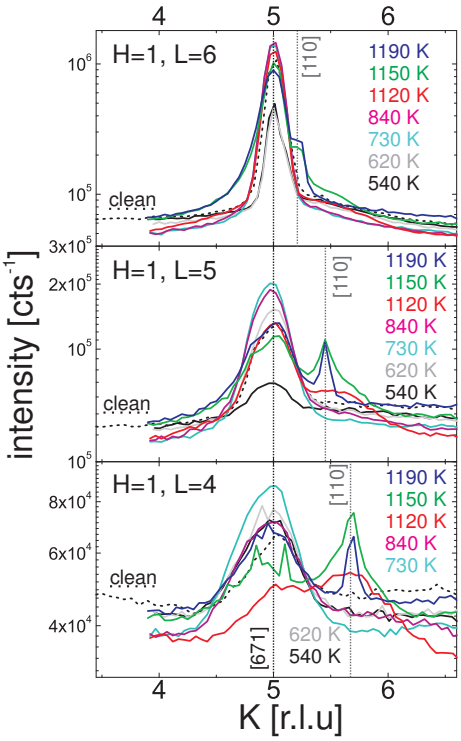

Figure 8.7: Temperature dependent K-scans along the $\mathbf{a}_2$-direction recorded after the oxidation for difference L values. A new peak arises at the (1,1,0) facet position (dashed grey line) while the CTR signal at K=5 (dashed black line) decreases at the same time. For comparison the K-scans of the clean surface are depicted by the black dashed lines. The K-scans at L= 4 are shown again in fig. 8.6a for clarity.

the signal has decreased compared to 1120 K. No new peaks are observed in the H-scans along the steps as no faceting occurs in this direction. Flashing the sample up to 1300 K reproduces the clean, regularly stepped (6,7,1) surface with no larger (1,1,0) facets.

8.1.3 Micro structure of the oxide

After annealing the oxidized sample to 1120 K for 240 s, LEED images were taken at room temperature and compared to the LEED pattern from the NiAl(1,1,0) surface prepared under the same conditions. As known from literature, twin domain formation is observed for the surface oxide on the (1,1,0) surface(see section 3.2.2) [42]. The twin domains are rotated by +24° and -24° with respect to the $[\bar{1},1,0]$-direction and are labelled "green" and "red" , respectively (see also fig. 8.8d). The LEED image of the low-index surface, presented in fig. 8.8b, shows reflections of both domains appearing with equal intensities. In the case of the vicinal surface, reflections from the "red" domain are much more intense than from the " green " one, as observed in the LEED image in fig. 8.8a. The suppression of one of the twin domains was also observed during the SXRD measurements. In fig. 8.8c

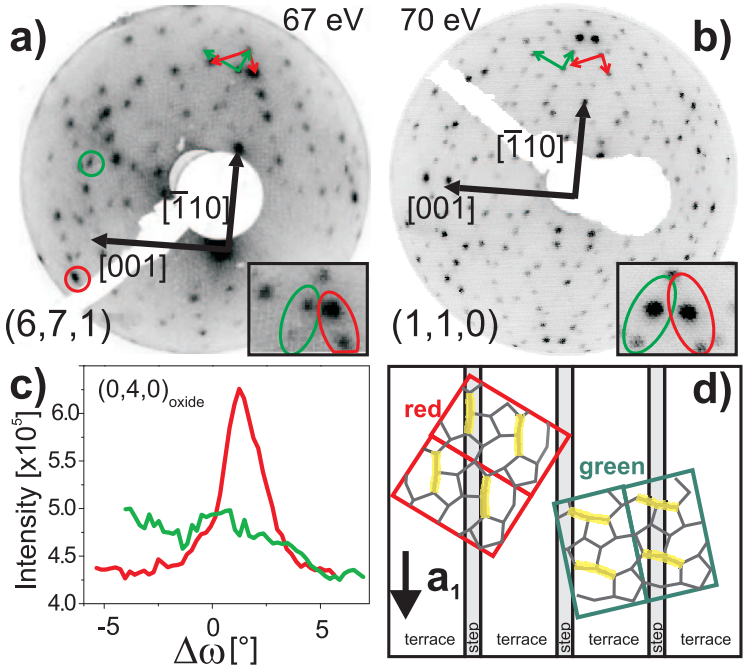

Figure 8.8: a and b are LEED images of the oxidized and annealed (6,7,1) and (1,1,0) surface, respectively. The black arrows mark bulk directions of the (1,1,0) NiAl surface. The green and red arrows show the reciprocal space unit cell of the two twin domains of the surface oxide. The insets highlight the more intense reflection of the "red" twin domain in case of the (6,7,1) surface showing preferential domain growth. In part c the rocking scans at the positions of the two twin domains confirm the single domain growth on NiAl(6,7,1). Fig. d shows a schematic top view of the vicinal surface and the two possible twin domain unit cell orientations. The grey grids inside the oxide unit cells mark the penta-heptagon pairs of interfacial Al-atoms. The yellow lines highlight dense, "quasi" rows of these Al-ions.

the corresponding rocking scans, recorded for each twin domain at the same oxide peak position (marked in the LEED image by a red and green circle), show a much stronger signal for the red domain. Therefore the experimental results demonstrate the preferential oxide growth of the "red" domain on the NiAl(6,7,1) surface.

8.1.4 Discussion

The Clean Surface

The CTR-measurements of the clean sample show that the regularly stepped and chemically ordered NiAl(6,7,1) surface is stable at room temperature under UHV conditions. It is also stable at 1190 K as the CTRs of NiAl(6,7,1) reappear after desorbing the oxide from the surface. No faceting of the clean surface is observed between room temperature and

1190 K. Thus, we conclude that the regularly stepped surface is thermodynamically stable in the investigated temperature and pressure range. The stability of clean vicinal surfaces against faceting is due to a step-step repulsion arising from the interaction of strain fields, present around every step. Capillary forces acting at the upper and lower side of a step create an elastic force dipole at the step. These dipoles are compensated by internal strain which is crucial for the stability on which temperature has only a little effect [14, 46].

The results from the CTR-measurements show a buckling of the Ni and Al atoms within the first two rows R1 and R2. The direction and the magnitude agree, within the error bars, with the buckling of around 0.2 Å and 0.04 Å found for NiAl(1,1,0) [12, 39]. This good agreement is reasonable as the relaxations of the central atoms of the relatively large, 7 atomic chains wide (1,1,0) terraces are only weakly affected by the occurrence of steps. The pronounced inward relaxation of Ni and Al at the step edge position S1, together with an outward relaxation of the atoms at the corner position C1 are characteristic for a surface step, as they arise from capillary forces acting at the surface on both sides across the step pulling atoms at the step inwards and at the corner outwards [14]. This leads to a rounding of the electron density at the steps, which is predicted by the theory of charge smoothing on surfaces and surface steps [13]. Similar relaxations of step and corner atoms are also found for Pt(9,7,7) in a combined MD and SXRD study or for Cu(1,1,5) in a DFT study [48, 144–147]. In one of few theoretical studies on vicinal binary alloy surfaces, LI_2-structured Cu_3Au(5,1,1) is investigated by DFT calculations [47]. The Cu_3Au(5,1,1) surface consists of 3 atomic chains wide (1,0,0) terraces, alternately composed of pure Cu and mixed Cu-Au chains with a buckling of Cu and Au within the mixed chains. The characteristic inward relaxation of step atoms and an outwards relaxations of the corner atoms is also reported. The study shows that buckling of the surface atoms which is found for many low-index surfaces of binary alloys can be also observed on vicinal surfaces. This finding is confirmed by our results on the NiAl(6,7,1) surface.

8.1.5 Oxidation of the surface

At 540 K and 6×10^{-6} mbar O_2 a vitreous alumina film is formed which possesses short-range but no long-range order. The formation of the Al_2O_3 layer does not remove the initial sequence of identical (1,1,0) terraces as shown by the CTR measurements (see also fig. 8.9a and b). Features like the oxide thickness, the Ni-, Al- and Ni anti-site- occupation profile and the relaxation profile observed for the surface region of the oxidized NiAl (6,7,1) surface are very similar to NiAl(1,1,0) [148]. On both surfaces the oxide film is 5 Å thick [4]. Strong inward relaxations of atoms especially within the first 3 rows are found for both surfaces. The step and corner atoms within the first two rows are also strongly shifted toward the bulk. As shown in the occupancy profiles (fig. 8.5c and d), Al vacancies reach up to a depth of 13 Å in the alloy and originate from preferential Al oxidation during the formation of the alumina film. Thereby the amount of Al missing in the alloy matches the amount of Al needed to form the 2 layer thin surface oxide known from NiAl(1,1,0) [4, 5]. At depths larger than 13 Å in the alloy the Ni sites are fully occupied. The Ni vacancies appear only very close to the oxide-alloy interface which could also be

interpreted as roughness. At a depth of around 5 Å only 23 % of the Al-sites are occupied by Al. As known from the NiAl bulk, an enhancement of the Ni concentration leads to the formation of Ni anti-sites (Ni on Al-sites) [149]. This effect is also found here at the depth of 5 Å. The relative increase of the Ni concentration due to preferential Al oxidation could also explain the aforementioned inward relaxation of the atoms within the surface region. For bulk NiAl the lattice constant decreases by 4 % if the Ni concentration is increased from 50 % up to 54 % due to Al vacancies [150]. Interestingly, the Al concentration directly at the interface within the first two rows is larger than in the deeper embedded third and forth rows. This might be due to Al drawn toward the interface during its preferential oxidation.

Oxygen-induced surface faceting and step bunching are found during the annealing of the oxidized NiAl(6,7,1) surface. Faceting during oxide formation was observed previously for other systems like Rh(5,5,3) or Pd(5,5,3) and for the NiAl(14,16,1) surface [49,50,52]. In this work we could demonstrate that after oxidation the kinetic barriers for faceting are removed at temperatures above 840 K. At these high temperatures material transport is possible. Both the substrate as well as the oxide undergo drastic structural changes where the former becomes faceted and the latter develops long range order. As depicted in the upper part of fig. 8.9b, the oxidized, but not annealed NiAl(6,7,1) surface can be schematically described by a regularly stepped interface covered by a disordered alumina film. It was shown that oxidation induces strong changes of the relaxation pattern within surface region, especially at the surface steps. The strain field around the steps is changed. We argue that these changes lower the strain-induced step-step interactions responsible for the stability of the clean surface. However, the regularly stepped structure is still maintained due to kinetic barriers. Annealing the sample provides the necessary energy and atom mobility for structural changes within the oxide, but also for material transport from the interface to the bulk. During the ordering of the oxide, the strain is also changed, because the oxide exerts a force on the substrate. At temperatures around 730 K this induces the transformation from short-range to small amounts of long-range ordered oxide on the regularly stepped terraces while kinetic barriers are still too high for faceting. The crystallization process is believed to start at the surface steps. Strain, set up between the ordered oxide and the alloy, is released preferentially along the steps, thereby lowering the barriers for surface oxide formation directly at the steps. This idea is supported by STM images of oxidized NiAl(14,16,1), taken after annealing up to 1000 K. They show the steps acting as nuclei for surface oxide formation [52]. At a temperature of 1120 K kinetic barriers for material transport are overcome. As more short-range ordered oxide is transformed into long-range ordered oxide, the regularly stepped (1,1,0) terraces are lifted in favour of large (1,1,0) facets, covered by long-range ordered alumina (see fig. 8.9c). At 1150 K oxide first starts to desorb from smaller facets, which adopt the regular pattern of the clean (6,7,1) surface again (see fig. 8.9d). Only large facets remain, covered by long-range ordered oxide, explaining the sharp peak found in the corresponding K-scan. Further annealing promotes this process until all oxide is desorbed. We conclude that the occurring (1,1,0) and (0,1,1) facets are energetically favourable for the oxide-alloy interface, while for the clean surface the regularly stepped (6,7,1) has the lowest surface free

energy.

The structure of the long-range ordered oxide was determined to be the complex, ultrathin $Al_{10}O_{13}$ surface oxide which is known in detail from the oxidized NiAl(1,1,0) surface(see section 3.2.2) [3–5, 42]. Our results show the step-induced preferential formation of one oxide twin-domain which is labelled "red" in fig. 8.8d. Such favoured domain growth was also reported for NiAl(14,16,1) where strain release along the direction of the anti-phase domain boundaries(APDBs) is argued to be a possible reason [52]. Unlike their study, the APDBs, which run along the short axis of the oxide unit cells, are not aligned parallel to the step direction $\mathbf{a}_2$ for the NiAl(6,7,1) surface. Therefore this explanation does not hold for the preferential domain growth observed here. In case of the surface oxide on NiAl(1,1,0) interfacial Al ions form pentagon-heptagon pairs as Al atoms prefer Ni neighbours [5]. These pairs are indicated as grey lines within the oxide unit cell in fig. 8.8d. They exhibit "dense" quasi rows of interfacial Al atoms running along certain directions. Along these rows, which are marked yellow in figure 8.8d, increased strain is built up. Strain can be preferentially released along the steps ($\mathbf{a}_1$-direction). This favours the initial growth of the "red" domain, where the Al quasi-rows are parallel to the $\mathbf{a}_1$-direction ($[\bar{1}1\bar{1}]_{\text{bulk}}$-direction), over the green domain. For the NiAl(14,16,1) it is reported that the step edges have a ragged shape with many sections running along the $[\bar{1}1\bar{1}]_{\text{bulk}}$-direction [52]. Therefore, this explanation would also hold for the preferential domain growth on NiAl(14,16,1).

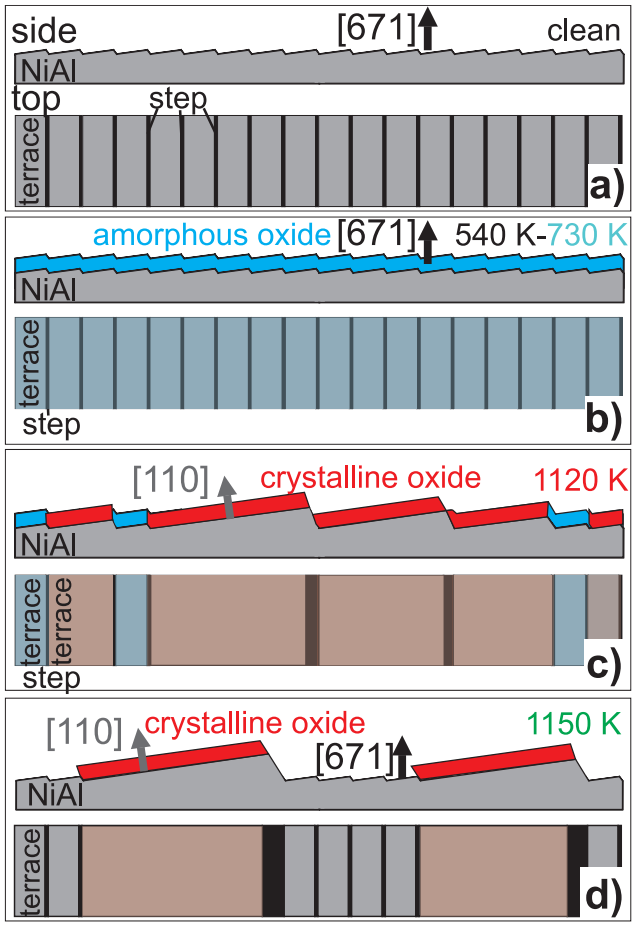

Figure 8.9: a-d show schematic top and side views of the clean sample and the oxidized sample at three different annealing steps. The clean regularly stepped (6,7,1) surface is maintained after oxidation and covered by disordered oxide between 540 K and 620 K. At higher temperatures of 1120 K oxide is transformed into long-range ordered alumina which induces the formation of large (1,1,0) facets. At 1150 K small oxide domains start to desorb and only large oxide domains remain on large facets.

8.2 The NiAl(4,3,0) Surface

8.2.1 Sample Preparation and Experimental Details

The single crystal was prepared in the same way like NiAl(6,7,1) and is investigated in the same experimental chambers (see section 5.1.4). After preparation AES was used to check for surface contaminations. The spectra (see fig. 8.10) of the prepared surface clearly show the signal of metallic Ni and Al while no signal of the major impurities like sulphur, carbon and oxygen could be detected. The contamination free sample surface was oxidized for 900 s at 550 K and the two different O_2 pressures of 6×10^{-6} mbar and 1×10^{-7} mbar, respectively. To obtain a long-range ordered surface oxide the sample was annealed stepwise at temperatures between 550 K and 1190 K.

The SXRD experiments were carried out with a photon energy of 20 keV ($\lambda = 0.62$ Å) at beamline ID03 of the ESRF, which is described in section 5.1.2. The incidence angle during the measurements was fixed very close to the critical angle of NiAl ($\alpha_c = 0.14°$ at 20 keV) which reduces the background signal originating from the NiAl bulk. For the measurements a 2D-MAXIPIX detector with 256×256 pixel^2 was used like a point detector as some CTR reflections were broad. The CTR data were obtained by taking rocking scans at each point along the CTR, followed by an integration and applying standard corrections [61]. Four fundamental and two superstructure CTRs were measured, resulting in 95 independent structure factors. In absence of redundancy of the data, the average error was set to 15 %. This is a relatively big error which was chosen due to a high noise on the data. To analyse the data, the program ROD was used again.

The HRCLS experiments were performed at the beamline I311 at Max Lab [94]. The photoemission measurements were performed at 130 K sample temperature, at a fixed in-

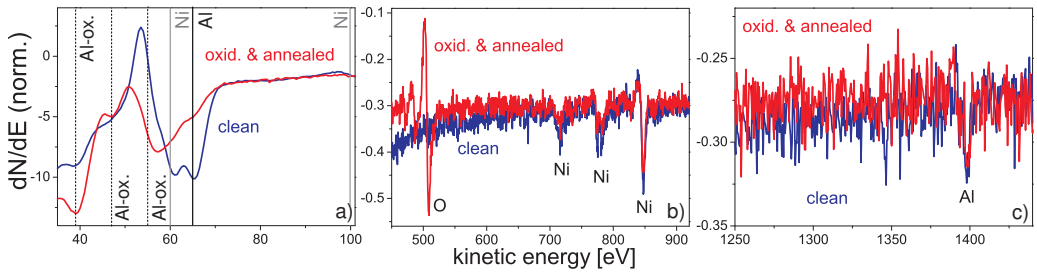

Figure 8.10: AES spectra of the NiAl(4,3,0) surface after the cleaning procedure (blue line) and oxidation and annealing (red line). a) Spectra of the low-energy part. The vertical lines indicate the following elements: metallic Al (LVV, 65 eV), metallic Ni(MVV, 60 and 100 eV) and oxidized Al (39, 47 and 55 eV). b) Spectra in the energy range of O (KVV, 510 eV) and Ni (LVV, 716, 775, 781 and 846 eV) where no O signal is detected for the clean surface. c) Spectra in the energy range of Al (KVV, 1390 eV); a small peak is detected for both surface conditions [129].

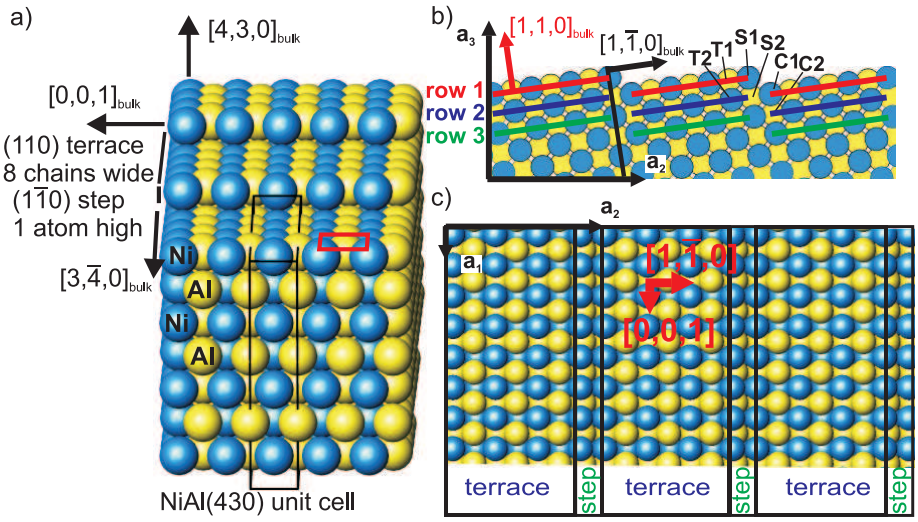

Figure 8.11: a) 3D view of the bulk-terminated NiAl(4,3,0) surface with the step atom occupied by Ni: Thin black lines mark the orthorhombic unit cell ($a_1 = 2.887$ Å, $a_2 = 14.435$ Å, $a_3 = 14.435$ Å). The red rectangle marks the surface unit cell of the (1,1,0) surface. b) Side view of the surface along the steps: one quasi row R consists of 7 layers perpendicular to the surface normal. Atoms within one row are allowed to relax element specifically. Characteristic step, corner and terraces atoms are labelled S1,S2,C1,C2,T1 and T2 and can relax independently from the other row atoms within the a_1-a_2 plane. c) Top view on the surface with the (1,1,0) surface unit cell.

cident angle of about $55°$ and at normal emission. For all measured spectra a scan of the Fermi level region was recorded immediately afterwards and used as binding energy reference. During the sample preparation for the core level measurement all major impurities could be removed except a small amount of carbon. In the experiment we find no characteristic changes of the spectra of the clean surface with respect to the amount of carbon on the surface. Therefore the contribution of carbon to the spectra can be neglected in this case.

The real space structure of the bulk terminated NiAl(4,3,0) surface is depicted in fig. 8.11. The [4,3,0]-direction makes an angle of 8.1° with respect to the [1,1,0] direction. The surface consists of 8 atomic rows wide (1,1,0) terraces (14 Å) with mono-atomic (1,$\bar{1}$,0) steps. The real space surface unit cell is defined by the orthogonal vectors ($\mathbf{a}_1$,$\mathbf{a}_2$,$\mathbf{a}_3$), where $\mathbf{a}_1$ runs along the steps in the [0,0,1] direction of bulk bcc NiAl, $\mathbf{a}_2$ across the steps in the $[3, \bar{4}, 0]$ direction and $\mathbf{a}_3$ defines the $[4, 3, 0]$ surface normal. The described unit cell contains 25 Ni and 25 Al atoms. Note, that the termination of the step atoms depends on the height of truncation. A unit cell with Ni terminated steps is depicted but, in principle, an Al terminated step is also possible. No ragged shape of the step edges is expected as the $\mathbf{a}_1$ direction points along a low-energy step orientation on the (1,1,0) surface [52]. The corresponding reciprocal lattice is also orthorhombic, with the reciprocal coordinates

(H,K,L) running in the directions described above. A side view of the reciprocal space along the $\mathbf{a}_1$-direction is shown in fig. 4.4b.

8.2.2 Experimental Results

Atomic Structure of the Clean Surface

A LEED image of the prepared NiAl(4,3,0) sample is shown in fig. 8.12a. It nicely shows the characteristics of a vicinal surface with a larger periodicity of the reflections along the steps, corresponding to the [0,0,1] lattice parameter, and a smaller periodicity across the steps. From the observation of numerous, sharp reflections along the $[1, \bar{1}, 0]$-direction we conclude that a well ordered, regular terrace-step structure is present at the surface. From the peak-to-peak distances within the intensity profile across the steps of fig. 8.12d, an average lattice parameter of 14.4 Å is calculated. This is in excellent agreement with the corresponding lattice parameter of the NiAl(4,3,0) surface of a_2=14.4(35) Å. The specular x-ray reflectivity, like shown in fig. 8.17, is fitted with a model of bulk-like NiAl, including roughness. The obtained roughness of 0.8 Å is small and confirms the presence of a smooth surface.

Like for the (6,7,1) surface in section 8.1, CTR measurements of the clean sample are performed. The experimental structure factors are shown in fig. 8.13. To fit the CTRs of the (4,3,0) surface a simplified structural model similar to the one used for the (6,7,1) surface is introduced. The parameters of this model are depicted in fig. 8.11b. During the annealing up to 1300 K Al atoms start to evaporate why the possibility of Al vacancies is included in all fitting models. On the NiAl(4,3,0) surface the step atom S1 can be either solely occupied by Al or Ni. Thus the sample surface could be either covered solely by Ni-terminated steps or Al-terminated steps or consist of fractions with both termination. All three possibilities are tested during the data analysis.

In fig. 8.13 the experimental data are compared with the CTRs calculated from the best fits of the structural model described above. The blue, red and green solid lines show the results of the Al-terminated, the Ni-terminated and the mixed-termination model, respectively. The corresponding real space models are presented in fig. 8.14, the parameter values of the fits are listed in the tables 8.3 and 8.4. The data agreement of the three models is very similar with residua of χ^2_{norm} = 2.7 (22 fitting parameters) for the Al-terminated surface, χ^2_{norm} = 2.6 (22 fitting parameters) for the Ni-terminated surface and χ^2_{norm} = 3.2 (24 fitting parameters) for both step-terminations present. The fit with the model of mixed step terminations results in a 4:1-ratio of Ni to Al terminated steps. As the lowest residuum is achieved with the Ni-terminated surface, the results point towards a clean NiAl(4,3,0) surface which is mainly covered with steps occupied by Ni atoms. However, the differences in the residua are too small to make a final conclusion. Fortunately, the found relaxations are similar for all three models which allows to determine the following results. All three models result in rumpling of Ni and Al within the first row R1 with values between 0.10 Å to 0.16 Å. The rumpling of the second row R2 lies between 0.00 Å and 0.02 Å. No relaxations are observed within the following rows. Al atoms relax

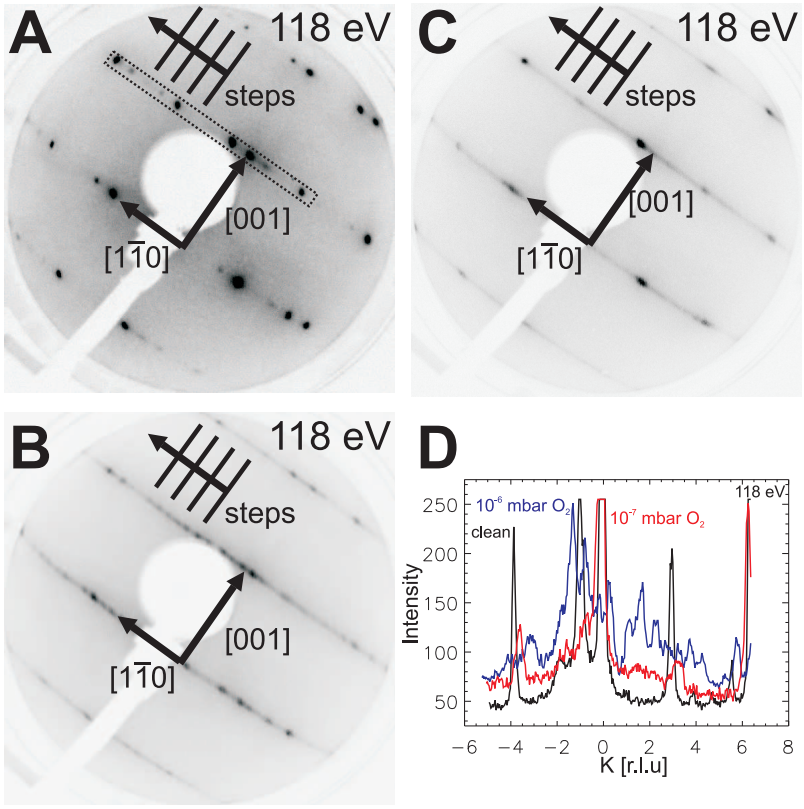

Figure 8.12: LEED images measured at a electron energy of 118 eV for different conditions. The [0,0,1]-direction runs along the steps, the [1,$\bar{1}$,0] point across the steps and lies in the (1,1,0) terraces. a) Image of the clean (4,3,0) surface with a smaller distance between the reflections across the steps and larger distance along the steps. b) Image taken after oxidation at 550 K and 1×10^{-7} mbar O_2 and annealing to 1100 K. The periodicity of the clean surface is maintained along the step, diffuse stripes of intensity across the step are observed. c) Image taken after oxidation at 550 K and 5×10^{-6} mbar O_2 and annealing to 1100 K. Along the [1,$\bar{1}$,0] direction peaks with short periodicity occur. d) Intensity profile of the three LEED images along the area marked in image a) by the dashed box. The black line shows the profile of the clean image, the red and blue line correspond to the sample oxidized at 1×10^{-7} mbar and 5×10^{-6} mbar O_2, respectively.

outwards, Ni inwards. The atoms at the step position S1 and at the neighbouring terrace position T1 are strongly relaxed inward towards the bulk. Atoms at the corner positions S2 and the neighbouring terrace position C1 are relaxed outwards. For the other positions T2 and S3 no relaxation direction consistent with all three models could be determined. Allowing vacancies of Ni and Al within the first three rows results in fully occupied sites for the Al-terminated and the mixed model, while 26 % Al vacancies occur within row R1 for the Ni terminated model.

In addition to the best-fitting structural models described above, the influence of sev-

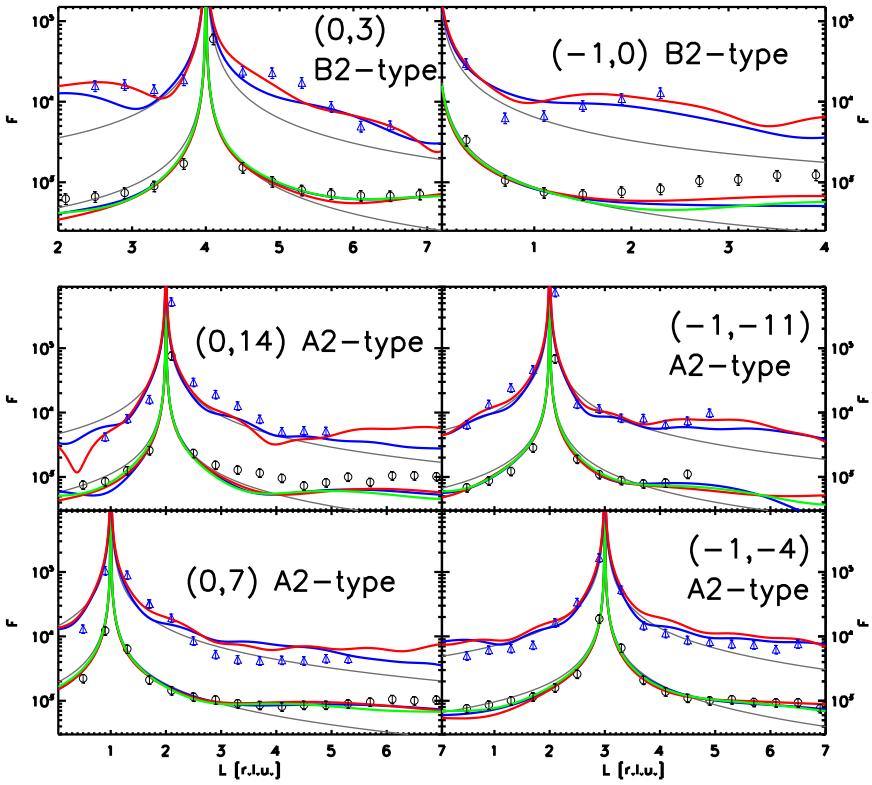

Figure 8.13: Four fundamental(A2-type) and two superstructure (B2-type) CTRs were measured for the clean (black circles) and oxidized, but not annealed surface (blue triangles),respectively. The results of the bulk terminated structural model are shown by grey solid lines. The results of the best fitting models with Al or Ni terminated step are depicted by blue and red lines, respectively. The green line belongs to the results of the model with both step termination on the surface. The two data sets are shifted for clarity.

eral other parameters was investigated systematically. From the grey line in fig. 8.13 it is obvious that a bulk terminated crystal does not reproduce the fundamental and the superstructure CTRs (χ^2_{norm}=9.8). Allowing only a_3-relaxations of the Al and Ni atoms in the rows R1 and R2, like known from NiAl(1,1,0), but no individual relaxations of atoms around the steps improves the residue resulting from the bulk-like crystal only slightly [12]. Applying the same model like for the best fit of the clean (6,7,1) surface strongly improves the residuum to χ^2_{norm}=3.1 for the Al-terminated model and χ^2_{norm}=3.9 for the Ni-terminated model. This shows the importance of the characteristic relaxations of step and corner atoms for the fit results. Fitting of the static Debye-Waller factor of the undercoordinated surface atoms did not improve the residue. Despite the intensive test of different parameters the agreement between data and fits is not perfect. Allowing even more atoms around the steps to relax individually in the $\mathbf{a}_2$- and $\mathbf{a}_3$-direction increases the residue again. The residuum depends on the number of parameter and of data points.

Table 8.3: Results of the structural refinement of the clean (4,3,0) surface for the model with Ni terminated step and the model with Al terminated step. Listed are the displacements Δz along the surface normal and Δy in the direction across the steps for each atom in the rows R1 and R2 as well as at the steps, corners and terraces (S1, S2, S3, T1, T2, C1 and C2). All displacements from the bulk positions are given in Å. The fit with the Ni terminated step results in (24$\pm$12) % Al vacancies in row R1, no vacancies are found applying the Al terminated model.

	Ni term. step		Al term. step	
El./Pos.	Δz (-)	Δy (-)	Δz (-)	Δy (-)
Al/R1	0.00(12)	0.00(3)	0.00(12)	0.00(3)
Ni/R1	-0.12(3)	-0.02(1)	-0.16(3)	-0.02(1)
Al/R2	0.00(12)	0.00(3)	0.00(12)	0.00(3)
Ni/R2	-0.02(3)	-0.00(6)	0.00(3)	0.00(6)
-/S1	-0.4(2)	-0.1(4)	-0.4(9)	-0.1(9)
-/S2	0.3(3)	0.1(5)	0.3(3)	0.0(4)
-/S3	0.0(2)	-0.1(2)	-0.1(2)	0.3(4)
-/C1	0.4(3)	-0.1(4)	0.4(6)	0.0(8)
-/C2	0.3(6)	-0.1(8)	0.0(3)	-0.2(4)
-/T1	-0.3(9)	-0.2(9)	-0.3(2)	-0.1(4)
-/T2	0.3(3)	0.0(4)	-0.3(3)	-0.2(5)

Table 8.4: Results of the structural refinement of the clean (4,3,0) surface for the model with Ni and Al step atoms present at the surface. Listed are the displacements Δz along the surface normal and Δy in the direction across the steps for each atom in the rows R1 and R2 as well as at the steps and corners (S1, S2, C1 and C2). All displacements from the bulk positions are given in Å. The fit results in (2$\pm$10) % Al vacancies within the first row. (77$\pm$8) % of the surface is covered with Ni step atoms, (23$\pm$10) % with Al step atoms.

	Ni term. step		Al term. step	
El./Pos.	Δz (-)	Δy (-)	Δz (-)	Δy (-)
Al/R1	0.00(12)	0.00(3)	0.00(12)	0.00(3)
Ni/R1	-0.13(3)	-0.02(1)	-0.13(3)	-0.02(1)
Al/R2	0.00(12)	0.00(3)	0.00(12)	0.00(3)
Ni/R2	0.00(3)	-0.00(6)	0.00(3)	0.00(6)
-/S1	-0.4(2)	-0.1(4)	0.0(9)	-0.2(9)
-/S2	0.4(3)	0.1(5)	0.4(3)	-0.1(4)
-/C1	0.4(3)	0.0(4)	-0.4(6)	-0.4(8)
-/C2	0.4(6)	-0.4(8)	-0.4(3)	-0.4(4)

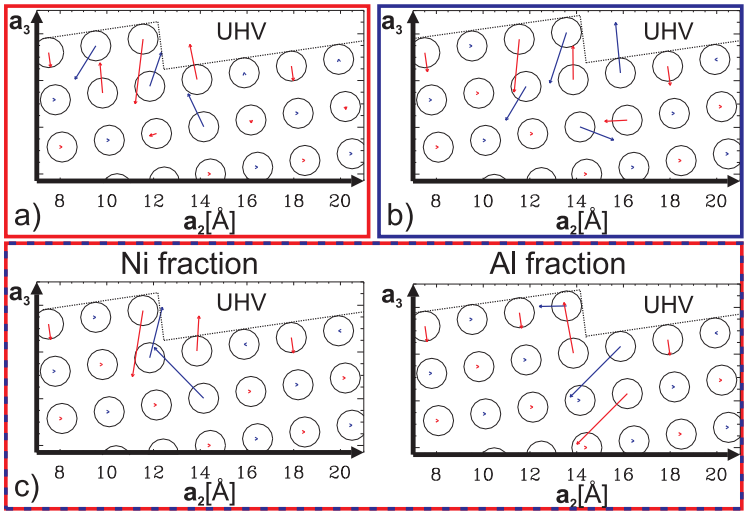

Figure 8.14: The figures show schematic side views of the relaxation profiles of the clean sample, resulting from the CTR fits of fig. 8.13. The red and blue arrows illustrate the displacements of Ni and Al atoms from their bulk positions, respectively. The arrows are enlarged by a factor of 5 for clarity. Part a, b and c depict the results of the Ni terminated model, the Al terminated model and the model with both terminations, respectively.

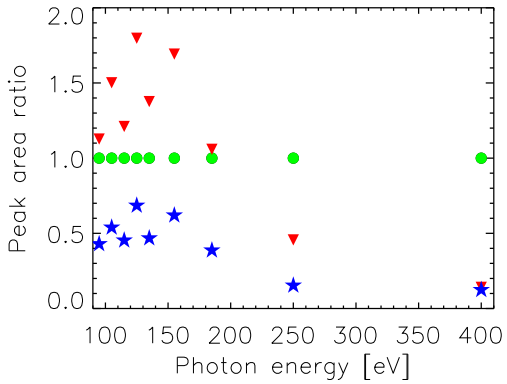

Figure 8.15: Intensity ratio of the three Al2p components of fig. 8.16b versus photon energy. The ratio of the surface component "a" to the bulk component "b" is shown by red triangles, the ratio of the corner component "c" to component "b" by blue stars.

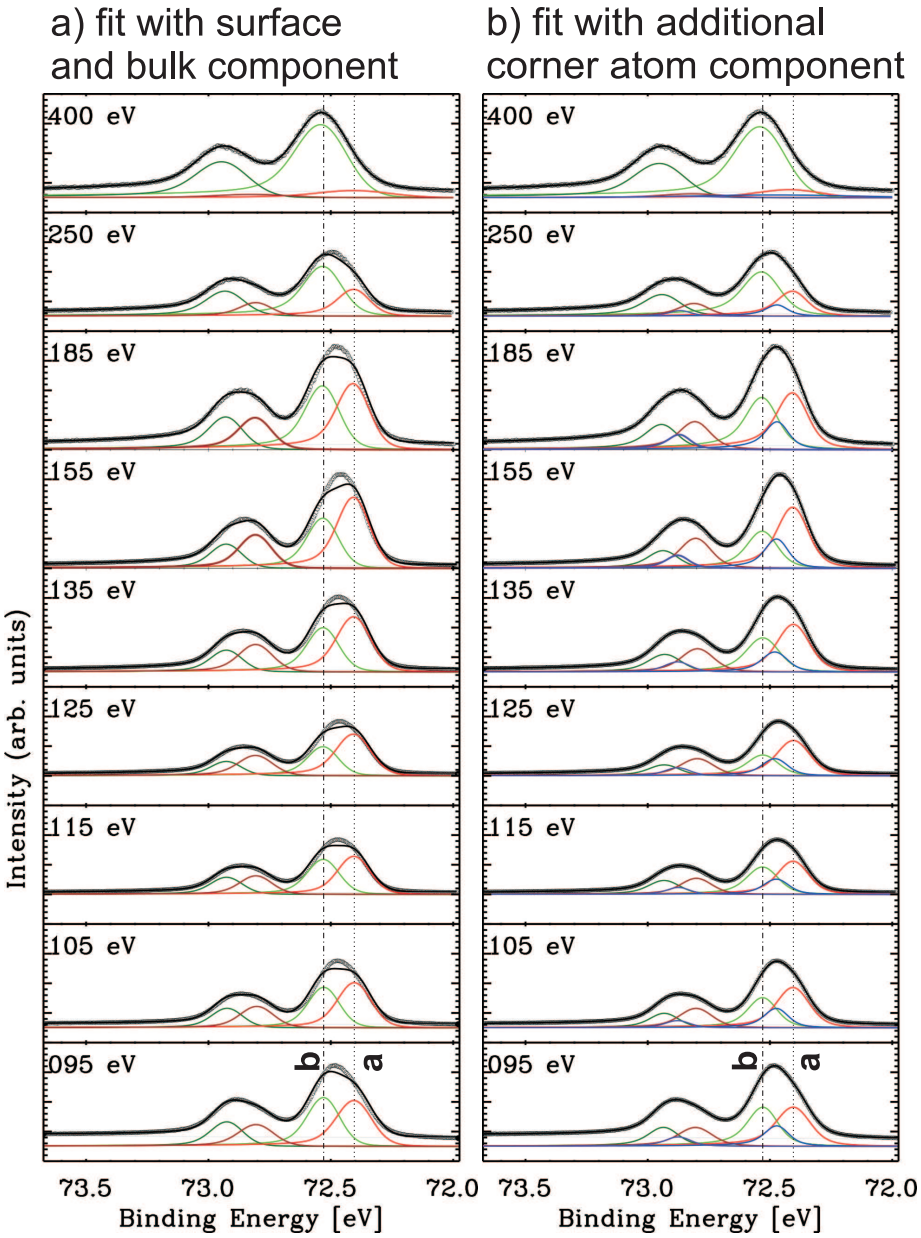

Figure 8.16: Normal emission Al2p spectra (open circles) measured at the indicated photon energies. Part a) shows the decomposition of the spectra into shifted components. The green lines are the spin-orbit doublet of the bulk component "b", the red lines are the spin-orbit doublet of the surface component "a". Part b) shows the decomposition of the spectra into three chemically shifted components with the new signal "c" (blue lines) lying energetically between bulk and surface component. The grey lines represent the linear background, the black solid lines represent the total fit curve.

For complementary information a series of HRCLS spectra was measured of the clean surface at different photon energies, like shown in fig. 8.16. From HRCLS measurement of the NiAl (1,1,0) surface it is known that the spectra arise from two type of photoelectrons emitted from bulk and surface Al, respectively [82]. While the Al2p bulk and surface component, labelled "a" and "b" in fig. 8.16, can be nicely resolved for the flat (1,1,0) surface, this is not possible for the stepped (4,3,0) surface. Two effects can explain this observation. On the one hand disorder of atoms at the surface can lead to a broadening of the surface signal. However, a LEED image, taken immediately after the HRCLS-measurements, is very similar to fig. 8.12a and shows sharp reflections. This indicates that only little surface disorder is present, which revises this first explanation. On the other hand it is known for HRCLS spectra of vicinal surfaces that fingerprints of terrace (here: T1,...), step (here:S1) and corner (here:S2) atoms can be detected as they all have different coordination numbers [151]. The signal of the most undercoordinated step atom is shifted to lower binding energies with respect to the terrace (or surface) atom component. The signal of corner atom underneath the step atom has a binding energy between the signal of the terrace and the bulk atoms. For the HRCLS data of NiAl(4,3,0) this could mean that an additional component occurs between the bulk and surface component making it impossible to resolve the surface from the bulk signal. No shoulder toward lower binding energies is detected for the Al2p peaks. According to the second explanation this indicates that most of the steps are Ni terminated. The corner atoms underneath the step atoms are occupied by Al, then.

A detailed analysis of the presented spectra affirm the idea of Al atoms present at the corner position S2. Fig. 8.16a shows the best fit achieved with a two component model like it was used for the (1,1,0) surface. The energy position of component "a" was determined from the spectra with the highest photon energy and therefore the highest contribution of bulk electrons. The energy of Al2p3/2 electrons was set to E_a = 72.53 eV, the spin orbit shifted energy of Al2p1/2 electrons to E_a = (72.53 + 0.40) eV [152]. The energy shift of (-0.13 $\pm$ .01 eV) for the signal of the surface electrons was assumed to be identical to the (1,1,0) surface. The fit results fulfil the 2-to-1 ratio expected for the spin orbit Al2p doublets within the experimental errors. The best fit with this model does not reproduce the maxima of the measured spectra well and results in a high average residue of $R_\varnothing$ = 5.2 per spectra. Introducing a new component "c" between the surface and bulk signal, arising from electrons of Al at the corner position S2, strongly improve the data agreement with $R_\varnothing$ = 0.9, like shown in fig. 8.16b. Again the fit results fulfil the 2:1 ratio of the peak areas, expected for the spin orbit splitting. The photon energy dependent ratios of the peaks areas are plotted in fig. 8.15. The surface and the corner signal decrease for high photon energies as the contribution of the bulk signal is getting stronger for longer electron mean free paths. The averaged area ratio of corner with respect to the surface component is 0.36. This is reasonable as for every Al atom at the corner position there are 3 Al atoms on the terrace, resulting in a ratio of 1/3.

parameter	clean	oxidized	oxid. and annealed
σ_{NiAl} (Å)	0.8	1.0	1.0
σ_{ox} (Å)	-	1.4	3.4
t_{ox} (Å)	-	5.5	5.1
$\rho_{ox}/\rho_{Al_2O_3}$	-	1	0.7

Table 8.5: Results of the x-ray reflectivity measurements of the clean, oxidized and oxidized and annealed surfaces. The root-mean-square roughness (σ) for the interfaces, the oxide thickness (t) and the oxide density ρ_{ox} (compared to corundum) are shown.

Atomic Structure after Oxidation

X-ray reflectivity measurements (see fig. 8.17) after the oxidation at 550 K and 6×10^{-6} mbar O_2 show the presence of a 5.5 Å thick oxide layer. The layer possesses no long-range order, since no diffraction pattern could be detected by LEED. Fig. 8.22 shows K-scans through the (0,7) CTR recorded after the oxidation. We observe that the detected peak is not centred at K=7 any more but shifted to lower K values. The new K positions can be explained by the formation of (1,1,0) facets which nominal position is also marked in fig. 8.22. The facet signal is very broad, which means that the formed facet are small. Furthermore the signal is very weak and the background relatively high which indicates

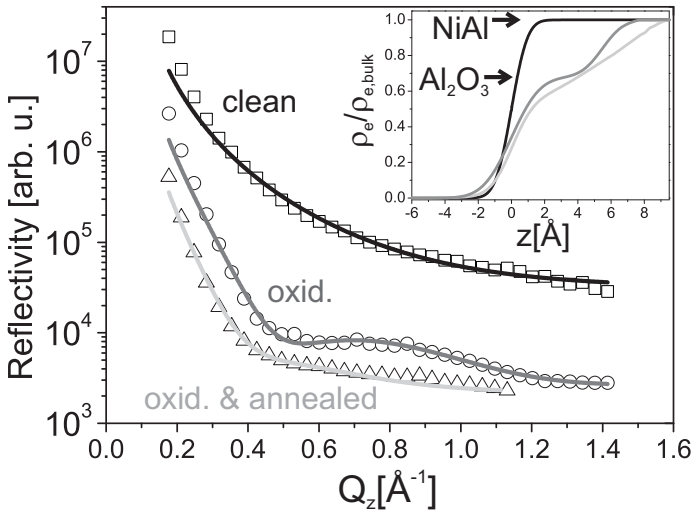

Figure 8.17: X-ray reflectivity curves obtained from the clean (squares), the oxidized (circles) and the oxidized and annealed (triangles) surface; the curves are shifted for clarity. The fits (solids lines) were obtained using the Parrat formalism, the results are given in table 8.5. The inset shows the resulting electron density (ρ_e) profiles as a function of the z direction along the surface normal.

a oxygen induces increase of the surface roughness. The nearly complete disappearance of the CTR signal at its original position can be explained by roughness or by a complete disappearance of the regular terrace-step structure of the (4,3,0) surface.

To characterize the morphology and oxidation induced segregation of the interfacial region, we still measured the CTRs of the oxidized, but not yet annealed surface. They are shown in fig. 8.13. The noise on the rocking scan signal increased compared to the measurements on the clean surface. It increases the systematically error and further limits a detailed structural analysis. Compared to the CTRs of the clean sample, oscillations are visible after the oxidation, in line with a disturbed chemical composition in the near surface region. The defects and distortions occur up to a well defined depth, which is observed by characteristic oscillations on the CTRs. Therefore the structural fitting model, described in the previous paragraph, was extended for the analysis of the oxidized surface. Atomic relaxations as well as Ni and Al vacancies and Ni anti-sites were allowed within the first 6 rows (R1 to R6, see fig. 8.11). As for the clean surface, the influence of the parameters was tested for the three possible scenarios: the presence of solely Ni-terminated steps, solely Al-terminated steps or a mixture of both.

The best fit results for the Al-terminated ($\chi^2_{norm} = 5.4$, 34 parameters) and Ni-terminated ($\chi^2_{norm} = 4.1$, 30 parameters) model are shown in fig. 8.13. The corresponding relaxations of the Ni-terminated model are given in table 8.6 and schematically depicted in fig. 8.18. The best fit of the model with Al and Ni steps resulted in a surface purely covered with Ni steps. The best-fit residue of the Ni terminated model is 25 % lower than for the Al terminated model. This trend of the fitting results towards a surface with solely Ni steps is in good agreement with the preferential Al oxidation. Most Al atoms at the surface, especially at the steps, are oxidized. This leaves the oxide-alloy interface Ni-terminated. An inward relaxation of Ni is found in the first four rows (R1 to R4) and on the positions S1 and C1. Al relaxes inward within the first row R1 and outward in the further three rows. No relaxations are found from the fifth row onward.

The occupation profiles for the Ni and Al sites resulting from the best fit achieved with the Ni-terminated model are shown in fig. 8.18b and c, respectively. In fig. 8.18b we observe, that the occupancy of Ni-sites is disturbed within the first three rows away from oxide-alloy interface. From row R4 onwards Ni sites are occupied bulk like. It can be shown that the fundamental but not the superstructure CTRs are reproduced well by a structural model with only three disturbed surface rows. This shows that the electron density reaches a bulk-like value from the forth row onwards. The occupancy profile of the Al sites, depicted in fig. 8.18c, shows the oxidation induced decrease of the Al concentration within the first 6 rows of the alloy. This corresponds to a depth of 12 Å away from oxide-alloy interface. The Al concentration decrease is accompanied by the formation of Ni anti-site atoms (Ni on Al sites). It can be observed that the more Al is missing the more Ni anti-sites occur.

As for the clean surface, the influence of the several parameters on the quality of the fit was examined by applying different structure models. In all tested models the occupancy profile was allowed to vary. For the presented best-fit model only the atoms at position S1 and C1 are relaxed individually along the $\mathbf{a}_2$- and $\mathbf{a}_3$-directions. These individual re-

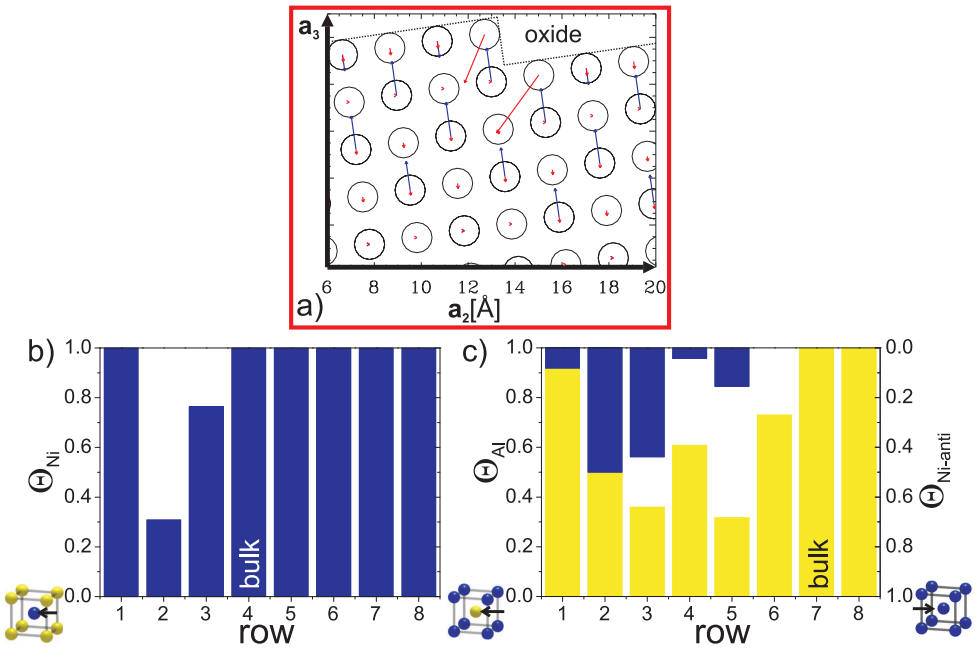

Figure 8.18: a) Schematic side view of the relaxation profile of the oxidized sample, resulting from the CTR fit with Ni terminated step atoms. The relaxations of the Al and Ni atoms are presented by blue and red arrows, respectively. The arrows are magnified by a factor of 5. The black circles show the bulk positions of the atoms. b)+c) Row-dependent (R1,R2,...) occupancy profile for Ni, Al and Ni anti-sites of the oxidized surface region. "Quasi"-row 1 is at the oxide-alloy interface. The sketched bulk unit cells indicate the different sites.

laxations might occur for many atoms in the vicinity of the steps (S2,S3,T1,T2, 2,C3,...). Furthermore, the segregation profile close to the steps might be different than along the terraces. However, the measured data set is not large enough and the systematical error is too large to include all these described additional parameters.

The HRCLS Al2p spectra of the oxidized sample are shown in fig. 8.19a. Three spin-orbit split doublets, labelled "b" (green line), "d" (blue line) and "e" (red line), can be observed. Component "b" is attributed to metallic Al atoms within the NiAl alloy. Component "d" and "e" are assigned to Al bonding to oxygen atoms. While doublet "e" is ascribed to Al coordinated like in bulk Al oxide, doublet "d" occurs due to Al atoms bonded to three oxygen atoms [153]. Fitting the spectra with the described three spin-doublets results in a good average residue of 0.9 per spectrum. The three spin doublet components and their sum are shown in fig. 8.19a. Dividing the doublet "b" into a surface and bulk peak like for the clean surface does not improve the residue. Fig. 8.21a depicts the area ratio of component "b" and "e" to component "d" as a function of photon energy, i.e. as function of the electron mean free path. The relative signal of component "d" (compared to component "e") is getting stronger toward higher photon energies and therefore larger information

Table 8.6: Results of the structural refinement of the oxidized surface for the model with Ni terminated step. Listed are the displacements Δz along the surface normal and Δy in the direction across the steps for each atom in the rows R1 to R4 as well as at the steps and corners S1 and C1. All displacements from the bulk positions are given in Å. The corresponding occupancy profile is shown in fig. 8.18

	Ni term. step	
El./Pos.	Δz (-)	Δy (-)
Al/R1	-0.14(12)	-0.02(3)
Ni/R1	-0.06(3)	-0.01(1)
Al/R2	0.29(12)	0.04(3)
Ni/R2	0.00(3)	0.00(6)
Al/R3	0.29(10)	0.04(3)
Ni/R3	-0.05(3)	-0.01(5)
Al/R4	0.25(10)	0.03(3)
Ni/R4	-0.04(3)	-0.01(5)
Ni/S1	-0.4(2)	-0.2(4)
Ni/C1	-0.4(3)	-0.4(4)

depth. It is assigned to photo electrons of Al at the oxide-alloy interface. The O1s spectra of the oxidized sample recorded at different incoming photon energies are shown in fig. 8.20a. The shoulder of the O1s signal towards higher binding energies shows that two differently bonded O atoms are present in the oxide layer. A detailed analysis of the spectra, using a two peak model, results in a good average residue of 1.1. The results is depicted in fig. 8.20b. The fitted spectra consist of a peak at $E_{BE,I}$= 531.85 eV and a peak at a lower binding energy of $E_{BE,II}$=531.10 eV, labelled "I" and "II", respectively. As seen from the single components of the spectra, the area ratio of component "I" to "II" versus the photon energy shows a small decrease towards higher photon energies. This indicates that the O atoms of type "I" are located closer to the oxide surface.

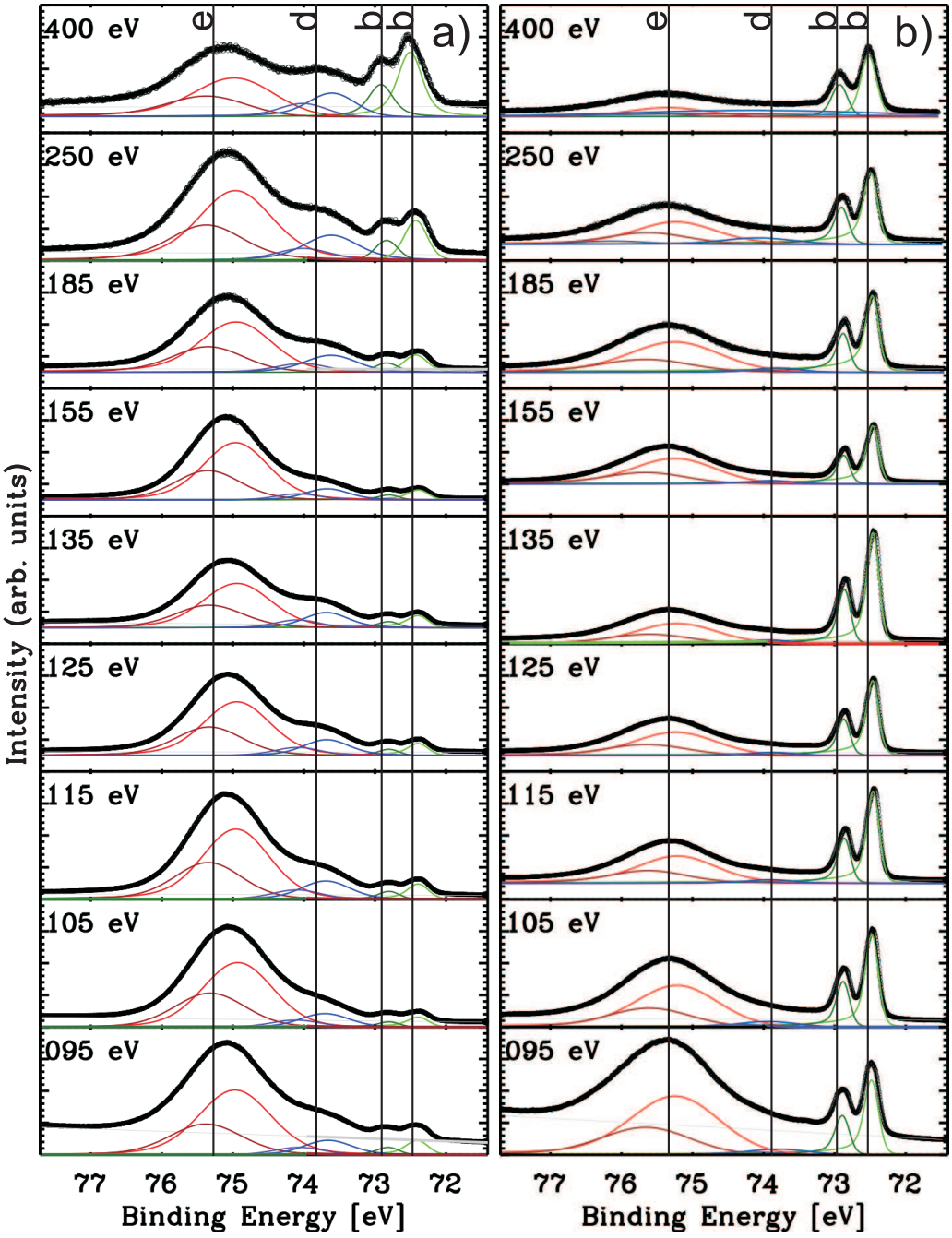

Figure 8.19: Normal emission Al2p spectra measured at the indicated photon energies measured for the oxidized surface (a) and the oxidized and annealed surface (b). The three observable spin-orbit doublets, labelled "b", "d" and "e", are indicated by vertical black lines. The fit is decomposed into these three doublets. The solid black line represents the total fit curve.

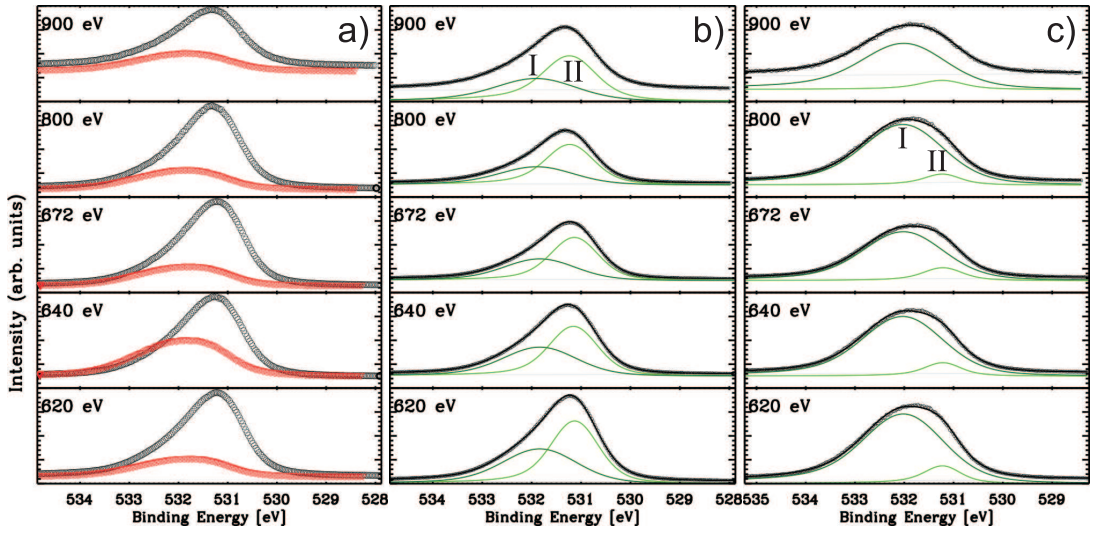

Figure 8.20: Normal emission O1s spectra measured at the indicated photon energies. a) Comparison of the spectra of the oxidized surface (black) and the oxidized and annealed surface (red). b) and c) show the spectra of the oxidized surface and the oxidized and annealed surface, respectively. Both series of spectra are decomposed into two oxygen components at $E_{BE,II}$=531.10 eV and $E_{BE;I}$=531.85 eV. The solid black line represents the total fit curve.

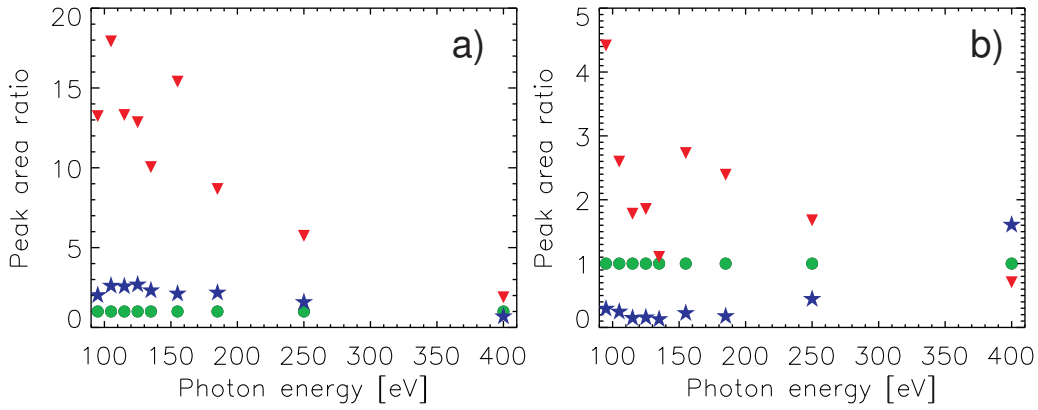

Figure 8.21: Intensity ratios of the components of oxidized Al with respect to the component of metallic Al, plotted versus photon energy. Red triangles show the ratio of component "d" to "b", blue stars show the ratio of component "e" to "b". a)+b) correspond to the situation of the oxidized sample (see fig. 8.19b)and the oxidized and annealed sample (see fig. 8.19c),respectively.

Structural Changes during Annealing

It is known from different NiAl surfaces like the (1,1,0), the (6,7,1) (see section 8.1) and the (16,14,1) surface that a long-range ordered surface oxide is formed by annealing the oxidized surface [42, 52]. For the two vicinal NiAl surfaces the oxide ordering is accompanied by (1,1,0) facet formation. In order to follow a possible ordering of the oxide on the (4,3,0) surface, the sample is annealed stepwise in UHV after its oxidation. Morphology changes at the oxide-alloy interface are followed by SXRD measurements. To detect a faceting of the surface, K-scans across the steps through the (0,7)-CTR were performed for different L-values, as shown in fig. 8.22. The CTR signal at K=7 is strongly decreased already at the oxidation temperature of 550 K. Simultaneously a broad signal arises, centred around the vertical black lines. The position of the new signal can be ascribed to the formation of (1,1,0) facets as the vertical black lines mark the nominal position of (1,1,0) facets. While the intensity at K=7 further decreases with increasing the temperature, the facet signal increases by annealing to higher temperatures. The FWHM value of the arising peak of the (1,1,0) facet is decreasing with increasing temperatures. This corresponds to an increase of the average facet width which can be estimated from the FWHM value of the peak. Fig. 8.23 shows the resulting temperature dependence of the average facet width. Up to 823 K the width remains approximately constant at 30 Å. It then start to rise and reaches its maximum of 69 Å at 1173 K.

To detect the formation of long-range ordered oxide on NiAl(4,3,0) rocking scans at the positions of two possible oxide structures were performed for different annealing temperatures. The formation of the complex surface oxide, known to form on NiAl(1,1,0) at the applied conditions, was checked. Rocking scans were recorded at the $(0,4)_{oxide}$ inplane position of the two oxide twin domains. The formation of θ-like oxide, known to form on NiAl(1,0,0) at the applied conditions, was also checked. Rocking scans were recorded at the $(5.47, 1, 2)_{\theta-oxide}$ position of the two 90° rotated oxide domains [154]. The formation of (1,1,0) facets was considered when performing the rocking scans. No arising peak was found in the described scans while annealing the sample from 550 K up to 1100 K. None of the two investigated oxides seems to form long-range ordered domains on the (4,3,0) surface. Flashing the sample up to 1350 K reproduces the CTR pattern arising from the clean, regularly stepped (4,3,0) surface with no larger (1,1,0) facets.

Micro Structure of the Oxide

Fig. 8.12b and c show LEED images recorded of the sample, which is oxidized at 5×10^{-6} mbar and 1×10^{-7} mbar O_2, respectively, and annealed to 1100 K in UHV afterwards. LEED images recorded after annealing the oxidized sample up to 1150 K show identical features. In the $\mathbf{a}_1$-direction along the steps the oxide has the same lattice parameter as the substrate and grows commensurate. In the $\mathbf{a}_2$-direction across the steps the intensity distribution is stripe like for the surface oxidized at 1×10^{-7} mbar O_2. The formed oxide is disordered along this direction. Note, that sharp reflections on top of the diffuse stripes create a NiAl(1,1,0) like pattern indicating that (1,1,0) facets are present after an-

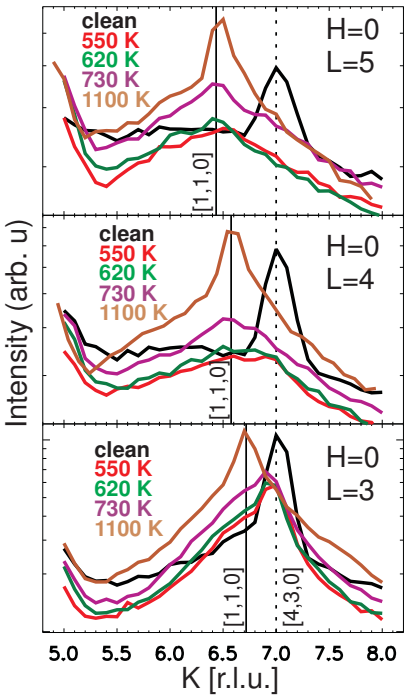

Figure 8.22: Temperature dependent K-scans along the $\mathbf{a}_2$-direction recorded of the clean sample (black lines) and after the oxidation (coloured lines) for different L- values: A new peak arises at the [1,1,0] facet position (solid vertical line) while the CTR signal at K=7 (dashed solid line) decreases at the same time.

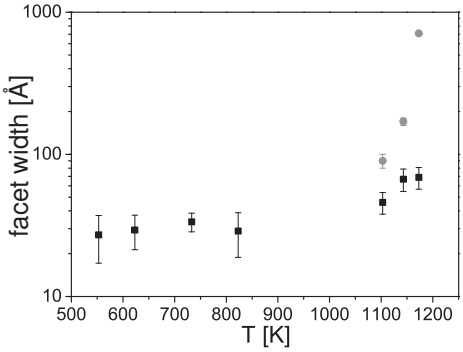

Figure 8.23: Average (1,1,0) facet width on logarithmic scale versus annealing temperature: Black squares show the results of the oxidized (4,3,0) surface, grey circles of the (6,7,1) surface.

nealing the oxide. The red line in fig. 8.12d shows the intensity profile along one stripe within LEED image c. The distance between two reflections on a stripe is determined to ΔK=4.59 which corresponds to a lattice parameter of (4.03$\pm$0.15) Å. It agrees well with

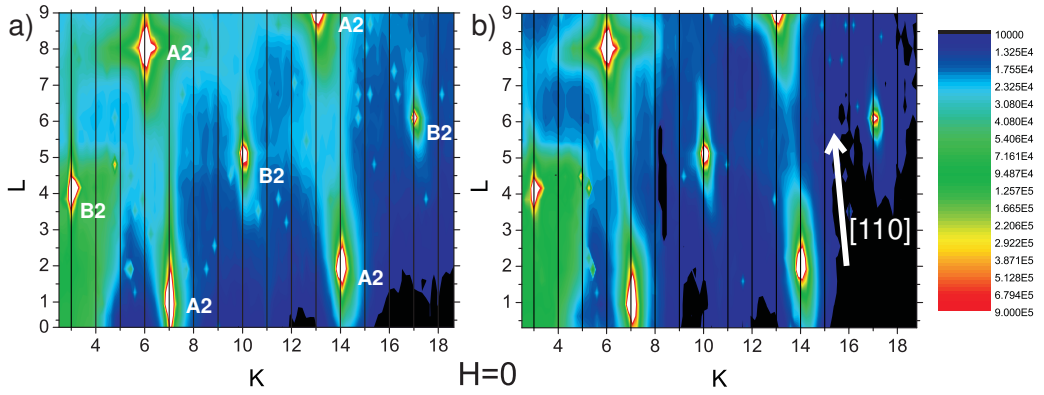

Figure 8.24: K-L-Maps at H=0 of the reciprocal space recorded for the clean (a) and the oxidized and annealed (b) NiAl(4,3,0) surface. A2 and B2 mark the fundamental and the superstructure Bragg peaks, respectively. In a), the CTR signal is observed along the L-direction. In b) the CTR signal is observed along the [1,1,0] direction, indicated by the white arrow.

the lattice parameter $d_{1\bar{1}0}$=4.08 Å of the [1,$\bar{1}$,0]-direction of the NiAl bulk. With respect to the NiAl(4,3,0) surface the [1,$\bar{1}$,0]-direction lies in the plane of the (1,1,0) terraces pointing across the steps (see fig. 8.11). The LEED image of the sample, oxidized at 5×10^{-6} mbar O_2 and annealed to 1100 K (see fig. 8.12b), shows additional reflections on top of the diffuse stripes. The additional peaks are clearly visible in the intensity profile of fig. 8.12d. The distance between two peaks is determined to ΔK=0.51 which corresponds to a real space distance of (28.3$\pm$1.6) Å. The axes of the surface unit cell of the NiAl(1,1,0) facets point along the $[0, 0, 1]$- and the $[1, \bar{1}, 0]$-direction. With respect to this facet surface cell the new oxide forms a (1×7) superstructure[2].

SXRD measurements of the oxidized and annealed NiAl(4,3,0) sample were performed to further characterise the oxide structure detected with LEED. Fig. 8.24a and b show K-L maps of the reciprocal space at H=0 for the clean sample and the oxidized and annealed sample, respectively. The K-L map of the clean surface shows the fundamental and superstructure Bragg peaks by the white spots. The signal of the CTRs is clearly observable. It is distributed along the L-direction marked by black solid lines. A small signal is also found along the [1,1,0]- and [1,$\bar{1}$,0]- direction. This is attributed to thermal diffuse scattering as it gets more pronounced with increasing wave vector transfers. The K-L map of the oxidized and annealed surface clearly shows the formation of (1,1,0) facets like already described in the previous paragraph. The CTR-signal along the L-direction disappears. It now runs along the [1,1,0] direction. However, no new oxide rods or peaks, like detected with LEED, are observed. No long-range ordered oxide can be detected with the SXRD measurements.

[2]superstructure in the $[1, \bar{1}, 0]$-direction:(28.3 Å)/($d_{1\bar{1}0}$×cos α_{miscut})=28.3 Å/(4.08 Å×cos 8.13°)=7.0≈7

AES measurements of the oxidized and annealed surface are depicted in fig. 8.10. A strong oxygen signal at an electron energy of 510 eV is observed. The characteristic signal of oxidized Al is detected at energies of 39 eV, 47 eV and 56 eV. The spectra clearly shows the existence of Al oxide after the annealing.

According to fig. 8.19b, this is confirmed by HRCLS-measurements after the annealing the oxidized surface. Like for the oxidized, but not annealed surface, the Al2p spectra after the annealing consist of three spin-orbit doublets. Therefore the same model like for the oxidized surface was used to analyse the spectra. The results for the single components as well as the total fit are shown in fig. 8.19b. The area ratio of component "b" and "e" to component "d" versus the photon energy are depicted in fig. 8.21b. Three main features are obvious. First, the area ratio of component "d" and "e" assigned to oxidized Al are about a factor of 6 smaller compared to the oxidized sample without annealing. Some fractions of the oxide must have desorbed already from the surface during the annealing. This is consistent with the results of a reflectivity measurement performed after the annealing (see fig. 8.17). While a thin oxide film is still observed, the electron density of this film decreased. This indicates that the film is not homogeneous any more. Second, the average area ratio of component "d" to component "e" is by a factor of 2 smaller than it was directly after oxidation. From a relative point of view, more bulk oxide like, "e"-type Al atoms (less 3-fold oxygen bonded, "d"-type Al atoms) are present in the oxide after annealing the sample. Third, the binding energy of component "e" is shifted by 0.1 eV toward higher binding energy. Again, this points to relatively larger amount of bulk-oxide present in the oxide layer. The O1s spectra of the oxidized and annealed sample are shown in fig. 8.20a, the corresponding analysis in fig. 8.20c. The fit was performed, using the same two components like for the oxidized but not annealed surface. The results show two main features. First, a decrease of the intensity is observed, compared to the just oxidized sample. Again, this is explained by a start of oxide desorption. Second, a signal increase of the component "I" and a strong signal decrease of component "II" are observed when comparing the spectra recorded from the oxidised and the oxidized and annealed sample. The area of component "I" increases by a factor of 1.6, the area of component "II" decreases by a factor of 7 after the annealing[3]. This shows that the ordered oxide on top of NiAl(4,3,0) is mainly formed of the oxygen species "I" with higher binding energies.

8.2.3 Discussion

The Clean Surface

The LEED and CTR measurements of the clean sample show a regularly stepped NiAl(4,3,0) surface under UHV conditions even after annealing it to 1350 K. Thus, like the (6,7,1) surface, the vicinal (4,3,0) surface is stable in UHV over a huge temperature range. The relaxations of the clean surface are also similar to the (6,7,1) surface. The buckling of the Ni and Al atoms on the terraces agrees within the error bars. Independent of the step atom termination of the fitting model a pronounced inward relaxation of the step atom S1,

[3]The comparison is based on the spectra recorded at 900 eV photon energy

together with an outward relaxation of the corner atom S2 is observed. This relaxation behaviour around the steps qualitatively agrees with the (6,7,1) surface where the step and corner atoms relax in the same direction. As described in section 8.1.4 these relaxations are typical for a surface step. The CTR results also show that, in addition to the step and corner atoms of the first two rows, the relaxations of neighbouring terrace atoms and of deeper lying atoms below the actual step are affected. According to a recent embedded atom calculation the surface energy of NiAl(4,3,0) is very close to NiAl(1,1,0) [155]. A long-ranging strain field around the steps could explain this high stability of the (4,3,0) surface.

In principle, the step position of the clean (4,3,0) surface can either be solely occupied by Ni or Al. Both, the CTR and the HRCLS results, point towards a surface with mostly Ni terminated steps. This indicates that the Ni terminated steps might be energetically favoured over Al terminated steps. However, a embedded atom calculation results in a lower surface energy for the Al-terminated step [155]. For the low-index NiAl(100) surface, where also an Al or Ni terminated surface is possible, it is known that the surface configuration strongly depends on the preparation procedure [154, 156]. Too high annealing temperatures can lead to Al evaporation, especially from the step, and could explain our result.

Oxidation and Annealing of the Surface

At 550 K and 6×10^{-6} mbar O_2 for 900 s a vitreous alumina film is formed which possesses no long-range order. The SXRD results show that oxidation at these conditions changes parts of the initial sequence of identical (1,1,0) terraces into a (1,1,0) faceted surface. The average facet width of 30 Å corresponds to two initial terraces bunched together, like schematically shown in fig. 8.25b. We conclude that the formation of (1,1,0) facets is thermodynamically favoured for the oxidized NiAl(4,3,0) surface. Further results like the oxide thickness, the Ni , Al and Ni anti-site occupation profiles and the relaxation profile of the oxidized NiAl (4,3,0) surface region are very similar to NiAl(1,1,0) [148, 153]. On both surfaces the oxide film is about 5 Å thick [4]. Inward relaxations of the Ni atoms, especially within the first 3 rows, are found for both surfaces. The Ni atoms at the step and corner position S1 and S2 are also strongly shifted toward the bulk. For the oxidized (1,1,0) surface the Al atoms of the first two layers are relaxes inward. Al of the third layer relaxes outward. For the (4,3,0) surface only the first row of Al relaxes inwards, while Al atoms in the following three row are relaxed outwards. The buckling of the Ni and Al atoms is maintained for both surface. Consequently, very similar relaxation profiles for the low-index and the vicinal surface are found.

As shown in the occupancy profiles (fig. 8.18b and c), Al vacancies reach up to a depth of 12 Å in the alloy. They originate from preferential Al oxidation during the formation of the alumina film. Thereby the amount of Al missing in the alloy is 30% higher than the amount of Al needed to form the 2 layer thin surface oxide known from NiAl(1,1,0) [4, 5]. At alloy depths larger than 6 Å the Ni sites are fully occupied. The Ni vacancies appear only close to the oxide-alloy interface which could be interpreted as roughness. Especially

between 3 and 5 rows below the oxide-alloy interface only about 40 % of the Al-sites are occupied by Al. As known from the NiAl bulk, an enhancement of the Ni concentration leads to the formation of Ni anti-sites (Ni on Al-sites) [149]. This effect is also found here at depths between row 3 and 5 ($\approx$ 8 Å). The relative increase of the Ni concentration due to preferential Al oxidation could also explain the aforementioned inward relaxation of the atoms within the surface region like already mentioned for the NiAl (6,7,1) system. Like on the (6,7,1) surface the Al concentration directly at the interface is larger than in the deeper embedded third and forth rows.

The HRCLS Al2p and O1s spectra of the oxidized but not annealed NiAl(4,3,0) surface are in qualitative agreement with the spectra recorded for the NiAl(1,1,0) surface which was oxidized at the same conditions, but annealed afterwards [42, 153, 157]. The area ratio of the Al2p components, plotted in fig. 8.21a, shows the same dependence on the photon energy like for oxidized and annealed NiAl(1,1,0). A former XPS-study on the oxidized NiAl(1,1,0) surface shows no changes in the Al2p spectra after a 1070 K annealing process [158]. We conclude that the chemical environment of Al and O atoms on the oxidized (4,3,0) surface is very similar to the oxidized (1,1,0) surface. Like for the oxide formed on the (1,1,0) surface, we assign the Al2p component "e" (see fig. 8.19) to Al atoms within the oxide layer and Al2p component "d" to Al atoms at the oxide alloy interface [5, 153, 157]. Although the Al2p spectra of oxidized NiAl(4,3,0) and NiAl(1,1,0) qualitatively agree well, the Al2p component "e" is quantitatively stronger on the (4,3,0) surface, especially for lower photon energies. This indicates the growth of slightly thicker oxide on NiAl(4,3,0).

In this chapter the temperature dependence and the kinetics of the faceting of the oxidized NiAl(4,3,0) surface were demonstrated. Fig. 8.25b shows that the NiAl(4,3,0) surface, oxidized at 550 K, can be schematically described by a faceted surface covered by a disordered alumina film. Minor parts of the regularly stepped interface, known from the clean surface, are still present. As described above, oxidation induces strong changes of the relaxation pattern within surface region, especially at the surface steps. The strain field around the steps is changed. We argue that these changes lower the strain-induced step-step interactions responsible for the stability of the clean surface. This allows the formation of energetically favoured (1,1,0) facets covered by oxide. Due to kinetic barriers and a reduced material transport the average facet width of 27 Å is still small. To form the small facets two 14 Å-wide terraces of the clean surface have to bunch together. This situation is only changed slightly up to an annealing temperature of 830 K, as depicted in fig. 8.25c. The facet width remains at approximately 30 Å, while the fraction of initial (1,1,0) terraces at the interface gets smaller. LEED results show no long-range order of the oxide. At a temperature of 1100 K kinetic barriers for material transport and oxide ordering are overcome and the average facets width start to increase. Fig. 8.25d schematically demonstrates this situation. LEED proves the formation of long-range ordered oxide, probably covering the (1,1,0) facets. At the same time oxide already starts to desorb from the surface, as shown by the x-ray reflectivity and HRCLS results. We conclude that smaller oxide domains on smaller facets desorb, and larger long-range ordered structures on larger facets remain. An increase of the annealing temperature up to 1170 K increases the facets

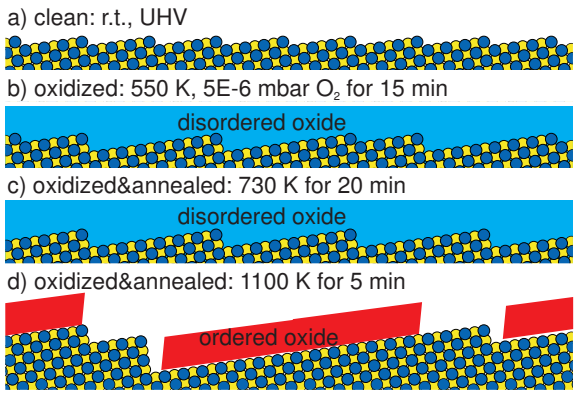

Figure 8.25: Schematic side views of the NiAl(4,3,0) surface depict the different scenarios of the clean (a) and oxidized(b) surface and during the annealing procedure(c+d).

width to a maximum of 69 Å. While more oxide is desorbed, only the larger oxide covered facets remain. We conclude that the occurring (1,1,0) and (1,$\bar{1}$,0) facets are energetically favourable for the surface oxide-alloy interface, while for the clean surface the regularly stepped (4,3,0) surface has the lowest surface free energy. This was also found during the oxidation and annealing of the (6,7,1) surface. However, a faceting has been observed only at temperatures above 1120 K which indicates different kinetic barriers on the two differently stepped surfaces.

From the LEED and SXRD experiments it is obvious that the formed oxide does not possess the complex structure of the surface oxide, known to form on the NiAl(1,1,0) and NiAl(6,7,1) surface. This result is unexpected. As the (6,7,1) surface, the NiAl (4,3,0) surface consists of (1,1,0) terraces which transform into 69 Å-wide (1,1,0) facets upon oxidation and annealing. Comparing the oxide structures formed on the two vicinal surfaces shows the strong influence of surface steps on the oxide formation. The steps on the (4,3,0) surface induce the formation of a "new" oxide structure. While the LEED images show the formation of this "new" oxide, no signal of this oxide could be detected with SXRD. In the following we derive a structural model for the "new" oxide which can explain why no oxide peaks are found with SXRD.

With respect to the (1,1,0) facets, which have inplane unit cell vectors along the $[0,0,1]$- and $[1,\bar{1},0]$- direction (see fig. 8.11), the observed oxide forms a (1×7) superstructure. θ-oxide, like shown in fig. 6.3, has a lattice parameter b_{ox}=2.92 Å which has a lattice mismatch of only 1.1 % with respect to $a_1=d_{[001]}$=2.887 Å. This very small mismatch with the NiAl substrate most likely triggers the formation of the θ-oxide. The initial ordering of the oxide starts at the surface steps due to preferential strain release along the steps. Five unit cells of θ-oxide, lined up along its c-direction, have a mismatch of only -1.3 % with respect to seven $[1,\bar{1},0]$ lattice parameters[4]. As the annealed oxide layer is 5 Å thick, we conclude that θ-Al_2O_3 is formed on the NiAl(4,3,0) surface which is made up of

[4] $(5\times c_{ox})/(7\times d_{[1\bar{1}0]})$=(5×5.64 Å)/(7×4.08 Å)=-1.3 %

two layers of Al ions, like marked in fig 6.3 by the dashed line. Fig. 8.26 shows that b_{ox} is aligned parallel to the $\mathbf{a}_1$-direction of NiAl(4,3,0) and c_{ox} is parallel to the [1,$\overline{1}$,0]-direction of bulk NiAl. The LEED images show perfect long-range order in the direction along the steps. Across the steps the oxide is disordered for temperatures of 1040 K and adopts the described long-range order above 1100 K. The resulting stripe-like structure is shown in fig. 8.26. Note, that at least two initial terraces have to bunch together to form one oxide stripe. This might induce the described faceting, already observed at 550 K for the (4,3,0) surface. The formation of θ-oxide on NiAl has been observed before on the (0,0,1) surface [8, 82, 159]. For annealing temperatures up to 1300 K a (2×1) reconstruction is observed, for higher annealing temperatures the θ-oxide looses its long-range order along its c_{ox}-axis. The θ-oxide domains on NiAl(0,0,1) are also stripe like with their long axis oriented along [0,0,1]. This is consistent with the oxide stripes observed on NiAl(4,3,0). In a low energy electron microscopy (LEEM) study of the high temperature (850-1350K) oxidation of NiAl(1,1,0) the formation of stripe-like oxide domains is reported as well [160]. There, the oxide stripes run along the [0,0,1]-direction of bulk NiAl and the domain width is much larger than in the $[1, \overline{1}, 0]$- direction. Furthermore, the stripes are predominantly found at substrate steps running along the [0,0,1]-direction which agrees perfectly with observed oxide stripes on the (1,1,0) terraces of NiAl(4,3,0).

The model presented in fig. 8.26 could explain why an oxide signal was observed with LEED but not with SXRD measurements. The coherence length of electrons is $50 - 100$ Å which is more than 100 times smaller than the coherence length of x-rays at a synchrotron source like the ESRF. The size of the grown oxide domains on the facets has been determined to approximately 30 Å. This size is of the same order of magnitude like the coherence length of the electrons. Thus, in LEED the signal of one or two oxide-stripes are added coherently and the corresponding reflexions are observed. In case of x-rays the diffracted signal results from the coherent sum of numerous oxide stripes on regularly arranged facets. In the direction across the steps the two neighbouring oxide structures are shifted by half a unit cell which leads to a destructive interference in this direction. Thus, no reflection can be observed in the diffraction pattern in this direction. Finally, the stripe model can explain the desorption behaviour of the oxide. The width of the stripes is very small and results in small oxide domains. Small oxide domains do desorb faster. This explains why at the same annealing temperature more oxide desorbs from the NiAl(4,3,0) surface compared to the NiAl(1,1,0), where the oxide domains are much larger.

The HRCLS spectra of the oxidized and annealed (4,3,0) surface show clear differences compared to the spectra of NiAl(1,1,0) prepared at the same conditions [153, 157]. First, the intensity of the signal is much weaker for the (4,3,0) which is explained by the desorption of small oxide domains. Second, in the Al2p spectra recorded after annealing the (4,3,0) surface, the energetical position of component "e" is shifted by 2.8 eV toward higher binding energies with respect to the bulk Al2p component "b". This shift is 2.5 eV in case of the just oxidized (4,3,0) surface and 2.2 eV in case of the oxidized and annealed (1,1,0) surface [153, 157]. For θ-oxide on NiAl(0,0,1) the shift has a value of 2.5 eV [161]. The shifts indicate a slightly different chemical environment for oxidized Al on the (4,3,0) surface compared to the (1,1,0) surface which points towards θ-oxide formation again. At

last, in the O1s spectra, recorded after annealing the (4,3,0) surface, the component "II" is much stronger when compared to the case of the (1,1,0) surface [157]. For more detailed conclusions from the HRCLS spectra DFT calculation would be necessary.

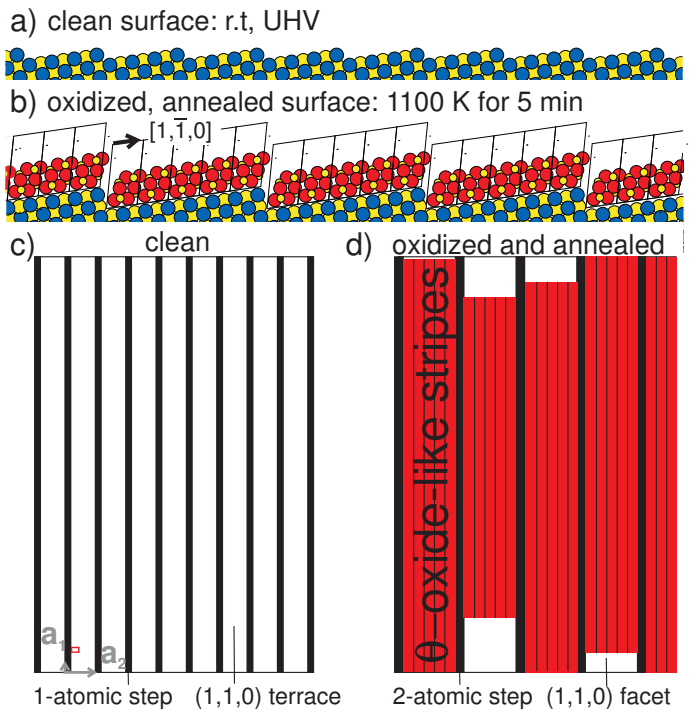

Figure 8.26: Side and top view of the clean (a+c) and oxidized and annealed (b+d) NiAl(4,3,0) surface. In the schematic model two initial terraces bunch together and are covered by 5 unit-cell wide θ-oxide stripes. The stripes are elongated along the steps. The little red rectangle in c) marks the (1,1,0) surface unit cell.

8.3 Conclusions

In the final section of this chapter the results of the NiAl(6,7,1) and the NiAl (4,3,0) surface are discussed. Similarities and differences of both surfaces are pointed out with respect to the questions raised at the beginning of this chapter. Comparisons with the low-index NiAl(1,1,0) surface, oxidized at the same conditions, are presented.

8.3.1 The clean vicinal NiAl surfaces

Both investigated, chemically well ordered, clean surfaces are stable in UHV up to at least 1350 K. No faceting of the clean surfaces is observed. Both surfaces consist of regular arrays of (1,1,0) terraces and monoatomic steps. On the (6,7,1) surface the steps run along the $[\bar{1}, 1, \bar{1}]$-direction of bulk bcc NiAl, on the (4,3,0) surface the steps run along the $[0, 0, 1]$-direction. A buckling of Ni and Al atoms in the topmost and second topmost terraces is found for both systems. The larger Al atoms relax outwards, Ni inwards. This rumpling is also known from low-index NiAl(1,1,0) surfaces and a quantitative comparison of the resulting values shows good agreement [12, 39]. Both vicinal surfaces show similar pronounced atomic relaxation around the steps. The atoms at the surface steps are relaxed towards the bulk, while atoms at the corner below the step relax outwards. These relaxations introduce strain fields around every surface step. The strain fields then interact with each other and lead to a step-step repulsion, which is crucial for the observed stability of the vicinal surfaces. In summary, both investigated clean surfaces show very similar features. A recent STM study on clean NiAl(16,14,1) showed no surface faceting as well [52]. We presume that NiAl surfaces vicinal to the (1,1,0) surface are thermodynamically stable.

8.3.2 The oxidation of vicinal NiAl surfaces

Upon oxidation at 550 K and 10^{-6} mbar of molecular oxygen for 900 s, a 5 Å thin, disordered alumina film is formed on the both vicinal surfaces. Preferential Al oxidation produces a decrease of the Al concentration up to 1 nm within the alloy for both samples. Al vacancies occur which are accompanied by Ni anti-sites at a depth between 6 and 8 Å. Ni vacancies are mainly found directly at the oxide-alloy interface. For both surfaces the relaxation profile of the clean surface is changed upon oxidation. Especially the strain fields around the steps are changed drastically, most likely lifting the step-step repulsion. For the NiAl(1,1,0) surface oxygen-induced defect formation results in very similar occupancy profiles [148]. The formation of a 5 Å thin, alumina film and a change of the structural relaxations upon oxidation are also reported for the low-index surface [4]. Therefore we conclude that the changes of the segregation profile and the ordering in the interfacial region are very similar for the low-index and the vicinal surfaces at the mentioned oxidation conditions. No strong influence of the surface steps, e.g. as diffusion pathway, is observed.

However, the surface steps and their surface orientation do have a strong influence on

the temperature-dependent morphology changes of the oxidized vicinal surfaces. Oxidized NiAl(6,7,1) and NiAl(4,3,0) show clear differences in the temperature-dependent faceting behaviours. For NiAl(6,7,1) the terrace-step structure of the clean surface is maintained at the oxide-alloy interface up to annealing temperatures of 730 K. At annealing temperatures of 1120 K, the thermal energy is large enough to overcome kinetic barriers for material transport and massive (1,1,0) faceting is observed. The facets widths are over 50 times larger that those of the initial terraces. For NiAl(4,3,0) the regular terrace-step structure is lifted in favour of small (1,1,0) facets immediately during the oxidation at 550 K. Two initial terraces bunch together to form 27 Å wide facets while this facet width is not changed up to 840 K. At temperatures of 1120 K the facets width starts to increase again as kinetic barriers are removed. However, the maximal facet width is only 5 times larger than the width of the clean terraces and 10 times smaller than observed for the (6,7,1) surface. (1,1,0) faceting of the oxide-alloy interface is observed at much lower temperatures for the (4,3,0) than for the (6,7,1) surface. Thus, first small kinetic barriers can be overcome at 550 K on NiAl(4,3,0) but not on NiAl(6,7,1). This indicates that the intradiffusion of atoms at interface is enhanced for the (4,3,0) surface and that intradiffusion processes can be step-dependent. We conclude for both investigated surfaces that (1,1,0) facets are energetically favourable for the oxide-alloy interface.

For both vicinal surfaces the formation of larger (1,1,0) facets around 1120 K is going along with the transformation of disordered to long-range ordered oxide. Surprisingly, the oxide structure, the desorption behaviour as well as the oxide domain size are different for the two vicinal surfaces although (1,1,0) facets are present at both oxide-alloy interfaces. A characterization of the surface oxide on the NiAl (6,7,1) surface showed the existence of the complex structure which is known to form on the NiAl(1,1,0) surface (see section 3.2.2). Mainly single domain oxide growth is observed, which is in contrast to a twin domain formation on NiAl(1,1,0). Strain, set up within Al rows at the oxide-alloy interface, can preferentially be released for the observed domain, where these Al rows run in the direction along the steps. During the initial formation of long range-ordered oxide this favours the growth of one twin domain over the other. Characterization of the oxide on the NiAl (4,3,0) surface showed the existence of a θ-Al_2O_3-like structure, forming a (1×7) reconstruction on the (1,1,0) facets. The oxide grows in stripe-like domains which are extended in the direction along the steps but have very small domain widths in the direction across the steps. Only one domain is observed. One lattice parameter of θ-Al_2O_3 and the [0,0,1]-direction along the steps have a very small lattice mismatch. Again, strain at the oxide alloy interface can preferentially be released in the direction along the steps which minimizes the strain for θ-Al_2O_3. During the initial formation of long range-ordered oxide this favours the growth of θ-Al_2O_3 over the other oxide structures. In the $[1,\overline{1},0]$-direction across the (1,1,0) terraces the lattice mismatch of the (1×7) reconstruction is larger and strain release is more difficult across the steps. Consequently, the domain size of the θ-Al_2O_3 stripes in this direction is small which leads to small (1,1,0) facet widths covered by the stripes. In summary, the results show the crucial influence of the step direction on the oxide structure and the domain growth. On stepped surfaces strain, set up at the oxide-alloy interface, is preferentially released in the direction along the steps. During

transformation of disordered into long-range ordered oxide this directed strain release determines the structure of the formed oxide.

The two different oxide structures also explain the different desorption behaviours of the oxides. On the (6,7,1) surface interfacial strain release across the steps enables large oxide domains grown on large (1,1,0) facets. On the (4,3,0) surface the oxide domains are small in the direction across the steps. Small domains desorb faster than large domains. This explains why oxide domains on the (4,3,0) surface were observed to desorb faster compared to the (6,7,1) surface.

In summary, similarities in the stability of the clean surfaces and in the defect formation during the preferential Al oxidation are reported. Clear, step-induced differences are found for the formed oxide structures as well as the temperature dependent faceting and oxide desorption behaviours. These results are of importance to the applications of alumina films on NiAl as nanotemplate in catalytic studies or tunnelling barrier in future magnetic devices. The ideal support for metal clusters in catalytic model studies would be a highly reproducible, single domain, ultrathin, smooth, stable and homogeneous oxide film. Such properties are also needed for the further miniaturization of magnetic transistors. The work presented here shows that such ideal oxide films can be in principle realized by tailoring the oxide growth with surface steps running along dedicated directions. Tailoring with respect to the oxide structure and with respect to single domain growth is possible. However, massive morphology changes of the interfacial region during the formation of the oxide film and the oxide domain sizes should be taken into account.

Chapter 9

The Oxidation of a Vicinal CoGa Surface

Ultra-thin, crystalline Ga oxide films are discussed as candidates in applications of tunnelling magneto-resistive insulating barriers and gas sensors [6]. Such films are formed on the flat CoGa (1,0,0) surface by thermal oxidation. As summarized in section 3.2.3, the structure and the growth behaviour of the surface oxide on the (1,0,0) surface are known. (2×1) and $90°$-rotated (1×2) oxide domains are observed to grow, with an initial nucleation at the equally distributed [0,0,1] and [0,1,0] oriented surface steps. To further investigate this nucleation process and to promote the growth of only one domain, a CoGa (1,0,0) sample with a slight miscut of $0.8°$ along the [0,1,0] direction has been prepared for the presented experiments. This miscut leads to a vicinal surface with steps only running along the [0,0,1] direction. Like for the NiAl(6,7,1) surface, the idea is to tailor a single domain oxide film via dedicated step orientations. SXRD and LEED studies are preformed to to detect the assumed, step-induced anisotropies in the growth of the two domains and to investigate the structure of the oxide on the regularly stepped surface. Additionally, the oxide growth was investigated for different oxidizing environments, first in an O_2- then in a H_2O atmosphere.

This chapter is organized as follows. In section 9.1 details on the SXRD set-up, the sample preparation and the regularly stepped CoGa surface are given. The results of section 9.2 show that the oxide structure, formed during oxidation with O_2 and H_2O pressures between 10^{-9} and 10^{-5} mbar and at temperatures between 700 and 810 K, is identical to the structure known from the flat CoGa (1,0,0) surface. The presence of preferentially oriented steps does not tailor a single domain oxide growth as both oxide domains are observed for all investigated conditions. The time-dependent growth of the surface oxide during O_2 oxidation can be described by a hetero epitaxial model which consists of two exponentially slowed down growth steps. During the water vapour oxidation the oxide formation is retarded compared to the O_2 oxidation. It starts at higher pressures and with much slower oxidation rates at comparable pressures. Furthermore, less oxide is formed at all applied water vapour pressures. In section 9.3 and 9.4 the results are discussed and conclusions are drawn.

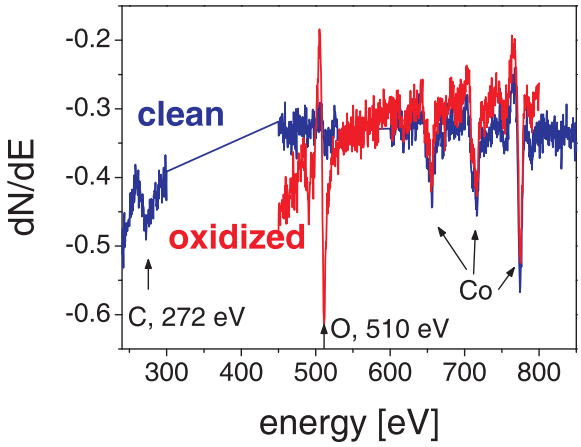

Figure 9.1: AES spectra of the miscut CoGa (1,0,0) surface recorded after preparation of the clean sample (blue) and after oxidation at 770 K and 10^{-8} mbar O_2 (red). The position of Auger electrons from O, C and Co are indicated.

9.1 Experimental Details and Sample Preparation

A nominally $Co_{.5}Ga_{.5}$ single crystal with a diameter of 10 mm and a thickness of 2 mm has been cut from a CoGa rod parallel to the (1,0,0) planes with a miscut of $0.8°$ along the [0,1,0] direction. After a polishing procedure, similar to the one described in section 7.1, a clean surface is prepared by one Ar^+ sputtering (argon pressure $p_{Ar} = 3 \times 10^{-6}$ mbar, energy E=0.75 keV, sputter current density 10 μAcm^{-2}, sputtering time t_{sp}=1200 s) and high temperature annealing cycle (1070 K for 300 s), followed by several oxidation (oxygen pressure $p_O = 3 \times 10^{-7}$ mbar, oxidation temperature $T_{ox} = 690$ K, oxidation time t_{ox}=600 s) and annealing (850 K for 600 s) cycles. The AES spectrum of the prepared sample in fig. 9.1 shows that minor amounts of C and O are still present. Nevertheless the recorded LEED image (see fig. 9.3a) shows the $c(4 \times 2)$ reconstruction known to exist on the clean CoGa(1,0,0) surface.

The x-ray diffraction experiments are performed in the *in situ* chamber, described in section 5.1.4, on the MS beamline at the SLS at a photon energy of 10.3 keV [162]. The incidence angle during the measurements was fixed 0.06° below the critical angle of CoGa ($\alpha_c = 0.30°$). The data are recorded in stationary diffractometer geometry using the PILATUS 2D detector and are corrected for the monitor counts, the polarisation and the Lorentz factor [61, 93]. For every oxidation condition at least two CTRs with 66 structure factors and one surface rod with 51 structure factors are recorded. To analyse the data, the program ROD is used [123].

The regularly stepped CoGa surface, resulting from the miscut of $0.8°$ along the [0,1,0] direction, is depicted schematically in fig. 9.2a. According to literature double atomic steps are observed for the CoGa (1,0,0) surface which leads to 200 Å wide terraces and 2.9 Å high steps on the stepped surface [44, 163]. The steps run along the [0,0,1] direction

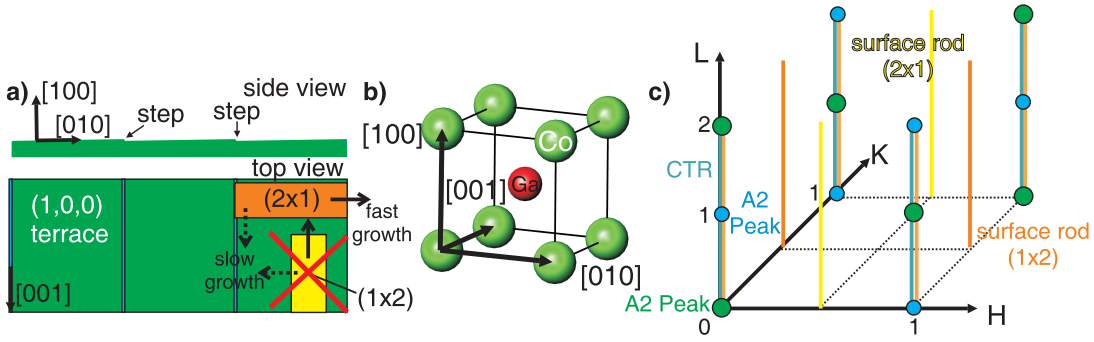

Figure 9.2: a) Side and top view of the stepped CoGa surface with its 200 Å wide (1,0,0) terraces. All steps are running along the [0,0,1] direction to favour nucleation of the (2×1) oxide domains. The solid and dashed arrows indicate the directions of fast and slow oxide growth, respectively. b) Real space (surface) unit cell of β-CoGa(1,0,0). c) Corresponding reciprocal space: Green and blue circles mark fundamental and superstructure reflection, respectively, connected by the CTRs (blue-green lines). The surface rods of both domains are represented by yellow and orange lines.

of β-CoGa. Since the miscut is small, the system of the vicinal surface is described by the unit cell of the low-index CoGa (1,0,0) surface, like shown in fig. 9.2b together with its reciprocal space in fig. 9.2c. The resulting error was taken into account during the CTR measurements. The real space lattice parameters of β-CoGa are $a = b = c = 2.878$ Å and $\alpha = \beta = \gamma = 90°$. A calculation of the structure factor F_{HKL} shows the presence of so-called fundamental reflections, arising from diffraction of the fundamental bcc lattice, and of superstructure reflections due to diffraction of the B2-type, chemically ordered lattice:

$$\begin{aligned} F_{HKL} &= f_{Co} + f_{Ga} \text{ if H+K+L=even (fundamental)} \\ F_{HKL} &= f_{Co} - f_{Ga} \text{ if H+K+L=odd (superstructure)} \end{aligned}$$

As described in section 3.2.3, the ultrathin surface oxide grows epitaxially on the CoGa(1,0,0) surface, forming a (2×1) and a $90°$ rotated (1×2) reconstruction. The crystalline oxide slab gives rise to surface rods of scattered intensity. Due to the (2×1) superstructure with respect to the substrate surface rods are found also at half-integral H and K values. At integer H and K values the diffracted intensity of both oxide domains is superimposed coherently with the diffracted intensity of the truncated CoGa substrate. Consequently, the CTRs contain information on oxide-alloy interface and the oxide coverage, while the discrete surface rods are sensitive to the oxide structure and the oxide coverage.

9.2 Results

9.2.1 Oxide growth at various oxidation conditions

Oxidation with oxygen

On the flat CoGa (1,0,0) surface two $90°$-rotated oxide domain grow during thermal oxidation at low O_2 pressures. Like shown in fig. 9.2a, the exclusively [0,1,0] aligned surface steps are expected to promote nucleation of solely (2×1) oxide domains as oxide nucleation is expected to start at the steps and the (2×1) domain grows fast perpendicular to the steps. However, a LEED study during the oxidation, performed at oxygen pressures between 10^{-9} and 10^{-7} mbar (and $\approx$ 10 L) and temperatures between 700 and 770 K, always resulted in images, like shown exemplarily in fig. 9.3b. Reflexions of the (1×2) and (2×1) domain are observed with equal intensity. Therefore the surface steps have no strong influence on the domain formation.

The results of an oxidation cycle, conducted at 10^{-7} mbar O_2 and a temperature of 820 K, are shown in fig. 9.3c and d. No oxide or substrate reflections are observed for the hot, clean surface in UHV. After oxygen dosing the reflections of the oxide domains appear. Pumping off the oxygen leads to a disappearance of the reflexion again. This can be explained as follows. At 820 K the Co and Ga atoms are very mobile and no crystalline order is present at the clean surface. Even the steps are not well defined which could also explain their minor influence on the domain formation. No reflection are observed in the LEED image. Upon oxidation the formation of Ga-O bonds pins the atoms down and the crystalline superstructure of the oxide is formed. Thus, the reflexions, resulting from the oxide structure, appear in the LEED image.

To gain a more detailed understanding on the time dependence of the growth process and of the oxide domain sizes during oxidation, SXRD experiments are performed *in situ*. O_2 pressures between 4×10^{-9} and 5×10^{-6} mbar and a temperature of 700 K are applied. With a 2D detector the surface oxide formation is followed in real time at the equivalent surface rods positions of (1,0.5,0.55) for the (1×2) domain and of (0.5,1,0.55) for the (2×1) domain. One out of many typical images of an oxide reflection, recorded during the oxidation, is shown in fig. 9.4a. The amount of formed oxide as well as the oxide coverage are proportional to the integrated intensity recorded for the reflection (called "oxide signal" in the following). For every 2D image, H (K) scans can be extracted from the image like shown in fig. 9.4b. From the profile of the H (K) scan, the average oxide domain sizes along the H (K) direction can be determined. The observed Lorentzian lineshapes are characteristic for an exponential island width distribution $P(W) = \frac{1}{W_0}\mathrm{e}^{-W/W_0}$ with a mean island width W_0 [164].

To transform every position of the detector image to the reciprocal space of the sample, the following equation has to be solved for the used diffractometer [61, 165–167]:

$$\mathbf{SUB}\begin{pmatrix} H \\ K \\ L \end{pmatrix} = \mathbf{k_{out}} - \mathbf{k_{in}} \tag{9.1}$$

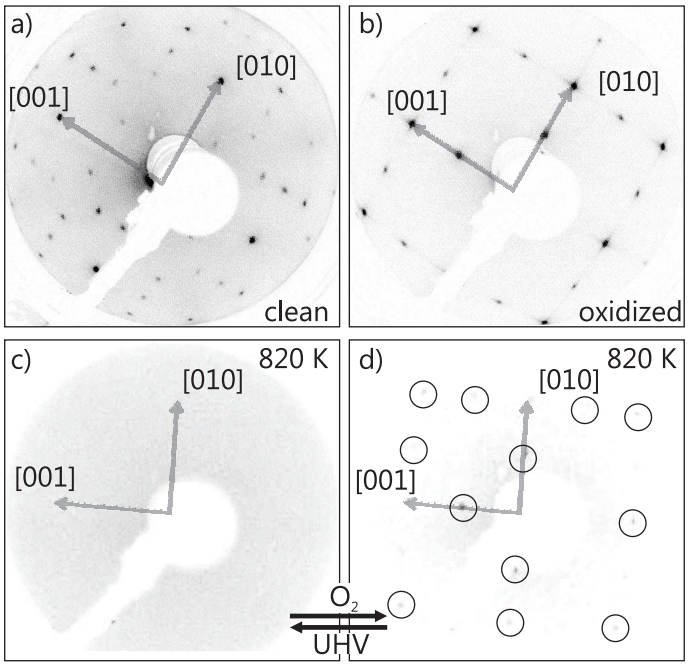

Figure 9.3: LEED images of the CoGa(1,0,0) surface recorded at an electron energy of 88 eV: a) Clean surface with a $c(4 \times 2)$ reconstruction. b) Surface after oxidation at 770 K and 5×10^{-9} mbar O_2 with the (2×1) and (1×2) reflexions of the surface oxide. c) LEED image, taken at 820 K and in UHV, shows no reflexions. The surface is structurally disordered at this temperature. d) After an increase of the oxygen pressure to 10^{-7} mbar at 820 K, reflexions of the surface oxide occur which are marked by the circles. The atoms in the oxide are pinned and form the ordered surface oxide structure.

Matrix **S** describes the rotation of the sample in the laboratory frame of the diffractometer, matrix **U** describes the orientation of the crystal within the laboratory frame and matrix **B** is defined by the reciprocal lattice parameters of the used crystal system. (H,K,L) are the Miller indices. The incoming and outgoing wave vectors $\mathbf{k}_{in}$ and $\mathbf{k}_{out}$ have to be expressed in the system of the diffractometer. $\mathbf{k}_{out}$ depends on the actual position of the detector. After solving the equation for the miscut CoGa (1,0,0) surface and the used 5-circle diffractometer, the H, K and L values can be calculated for every pixel of the recorded images like depicted in fig. 9.4a. In addition, every pixel of the image is corrected with a beam polarisation correction factor and a Lorentz factor for a stationary measurement set-up [61, 165, 167]. All images are normalized on the incoming flux. A background, measured before every oxidation experiment, is subtracted. The H (K) scans are extracted via a box scan with a width of ΔK$= 0.05(0.0005)$ in K and ΔH$= 0.0005(0.05)$ in H. The change of the L value during the H or K scan and the accompanied movement on the surface rod is also corrected.

Fig. 9.5a(top) plots the integral oxide signal, which is proportional to the oxide cov-

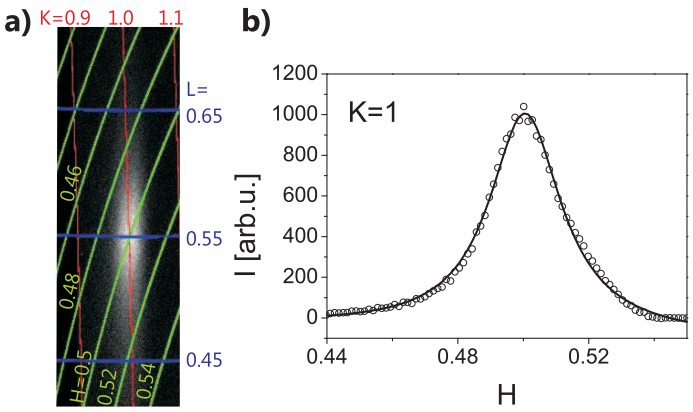

Figure 9.4: a) Typical 2D diffraction pattern, recorded at the (0.5,1,0.55)-position of the surface oxide rod after oxidation at 700 K and 5×10^{-7} mbar O_2. The coloured lines show values of constant wave vector transfer in units of H, K or L. b) H-scan extracted from the shown image (data points) and a Lorentzian fit (solid line). From the FWHM value of the fit curve the average island width along the H-direction can be calculated.

erage θ, as a function of the oxidation time t for different O_2 oxidation pressures. The oxidation temperature is kept constant at 700 K. For all investigated pressures the (1×2) and (2×1) surface oxide domain show very similar growth behaviours. The deliberate oriented steps do not favour single domain growth. For low O_2 pressures (4×10^{-9} and 5×10^{-8} mbar) and therefore lower oxygen exposures, the temporal evolution of the oxide signal can be described by the simple growth law [168]:

$$\frac{\mathrm{d}\theta}{\mathrm{d}t} = \frac{1}{\tau_0}(1-\theta) \;\Rightarrow\; \theta(t) = \theta_0 - \mathrm{e}^{-t/\tau_0}. \tag{9.2}$$

It represents an exponentially slowed down growth close to the maximum coverage θ_0 with an initial growth rate $1/\tau_0$. $\theta_0 = 1$ would mean full surface coverage for $t \to \infty$. This simple growth law is used to fit the curves, recorded for the low oxygen pressures of 4×10^{-9} and 5×10^{-8} mbar. The fit results are presented by solid lines in fig. 9.5a and listed in table 9.1. One observes that the initial growth rate $1/\tau_0$ strongly increases with the oxygen pressure. For low pressures the simple model reproduces the first saturation of the oxide signal well. However, the second increase of the oxide signal, observed for long oxidation times at the low pressures, is not modelled correctly. At higher O_2 pressures of 5×10^{-7} and 5×10^{-6} mbar this second oxide signal increase and the failure of the simple model become obvious. The oxide coverage reaches a first saturation level at an oxide signal around 1.2×10^5 cts/s before it starts to increase again up to 3.3×10^5 cts/s. Thereby, the second saturation of the intensity is attributed to a full coverage of the surface with surface oxide. To describe this temporal evolution, equation 9.2 is extended with a second term of an exponentially slowed down growth with a smaller growth rate $1/\tau_1$:

$$\theta(t) = \theta_0 - \mathrm{e}^{-t/\tau_0} + \theta_1 - \mathrm{e}^{-t/\tau_1} \text{ with } \theta_0 + \theta_1 = 1 \tag{9.3}$$

A fit, using the extended growth model, describes the measured growth curves well, like shown by the solid lines in fig. 9.5a(top). The fit results in table 9.1 show high initial growth rate $1/\tau_0$. The growth rate $1/\tau_1$, corresponding to the second type of growth, is always one order of magnitude smaller. Both growth rates strongly increase with the oxidation pressure. Note, that the first saturation coverage θ_0 has roughly the same value of 1.2×10^5 ct/s for all applied O_2 pressures. It corresponds to a coverage of $2/5$ of the surface.

The STM images in fig. 9.6a and b show the oxidation of the flat CoGa (1,0,0) surface at the similar conditions like applied here [16]. They show that the oxide domains grow stripe like with a fast oxide growth along the direction of the long oxide axis(see also fig. 9.2) [15]. After a fast initial growth oxide stripes of both domains block each other from growing further, like also shown schematically for the stepped surface in fig. 9.6c. Furthermore, the oxide domains cannot grow further as they only grow on the terraces but not across the surface steps. The emerging grid of oxide stripes leaves parts of the surface uncovered during the initial growth, preventing a full surface coverage. This initial growth scenario is assigned to the growth rate $1/\tau_0$ and the first saturation coverage θ_0. After this initial formation, oxide growth in the slow-growth direction covers the remaining, clean surface parts on the terraces with oxide. This slower growth scenario is assigned to the growth rate $1/\tau_1$ and the final coverage $\theta_1 + \theta_0$.

Fig. 9.5a (bottom) shows the average island width along the direction of slow growth as a function of the intensity of the oxide reflection. For oxidation pressures between 5×10^{-8} and 5×10^{-6} mbar the curves can be splitted into two linear parts, like shown exemplarily for the oxidation at 10^{-7} mbar by the straight lines in fig. 9.5a (bottom). Up to an oxide signal of approximately 1.2×10^5 cts/s the width growths linearly. Then a kink is observed in the growth curve of the oxide width. From an oxide signal of circa 1.5×10^5 cts/s onwards, the island width increases linearly again but with lower speed. This behaviour of the island width as a function of the coverage is consistent with the fast and slow growth phases described above. At the very low O_2 pressure of 5×10^{-9} mbar the fast growth phase can be also divided into two sections. At very small oxide coverages the domain width increases very fast up to 22 Å and 28 Å for the (2×1) and (1×2) domain, respectively. This corresponds to a stripe width of 4-5 unit cells. Then the increase of the width slows down but its behaviour remains linear. For the (1×2) oxide domain the mean island width W_0 is very similar at O_2 pressures of 5×10^{-7} and 5×10^{-6} mbar, whereas for 5×10^{-8} and 4×10^{-9} mbar O_2 1.4-times wider oxide islands are formed. Higher oxygen pressures induce a higher nucleation probability on the terraces. At higher pressures more islands start to form, blocking each other from growing. This can explain the smaller widths observed for higher pressures. At lower O_2 pressures mainly oxide nucleation at the steps is expected.

For O_2 pressure of 5×10^{-7} and 4×10^{-9} mbar the increase of W_0 with the coverage is studied for both oxide domains, as shown in fig. 9.5a. When the average islands widths of the (2×1) and the (1×2) oxide domains are compared for the same oxide coverage, one observes that the widths of the (2×1) domains is 1.7-times larger than of the (1×2) domain for both pressures. Fig. 9.6d shows the final island width along the direction of

stepped surface						flat surface		
Pressure (mbar)	Domain -	$1/\tau_0$ (1/s)	θ_0 -	$1/\tau_1$ (1/s)	θ_1 -	Pressure (mbar)	Temp. (K)	$1/\tau$ (1/s)
4×10^{-9} O_2	(1×2)	0.001	0.43	-	-	1×10^{-8}	650	0.001
4×10^{-9} O_2	(2×1)	0.001	0.40	-	-	-	-	-
5×10^{-8} O_2	(1×2)	0.010	0.45	-	-	1×10^{-7}	650	0.02
5×10^{-7} O_2	(1×2)	0.056	0.34	0.001	0.66	-	-	-
5×10^{-7} O_2	(2×1)	0.059	0.30	0.001	0.70	1×10^{-6}	650	0.05
5×10^{-6} O_2	(1×2)	0.14	0.31	0.012	0.69	-	-	-
3×10^{-7} H_2O	(1×2)	0.001	0.22	-	-	-	-	-
2×10^{-6} H_2O	(1×2)	0.011	0.22	-	-	-	-	-
1×10^{-5} H_2O	(1×2)	0.024	0.26	-	-	-	-	-

Table 9.1: Results of the analysis of the oxide growth curves, recorded at the listed oxidation pressure and shown in fig. 9.5. $1/\tau$ is the growth rate. θ the surface coverage while full coverage is assumed after oxidation at 10^{-6} mbar O_2 which corresponds to a integrated intensity of 3.3×10^5 cts/s. The results are compared to an oxidation study of the flat CoGa (1,0,0) surface [15].

fast growth [1]. Here, the width of the (1×2) domain is 1.3-times larger than of the (2×1) domain. Conclusively, the island width along the steps (H-direction) on the CoGa surface is always larger than across the steps. Furthermore, the final island widths along the fast and slow -growing directions are both of the same order of magnitude and lie between 22 Å and 46 Å. The existence of regularly surface steps seem to prohibit large island length which is depicted in fig. 9.6c.

Oxidation with water vapour

Similar oxidation experiments, like described in the previous section, are also performed using water vapour instead of molecular oxygen. H_2O pressures between 2×10^{-8} and 1×10^{-5} mbar and temperatures of 700 K and 800 K are applied. Fig. 9.5b (top) shows the corresponding growth curves, recorded for the (1×2)-domain at the (1,0.5,0.55) surface rod position as a function of time. In comparison with the O_2 oxidation, much higher pressures are needed for initial oxide formation. Below 3×10^{-7} mbar H_2O no oxide formation was observed as shown by the curve recorded at 2×10^{-8} mbar. Furthermore, after the first saturation level is reached, the integrated oxide signal of 7.5×10^4 cts/s is 40 % lower compared to the O_2 oxidation. A detailed analysis of the growth curves confirms this results. Using the simple growth model of equation 9.2 results in much lower growth rates in case of H_2O oxidation. Like for O_2 oxidation, table 9.1 shows an increase of the growth rate with H_2O pressure. These results show that the density of

[1] The time-dependence of the growth could not be resolved in the experiment

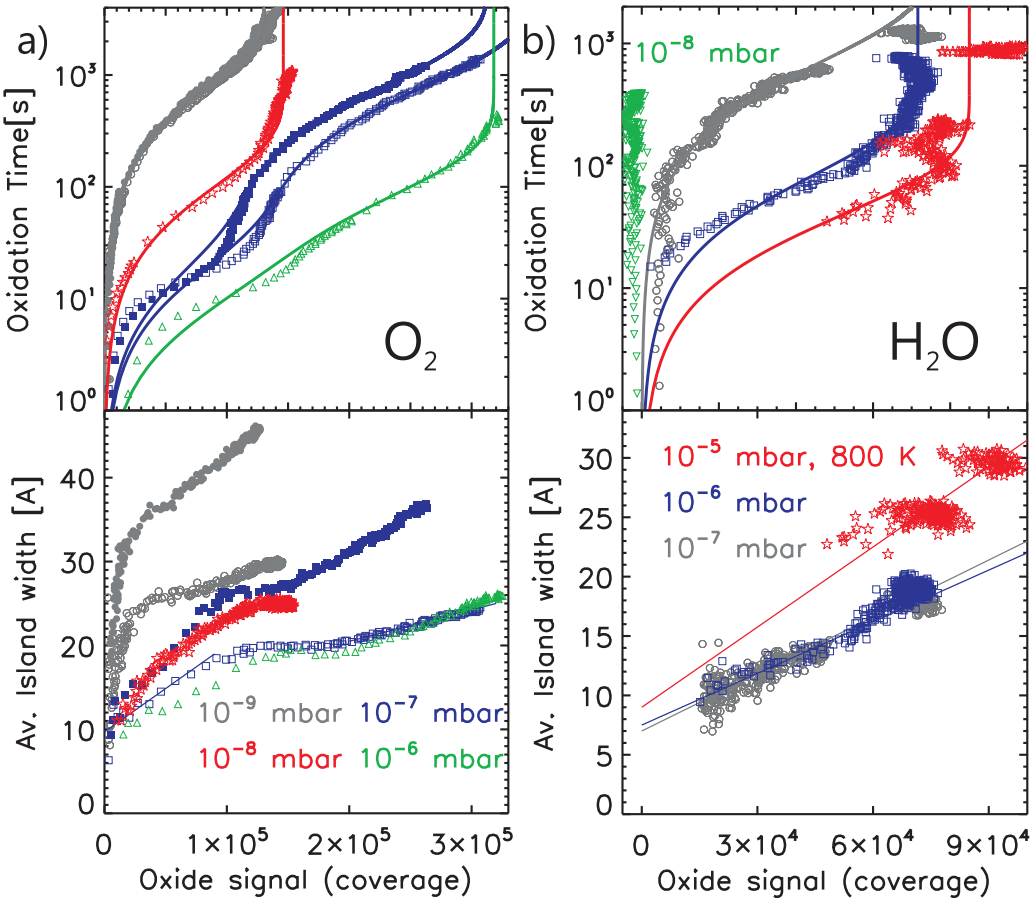

Figure 9.5: The integrated intensity of the oxide reflexion (proportional to the coverage) as a function of the oxidation time (upper part) and the island width along the direction of slow oxide growth as a function of the oxide intensity(lower part). Open and filled symbols mark data, recorded for the (1×2) and (2×1) domain, respectively. Solid lines represent fits according to the models described in the text. The oxide growth experiments are performed with molecular oxygen (part a; applied O_2 pressures: 4×10^{-9}, 5×10^{-8}, 5×10^{-7} and 5×10^{-6} mbar) or water vapour (part b, applied H_2O pressures: 2×10^{-8}, 3×10^{-7}, 2×10^{-6} and 1×10^{-5} mbar) at the indicated pressures and at T$= 700$ K (except the indicated experiment in part b). For clarity the growth curves of the top part are shown again on linear scale in fig. 9.8 at the end of this chapter.

diffusing oxygen atoms, which is needed to form oxide nuclei on the CoGa terraces and at the steps, is much lower during H_2O compared to O_2 oxidation at the same conditions. Dissociation of H_2O molecules on the CoGa surface is probably retarded compared to O_2 dissociation. Chemisorbed H_2O molecules might even block the steps which are favourite oxide nucleation and diffusion sites. H_2O-Oxidation might also roughen the surface or induce a faceting of the surface. No nicely ordered surface oxide could form on these

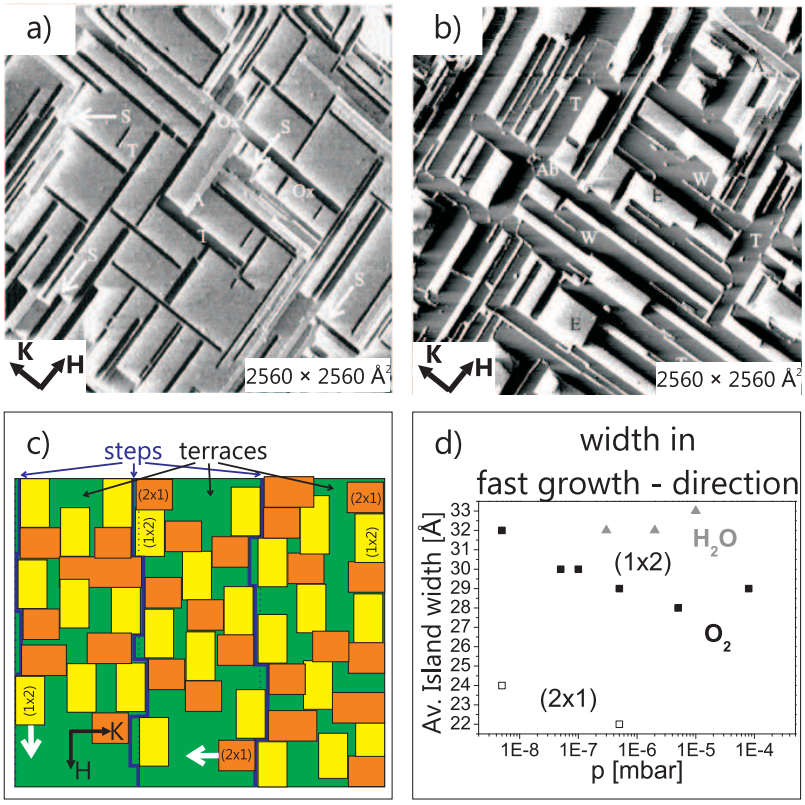

Figure 9.6: a)+b) STM images of the flat CoGa(1,0,0) surface after 3 L (a) and 10 L (b) oxygen exposure recorded by Franchy *et al.* (from [16]). The oxide island (dark parts, marked Ox) grow in stripes on the substrate (grey parts), starting at surface steps (marked S). Stripes of $90°$ rotated oxide domains block each other from growing further, leaving parts of the surface uncovered (marked E in part b). c) Possible scenario on the miscut, stepped CoGa(1,0,0) surface adopting the observations of the flat surface. The rotated oxide domains are coloured in orange and yellow, the substrate in green. The white arrows mark the fast-growth direction of the oxide stripes. d) Average oxide island width in the fast growing-direction as a function of oxygen pressures: Oxygen and water oxidation data are shown by black squares and grey triangles, respectively. Filled and open symbols show the results of the (1×2) and (2×1) domains, respectively.

surface fractions. This scenario could also explain the reduced surface oxide formation. However, no large signal of faceting could be detected and the measured CTR, shown later in this chapter, showed no significantly increased surface roughness.

The average island width along the direction of slow growth in fig. 9.5b (bottom) shows a strictly linear dependence on the oxide signal. This indicates that only the first step of the exponentially slowed down oxide growth takes place. A higher water vapour pressure leads to a higher islands width. Fig. 9.6d shows the final width in the fast growth direction of the oxide islands. The widths are around 32 Å which is comparable to the

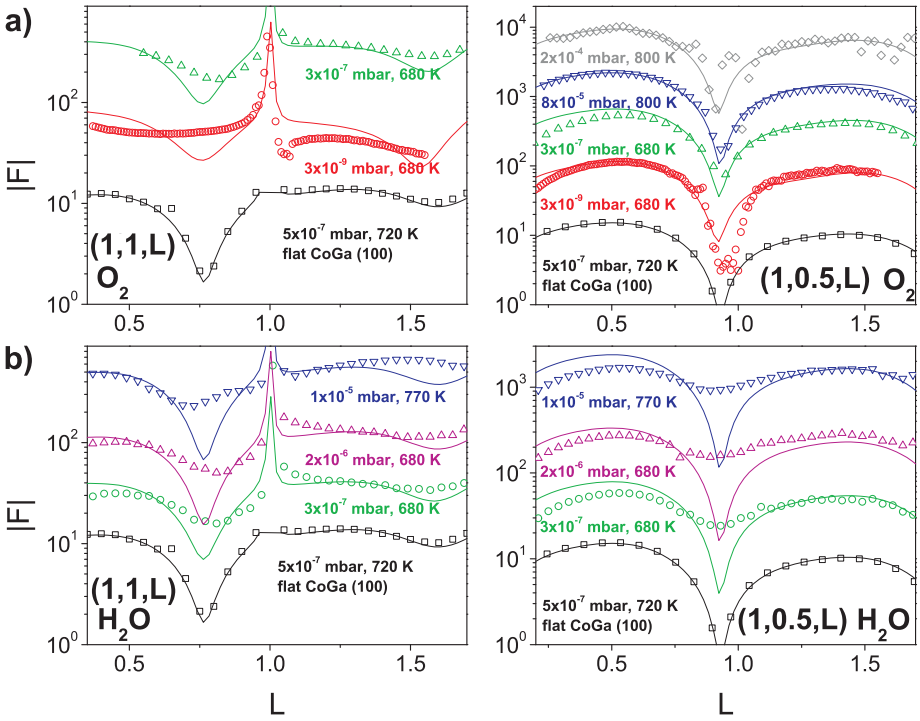

Figure 9.7: Data (open symbols) of the (1,1)-CTR (left) and the (1,0.5) surface rod (right) recorded of the CoGa surface after oxidation with oxygen (a) or water (b) at the indicated conditions. The results of the regular stepped CoGa are compared to the data of the flat, oxidized CoGa(1,0,0) surface (black squares) [40]. The solid lines (left part) show the fits calculated from the structural model known from the flat surface while different oxide coverages are assumed. Both rotated oxide domains are taken into account in the model by a coherent superposition. All rods are shifted for clarity.

maximum width observed during O_2 oxidation. Assuming a very low nucleation rate for the surface oxide, existing islands can grow larger for higher pressures. Although only the formation of the (1×2) oxide domain is followed in detail, the existence of the (2×1) domain was proven by surface rod measurements for all vapour pressures where oxide formation has been observed.

9.2.2 Oxide structure at various oxidation conditions

As described above, the CoGa surface is oxidized at temperatures between 680 K and 800 K and pressures ranging from 10^{-9} to 10^{-4} mbar while either molecular oxygen or water vapour is used for oxidation. To determine the structure of the surface oxide and the oxide-alloy interface structure, surface rods and CTRs are measured after every oxidation cycle. The data of one surface rod and one CTR are shown in fig. 9.7. The (1,0.5) surface rod, which is sensitive to oxide structure and the oxide coverage, is qualitatively identical

after all oxidation cycles. All rods, measured of the oxide on the stepped CoGa surface, have the same characteristic features as the rods, measured of the surface oxide formed on the flat CoGa(1,0,0) surface at similar conditions [15, 40]. Therefore, the structure of the oxide on the regularly stepped CoGa surface is identical to the oxide structure known from the flat CoGa surface [15, 40, 169]. No large structural differences are found after oxide formation with oxygen or water vapour.

The (1,1) CTR, which is sensitive to the structure of the oxide-alloy interface, shows characteristic changes, depending on the oxidation conditions. Especially the structure factor minimum, observed at L≈ 0.75, is pronounced differently. Different oxide coverages could explain these observations. To model this, two type of surface fractions are allowed which are added coherently. The oxide covered fraction is assumed to be covered by the oxide of the flat CoGa(1,0,0) surface. The remaining clean surface fractions are assumed to be purely metallic, with the same relaxations present like in the oxidized alloy. In comparison with a completely oxide covered CoGa surface the residuum χ^2_{norm} of the fits is improved by 20 to 50 % when applying the described fitting model on the data recorded for O_2 oxidation. The fitted CTRs are shown by solid lines in fig. 9.7a. For O_2 oxidation at 10^{-9}, 10^{-7}, 10^{-5} and 10^{-4} mbar oxide coverages of (55 ± 15) %, (74 ± 15), $(100 \pm 15)$and (65 ± 15) % are obtained, respectively. The surface oxide coverages shows an increase up to O_2 pressures of 10^{-5} mbar. At 10^{-4} mbar and 800 K Ga bulk-oxide might start to form which reduces the surface oxide coverage again. Applying the fitting model on the rods recorded for the H_2O oxidation did not improve the residua and always resulted in full coverage. This contradicts the small intensities measured in the growth curves which indicate a small surface oxide coverage. However, the rod fits, depicted in fig. 9.7b, shows no satisfying agreement with the CTR and surface rod data. The applied model is probably too simple. For an exact analysis the structure of the uncovered surface fractions as well as anisotropies in the fractions of the two surface oxide domains need to be taken into account. However, such an analysis lies beyond the information included in the recorded data and goes beyond the scope of this work.

9.3 Discussion

Surface rod and CTR measurements of the regularly stepped CoGa surface with its 200 Å wide (1,0,0) terraces are carried out after oxidation with molecular oxygen and water vapour to determine the structure of the formed oxide. The results indicate that the surface oxide has the same structure like determined by SXRD and DFT studies of the flat CoGa (1,0,0) surface oxidized at similar conditions [15, 169]. The epitaxial surface oxide consists of an oxygen ion double layer which contains the basic building block of bulk β-Ga_2O_3 but has a higher symmetry. In consistence with the results of the flat CoGa surface no formation of bulk oxide is observed on the stepped surface up to 10^{-5} mbar O_2 due to a hampered dissociative oxygen chemisorption on the surface oxide.

A STM study of the surface oxide formation on a flat CoGa (1,0,0) surface shows that the oxide islands are oriented in the [1,0,0] and [0,1,0] directions of the substrate. The sur-

face oxide domains with their (2×1) and (1×2) reconstructions grow fast along their long axis and slow perpendicular to it, producing stripe-like, $90°$-rotated oxide islands. The island formation starts mainly at the step edges of the large terraces [16]. According to this STM results, the miscut of the CoGa (1,0,0) surface investigated in the present work was chosen such that exclusively [0,1,0] aligned steps are present to preferentially promote the growth of the (2×1) domain. However, LEED and SXRD measurement clearly show no preferential oxide domain formation despite the steps. This is in contrast to other regularly stepped binary alloy surfaces like NiAl(6,7,1), NiAl(4,3,0) or NiAl(16,14,1) where a single oxide domain growth could be triggered by the existence of periodical steps (see chapter 8). The LEED study of the clean, miscut CoGa surface at 820 K shows a large disorder of the surface layers. This is consistent with a thermal-energy helium-atom scattering (TEAS) study on the clean CoGa(1,0,0) surface which reports a complete disorder of the surface region above 700 K [44]. A high surface disorder also affects the surface steps, which are -in contrast to the vicinal NiAl surfaces- not well defined any more but ragged shaped, like depicted schematically by the blue line in fig. 9.6c. This could explain their minor influence on the oxide domain growth on the stepped CoGa surface.

The results of the temporal evolution of the oxide coverage show that the growth process can be described by two steps of an exponentially slowed down growth for the O_2 oxidation. In the first stage of the growth, characterized by a fast rate, the fast growing oxide stripes with their $90°$ rotated domains grow on each terrace until they block each other from growing further. The coverage reaches a first saturation level at $2/5$ of the full coverage. In the second stage of the growth, characterized by a low rate, the oxide island continue growing along the slow growth direction until full coverage is reached. On the flat CoGa (1,0,0) surface only a single step, exponentially slowed down growth is observed at similar conditions [15]. Table 9.1 shows the growth rates of the flat surface which agree well with the growth rates of the first growth step on the stepped surface. The initial oxide growth on both surfaces, which takes place along the fast growth direction of the surface oxide, is probably the same for both surfaces. However, the surface steps seem to prevent a further oxide growth like on the flat surface as they block oxide growth across the steps. The new two-stage growth model is consistent with the images recorded from oxide domains near a surface step in the aforementioned STM study of the flat CoGa surface. The growth experiments of the this work show that approximately 750 L are needed for a full coverage of the surface. This value is of the same order of magnitude than the 200 L exposure for total coverage, resulting from the aforementioned STM study on the oxidation of CoGa (1,0,0) [16]

. The results of the evolution of the oxide islands width during the growth show that the initial oxide domains are approximately 10 Å broad in the direction of slow growth. This is consistent with the 10-20 Å found for the flat CoGa surface and corresponds to 2 unit cell wide oxide stripes [15, 16]. The final island width increases with decreasing O_2 pressures on both, the flat and stepped CoGa (1,0,0) surface. This indicates that the initial island density is set by the heterogeneous nucleation probability. For higher pressures the density of diffusing oxygen atoms is higher to form critical oxide nuclei on the CoGa terraces and at the steps. More islands nucleate next to each other. These nearby islands

can block each other from growing further as one oxide island grows into the other and stops growing. This model could explain the smaller island width at higher pressures. The observed final size of the approximately 30 Å long oxide stripes on the stepped surface is much smaller compared to the over 1000 Å long domains on the flat surface [15]. This shows that the oxide domains cannot grow across the steps, consequently forming many square-like oxide patches like shown in fig. 9.6c.

During H_2O oxidation higher vapour pressures are needed for oxide formation. The oxidation rate is much smaller compared to O_2 oxidation. A hampered dissociation of the water molecules and reduced rate of O atom diffusion could explains this behaviour as less nucleation takes place. H atoms or H_2O molecules might also block the steps edges as favourite nucleation sites.

9.4 Conclusions

In the present chapter the onset of the oxidation on a regularly stepped CoGa surface with 200 Å wide (1,0,0) terraces was investigated in real time and on an atomic length scale. Despite the terrace-step structure the ultra-thin Ga surface oxide known from the flat CoGa (1,0,0) surface is formed during O_2 and H_2O oxidation. The existence of surface steps along a dedicated direction could not trigger the expected preferential formation of one out of two $90°$-rotated oxide domains, probably due to a high, temperature related surface and step disorder. For O_2 and H_2O oxidation the oxide growth evolves via epitaxial growth modes by 2D nucleation of oxide islands. Thereby, the growth is characterized by two stages. In the initial, low oxygen-exposure growth the fast growing $90°$-rotated oxide domains block each other from growing further on the terraces, producing a unsystematic grid of oxide islands. In the following growth after longer oxygen exposure, the existing oxide island continue growing along their slow growth direction until the clean surface parts in the grid are fully covered by oxide. An oxygen pressure dependent transition in the growth behaviour is observed, accompanied by an increase of the mean oxide island width and a decrease in the initial nucleation rate for lower pressures. This is interpreted as a transition from heterogeneous oxide island nucleation on terraces to mainly step edge nucleation. In comparison with the flat CoGa surface, the formed oxide domains are much smaller on the stepped surface. This shows that an oxide growth across the step is not possible. Investigating the temporal surface oxide formation during water vapour oxidation shows tha higher pressures are needed for oxide formation and slower growth rates are observed. H_2O dissociation and O atom diffusion are probably hampered while water molecules block the steps which are favourite nucleation sites for oxide islands.

For applications of ultra-thin Ga oxide films the temperature related step-disorder prevents a tailoring towards a single domain oxide film. Furthermore, the presence of many steps and small terraces leads to the formation of only small oxide domains. Both observations lead to many domain boundaries and therefore many, undesirable defects in the oxide film. Thus, for producing a large ultra-thin homogeneous Ga oxide film a atomically flat substrate could be favourable. However twin domain formation cannot be avoided.

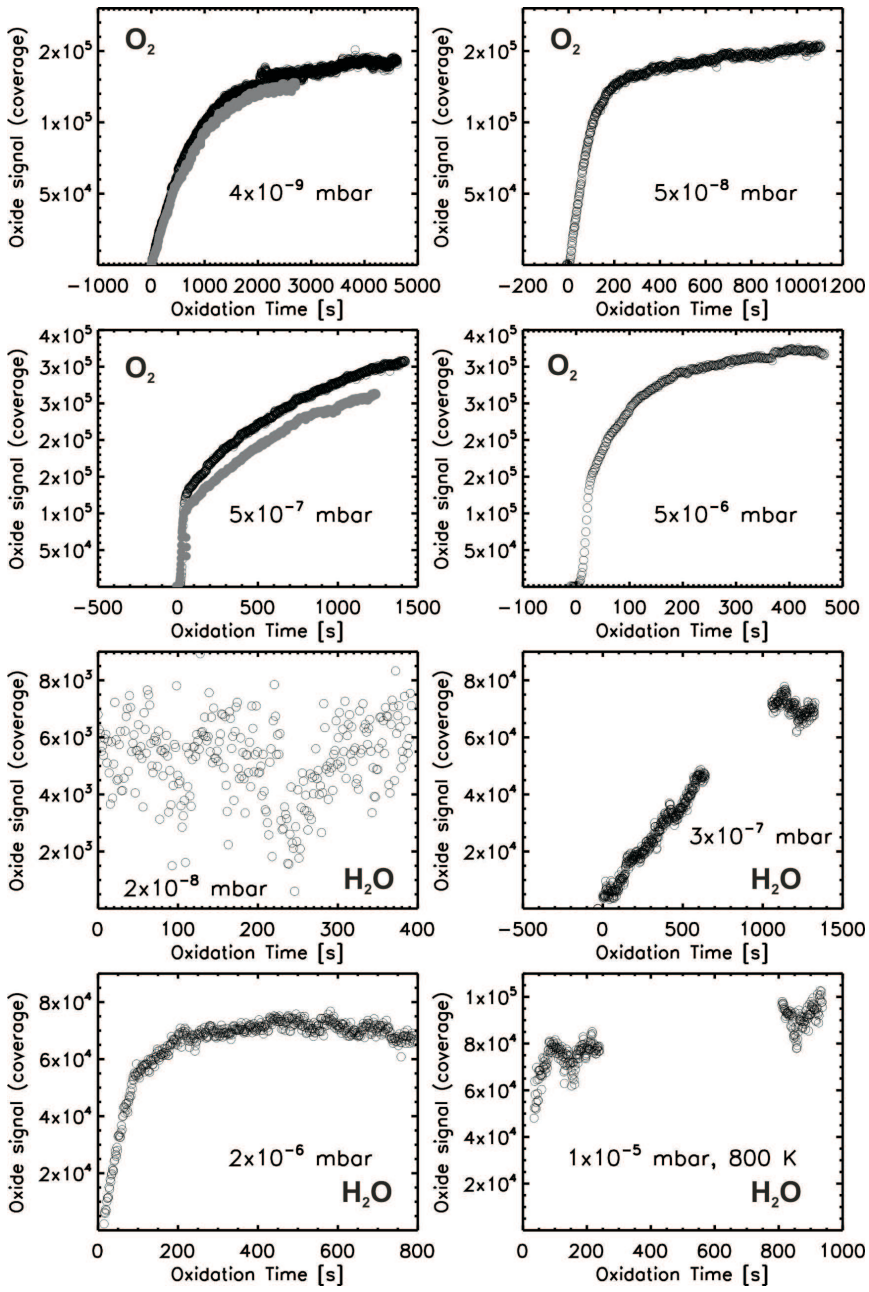

Figure 9.8: The oxide growth curves of the top part of fig. 9.5 on a linear scale.

Chapter 10

Conclusions and Outlook

Binary alloys like NiAl and Fe_3Al possess ordered intermetallic phases up to high temperatures. This order evokes a high mechanical stability up to elevated temperatures. To prevent the ordered alloys from further oxidation thin oxide layers are formed on the alloy surfaces. Thus, NiAl and Fe_3Al are used as basis for structural materials like light-weight steels which can be used under highly reactive conditions. Furthermore, it is known that during low-pressure oxidation of single crystal surfaces like CoGa(1,0,0) or NiAl(1,1,0) thin surface oxides are formed. In scientific research these films are often used as nanotemplate to study catalytic reactions or the electronic and vibrational features of organic molecules [17, 18]. Conclusively, a detailed understanding of the initial oxidation process is necessary to further improve the quality of oxide films on alloy surfaces. In former studies the oxidation of low-index binary alloy surfaces like NiAl(1,1,0), FeAl(1,1,0) or CoGa(1,0,0) has been studied in detail. Based on these results this thesis has continued the research of the initial oxidation process on atomic scale by increasing the complexity of the investigated systems.

The role of steps and kinks in the oxidation process is studied by SXRD for the regularly stepped NiAl (4,30) and the NiAl(6,7,1) surface as well as for a miscut CoGa (1,0,0) surface with 200 Å wide terraces. In addition, the interplay between intermetallic ordering and oxidation is investigated for the Fe_3Al(1,1,0) surface. While the (1,1,0) surface is flat and possesses only a small amount of surface steps, the complexity of the system is increased by investigating the oxidation of the highly ordered $D0_3$ phase of Fe_3Al. A short conclusion for every investigated system is given at the end of the corresponding chapters. In the following two sections the question raised in chapter 2 will be answered briefly by summarizing the results of this thesis.

10.1 Oxidation Induced Surface Disorder

The conducted SXRD study has shown that the clean Fe_3Al (1,1,0) surface possesses nearly perfect bulk-like $D0_3$- order. Only the order of the first atomic layer is disturbed due to Al segregation and exhibits B2-type order. CTR measurements on the clean vicinal

NiAl and CoGa surfaces show perfect bulk-like B2 order up to the topmost layer. This intermetallic order within the surface region is reduced upon oxidation for the NiAl and the Fe_3Al system while it is maintained for the CoGa surface, probably due to the significantly higher diffusion constants in case of CoGa. In Fe_3Al and NiAl the expansion of the oxygen induced disorder into the crystal is pronounced differently. Oxidation of the vicinal NiAl surfaces at 550 K and 10^{-6} mbar O_2 induces a preferential oxidation of Al. Consequently Al is drawn to the interface and Al and Ni vacancies and Ni anti-sites are formed up to a depths of around 1 nm. The B2 order of the surface is disturbed only slightly. For the Fe_3Al (1,1,0) surface the effect of oxygen induced surface disorder is much more pronounced after oxidation at 650 K and 10^{-6} mbar O_2. Up to a depth of 30 Å the $D0_3$- and B2-type order is destroyed. Directly at the oxide-alloy interface only the fundamental lattice is present while the order increases smoothly towards the bulk. $D0_3$-type ordered alloys like Fe_3Al have smaller bulk-diffusion constants for Al compared to B2-type ordered alloys like NiAl. This reduced diffusion rate probably prevents a sufficient Al supply from the bulk and therefore a reordering of the surface region, especially for the Fe_3Al system. Furthermore, it leads to the formation of a mixed Fe and Al oxide layer at high oxidation rates (10^{-6} mbar O_2). For slow oxidation rates at oxygen pressures of 10^{-8} mbar and temperatures above 470 K pure Al oxide films are formed on Fe_3Al (1,1,0). These smooth, pure alumina scales are important as protective layers in structural materials. As the high structural stability of the investigated alloy arises from the presence of intermetallic order, the surface region of Fe_3Al (1,1,0) might be more brittle compared to the investigated NiAl surfaces.

10.2 Oxidation of Regularly Stepped Alloy Surfaces

The investigated NiAl (6,7,1) and (4,3,0) surfaces both consist of 14 Å wide, (1,1,0) terraces while the steps runs along two different low-energetic directions. The CTR measurements carried out on the clean vicinal NiAl surfaces show that the regular terrace-step structures are thermodynamically stable in UHV up to high temperatures of at least 1350 K. No faceting is observed for the clean surfaces. For both surfaces a characteristic inward relaxation of the step atoms and an outward relaxation of the corner atoms below the steps could be detected, together with a rumpling of the Al and Ni atoms in the topmost terraces. Oxidation at 550 K and 10^{-6} mbar O_2, followed by a 1120 K annealing procedure lifts the initial terrace-step structure of both investigated surfaces and leads to the formation of large (1,1,0) facets which are up to 50 and 4 times larger then the original terraces of the (6,7,1) and (4,3,0) surface, respectively. For the oxidized (6,7,1) and (4,3,0) surface a (1,1,0)-oriented oxide-alloy interface is thermodynamically stable.

No large differences of oxygen induced Al segregation along the surface normal are observed, while comparing the vicinal with the flat, oxidized (1,1,0) surface. This indicates that the role of the steps as diffusion channels is small. However, two major effects of surface steps are observed in the experiments. The temperature dependence of the faceting of the oxidized surfaces is different. For the (6,7,1) surfaces the formation of (1,1,0) facets

starts at 1100 K while on the oxidized (4,3,0) surface small facets are already observed at 550 K. This indicates the presence of different kinetic barriers. The intralayer diffusion steps might be different due to the differently oriented steps. Surprisingly, also different oxide structures are observed after the annealing procedure of the two oxidized surfaces. LEED and SXRD experiments show that a complex, ultra-thin surface oxide is formed on the facets of the (6,7,1) surface. This complex oxide is known from the NiAl (1,1,0) surface where it grows in two twin-domains. On the (6,7,1) surface the preferential growth of one of the two twin domains is observed. This is most likely caused by strain release along Al rows at the oxide-alloy interface. The strain release happens preferentially along the weaker bound step atoms and triggers the formation of one domain where the Al rows are aligned in the direction of the steps. On the oxidized and annealed (4,3,0) surface with its (1,1,0) facets stripe-like domains of θ-Al_2O_3-like oxide are observed. Again strain release at oxide-alloy interface along the steps probably triggers θ-Al_2O_3 formation as the oxide and the alloy have a very little lattice mismatch in this direction.

These results nicely show the large influence of interfacial strain on the oxide formation and how weaker bound step atoms can release this strain in preferential directions. Thus, vicinal surfaces can be used to tailor the growth of different oxide structures or to form single-domain oxides. However, the steps need a certain temperature-stability to tailor the oxide growth. On a regular stepped CoGa surface with 200 Å wide (1,0,0) terraces a single oxide domain formation could not been tailored by distinctively oriented steps. The two $90°$-rotated domains, known to form on the flat CoGa (1,0,0) surface under oxidation at 700 K and 10^{-7} mbar O_2, are also observed on the stepped surface. LEED experiments indicate that the clean CoGa surface is disordered at temperatures around 700 K. Thus the surface steps are not well defined at the oxidation temperature and cannot tailor single-domain growths any more.

A investigation of the time-dependence of the oxide formation on CoGa at low oxidation pressures showed a exponentially slowed-down oxide growth which could be divided into two stages. In a stripe-like, fast growth process of the domains along their fast growth direction the terraces are covered by a grid of oxide domains, blocking each other from growing further. Then the uncovered parts within the oxide grid are filled by a slow oxide growth process. Comparing molecular oxygen and water vapour oxidation of the CoGa surface shows the formation of the same oxide structure. However, the oxide formation is retarded when using water vapour. Water molecules seem to block the step sites and therefore the oxide formation.

10.3 Outlook

The results of this thesis clearly show that the presence of highly ordered intermetallic phases and the existence of surface steps on binary alloy surfaces further complicate the initial oxidation process. In case of the Fe_3Al system detailed information on the interplay between intermetallic order and oxide layer formation could be achieved by combining several experimental techniques like SXRD and HRCLS. To understand the driving forces

for the oxygen induced Al segregation accompanying theoretical calculation are desirable. Combining quantum mechanics and statistical physics via DFT, cluster expansion and Monte Carlo simulations could be one important approach to reveal segregation processes in binary alloys [27]. For applications of Fe_3Al as structural material additives like Ti or Mn play an important role to increase the ductility of the alloys. Therefore, similar experiments like conducted in this study would be interesting for these ternary systems to understand the oxidation process. A pre-deposition of Al on the alloy surfaces could promote the desired formation of pure alumina on the surface and would be interesting to study. In case of the vicinal NiAl surfaces experimental methods like STM or AFM could provide additional information on the oxide structures. Especially for the θ-Al_2O_3-like oxide stripes on the NiAl (4,3,0) surface a STM image could be helpful. DFT calculations of the clean, vicinal NiAl surfaces could be interesting to confirm our results on the relaxation of the step and corner atoms. In further experiments metallic nanoparticles could be grown on the single-domain surface oxide films on NiAl(6,7,1) to study their catalytic behaviours. Furthermore, the oxidation and catalytic behaviour of NiAl nanoparticles could be studied in future experiments. Thereby, the results of this work could provide first fundamental insights on processes at the edges and facets of the nanoparticles.

Appendix A

Abbreviations and Acronyms

AES	**A**uger **E**lectron **S**pectroscopy
AFM	**A**tomic **F**orce **M**icroscope
ANKA	**AN**gströmquelle **KA**rlsruhe
APDB	**A**nti **P**hase **D**omain **B**oundary
ANKA	**AN**gströmquelle **KA**rlsruhe
bcc	**b**ody **c**entered **c**ubic
BM	**B**ending **M**agnet
CCD	**C**harge **C**oupled **D**evice
CTR	**C**rystal **T**runcation **R**od
DFT	**D**ensity **F**unctional **T**heory
DS	**D**oniach **S**unjic
DWBA	**D**istorted **W**ave **B**orn **A**pproximation
DWF	**D**ebye **W**aller **F**actor
ESRF	**E**uropean **S**ynchrotron **R**adiation **F**acility
fcc	**f**ace **c**entered **c**ubic
FWHM	**F**ull **W**idth of **H**alf **M**aximum
GID	**G**racing **I**ncidence **D**iffraction
HREELS	**H**igh **R**esolution **E**lectron **E**nergy **L**oss **S**pectroscopy
L	**L**angmuir
LEED	**L**ow **E**nergy **E**lectron **D**iffraction
LEIS	**L**ow **E**nergy **I**on **S**cattering
MAX-Lab	Synchrotron in Lund, Sweden
MD	**M**olecular **D**ynamic
MPI MF	**M**ax **P**lanck **I**nstitute for **M**etals **R**esearch
SEM	**S**canning **E**lectron **M**icroscopy
SLS	**S**wiss **L**ight **S**ource
STM	**S**canning **T**unneling **M**icroscopy
SXRD	**S**urface **X** **R**ay **D**iffraction

TDS	**T**hermal **D**iffuse **S**cattering
TEM	**T**ransmission **E**lectron **M**icroscopy
UHV	**U**ltra **H**igh **V**acuum
VdW	**V**an **d**er **W**aals
XAS	**X**-ray **A**bsorption **S**pectroscopy
XPS	**X**-ray **P**hotoelectron **S**pectroscopy
XRD	**X**-**R**ay **D**iffraction
XRR	**X**-**R**ay **R**eflectivity

Appendix B

Symbols used in Equations

Elementary constants

CODATA internationally recommended values of the fundamental physical constants where taken from NIST [170].

$e = 1.6022 \cdot 10^{-19}\,\mathrm{C}$	elementary charge
$\hbar = 1.0546 \cdot 10^{-34}\,\mathrm{Js}$	Planck constant $/2\pi$
$k_\mathrm{B} = 1.3807 \cdot 10^{-23}\,\mathrm{JK}^{-1}$	Boltzmann constant
$r_0 = \frac{e^2}{4\pi\epsilon_0 m_e c^2} = 2.8179 \cdot 10^{-15}\,\mathrm{m}$	classical electron radius

Symbols

$\alpha_\mathrm{c} \approx \sqrt{2\delta}$	critical angle of total reflection
α_f	exit angle
α_i	incidence angle
β	optical constant (imaginary part) or
-	occupancy parameter in roughness model
χ^2	deviation between fitted and experimental data
δ	optical constant (real part)
E	energy
f_j	atomic form factor
	in forward scattering
	in forward scattering
$F\,(q)$	structure factor
Φ	Work function
I	intensity
$\vec{k_\mathrm{i}}$	incidence wave vector

$\vec{k_\mathrm{f}}$	final wave vector
$\lambda = \frac{hc}{E}$	x-ray wavelength
Λ	information depth
m	mass
μ_material	mass attenuation coefficient of the specified material
$n = 1 - \delta + i\beta$	complex optical constant or refractive index
p	pressure
$P = \frac{1}{2}\left[1 + \cos^2 2\vartheta\right]$	polarization factor for non polarized x-rays
$P_\parallel = 1$	polarization factor for parallel polarization
$P_\perp = \cos^2 2\vartheta$	polarization factor for perpendicular polarization
$\vec{q} = \vec{k_\mathrm{f}} - \vec{k_\mathrm{i}}$	scattering vector
q_c	maximal wave vector transfer for total reflection
;q_max	maximum momentum transfer achieved in an experiment
q_z	z-component of the scattering vector
$R^2\left(q_z\right)$	x-ray reflectivity
ρ_e	electron density
t	time
T	temperature
Θ	coverage
2ϑ	scattering angle
Z	atomic number

Bibliography

[1] C. G. McKamey, J. H. DeVan, P. F. Tortorelli, and V. K. Sikka. A review of recent developments in Fe_3Al-based alloys. *J.Mater.Res.*, **6** 1779–1805, (1991).

[2] N. P. Padture, M. Gell, and E. H. Jordan. Material science - thermal barrier coatings for gas-turbine engine applications. *Science*, **296** 280, (2002).

[3] J. Libuda, F. Winkelmann, M. Bäumer, H.-J. Freund, T. Bertrams, H. Neddermeyer, and K. Müller. Structure and defects of an ordered alumina film on NiAl(110). *Surf. Sci.*, **318** 61–73, (1994).

[4] A. Stierle, F. Renner, R. Streitel, H. Dosch, W. Drube, and B. C. Cowie. X-ray diffraction study of the ultrathin Al_2O_3 layer on NiAl(110). *Science*, **303** 1652–1656, (2004).

[5] G. Kresse, M. Schmid, E. Napetschnig, M. Shishkin, L. Köhler, and P. Varga. Structure of the ultrathin aluminium oxide film on NiAl(110). *Science*, **308** 1440–1442, (2005).

[6] R. Franchy. Growth of thin, crystalline oxide, nitride and oxynitride films on metal and metal alloy surfaces. *Surf. Sci. Rep.*, **38** 195–294, (2000).

[7] H. Graupner, L. Hammer, K. Heinz, and D. M. Zehner. Oxidation of low-index FeAl surfaces. *Surf. Sci.*, **380** 335–351, (1997).

[8] P. Gassmann, R. Franchy, and H. Ibach. Investigations on phase transitions within thin Al_2O_3 layers on NiAl(001) - HREELS on aluminium oxide films. *Surf. Sci.*, **319** 95–109, (1994).

[9] J. Als-Nielsen and D. McMorrow. *Elements of Modern X-Ray Physics*. Wiley & Sons Ltd, Chichester, (2001).

[10] H. Dosch. *Critical Phenomena at Surfaces and Interfaces*. Springer Verlag, Berlin, (1992).

[11] I. K. Robinson. Crystal truncation rods and surface roughness. *Phys. Rev. B*, **33** 3830 – 3836, (1986).

[12] A. Stierle, F. Renner, R. Streitel, and H. Dosch. Observation of bulk forbidden defects during the oxidation of NiAl(1,1,0). *Phys. Rev. B*, **65** 165413, (2001).

[13] R. Smoluchowski. Anisotropy of the electronic work function of metals. *Surf. Sci.*, **60** 661–674, (1941).

[14] V. I. Marchenko and A. Y. Parshin. Elastic properties of crystal surfaces. *Sov. Phys. JETP*, **52** 129–131, (1980).

[15] A. Stierle *et al.* Real time observation of ultrathin epitaxial oxide growth during alloy oxidation. *New J. Phys.*, **9** 331, (2007).

[16] R. Franchy, M. Eumann, and G. Schmitz. Elemental steps in the growth of thin beta-$Ga_2 2O_3$ films on CoGa(100). *Surf. Sci.*, **470** 337–346, (2001).

[17] E. Napetschnig, M. Schmid, and P. Varga. Pd, Co and Co-Pd clusters on the ordered alumina film on NiAl(1,1,0): Contact angle, surface structure and composition. *Surf. Sci.*, **601** 3233–3245, (2007).

[18] X. H. Qiu, G. V. Nazin, and W. Ho. Vibrationally resolved fluorescence excited with submolecular precision. *Science*, **299** 542, (2003).

[19] C. Tegenkamp. Vicinal surfaces for functional nanostructures. *J. Phys. C: Cond. Mat.*, **21** 013002, (2002).

[20] K. R. Lawless. Oxidation of metals. *Rep. Prog. Phys.*, **37** 231–316, (1974).

[21] E. Bauer. Phenomenal theory of precipitation on surfaces. II. *Z. Kristall.*, **110** 395–431, (1958).

[22] N. Cabrera and N. F. Mott. Theory of the oxidation of metals. *Rep. Prog. Phys.*, **12** 163–184, (1948).

[23] A. T. Fromhold and E. L. Cook. Schottky emission as a rate-limiting factor in thermal oxidation of metals. *Phys. Rev. Lett.*, **17** 1212–1216, (1966).

[24] A. T. Fromhold and E. L. Cook. Kinetics of oxide film growth on metal crystals: Electron tunnelling and ionic diffusion. *Phys. Rev.*, **158** 600–612, (1967).

[25] A. T. Fromhold and E. L. Cook. Kinetics of oxide film growth on metal crystals: Thermal electron emission and ionic diffusion. *Phys. Rev.*, **163** 650–664, (1967).

[26] G. R. Wallwork. The oxidation of alloys. *Rep. Prog. Phys.*, **39** 401–485, (1976).

[27] S. Müller. Bulk and surface ordering phenomena in binary metal alloys. *J. Phys.: Condens. Matter*, **15** R1429–R1500, (2003).

[28] V. Blum, L. Hammer, W. Meier, K. Heinz, M. Schmid, E. Lundgren, and P. Varga. Segregation and ordering at $Fe_{1-x}Al_x(100)$ surfaces -a model case for binary alloys. *Surf. Sci.*, **474** 81–97, (2001).

[29] O. Kizilkaya, D. A. Hite, D. M. Zehner, and P. T. Sprunger. Surface reconstruction of FeAl(110) studied by scanning tunnelling microscopy and angle-resolved photoemission spectroscopy. *J. Phys.:Condens. Matter*, **16** 5395–5406, (2004).

[30] H. Graupner, L. Hammer, K. Müller, and D.M. Zehner. Composition and structure of the (100) and (110) surfaces of FeAl. *Surf. Sci.*, **322** 103–115, (1995).

[31] L. Hammer, W. Meier, V. Blum, and K. Heinz. Equilibration processes in surfaces of the binary alloy Fe-Al. *J. Phys.: Condens. Matter*, **14** 4145–4164, (2002).

[32] A. P. Baddorf and S. S. Chandavarkar. Identification of an incommensurate $FeAl_2$ overlayer on FeAl(110) using x-ray diffraction and reflectivity. *Physica B*, **221** 141–144, (1996).

[33] D. Voges, E. Taglauer, H. Dosch, and J. Peisl. Surface segregation on $Fe_3Al(110)$ near the order-disorder transition temperature. *Surf. Sci.*, **269/270** 1142–1146, (1992).

[34] H. Dosch, L. Mailänder, R. L. Johnson, and J. Peisl. Critical phenomena at the $Fe_3Al(1\bar{1}0)$ surface: A glancing angle x-ray scattering study. *Surf. Sci.*, **279** 367 – 379, (1992).

[35] L. Mailänder, H. Dosch, J. Peisl, and R. L. Johnson. Near-surface critical x-ray scattering from Fe_3Al. *Phys. Rev. Lett.*, **64** 2527–2530, (1989).

[36] B. Pöter, F. Stein, R. Wirth, and M. Spiegel. Early stages of protective oxide layer growth on binary iron aluminides. *Z. Phys. Chem.*, **219** 1489–1503, (2005).

[37] A. Velon and I. Olefjord. Oxidation behaviour of Ni_3Al and Fe_3Al: I. XPS calibration of pure compounds and quantification of the results. *Oxid. Metals*, **56** 415–424, (2001).

[38] O. Kizilkaya, D. A. Hite, D. M. Zehner, and P. T. Sprunger. Formation of aluminium oxide thin films on FeAl(110). *Surf. Sci.*, **529** 223–230, (2003).

[39] D. Mullins and S. Overbury. The structure and composition of the NiAl(110) and NiAl(100) surfaces. *Surf. Sci.*, **199** 141–153, (1988).

[40] A.-G. Vlad. *In-Situ Oxidation Study of Metallic Alloys from UHV to Atmospheric Pressures*. Max-Planck-Institut für Metallforschung, Stuttgart, (2008).

[41] A. Vlad, A. Stierle, N. Kasper, H. Dosch, and M. Rühle. In situ x-ray study of the γ- to α-Al_2O_3 phase transformation during atmospheric pressure oxidation of NiAl(110). *J. Mater. Res.*, **21** 3047–3057, (2006).

[42] R. M. Jaeger, H. Kuhlenbeck, H.-J. Freund, M. Wuttig, W. Hoffmann, R. Franchy, and H. Ibach. Formation of a well-ordered aluminium oxide overlayer by oxidation of NiAl(110). *Surf. Sci.*, **259** 235–252, (1991).

[43] J. P. Pierce, N. C. Bartelt, R. Stumpf, and K. F. McCarthy. Stability of ultrathin alumina layers on NiAl(110). *Phys. Rev. B*, **77** 195438, (2008).

[44] F. M. Pan, C. Pflitsch, R. David, L. K. Verheij, and R. Franchy. Reconstruction of the CoGa (100) surface studied by thermal-energy helium-atom scattering, LEED, and AES. *Phys. Rev. B*, **63** 125414, (2001).

[45] E. Eumann, G. Schmitz, and R. Franchy. Long rectangular islands of beta-Ga2O3 on CoGa(001) - studied by electron energy loss spectroscopy and scanning tunnelling microscopy. *Appl. Phys. Let.*, **72** 3440–3442, (1998).

[46] M. C. Desjonqueres, D. Spanjaard, C. Barreteau, and F. Raouafi. Stability of metal vicinal surfaces revisited. *Phys. Rev. Lett.*, **88** 056104, (2002).

[47] A. N. Al-Rawi, A. Kara, and T. S. Rahman. Theoretical study of the structure and vibrational dynamics of Cu_3Au(511). *J.Phys.: Condensed Matter*, **16** S2967–S2979, (2004).

[48] G. Prevot and S. Ferrer P. Steadman. Determination of the elastic dipole at the atomic steps of Pt(977) from surface x-ray diffraction. *Phys. Rev. B*, **67** 245409, (2003).

[49] J. Gustafson et. al. Oxygen-induced step bunching and faceting of Rh(553): Experiment and ab initio calculations. *Phys. Rev. B*, **74** 035401, (2006).

[50] R. Westerström et. al. Oxidation of Pd(553): From ultrahigh vacuum to atmospheric pressure. *Phys. Rev. B*, **76** 155410, (2007).

[51] U. Bardi, P. N. Ross, and G. Rovida. Initial stages of oxidation of binary alloys: the case of the stepped Pt_3Ti(510) single crystal surface. *Surf. Sci. Letters*, **205** L798–L804, (1988).

[52] S. Ulrich, N. Nilius, and H.-J. Freund. Growth of thin alumina films on a vicinal NiAl surface. *Surf. Sci.*, **601** 4603–4607, (2007).

[53] K. Lonsdale. The structure of the benzene ring. *Nature*, **122** 810–812, (1928).

[54] D. Crowfoot Hodgkin. X-ray single crystal photographs of insulin. *Nature*, **135** 591–592, (1935).

[55] M. Laue. Interferenzerscheinungen bei Röntgenstrahlen. *Annalen der Physik*, **41** 971–988, (1913).

[56] A. Guinier. *X-Ray Diffraction In Crystal, Imperfect Crystals, and Amorphous Bodies*. Dover Books, New York, (1956).

[57] B. E. Warren. *X-Ray Diffraction*. Dover Books, New York, (1969).

[58] M. Fähnle and L. Schimmele. Atomic defects and diffusion in intermetallic compounds with $D0_3$ structure: An ab-initio study. *Z. Metallkd.*, **95** 864 – 869, (2004).

[59] J. Meyer, C. Elsässer, and M. Fähnle. Concentrations of atomic defects in B2-Fe_xAl_{1-x}. *Phy. Stat. Sol. (b)*, **191** 283 – 298, (1995).

[60] A. Munkholm and S. Brennan. Influence of miscut on crystal truncation rod scattering. *J. Appl. Cryst.*, **32** 143 – 153, (1999).

[61] E. Vlieg. Integrated intensities using a 6-circle surface x-ray diffractometer. *J. Appl. Cryst.*, **30** 532 – 543, (1997).

[62] M. Tolan. *X-Ray Scattering from Soft Matter Thin Films*. Springer, Berlin, (1999).

[63] H. Dosch. Evanescent absorption in kinematic surface bragg diffraction. *Phys. Rev. B*, **35** 2137 – 2143, (1987).

[64] H. Dosch, B. W. Batterman, and D. C. Wack. Depth-controlled grazing-incidence diffraction of synchrotron x radiation. *Phys. Rev. Lett.*, **56** 1144 – 1147, (1985).

[65] M. Born and E. Wolf. *Principles of Optics*. Pergamon Press, Oxford, (1980).

[66] L. Nevot and P. Croce. Characterization of surfaces by grazing x-ray reflection. *Rev.Phys.Appl.*, **15** 761 – 779, (1980).

[67] P. Croce. On electromagnetic wave propagation through a scattering stratified medium. *J.Optics*, **10** 141 – 145, (1979).

[68] P. Beckmann and A. Spizzichino. *The Scattering Of Electromagnetic Waves From Rough Surfaces*. Pergamon Press, New York, (1963).

[69] A. Braslau, P. S. Pershan, G. Swislow, B. M. Ocko, and J. Als-Nielsen. Capillary waves on the surface of simple liquids measured by x-ray reflectivity. *Phys. Rev. A*, **38** 2457 – 2470, (1988).

[70] G. H. Vineyard. Grazing-incidence diffraction and the distorted-wave approximation for the study of surfaces. *Phys. Rev. B*, **26** 4146 – 4158, (1982).

[71] S. Dietrich and H. Wagner. Critical surface scattering of x-rays and neutrons at grazing angles. *Phys. Rev. Lett.*, **51** 1469 – 1471, (1983).

[72] H. v. Helmholtz. Über die physikalische Bedeutung des Princips der kleinsten Wirkung. *J.f.d.reine u. angew. Mathe.*, **100** 213, (1887).

[73] A. M. Afanas'ev and M. K. Melkonyan. X-ray diffraction under specular reflection conditions. ideal crystals. *Acta Cryst. A*, **39** 207 – 210, (1983).

[74] J. Strong. *Concepts of Classical Optics*. Freeman, San Francisco, (1958).

[75] J. Picht. Article on the theory of total reflection. *Annalen der Physik*, **3** 433, (1929).

[76] L. G. Parratt. Surface studies of solids by total reflection of x-rays. *Phys. Rev.*, **95** 359–369, (1954).

[77] H. Hertz. —. *Ann. der Physik und Chemie*, **267** 983, (1887).

[78] A. Einstein. —. *Ann. der Physik*, **322** 132–148, (1905).

[79] G. Ertl and J. Küppers. *Low Energy Electrons and Surface Chemistry*. VCH, Weinheim, (1985).

[80] M. Henzler and W. Göpel. *Oberflächenphysik des Festkörpers*. Teubner, Stuttgart, (1991).

[81] UK surface analysis forum: Online database. http://www.uksaf.org/data.html, (2008).

[82] A. Stierle, C. Tieg, H. Dosch, V. Formoso, E. Lundgren, J. N. Andersen, L. Köhler, and G. Kresse. Surface core level shift observed on NiAl(110). *Surf.Sci. Let.*, **529** L263–L268, (2003).

[83] S. Doniach and M. Sunjic. Many-electron singularity in x-ray photoemission and x-ray line spectra from metals. *J.Phys.C: Solid St.Phys.*, **3** 285–291, (1970).

[84] C. Davidson and L. H. Germer. Diffraction of electrons by a crystal of nickel. *Phys. Rev.*, **30** 705, (1927).

[85] P. Auger. The effect of a photoelectric compound. *J. Phys. Radium*, **6** 205, (1925).

[86] Handbook of auger electron spectrocopy. Physical Electronic Industries, Edina, (1972).

[87] H. Iser and G. R. Castro. The initial interaction of oxygen with a NiAl(110) single crystal: A LEED and AES study. *Surf. Sci.*, **211/212** 865–871, (1989).

[88] M. Seo, J. B. Lumsden, and R. W. Staehle. An AES analysis of oxide films on iron. *Surf. Sci.*, **50** 541–552, (1975).

[89] A. Stierle, A. Steinhäuser, A. Rühm, F. U. Renner, R. Weigel, N. Kasper, and H. Dosch. Dedicated max-planck beamline for the in situ investigation of interfaces and thin films. *Rev. Sci. Instruments*, **75** 5302–5307, (2004).

[90] ESRF-beamline ID03. www.esrf.eu/UsersAndScience/Experiments/SurfaceScience/.

[91] Certified scientific software, SPEC. http://www.certif.com.

[92] mar, usa: CCD-camera. http://www.mar-usa.com.

[93] C. Broennimann, E. F. Eikenberry, R. Horisberger, G. Huelsen, B. Schmitt, C. Schulze-Briese, and T. Tomizaki. Continuous sample rotation data collection for protein crystallography with the PILATUS detector. *Nuc. Instr. Meth. Phys. Res. A*, **510** 24–28, (2003).

[94] R. Nyholm, J. N. Andersen, U. Johansson, B. N. Jensen, and I. Lindau. Beamline I311 at MAX-LAB: a VUV/soft x-ray undulator beamline for high resolution electron spectroscopy. *Nucl. Instr. Meth. Phys. Res. A*, **467-468** 520–524, (2001).

[95] N. Martensson, P. Baltzer, P. A. Brühwiler, J.-O. Forsell, A. Nilsson, A. Stenborg, and B. Wannberg. A very high resolution electron spectrometer. *J. Electron Spectrosc. Relat. Phenom.*, **70** 117, (1994).

[96] A. Schneider, G. Frommeyer, and U. Brüx. Strukturen und mechanische Eigenschaften von Eisen -Aluminium-Legierungen. *http://www.mpie.de/1406/*, pages 1–7, (2005).

[97] H. Okamoto and P. A. Beck. Phase relationships in the iron-rich Fe-Al alloys. *Metal. Trans.*, **2** 569–574, (1971).

[98] S. M. Kim and D. G. Morris. Long range order and vacancy properties in Al-rich Fe_3Al and Fe_3Al(Cr) alloys. *Acta mater.*, **46** 2587–2602, (1998).

[99] Pearsons handbook of crystallographic data for intermetallic phases. Metals Park OH, (1985).

[100] S. C. Deevi and V. K. Sikka. Nickel and iron aluminides: an overview on properties, processing, and applications. *Intermetallics*, **4** 357–375, (1996).

[101] M. Fähnle and L. Schimmele. Atomic defects and diffusion in intermetallic compounds with $D0_3$ structure: an ab-initio study. *Z. Metallkd.*, **95** 864–869, (2004).

[102] G. Bester, B. Mayer, and M. Fähnle. Atomic defects and diffusion in intermetallic compounds with $D0_3$ structure: an ab-initio study. *Phys. Rev. B*, **60** 14492, (1999).

[103] B. Pöter, F. Stein, R. Wirth, and M. Spiegel. Early stages of protective oxide layer growth on binary iron aluminides. *Z. Phys. Chem.*, **219** 1489–1503, (2005).

[104] I. Levin and D. Brandon. Metastable alumina polymorphs: Crystal structure and transition sequences. *J. Am. Ceram. Soc.*, **81** 1995–2012, (1998).

[105] Numerical data and functional relationships in science and technology. Springer Verlag, (1997).

[106] L. Pauling and S. B. Hendricks. The crystal structures of haematite and corundum. *J. Am. Chem. Soc.*, **47** 781–790, (1925).

[107] W.E.Lee and K. P. D. Lagerlof. Structural and electron diffraction data for sapphire. *J. Electron. Micr. Tech.*, **2** 247–258, (1985).

[108] J. W. Halloran and H. K. Bowen. Iron diffusion in iron-aluminate spinels. *J. Americ. Ceramic Soc.*, **63** 58–65, (1980).

[109] L. M. Atlas and W. K. Sumida. Solidus, subsolidus, and subdissociation phase equilibria in the system Fe-Al-O. *J. Americ. Ceram. Soc.*, **41** 150–160, (1958).

[110] Binary alloy phase diagrams. http://gwdg-cd-www.gwedg.de/institute/mpimf.html.

[111] E. R. Jette and F. Foote. An x-ray study of the wuestite FeO solid solutions. *J. Chem. Phys.*, **1** 29–36, (1958).

[112] F. R. S. Cavendish W. H. Bragg. The structure of the spinel group of crystals. *Philos. Mag.*, **30** 305–315, (1915).

[113] F. Bouree, J. L. Baudour, E. Elbadraoui, J. Musso, C. Laurent, and A. Rousset. Crystal and magnetic structure of piezoelectric, ferrimagnetic and magnetoelectric aluminium iron oxide $FeAlO_3$ from neutron powder diffraction. *Acta Cryst. B*, **52** 217–222, (1996).

[114] C. E. Meyers, T. O. Mason, W. T. Petuskey, J. W. Halloran, and H. K. Bowen. Phase equilibria in the system Fe-Al-O. *J. Americ. Ceramic Soc.*, **63** 659–663, (1980).

[115] A. Velon and I. Olefjord. Oxidation behaviour of Ni_3Al and Fe_3Al: Ii. early stage of oxide growth. *Oxidat. Met.*, **56** 425–452, (2001).

[116] A. Taylor and N. J. Doyle. Further studies on the nickel-aluminium system I: The β-NiAl and δ-Ni_2Al_3 phase fields. *J. Appl. Cryst.*, **5** 201–209, (1972).

[117] M. Kogachi, Y. Takeda, and T. Tanahashi. Defect structure in Al-rich composition region in the β-NiAl intermetallic compound phase. *Intermetallics,* **3** 129–136, (1995).

[118] S. M. Kim. Vacancies in CsCl-type intermetallic compounds: Structural versus thermal. *Phys. Rev. B,* **33** 1509–1511, (1985).

[119] R. Krachler and H. Ipser. Triple-defect complexes in the B2 intermetallic compound NiAl. *Phys. Rev. B,* **70** 054113, (2004).

[120] D. Farkas, B. Mutasa, C. Vailhe, and K. Ternes. Interatomic potentials for B2 NiAl and martensitic phases. *Modelling Simul. Mater. Sci. Eng.*, **3** 201–214, (1995).

[121] M. Marcinkowski and N. Brown. Direct observation of antiphase boundaries in the Fe3Al superlattice. *J. Appl. Phys.*, **33** 537–552, (1962).

[122] N. R. Gleason and D. R. Strongin. A photoelectron spectroscopy and thermal desorption study of CO on FeAl(110) and polycrystalline TiAl and NiAl. *Surf. Sci.*, **295** 306–318, (1993).

[123] E. Vlieg. ROD: A program for surface x-ray crystallography. *J. Appl. Cryst.*, **33** 401 – 405, (2000).

[124] Y. Komura, Y. Tomiie, and R. Nathans. Scattering factor for outer electrons in ordered Fe_3Al. *Phys. Rev. Let.*, **3** 268–269, (1959).

[125] C. Berg, S. Raaen, A. Borg, J. N. Andersen, E. Lundgren, and R. Nyholm. Observation of a low-binding peak in the 2p core-level photoemission from oxidized Al(111). *Phys. Rev. B*, **47** 13063, (1993).

[126] D. T. Quinto and W. D. Robertson. Identification of auger spectra from aluminium. *Surf. Sci*, **27** 645, (1971).

[127] M. Suleman and E. B. Pattinson. Changes in auger spectra of Mg and Fe due to oxidation. *Surf. Sci*, **35** 75–81, (1973).

[128] V. S. Smentkowski and J. J. T. Yates. The adsorption of oxygen on Fe(110) in the temperature-range of 90 K to 920 K. *Surf. Sci*, **232** 113–128, (1990).

[129] H. Isern and G. R. Castro. The initial interaction of oxygen with a NiAl(110) single crystal: a LEED and AES study. *Surf. Sci.*, **211/212** 865–871, (1989).

[130] R. Drautz, H. Reichert, M. Fähnle, H. Dosch, and J. M. Sanchez. Spontaneous L1(2) order at Ni90Al10(110) surfaces: An x-ray and first-principles-calculation study. *Phys. Rev. Let.*, **87** 236102, (2001).

[131] H. L. Davis and J. R. Noonan. Rippled relaxation in the (110) surface of the ordered metallic alloy NiAl. *Phys. Rev. Let.*, **54** 566–69, (1985).

[132] L. Jurczyszyn, A. Krupski, S. Degen, B. Pieczyrak, M. Kralj, C. Becker, and K. Wandelt. Atomic structure and electronic properties of Ni3Al(111) and (011) surfaces. *Phys. Rev. B*, **76** 045101, (2007).

[133] V. Blum, C. Rath, G. Castro, M. Kottcke, L. Hammer, and K. Heinz. Ordered and disordered rippling in the CoAl(110)-(1x1) surface. *Surf. Rev. Let.*, **3** 1409–1415, (1996).

[134] M. Wuttig, Y. Gauthier, and S. Blügel. Magnetically driven buckling and stability of ordered surface alloys - Cu(100)C(2x2)Mn. *Phys. Rev. Let.*, **70** 3619–3622, (1993).

[135] J. Mathon. Magnetism at transition-metal surfaces. *Rep. Prog. Phys.*, **51** 1–56, (1988).

[136] M. J. Marcinkowski, M. E. Taylor, and F. X. Kayser. Relationship between atomic ordering and fracture in Fe-Al alloys. *J. Mater. Sci.*, **10** 406–414, (1975).

[137] M. P. Ryan, D. E. Williams, R. J. Chater, B. M. Hutton, and D. S. McPhail. Why stainless steel corrodes. *Nature*, **415** 770–774, (2002).

[138] M. Shimada, H. Kokawa, Z. J. Wang, Y. S. Sato, and I. Karibe. Optimization of grain boundary character distribution for intergranular corrosion resistant 304 stainless steel by twin-induced grain boundary engineering. *Acta Mater.*, **50** 2331–2341, (2002).

[139] L. Babout, T. J. Marrow, D. Engelberg, and P. J. Withers. X-ray microtomographic observation of intergranular stress corrosion cracking in sensitised austenitic stainless steel. *Mat. Sci. Technol.*, **22** 1068–1075, (2006).

[140] A. Jimenez-Gonzales and D. Schmeisser. Preparation and spectroscopic characterization of γ-Al_2O_3 thin films. *Surf. Sci.*, **250** 59–70, (1991).

[141] H. Mehrer and S. Divinski. Diffusion in metallic elements and intermetallics. *Def. Diff. Forum*, **289-292** 15–38, (2009).

[142] G. A. Somorjai and M. A. Van Hove. Adsorbate-induced restructuring of surfaces. *Prog. Surf. Sci.*, **30** 201–231, (1989).

[143] S. Ferrer and C. Comin. Surface diffraction beamline at ESRF. *Rev. Sci. Instrum.*, **66** 1674, (1995).

[144] P. Steadman, K. F. Peters, H. Isern, and S. Ferrer. Atomic relaxations near surface steps on Pt(977). *Phys. Rev. B*, **64** 125418, (2001).

[145] D. A. Walko and I. K. Robinson. Structure of Cu(115): Clean surface and its oxygen-induced facets. *Phys. Rev. B*, **59** 15446–15456, (1999).

[146] T. S. Rahman, A. Kara, and S. Durukanoglu. Structural relaxations, vibrational dynamics and thermodynamics of vicinal surfaces. *J.Phys.: Condensed Matter*, **15** S3197–S3226, (2003).

[147] E. Le Goff, L. Barbier, Y. Garreau, and M. Sauvage. Thermal roughening restrained by bulk chemical order: Cu-Pd(115) versus Cu(115) and Cu3Au(1112) surfaces. *Surf. Sci.*, **522** 143–160, (2003).

[148] A. Stierle. private communication.

[149] B. Meyer and M. Fähnle. Atomic defects in the ordered compound B2-NiAl: A combination of ab initio electron theory and statistical mechanics. *Phys. Rev. B*, **59** 6072–6082, (1999).

[150] G. Bozzolo, C. Amador, J. Ferrante, and R. D. Noebe. Modeling of the defect structure of beta-NiAl. *Scr. Met. et Mat.*, **33** 1907–1913, (1995).

[151] J. Gustafson, M. Borg, A. Mikkelsen, S. Gorovikov, E. Lundgren, and J. N. Andersen. Identification of step atoms by high resolution core level spectroscopy. *Phys. Rev. Let.*, **91** 056102, (2003).

[152] A. Stierle, C. Tieg, H. Dosch, V. Formoso, E. Lundgren, J. N. Andersen, L. Köhler, and G. Kresse. Surface core level shift observed on NiAl(1,1,0). *Surf. Sci. Let.*, **529** L263–L268, (2003).

[153] C. Tieg. *In-situ-Strukturuntersuchung von Keramik/Legierungsgrenzflächen*. Max-Planck-Institut für Metallforschung, Stuttgart, (2002).

[154] A. Stierle, V. Formoso, F. Comin, and R. Franchy. Surface x-ray diffraction study on the initial oxidation of NiAl(1,0,0). *Surf. Sci.*, **467** 85–97, (2000).

[155] J.-M. Zhang, D.-D. Wang, G.-X. Chen, and K.W. Xu. Surface structure and energy of B2 type intermetallic compound NiAl. *Appl. Surf. Sci.*, **254** 2540–2543, (2008).

[156] R.-P. Blum, D. Ahlbehrendt, and H. Niehus. Preparation-dependent surface composition and structure of NiAl(001): SPA-LEED and NICISS study. *Surf. Sci.*, **366** 107, (1996).

[157] E. Lundgren. private communication.

[158] T. T. Lay, M. Yoshitake, and W. Song. Epitaxial growth of well-ordered ultra-thin Al_2O_3 film on NiAl(110) by a single-step oxidation. *Appl. Surf. Sci.*, **239** 451–457, (2005).

[159] R.-P. Blum, D. Ahlbehrendt, and H. Niehus. Growth of Al_2O_3 stripes on NiAl(001). *Surf. Sci.*, **396** 176–188, (1998).

[160] J. P. Pierce and K. F. McCarty. Self-assembly and dynamics of oxide nanorods on NiAl(110). *Phys. Rev. B*, **71** 125428, (2005).

[161] E. Ozensoy, J. Szanyi, and C. H. F. Peden. Interaction of water with ordered θ-Al_2O_3 ultrathin films grown on NiAl(100). *J. Phys. Chem. B*, **109** 3431–3436, (2005).

[162] B. D. Patterson *et al.* The materials science beamline at the swiss light source: design and realization. *Nuc. Instr. Meth. Phys. Res. A*, **540** 42–67, (2005).

[163] G. Schmitz, P. Gassmann, and R. Franchy. Elemental steps in the growth of thin, amorphous gallium oxide films on CoGa(001). *Surf. Sci.*, **397** 339–345, (1998).

[164] C.S. Lent and P. I. Cohen. Diffraction from stepped surfaces. I. reversible surfaces. *Surf. Sci.*, **139** 121–154, (1984).

[165] E. Vlieg. A (2 + 3)-type surface diffractometer: Mergence of the z-axis and (2 + 2)-type geometries. *J. Appl. Cryst.*, **31** 198–203, (1998).

[166] P. Nolte. *In-situ Wachstumsuntersuchung von Oxid-Nanoinseln auf Legierungskristallen*. Max-Planck-Institut für Metallforschung, Stuttgart, (2004).

[167] Angle calculations for the 5-circle surface diffractometer of the materials science beamline at the swiss light source. http://sls.web.psi.ch/view.php/beamlines/ms/, (2007).

[168] P. I. Cohen, G. S. Petrich, P. R. Pukite, G. J. Whaley, and A. S.Arrott. Birth-death models of epitaxy: I. diffraction oscillations from low index surfaces. *Surf. Sci.*, **216** 222–248, (1989).

[169] A. Vlad, A. Stierle, M. Marsman, G. Kresse, I. Costina, H. Dosch, M. Schmid, and P. Varga. Metastable surface oxide on CoGa(100): structure and stability. *Phy. Rev. B*, page To be published, (2009/2010).

[170] The NIST reference on constants, units, and uncertainty. http://www.physics.nist.gov/cuu/, (2006).

List of Publications

V. Vonk, C. Ellinger, N. Khorshidi, A. Vlad, A. Stierle, and H. Dosch
In situ x-ray study of $Fe_3Al(110)$ subsurface superlattice disordering during oxidation
Physical Review B **78**, 165426 (2008)

C. Ellinger, V. Vonk, N. Khorshidi, A. Vlad, A. Stierle, and H. Dosch
In situ x-ray study of the oxidation of a vicinal NiAl(6,7,1) surface
New Journal of Physics **11**, 113004 (2009)

Danksagung

Ich möchte mich ganz herzlich bei all denjenigen bedanken, die zum Gelingen dieser Arbeit beigetragen haben. Mein besonderer Dank gilt Herrn **Prof. Dr. Helmut Dosch** für die freundliche Aufnahme am Max-Planck-Institut für Metallforschung, seine Diskussionsbereitschaft, sowie das Interesse mit dem er die Entwicklung dieser Arbeit verfolgte. Ebenso danke ich meinem Betreuer Herrn **Prof. Dr. Andreas Stierle** für die Vermittlung der experimentellen Fertigkeiten, die zahlreichen Ideen während den Experimenten, den fruchtbaren Gedankenaustausch bei der Datenanalyse und der Dateninterpretation, die schöne Zeit in seiner Gruppe sowie die konstruktive Mithilfe bei der Korrektur dieser Arbeit. Bei Herrn **Prof. Dr. Peter Michler** bedanke ich mich für die Übernahme des Mitberichts. Dank gilt auch Herrn **Prof. Dr. Manfred Rühle** für die Übernahme der kommissarischen Leitung der Abteilung, mit der er auch nach Prof. Doschs Berufung zum DESY-Direktor ein sorgenfreies Arbeiten am Institut ermöglichte.

Bei **Dr. Vedran Vonk** möchte ich mich für die Mithilfe bei zahlreichen Experimenten, die wissenschaftlichen und nicht-wissenschaftliche Diskussionen, sowie die Hilfe bei der Analyse der Daten bedanken. Ohne die unermüdliche Hilfe von **Navid Khorshidi** und **Dr. Alina Vlad** während den Strahlzeiten in Grenoble, Villingen, Karlsruhe und Lund wären die experimentellen Ergebnisse nicht möglich geworden. Dank natürlich auch für die Diskussionen und Gespräche, welche auch über den Tellerand der Wissenschaft hinausschauten. Auch den übrigen aktiven und ehemaligen Mitgliedern der Oxidationsgruppe, **Dr. Melissa Delheusy**, **Dr. Dmitry Kukuruznyak**, **Dr. Quang Vu Van**, **Dr. Philipp Nolte**, **Patrick Singer** und **Uta Hejral**, danke ich für die Hilfestellung bei Laborarbeiten, die wissenschaftlichen Diskussionen und die schöne Zeit in der Gruppe.

Die Ergebnisse der Fe_3Al-Oberfläche konnte ich auch mit **Prof. Dr. Manfred Fähnle** diskutieren, was sehr zu meinem theoretischen Verständnis beigetragen hat.

Für die exzellente technische Unterstützung möchte ich mich bei **Annette Weißhardt**, **Ralf Weigel**, **Frank Adams**, **Peter Schützendübe**, **Taufan Zimmer**, **Rolf Henes**, **Arnold Weible**, **Thomas Meisner** und **Ingrid Sorger** ganz herzlich bedanken. Auf meine Bürokollegen **Dr. Alexander Reicho**, **Dr. Markus Mezger** und **Mathias Schmidt** konnte ich stets zählen. In kritischer gegenseitiger Betrachtung unserer Experimente und Ergebnisse lernte ich Fragestellungen abseits meines Themengebiets kennen, wurde aber auch auf interessante Aspekte meiner eigenen Arbeit aufmerksam gemacht.

Für die gute Zusammenarbeit, die freundliche Arbeitsatmosphäre und die gemeinsame Zeit bei außerdienstlichen Unternehmungen möchte ich mich darüber hinaus bei allen

Mitarbeitern der ehemaligen Abteilung Dosch bedanken.

Schließlich danke ich meinen **Eltern** ganz herzlich, dass sie mir das Studium ermöglicht haben und in allen Dingen immer für mich da sind. Besonders und von ganzem Herzen möchte ich mich auch bei meiner Freundin **Nina** bedanken, dass sie mit mir durch Dick und Dünn geht und mir immer wieder die nötige Ablenkung von der Physik verschafft hat, um mich wieder mit klarem Kopf auf die Arbeit konzentrieren zu können.